Probing Supersymmetry with Recursive Jigsaw Reconstruction

1st December 2017

Marco Santoni

A Thesis Submitted for the Degree of Doctor of Philosophy in Physics

Supervisors:

Prof. Paul Jackson

Prof. Martin White

Department of Physics, School of Physical Sciences

I certify that this work contains no material which has been accepted for the award of any other degree or diploma in my name, in any university or other tertiary institution and, to the best of my knowledge and belief, contains no material previously published or written by another person, except where due reference has been made in the text. In addition, I certify that no part of this work will, in the future, be used in a submission in my name, for any other degree or diploma in any university or other tertiary institution without the prior approval of the University of Adelaide and where applicable, any partner institution responsible for the joint-award of this degree. I give consent to this copy of my thesis, when deposited in the University Library, being made available for loan and photocopying, subject to the provisions of the Copyright Act 1968. I also give permission for the digital version of my thesis to be made available on the web, via the University's digital research repository, the Library Search and also through web search engines, unless permission has been granted by the University to restrict access for a period of time.

I acknowledge the support I have received for my research through the provision of an Australian Government Research Training Program Scholarship.

Nessuno effetto è in natura senza ragione; intendi la ragione e non ti bisogna sperienza

La esperienza non falla, ma sol fallano i nostri giudizi, promettendosi di lei cose che non sono in sua potestà

Leonardo Da Vinci

Abstract

This thesis describes Recursive Jigsaw Reconstruction, a technique for analysing final state topologies with weakly interacting particles at collider experiments. Constructed to extract information from indirect hints of dark matter candidates, bases of observables are used for proposed analyses of proton-proton collision events at the Large Hadron Collider (LHC) focused on probing supersymmetry.

This dissertation presents a number of phenomenological studies targeting potential pair-production of supersymmetric partners of the Standard Model particles assuming a centre-of-mass collision energy of the LHC consistent with the designed energy of 14 TeV, for various luminosity scenarios.

The first is a partially inclusive study dedicated to probe compressed scenarios concerning the production of a pair of gluinos and the first two generations of squarks decaying to hadronic jets and neutralinos ($\tilde{g} \to qq\tilde{\chi}_1^0$ and $\tilde{q} \to q\tilde{\chi}_1^0$). In this scenarios the $\tilde{\chi}_1^0$ is considered to be the lightest supersymmetric particle (LSP). Putative gluinos would be discovered above 1 TeV with a LSP mass up to 800 GeV, while squarks would be excluded up to 900 GeV for an integrated luminosity of 100 fb^{-1} at LHC14.

Similar compressed investigations are dedicated to probe associated neutralino-chargino production events with initial state radiation focusing on final states with three leptons ($\tilde{\chi}_2^0 \to Z^*(l^+l^-)\tilde{\chi}_1^0$, $\tilde{\chi}_1^{\pm} \to W^{*\pm}(l^{\pm}\nu)\tilde{\chi}_1^0$) and potential exclusion limits are presented for the chargino pair-production for a data sample of 3 ab^{-1}.

Other studies are focused on the production of light scalar bottoms either directly or mediated by gluinos. The gluino-mediated sbottom pair-production in final states with four b-jets and missing transverse momentum ($\tilde{g} \to b\tilde{b}_1(b\tilde{\chi}_1^0)$) is investigated for several values of the masses of the three superparticles. Gluinos could be discovered above 2 TeV and neutralinos up to 500 GeV almost independently of the scalar bottom mass with an integrated luminosity of 50 fb^{-1}.

The results of the proposed analysis for the direct production of light sbottoms in final

states with two b-jets and missing transverse momentum are presented in the $M_{\tilde{b}_1}$ vs $M_{\tilde{\chi}_1^0}$ plane for an integrated luminosity of 50 fb^{-1}. Assuming a systematic uncertainty of the 20% for the SM background, superpartner of the bottom quark would be excluded at the 95% CL with masses above 1.2 TeV and LSP with masses up to 400 GeV, while in the compressed regime, results demonstrate the third generation scalar would be excluded with masses above 800 GeV, well beyond the current experimental limit.

Acknowledgements

I would like to express my gratitude to the smart advisors and colleagues I had the opportunity to collaborate and initiate friendships. Firstly, I really want to thank my supervisor Paul Jackson for his guidance and support during this years. Without him and his inventiveness for kinematic observables, this journey of my life would have been impossible. A big thank you goes to my co-supervisor Martin White for his dedication and continuous feedback to this work. His passion for physics is contagious. I want to thank Christopher Rogan who first introduced me to the maths and philosophy of the RJR technique, for his help and inspirational conversations any time he has been in Adelaide. I would like to thank all the guys of the CoEPP group in Adelaide I had the opportunity to have productive and casual talks: Andreas, Larry, Abhishek, Anum, Damir, Jason and Lei and You for their precious help in the collaboration for the project dedicated to the SM process Higgs plus $t\bar{t}$ in the dileptonic channel.

Outside the university, my gratitude goes most of all to my girlfriend Jillian. She has always been a pillar at my side, no matter what and her love and passion have inspired me and made me stronger. I want to thank her family and my friend Alberto who has supported me during these years. With him and all the folks of the Uni football, I have spent the most enjoyable recreational time. This journey has also been possible thanks to the great support from distance received by the numerous Italian friends and in particular for the several chats had with Paolo, Mirco and Giorgio and with my former supervisor during my MPhys in Perugia, Orlando Panella.

Finally, I want to dedicate this thesis to my parents Vittorio and Rosella for their love and support.

Contents

Chapter 1

Introduction

The realisation of the Large Hadron Collider (LHC) and its experiments has opened a new frontier in high energy physics. Armed with an increasing data-set of proton-proton collisions, experimentalists have the possibility to shed light on our understanding of fundamental phenomena at the smallest length scales ever achieved, with a multitude of choices for the search of signatures of Beyond the Standard Model (BSM) physics. This thesis concerns the introduction of an original technique for analysing such events at collider experiments and proposes phenomenological studies in the context of Supersymmetry (SUSY).

Firstly, a brief overview of the Standard Model (SM) of particle physics, the current theoretical framework describing with remarkable success the fundamental particles and their interactions, is presented in Chapter 2. Then an introduction to some of its failings together with possible theoretical solutions is given. In particular, the supersymmetric extension of the SM is discussed in some detail.

Secondly, the typical strategy for probing beyond the Standard Model signatures at proton-proton colliders is given in Chapter 3. A brief description of the Large Hadron Collider and its two main experiments ATLAS and CMS, is followed by a discussion of many analysis tools used in the rest of the thesis along with the canonical observables handled in the experimental analyses.

In Chapter 4, Recursive Jigsaw Reconstruction is presented: a technique for probing final state topologies containing weakly interacting particles. Specific examples are used to illustrate the method, from the two hemispheres tree view, typical of supersymmetric topologies, to the compressed scenarios phenomenology.

The remaining chapters describe several proposed physics analyses based on the Recursive Jigsaw Reconstruction technique. A study for gluino and squark pair-production is presented in Chapter 5. The focus is on compressed scenarios in fully hadronic final states. Chapter 6 contains two proposed analyses for compressed mass spectra of electroweakinos in leptonic decay products. A study of gluino mediated scalar bottom pair-production is described in Chapter 7, while in Chapter 8 the RJR technique is applied for probing the direct production of sbottoms employing a more sophisticated strategy. Other studies in which the author has had part and possible future works are discussed in Chapter 9. Finally a summary of the main results obtained and the conclusions are presented in Chapter 10.

Chapter 2

Theoretical Motivation

2.1 The Standard Model in a nutshell

2.1.1 Introduction to the Standard Model

The Standard Model (SM) of particle physics is a quantum field theory describing all the known elementary constituents and their strong, weak and electromagnetic interactions [1–4]. Theoretical calculations and experimental measurements agree with remarkable precision for a wide variety of phenomena. Forces and constituents are treated as point-like fundamental particles with an internal angular momentum quantum number called spin. Two main categories emerge from the spin value: fermions are half-integer spin particles respecting Fermi-Dirac statistics, while bosons are integer spin particles respecting Bose-Einstein statistics.

Spin $1/2$ elementary fermions are the constituents of matter and are composed of two groups, quarks and leptons, each with three families or generations. Each particle has a corresponding anti-matter counterpart with opposite quantum numbers but the same mass. Quarks interact via all three forces of the SM and are the only fermions to interact strongly. The charged leptons interact via the electromagnetic and weak forces while neutrinos are neutral leptons, usually assumed to be massless in the SM

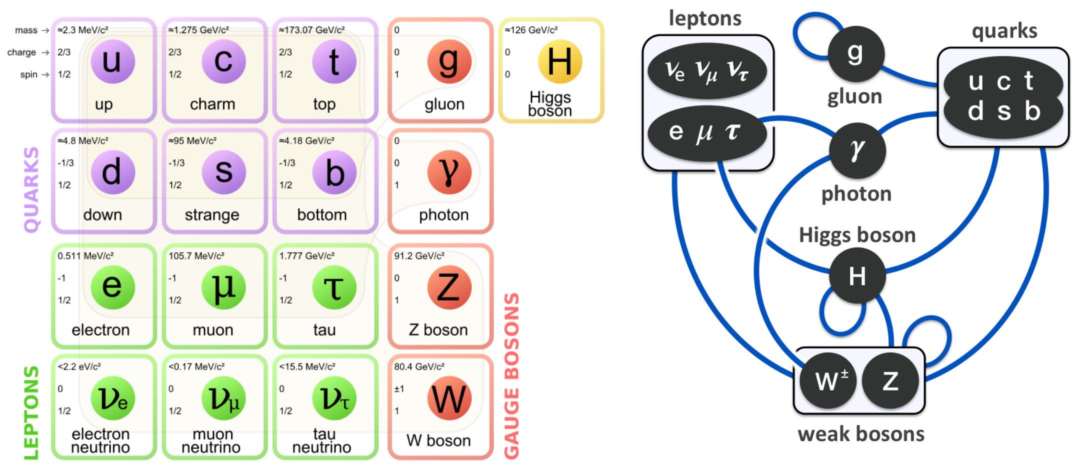

Figure 2.1.1: Schematic representation of the Standard Model elementary particles and their interactions.

and interact only weakly. Charged fermions are classified with an increasing mass into three generations which appear identical in every other aspect.

Spin 1 elementary bosons are force carriers or mediators of the forces acting on fermions. The photon (γ), W/Z bosons and gluons (g) are the mediators of the electromagnetic, weak and strong forces, respectively.

The discovery of the Higgs boson (2012), after the top quark (1995) and tau neutrino (2000), has located the last missing piece of the Standard Model of particle physics. The SM-like Higgs is a scalar (spin 0 particle) responsible for giving masses to all the other known particles.

Figure 2.1.1 shows the particles of the SM and how they interact. Electrons, muons and taus have electric charge defined by convention to be -1 and 1 for their anti-particle. The quarks have fractional electric charges, respectively $+^2/_3$ and $-^1/_3$, for each up and down *type* quark for each family. Quarks exist in three different colour species, whilst gluons carry colour charge with eight independent combinations of two separate colour labels, so they allow the quarks of different colours to interact through their exchange. The current theoretical framework includes a total of 61 fundamental particles.

The weak interaction couples to the leptons in each generation (see Figure 2.1.1). The vector bosons couple to the weak eigenstates of the quarks which correspond to a linear combination of the mass eigenstates ("physical" quarks) mixed by the Cabibbo-Kobayashi-Maskawa (CKM) matrix. The result is that the weak interaction violates quark flavour. Kobayashi and Maskawa proposed the existence of the third generation, necessary for the CP-violating phase, before the second one was experimentally fully discovered. At the current time, there is no experimental evidence for a fourth generation and neutrino sector experiments suggest only three families.

The Standard Model does not explain several phenomena and so it fails to be a "*Theory of everything*". Firstly, it does not incorporate general relativity which is a very weak force on microscopic scales, and for which a quantum description is currently unavailable.[1] It does not contain any viable dark matter particle candidate that possesses all of the required properties deduced from observational cosmology (described in Section 2.2.1). The model does not address the strong CP problem or why QCD does not break CP-symmetry. It does not explain why our universe is dominated by matter with minuscule amounts of anti-matter. The reason for there being exactly three generations of particles is an unsolved question. It does not predict a correct unification at the GUT scale of the running interaction-strength coupling (described in Section 2.2.3).

Every theory can be considered an effective theory, or an approximation, of an underlying theory valid for higher energy scale or shorter distances. When the energy scale of new physics is very large, such as the GUT or Plank scale, a *hierarchy problem* arises: why does the Higgs mass at the electroweak scale result in a large discrepancy between gravity and the other forces (described in Section 2.2.2)?

These are some of the most important unsolved problems in physics. In order to fix its inconsistencies, the SM needs some kind of extension. Beyond the Standard Model (BSM) physics is the paradigm in which theoretical and experimental physicists all around the world try to brighten the darkness surrounding our understanding of Nature (Figure 2.2.1).

[1] The Einstein theory of gravitation is not renormalizable when quantised [5].

2.1.2 Symmetry and Quantum Field Theory

In physics the concept of symmetry plays a pivotal role in the investigation of Nature's behaviour. We can imagine, for example, that the total amount of energy of an isolated system must remain constant if we rotate or translate the system *in toto*, or, in other words, if we change our frame of reference. For the microscopic as well as the macroscopic world that we experience, symmetries are associated with conservation laws. In the microscopic world the mathematical paradigm describing physical phenomena is Quantum Field Theory (QFT). Point-like entities are generalised to quantised fields permeating the whole space.

The starting point is the action defined as the space-time integral of the Lagrangian density[2]

$$S = \int d^4x \mathcal{L}(\Phi(x), \partial_\mu \Phi(x)), \tag{2.1.1}$$

which depends on a generic field $\Phi(x)$ and its derivatives.

The dynamics of, and interactions between, different fields are expressed by the Euler–Lagrange equation:

$$\partial_\mu \left(\frac{\delta \mathcal{L}}{\delta \left(\partial_\mu \Phi \right)} \right) - \frac{\delta \mathcal{L}}{\delta \Phi} = 0. \tag{2.1.2}$$

Whenever the action has a continuous symmetry, there is a procedure, known as Noether's theorem, which allows us to construct a conserved current, J^μ, where

$$\partial_\mu J^\mu = 0 \tag{2.1.3}$$

and the associated charge

$$Q \equiv \int d^3x J^0 \tag{2.1.4}$$

is a constant of the motion

$$\frac{dQ}{dt} = 0. \tag{2.1.5}$$

[2]In this work the author refers to $\mathcal{L}$ simply as the Lagrangian from now on.

In the quantum theory, this is translated to

$$[Q, H] = 0 \tag{2.1.6}$$

and the transformation is said to be a symmetry of the Hamiltonian. The analogy with the macroscopic example is clear: the total energy of the system is unchanged for such transformation.

The SM framework is a relativistic QFT based on *gauge* transformations: internal symmetry transformations related to abstract transformations of the matter fields. The application of the concept of symmetry to the Lagrangian by imposing local gauge invariance introduces new vector fields. The introduction of *spontaneous symmetry breaking* and the *Higgs mechanism* are necessary to explain the experimental evidence for the massive W and Z bosons. The SM is based on the internal symmetries of the unitary product group $SU(3)_C \times SU(2)_L \times U(1)_Y$, where C, L and Y are quantum numbers referred to as colour, left-handed weak isospin and hypercharge.

2.1.3 Quantum Electrodynamics

Quantum electrodynamics (QED) is the prototype gauge field theory. The laws describing the phenomena involving electrically charged particles and light are invariant under complex phase rotations applied to particle fields. In group theory jargon, QED is based on the Abelian $U(1)_Q$ symmetry group, where the electric charge (Q) is the generator. Feynman used to refer to QED as "*the jewel of physics*" because of its remarkably accurate predictive power.

The Lagrangian of a free fermionic field is described by the Dirac formulation

$$\mathcal{L}_D = i\bar{\Psi}_D\gamma^\mu\partial_\mu\Psi_D - m\bar{\Psi}_D\Psi_D, \tag{2.1.7}$$

where Ψ_D is a four component Dirac field.[3] The Lagrangian is invariant under global transformations, but when we promote a global transformation to a local gauge one[4]

$$\Psi_D \rightarrow e^{i\theta(x)}\Psi_D \tag{2.1.8}$$

an extra term appears in the Lagrangian. The gauge invariance is restored by adding an additional term

$$\mathcal{L} \rightarrow \mathcal{L}_D - g_e \bar{\Psi}_D \gamma^\mu A_\mu \Psi_D \tag{2.1.9}$$

where the gauge field A_μ, transforms

$$A_\mu \rightarrow A_\mu + \partial_\mu \lambda, \qquad \text{with} \;\; \lambda(x) = -\frac{\theta(x)}{g_e}. \tag{2.1.10}$$

A free term must be added to the Lagrangian. Defining the electromagnetic field tensor $F_{\mu\nu} \equiv \partial_\mu A_\nu - \partial_\nu A_\mu$ we can write a non interacting Lagrangian for the field A_μ

$$\mathcal{L} = -\frac{1}{4}F^{\mu\nu}F_{\mu\nu} + \frac{1}{2}m_A^2 A^\mu A_\mu, \tag{2.1.11}$$

where the mass term is not invariant under transformations of the form given by Eq. 2.1.10. The vector field is imposed to be massless ($m_A = 0$) in order to preserve the local gauge invariance. Finally the QED Lagrangian is

$$\mathcal{L}_{QED} = \bar{\Psi}_D \left(i\gamma^\mu \mathcal{D}_\mu - m\right)\Psi_D + \mathcal{L}_\gamma \tag{2.1.12}$$

where $\mathcal{L}_\gamma = -\frac{1}{4}F^{\mu\nu}F_{\mu\nu}$ is the free massless photon term and $\mathcal{D}_\mu \equiv \partial_\mu + i g_e A_\mu$ is the covariant derivative.

QED, like all the gauge theories of the SM, is a renormalizable theory. The infinities resulting from loop Feynman diagrams contributing to fields self-energies can be eliminated from the theory. The physical consequence is that the QED coupling $g_e(E)$, or

[3] For more details see Section 2.1.8.

[4] In QED the convention for the electric charge is $Q = -1$.

the fine structure constant $\alpha_e(E) = \frac{g_e^2(E)}{4\pi}$, is a function of energy, running with the scale of the interaction.

2.1.4 Quantum Chromodynamics

In order to explain the existence of baryons like Δ^{++}, Han and Nambu introduced a gauge group of dimension $N = 3$ following the Yang and Mills theory [6] describing Non-Abelian local gauge transformations. The transformation of Quantum Chromodynamics (QCD) [7,8] belongs to the $SU(3)_C$ group, where C is the colour charge. Imposing the local gauge invariance under $SU(3)_C$ to the quark fields introduces $N^2 - 1 = 8$ gauge coloured fields called gluons.

The six flavour quarks (q) are fermionic fields (Ψ_D) populating a triplet

$$\psi \equiv \begin{pmatrix} q_r \\ q_g \\ q_b \end{pmatrix}, \ \bar{\psi} \equiv (\bar{q}_r, \bar{q}_g, \bar{q}_b) \tag{2.1.13}$$

which allows us to write the QCD Lagrangian in a very compact form and similar to the QED case

$$\mathcal{L}_{QCD} = \bar{\psi}\left(i\gamma^\mu \mathcal{D}_\mu - m\right)\psi - \frac{1}{4}\mathbf{G}^{\mu\nu} \cdot \mathbf{G}_{\mu\nu}, \tag{2.1.14}$$

where the covariant derivative and the field strength are defined [5]

$$\mathcal{D}_\mu \equiv \partial_\mu - ig_s \mathbf{T} \cdot \mathbf{A}_\mu, \tag{2.1.15}$$

$$\mathbf{G}_{\mu\nu} \equiv \partial_\mu \mathbf{A}_\nu - \partial_\nu \mathbf{A}_\mu - ig_s\left[\mathbf{A}_\mu, \mathbf{A}_\nu\right] . \tag{2.1.16}$$

The generators $T^a \equiv \frac{\lambda^a}{2}$, are the 8 Gell-Mann matrices apart from a factor, satisfying the non-commuting algebra

$$\left[\lambda^a, \lambda^b\right] = 2if^{abc}\lambda^c, \tag{2.1.17}$$

[5] The last terms in Eq. 2.1.16 and 2.1.15 are often defined with opposite signs.

where f^{abc} is the constant structure of the group and a, b and c the colour labels. The commutator in Eq. 2.1.16

$$[\mathbf{A}_\mu, \mathbf{A}_\nu]^a = i f^{abc} A^b_\mu A^c_\nu \tag{2.1.18}$$

gives rise to the triple and quartic gluon coupling terms and manifests the peculiar nature of the strong interaction: gluons interact with each other because they carry colour charge.

Two key features of QCD are *asymptotic freedom* and *confinement*. The QCD beta function, which describes the running of $\alpha_s(E)$ as discussed in paragraph 2.2.3, is negative and decreases logarithmically with increasing energy. At the collision energies reached by the modern collider experiments such as the LHC, the quarks and gluons of colliding protons interact directly: the partons are practically *free* at very short distances.

Perturbative theories cannot be used at a lower energy where baryons and mesons are observed as colour singlets. Confinement refers to the impossibility for coloured particles to be isolated and so detected individually. The consequence of confinement is that it causes free partons to hadronise. In order to understand the hadronisation phenomenon, we can imagine two quarks pushed apart from each other from their kinetic energies while the gluon fields pull them together, forming characteristic narrow tubes of colour charge. If there is enough energy to “separate” the two quarks, at some point it becomes energetically favourable for a new quark/anti-quark pair to appear from the vacuum along the colour tube. For very energetic coloured particles, this process will repeat recursively. High energy quarks and gluons produced in collisions reach the detector as a collimated spray referred to as a *jet* of hadrons.

2.1.5 Electroweak unification

The unification of the electromagnetic and weak forces $SU(2)_L \times U(1)_Y$ was first suggested by Glashow in 1961 [9]. The weak current is constructed from the $SU(2)_L$ group of weak isospin which is observed to only couple to left-handed fermions or right-handed anti-fermions. $U(1)_Y$ is the group of weak hypercharge, where the hypercharge[6]

$$Y = Q - I_3/2 \tag{2.1.19}$$

is the average electric charge of the multiplet, Q is the electric charge and I_3 is the third component of weak isospin. The chiral-left component of the electric charged leptons and respective neutrinos belong to the $SU(2)_L$ doublet, while the chiral-right electron, muon and tau are in their own singlet. Optionally one could introduce to the SM a *sterile* particle, namely not interacting via the weak force, such as a chiral-right neutrino or chiral-left antineutrino. For the weak interaction up-type quarks behave like neutrinos while down-type quarks like charged leptons

$$\begin{gathered}\psi_L^{doublet} \equiv \begin{pmatrix} \nu_L^e \\ e_L \end{pmatrix} = \begin{pmatrix} \nu_e \\ e \end{pmatrix}_L, \begin{pmatrix} \nu_\mu \\ \mu \end{pmatrix}_L, \begin{pmatrix} \nu_\tau \\ \tau \end{pmatrix}_L, \\ \begin{pmatrix} u \\ d \end{pmatrix}_L, \begin{pmatrix} c \\ s \end{pmatrix}_L, \begin{pmatrix} t \\ b \end{pmatrix}_L,\end{gathered} \tag{2.1.20}$$

$$\psi_R^{singlet} \equiv e_R,\ \mu_R,\ \tau_R,\ u_R,\ d_R,\ c_R,\ s_R,\ t_R,\ b_R. \tag{2.1.21}$$

Through the imposition of local gauge invariance, four new massless gauge bosons with spin 1 are introduced. The covariant derivative is defined

$$\mathcal{D}_\mu \equiv \partial_\mu - ig_w \boldsymbol{\tau} \cdot \mathbf{W}_\mu - ig_Y Y B_\mu, \tag{2.1.22}$$

where g_w and g_Y are the weak and electromagnetic running coupling constants, $\tau^i = {}^{\sigma^i}\!/_2$ are the 3 generators, or the Pauli matrices apart from a factor, of $SU(2)_L$.

[6]Sometimes the weak hypercharge is defined as twice the average electric charge of the multiplet $Y/2 = Q - I_3$

The Dirac Lagrangian for the electro-weak theory is

$$\mathcal{L}_{EW} = \bar{\psi}\left(i\gamma^{\mu}\mathcal{D}_{\mu} - m\right)\psi - \frac{1}{4}\mathbf{W}^{\mu\nu}\cdot\mathbf{W}_{\mu\nu} - \frac{1}{4}B^{\mu\nu}B_{\mu\nu}, \tag{2.1.23}$$

where ψ are chiral-left or chiral-right fields. The term W_{μ} in the covariant derivative is zero for right-handed eigenstates.

2.1.6 Higgs Mechanism and spontaneous electroweak symmetry breaking

The weak nature of the weak interaction was known before a modern version of QFT was introduced. Fermi was the first to describe the nuclear beta decay $n \to p\,e\,\bar{\nu}_e$ with the introduction of the neutrino. The half-life of the neutron is about 15 minutes and the Hamiltonian H was approximated by a contact interaction

$$H = \frac{G_F}{\sqrt{2}}(\bar{p}\gamma^{\mu}n)(\bar{e}\gamma_{\mu}\nu_e) + h.c., \tag{2.1.24}$$

where the Fermi constant is a parameter with a small numerical value related to the proton mass

$$G_F \simeq \frac{10^{-5}}{m_p^2}. \tag{2.1.25}$$

The discovery of parity violation suggested a vector-axial theory and when the weak interaction was incorporated in the structure of a gauge theory, the necessity of massive boson fields was clear. The weakness of the weak force is not related to the coupling and it is theoretically solved with the introduction in the Feynman propagator of a mass term.

Weinberg and Salam provided a complete solution utilising the *Higgs mechanism* capable of incorporating massive gauge fields through spontaneous electroweak symmetry breaking (EWSB) [10–15]. The Higgs acquires a non-zero vacuum expectation value (VEV) which breaks the groups $SU(2)_L \times U(1)_Y$.

The idea is to introduce four real scalar fields ϕ_i or a complex $SU(2)_L$ doublet of scalar fields, as proposed by Weinberg in 1967. One adds to the $\mathcal{L}_{EW}$ in Eq. 2.1.23 a $SU(2)_L \times U(1)_Y$ gauge invariant Lagrangian for the scalar field ϕ

$$\mathcal{L}_\phi = \left|(\partial_\mu - i g_w \boldsymbol{\tau} \cdot \mathbf{W}_\mu - i g_Y Y B_\mu)\phi\right|^2 - V(\phi) \tag{2.1.26}$$

where $|\cdot|^2 = (\cdot)^\dagger (\cdot)$ and the four fields ϕ_i are arranged in an isospin doublet with hypercharge $Y = \frac{1}{2}$

$$\phi = \begin{pmatrix} \phi^+ \\ \phi^0 \end{pmatrix} \equiv \begin{pmatrix} \frac{1}{\sqrt{2}}(\phi_1 + i\phi_2) \\ \frac{1}{\sqrt{2}}(\phi_3 + i\phi_4) \end{pmatrix}. \tag{2.1.27}$$

The potential in Eq. 2.1.26 can be written

$$V = \mu^2 \phi^\dagger \phi + \lambda \left(\phi^\dagger \phi\right)^2, \tag{2.1.28}$$

with $\mu^2 < 0$ and $\lambda > 0$ and can be imagined as the famous "sombrero" or "Mexican hat" shape for each complex field.

Minimising the potential one finds for the ground state the relation

$$\phi^\dagger \phi = -\frac{\mu^2}{2\lambda}. \tag{2.1.29}$$

The choice of one of the ground states spontaneously breaks the symmetry: the intrinsic symmetry of the Lagrangian is *hidden* by the arbitrary choice of an asymmetric vacuum. The usual choice in literature for the vacuum expectation value is

$$\phi_0 = \frac{1}{\sqrt{2}} \begin{pmatrix} 0 \\ v \end{pmatrix}, \tag{2.1.30}$$

because one can only allow neutral scalars to acquire a VEV if one wants the conservation of electric charge. The Weinberg and Salam theory retains a massless photon. Any choice of ϕ_0 which breaks the symmetry will generate a mass for the corresponding gauge boson as will be clear in the next paragraph. The choice in Eq. 2.1.30 is suitable because the vacuum is left invariant by subgroup $U(1)_Q$ and the corresponding gauge boson remains massless:

$$Q\phi_0 = 0 \tag{2.1.31}$$

which is valid just for the combination expressed in Eq. 2.1.19.

When one expands around the vacuum, because of the $SU(2)_L$ gauge invariance, one can simply substitute the expression

$$\phi = \frac{1}{\sqrt{2}} \begin{pmatrix} 0 \\ v + H(x) \end{pmatrix} \tag{2.1.32}$$

in the Lagrangian , where $H(x)$ is the famous Higgs boson of the SM. The Higgs field can be imagined as the excitation along the real radial direction of the Mexican hat. The generic expansion of the scalar field $\varphi = \frac{1}{\sqrt{2}}(v+\eta+i\xi)$ can be chosen fixing $\eta \to H$ and $\xi \to \theta$ real, $\varphi \to \frac{1}{\sqrt{2}}(v + H(x))e^{i\theta(x)/v}$. The unwanted massless Goldstone boson ($\xi \to \theta$) actually does not appear in the theory and its kinetic term is reabsorbed in the definition of the gauge field. The net result is a mass for the gauge field coming from the VEV. For $SU(2)_L$ the theory is parametrised with 4 real fields, but only the Higgs remains in the Lagrangian while $\theta_1, \theta_2, \theta_3$ are "eaten" by the gauge bosons providing the masses for the $W^{\pm}$ and Z bosons of the SM.

The Higgs mechanism refers to the combination of gauge invariance and spontaneous symmetry breaking applied to the electroweak theory, eventually providing mass for the Higgs itself, for the fermions and for the vector bosons of the SM.

2.1.7 Masses of the SM particles

Firstly, the Higgs mechanism predicts the existence of a massive Higgs boson. The quartic term in the Higgs potential (Eq. 2.1.28) gives rise to the mass for the Higgs field

$$m_H = \sqrt{2\lambda}v. \tag{2.1.33}$$

The 3 massless Goldstone bosons from $SU(2)_L$ are eaten by the gauge fields. In other words, these degrees of freedom (d.o.f.) become the longitudinal polarisations of the massive vector bosons of the SM. The W and Z bosons and the photon are linear combinations of the weak and hypercharge fields

$$W^{\pm}_{\mu} = \frac{1}{\sqrt{2}}(W^1_{\mu} \mp iW^2_{\mu}), \tag{2.1.34}$$

$$Z_{\mu} = \cos\theta_W W^3_{\mu} - \sin\theta_W B_{\mu}, \tag{2.1.35}$$

$$A_{\mu} = \cos\theta_W B_{\mu} + \sin\theta_W W^3_{\mu}, \tag{2.1.36}$$

where θ_W is the Weinberg angle satisfying the relation $\tan\theta_W = \frac{g_Y}{g_w}$. Taking the term $\left|(ig_w\frac{\boldsymbol{\sigma}}{2}\cdot\mathbf{W}_{\mu} - ig_Y Y B_{\mu})\phi\right|^2$ in Eq. 2.1.26 and comparing the expected mass terms with the terms proportional to the VEV of the Higgs, one has

$$M_{W^{\pm}} = \frac{1}{2}vg_w \tag{2.1.37}$$

$$M_Z = \frac{1}{2}v\sqrt{g_w^2 + g_Y^2} \tag{2.1.38}$$

where the ratio between the masses can be expressed by θ_W as $\frac{M_{W^{\pm}}}{M_Z} = \cos\theta_W$.

Finally, the field ϕ couples with left and right-handed fermionic fields providing a mass for them. For the electron one can write the interaction

$$\mathcal{L}^{int}_{e\phi} = -y_e\left[(\bar{\nu}_e, \bar{e})_L \begin{pmatrix} \phi^+ \\ \phi^0 \end{pmatrix} e_R + \bar{e}_R\left(\phi^-, \bar{\phi}^0\right)_L \begin{pmatrix} \nu_e \\ e \end{pmatrix}_L\right] \tag{2.1.39}$$

and for the EWSB one can simply substitute the Eq. 2.1.30

$$\mathcal{L}^{int}_{e\phi} = -\frac{y_e}{\sqrt{2}}v(\bar{e}_L e_R + \bar{e}_R e_L) - \frac{y_e}{\sqrt{2}}(\bar{e}_L e_R + \bar{e}_R e_L)H. \tag{2.1.40}$$

The actual mass of the electron $m_e = \frac{y_e v}{\sqrt{2}}$, and all other fermion masses, is not predicted since y_e is arbitrary. In a similar way the masses for the quarks are generated, but for the up-type quarks one rewrites the Higgs doublet with an opposite hypercharge $\phi_c = -i\sigma_2\phi^*$, which transforms identically to ϕ for the $SU(2)_L$ proprieties. The parameter $v \sim 246$ GeV is the scale responsible for all the masses of the SM. The Yukawa couplings are related to the mass of the fermions, as discussed for the electron, via the equation

$$m_f = \frac{y_f v}{\sqrt{2}} \tag{2.1.41}$$

and their different values are experimentally measured with an increasing accuracy.

The Higgs is responsible for giving mass to all the known fundamental particles of the SM. It must be pointed out, however, that the masses of colourless mesons and baryons are not the simple sums of the valence quark masses. The hadronic mass of the universe is mostly made of protons and neutrons and its value is a consequence of the QCD effects. Furthermore, the baryonic matter accounts for barely ∼5% of the total energy of our universe.

2.1.8 Some conventions and the SM in two-component spinors representation

QED and QCD are parity-conserving theories and the four-component fermion notation is well-suited. However, it is natural to employ Weyl spinors to describe phenomena at and above the scale of electroweak symmetry breaking. Moreover, the two-component fermion notation is particularly useful for the description of supersymmetry. Herein, the writer presents a brief overview of the notations and conventions used, and how the SM can be described with the Weyl spinors.

The “west-coast” metric is

$$g_{\mu\nu} = g^{\mu\nu} = \mathrm{diag}\,(1, -1, -1, -1) \tag{2.1.42}$$

with the position, momentum and derivative four-vectors given by

$$x^\mu = (t, \bar{\mathbf{x}}),\; p^\mu = (E, \bar{\mathbf{p}}) \text{ and } \partial_\mu \equiv \frac{\partial}{\partial x^\mu} = (\partial_t, \bar{\nabla}). \tag{2.1.43}$$

The projector operators, or chiral operators, are expressed in terms of the γ_5 matrix via

$$P_L = \frac{(1-\gamma_5)}{2}, \qquad P_R = \frac{(1+\gamma_5)}{2}, \quad \text{with } \gamma^5 = \begin{pmatrix} -I & 0 \\ 0 & I \end{pmatrix} \tag{2.1.44}$$

and select the left-handed and right-handed two-component of a Dirac field

$$\Psi_D = \begin{pmatrix} \psi_L \\ 0 \end{pmatrix} + \begin{pmatrix} 0 \\ \psi_R \end{pmatrix} = P_L\Psi_D + P_R\Psi_D = \begin{pmatrix} \xi_\alpha \\ \chi^{\dagger\dot{\alpha}} \end{pmatrix}. \tag{2.1.45}$$

The γ-matrices appearing in the covariant formulation of the Dirac Lagrangian (Eq. 2.1.7) are defined as

$$\gamma^\mu = \begin{pmatrix} 0 & \sigma^\mu \\ \bar{\sigma}^\mu & 0 \end{pmatrix} \tag{2.1.46}$$

where $\sigma^\mu = (\sigma^0, \vec{\sigma})$ and $\bar{\sigma}^\mu = (\bar{\sigma}^0, -\vec{\sigma})$ with $\sigma^0 = \bar{\sigma}^0 = \begin{pmatrix} 1 & 0 \\ 0 & 1 \end{pmatrix}$ and $\vec{\sigma}$ the Pauli matrices: $\sigma^1 = \begin{pmatrix} 0 & 1 \\ 1 & 0 \end{pmatrix}$, $\sigma^2 = \begin{pmatrix} 0 & -i \\ i & 0 \end{pmatrix}$ and $\sigma^3 = \begin{pmatrix} 1 & 0 \\ 0 & -1 \end{pmatrix}$.

In the last term of Eq. 2.1.45 one uses the same convention utilised in [16], with

$$\bar{\Psi}_D = \Psi_D^\dagger \beta = \Psi_D^\dagger \begin{pmatrix} 0 & I \\ I & 0 \end{pmatrix} = \begin{pmatrix} \chi^\alpha \; \xi^\dagger_{\dot{\alpha}} \end{pmatrix}. \tag{2.1.47}$$

All the fermionic d.o.f. can be described using only left-handed ($\frac{1}{2}$,0) fermions ψ_α and their conjugates

$$\psi^\dagger_{\dot{\alpha}} \equiv (\psi_\alpha)^\dagger = (\psi^\dagger)_{\dot{\alpha}}. \tag{2.1.48}$$

In the two-component representation the Dirac Lagrangian is

$$\mathcal{L}_D = i\xi^\dagger \bar{\sigma}^\mu \partial_\mu \xi + i\chi^\dagger \bar{\sigma}^\mu \partial_\mu \chi - m\left(\xi\chi + \chi^\dagger \xi^\dagger\right), \tag{2.1.49}$$

while for a Majorana spinor $\chi = \xi$ the Lagrangian becomes

$$\mathcal{L}_M = i\xi^\dagger \bar{\sigma}^\mu \partial_\mu \xi - \frac{m}{2}\left(\xi\xi + \xi^\dagger \xi^\dagger\right). \tag{2.1.50}$$

Any theory involving fermions can be written in terms of only left-chiral Weyl spinor. For the Standard Model the Lagrangian can be summarised as

$$\mathcal{L}_{SM} = \mathscr{F}^\dagger \left(i\sigma^\mu \mathscr{D}_\mu - \mathcal{M}\right) \mathscr{F} - \frac{1}{4}\mathscr{A}^{\mu\nu}\mathscr{A}_{\mu\nu} + \left|\mathscr{D}_\mu H\right|^2 + \mathcal{L}_{M(\mathscr{B})} + \mathcal{L}^{int}_{\mathscr{X}H}, \tag{2.1.51}$$

where all the flavour and colour indices are removed. The first term is the fermion Lagrangian with $\mathscr{F}$ the left-handed piece of a Dirac spinor populating the $SU(2)_L$ doublet or the conjugate of the right-handed piece populating the singlet. When $\mathscr{F}$ refers to a quark (anti-quark), the field is one of the three colour in the 3 ($\bar{3}$) representation. $\mathscr{D}_\mu$ is the appropriate covariant derivative of the SM for the field. The second term summarises the free contributions of the gauge bosons ($\mathscr{A}^\mu$). The third term is the free contribution for the scalar of the SM. The fourth term is the mass term for the massive bosons $\mathcal{L}_{M(\mathscr{B})} = \frac{1}{2}m_H^2 H^2 + M_W^2 W^+W^- + \frac{1}{2}M_Z^2 Z_\mu^2$. The fifth term is the interaction between the Higgs field and the other particles ($\mathscr{X}$) of the SM $\mathcal{L}^{int}_{\mathscr{X}H} = \mathcal{L}^{int}_{\mathscr{F}H} + \mathcal{L}^{int}_{\mathscr{A}H}$.

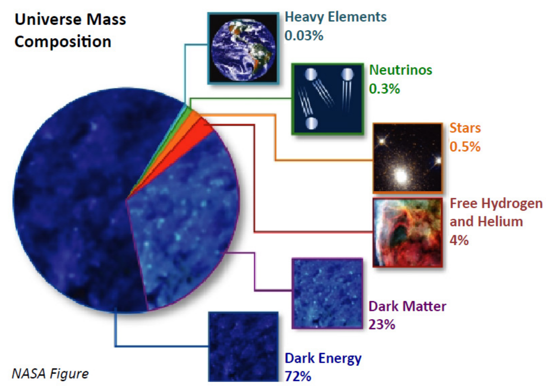

Figure 2.2.1: Composition of the Universe.

2.2 Shortcomings of the Standard Model

2.2.1 Dark Matter and Freeze-Out

2.2.1.1 What is Dark Matter?

For the current parametrisation of the Lambda Cold Dark Matter (ΛCDM) model [17, 18], about 85% of the mass of the universe is a form of matter we do not know .[7] Several independent observations at different astronomical length scales require the existence of an additional form of non-relativistic matter different from the baryonic component.[8]

The earliest indication arose from the study of the velocity dispersion of the stars in the Milky Way and, on a larger scale, of clusters of galaxies in the 1930s. Another phenomenon to probe Dark Matter (DM) is the distribution of galaxy rotation curves. The velocity as a function of the radius of the spiral galaxy can be explained by the conservation of the angular momentum and should reproduce a "Keplerian" behaviour. The roughly constant speed of the stars, independently from their distance to the centre

[7] Other possibilities assume modifications of the Einsteinian general relativity, but are disfavoured by various astrophysical measurements.

[8] The remainder of this section follows arguments taken mainly from [19] and [20].

of the galaxy, implies a uniformity of the mass density well beyond the visible bulge. Other evidence results from the *gravitational lensing*. The bending of light due to the presence of mass (such as a cluster of galaxies) in between the very distant source (such as a quasar) and the observer (such the Hubble Space Telescope) produces the spectacular phenomenon of lensing arcs. The mass required to reproduce the "Einstein radius" is much larger than the amount inferred from the luminosity of the cluster.

The potential candidates for DM populate a mass spectrum from the axion to the black hole. In any case, every form of baryonic candidate or massive astrophysical compact halo objects (MACHOs) cannot account for the amount of DM in the universe. Modern evidence, coming from Big Bang Nucleosynthesis (BBN) and Cosmic Microwave Background (CMB), can estimate the amount of baryonic matter in the universe.

Primordial neutrons can survive if bounded in nuclei. BBN refers to the period after the Big Bang when neutrons and protons fused together to form deuterium and light elements. The abundance of deuterium is particularly important being a lower limit on the amount created during the BBN because it fuses creating helium in the stars with no remnants. Abundances of ^{4}He, D and ^{3}He as a residual for the ^{4}He formation and ^{7}Li can be theoretically calculated and are related to the photon to baryon ratio (η) and so, to the baryonic density.

Recombination refers to the epoch at which charged electrons and protons first became bound to form electrically neutral hydrogen atoms. The Wilkinson Microwave Anisotropy Probe (WMAP) operating from 2001 to 2010 and the Planck space observatory from 2009 to 2013 have provided a deep understanding of the primordial thermal radiation left over from the time of recombination. WMAP has achieved precise measurements of the angular fluctuations in the CMB spectrum with a resolution of $\sim 10^{-6}$ of a degree in the temperature variation, while the Planck spacecraft has a more sensitive angular resolution, and its data will continue to be analysed in the years to come.

The temperature fluctuations of the CMB are really small (30 ± 5 μK) and are due

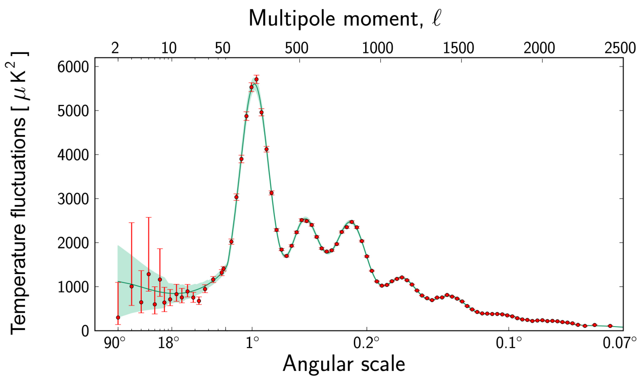

Figure 2.2.2: The CMB Anisotropy Power Spectrum from Planck experiment (2013) and its fit using the ΛCDM model.

to two effects: large and small scale anisotropies. Lower energy photons are observed today from areas that were more dense because they escaped from a deeper potential well: these are large scale fluctuations. On small scales, the anisotropy is caused by the acoustic oscillation of the photon-baryon fluid until the photon decoupling. Dark matter accounts only for the first phenomenon and varying the baryonic and dark components of the energy density it is possible to reproduce the power spectrum as shown in Figure 2.2.2. Furthermore, in order to explain how the large-scale structure of our universe evolved from the anisotropy of CMB, the baryonic matter component is not enough.

The most recent evidence for DM comes from the collision of a sub-cluster (the Bullet cluster) and a cluster. Baryonic mass estimations of galaxy clusters can be obtained from X-ray emission from the hot gas within the galaxies and do not match with the gravitational lensing estimations. During the collision between two galaxy clusters, the hot gas encounters friction (and emits X-rays) and its distribution remain concentrated in the centre as shown in Figure 2.2.3, while DM passes through with weaker interactions.

DM could be the sum of different species of non-baryonic particles and most BSM theories provide a unique stable candidate. The identikit of the “good candidate” satisfies some important requirements. DM must be stable otherwise it would decay to SM

Figure 2.2.3: In pink the X-ray emission of hot gas from a bullet-shaped and a larger cluster, whilst in blue the distribution of DM calculated via lensing observations.

particles. It is dark, or has no electric charge, and it is colourless otherwise it would form strongly bound states and would be simply detected from direct searches, from the scattering with nuclei as in the Large Underground Xenon experiment (LUX)[21].

DM must also reproduce the observed relic density [22]

$$\Omega_{DM}h^2 \simeq 0.1186 \pm 0.0020, \tag{2.2.1}$$

where h is the Hubble constant nowadays in unit of $100\,\mathrm{km\,s^{-1}\,Mpc^{-1}}$observed to be $h^2 \simeq 0.5$ and

$$\Omega_{DM} = \frac{\rho_{DM}}{\rho_c} \tag{2.2.2}$$

is the average density of non-baryonic DM divided by the total critical density. Their values are approximately $\rho_c = {}^{3H_0}/_{8\pi G_N} \simeq 10h^2$ GeV m^{-3} that would lead to a spatially flat homogeneous universe and $\rho_{DM} \simeq 1.2 \times 10^{-6}$ GeV/cm^3, roughly the equivalent of 6 protons every 5 m^3.

2.2.1.2 Why WIMP?

Freeze-out refers to the mechanism for a particle going out of thermal equilibrium during the history of the universe. The result is a constant residual number of particles. Herein we consider for simplicity only a single DM particle χ. Since dark matter is in equilibrium[9]

$$x \equiv \frac{M_\chi}{T} \ll 1 \tag{2.2.3}$$

in the canonical ensemble with the other SM particles, the creation-annihilation processes have the same rate in both directions

$$\chi\bar{\chi} \longleftrightarrow f\bar{f}, \tag{2.2.4}$$

where $\bar{\chi}$ represents the anti-DM particle and f is a Standard Model fermion.

The density at equilibrium is given by

$$n_\chi^{EQ} = \frac{g_{dof}}{(2\pi)^3}\int f(\mathbf{p})d^3\mathbf{p} = \frac{g_{dof}}{(2\pi)^3}\int_0^\infty \frac{4\pi p^2}{\exp\left(\frac{M_\chi-\mu}{T}\right)}d^3p, \tag{2.2.5}$$

where g_{dof} is the number of d.o.f., $f(\mathbf{p})$ is the Fermi-Dirac statistics and the number of DM particles in the comoving volume $N = a^3 n_\chi^{EQ}$ is constant. The chemical potential μ in Eq. 2.2.5 can be neglected.

If the actual number density of DM is larger than the equilibrium density the reaction will go faster to the right: the annihilation dominates the creation process. The depletion rate is proportional to $\sigma_{\chi\bar{\chi}\to f\bar{f}}|\mathbf{v}|n_\chi^2$, but there is a term with opposite sign because of the inverse process proportional to $\left(n_\chi^{EQ}\right)^2$. The time evolution of the density number can be expressed in two terms $\frac{1}{V}\dot{N}_\chi = \frac{1}{a^3}\frac{d\left(n_\chi a^3\right)}{dt} = \frac{dn_\chi}{dt} + 3n_\chi a\dot{a}$ and finally the Boltzmann transport equation governing the phenomenon can be written

$$\dot{n}_\chi + 3Hn_\chi = \langle\sigma_{tot}|\mathbf{v}|\rangle\left[\left(n_\chi^{EQ}\right)^2 - n_\chi\right], \tag{2.2.6}$$

where the second term accounts for the expansion of the universe and $\langle\sigma_{tot}|\mathbf{v}|\rangle$ stands for the thermally averaged total annihilation cross-section times the velocity.

This equation has no analytic solution. Using the time-temperature relation for radi-

[9]One uses units in which $k_B = 1$.

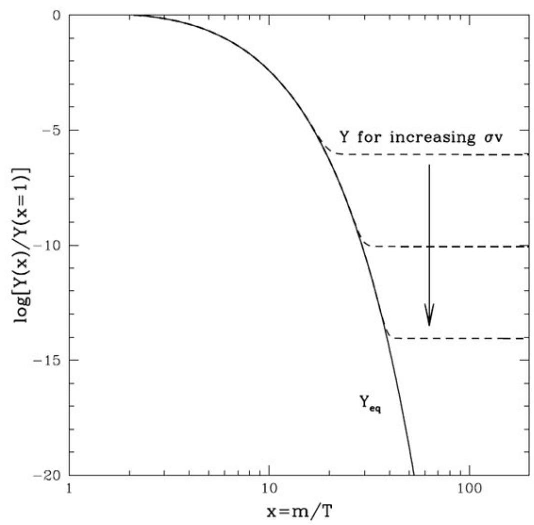

Figure 2.2.4: Dark matter freeze out mechanism.

ation dominance $t = 0.3\frac{m_{Pl}}{T^2\sqrt{g_{eff}}}$, Eq. 2.2.6 can be transformed to an evolution equation as a function of the temperature. Defining $Y_x \equiv n_\chi/s$ where s is the entropy density Eq. 2.2.6 can be rearranged as

$$\frac{x}{Y_x^{EQ}}\frac{dY}{dx} = -\frac{\Gamma_{tot}}{H}\left[\left(\frac{Y_x}{Y_x^{EQ}}\right) - 1\right] \tag{2.2.7}$$

and can be solved numerically with the thermal equilibrium boundary conditions $x \ll 1$ and $Y_x = Y_x^{EQ}$.

The rate of interaction at the equilibrium $\Gamma_{tot} = n_\chi^{EQ}\langle\sigma_{tot}|\mathbf{v}|\rangle \gg H(t)$ is much larger than the expansion of the universe. The freeze-out condition is achieved when

$$\Gamma_{tot} = H(t_f) \tag{2.2.8}$$

and can be roughly interpretable as the point in Figure 2.2.4 where the dashed line decouples from the continuum line. The solution of Eq. 2.2.7 provides T_f, therefore x_f at the freeze-out and the asymptotic value $Y_f = Y_x(\infty)$. The number of DM particles is frozen because neither the creation nor the annihilation process are allowed $\chi\bar{\chi} \nleftrightarrow f\bar{f}$ and the density evolves in time just due to the expansion of the universe.

In the literature, DM is usually referred to as hot, warm or cold depending on the velocity of the DM particles at the time of decoupling. Very light particles (such as neutrinos) were hot during the freeze-out or, in other words, they were relativistic. Large-scale structure formation disfavours hot DM. Qualitatively we can imagine how cold or warm DM tends to not move too much and naturally amplifies the initial density contrast because of the gravitational attraction.

DM could interact with SM particles only gravitationally or via some unknown coupling. In any case, making some reasonable assumption regarding the freeze-out temperature $T_f \sim {}^{M_\chi}\!/_{20}$, the estimate of the order of magnitude for the cross section is typically weak for $M_\chi \sim O(100 \text{ GeV})$.

We thus arrive at the paradigm of a warm or cold Weakly Interacting Massive Particle (WIMP) which is capable of naturally reproducing the value in Eq. 2.2.1 and being potentially observable in the near future.

2.2.2 Hierarchy problem

The self-energy of the Higgs (m_h^2) receives divergent quantum corrections from the virtual effects of every particle that couples, directly or indirectly, to the Higgs field. Pauli-Villars regularisation introduces an ultraviolet cut-off Λ_{UV} that could be interpreted as the energy scale at which new physics enters to alter the high-energy behaviour of the theory. The SM particles give one-loop quadratic corrections to the Higgs mass

$$\Delta m_H^2|_{\text{fermion}} = -\frac{y_f^2\Lambda_{UV}^2}{8\pi^2}, \quad \Delta m_H^2|_{\text{gauge}} = \frac{9g^2\Lambda_{UV}^2}{64\pi^2}, \quad \Delta m_H^2|_{\text{Higgs}} = \frac{-\lambda\Lambda_{UV}^2}{16\pi^2} \tag{2.2.9}$$

with the top giving the greatest contribution, due to its Yukawa coupling of order one ($y_t \sim O(1)$). If we consider that there is no new physics between the electroweak scale and the Planck or GUT scale ($\Lambda_{UV} \sim O(M_{Plank})$ or $O(M_{GUT})$), the level of cancellation will be unnatural. For example for ${}^{M_{GUT}}\!/_{M_{Higgs}} \sim O(10^{14}$ GeV) the cancellations in the various contributions to m_H must be precise to 14 orders of magnitude: this is referred

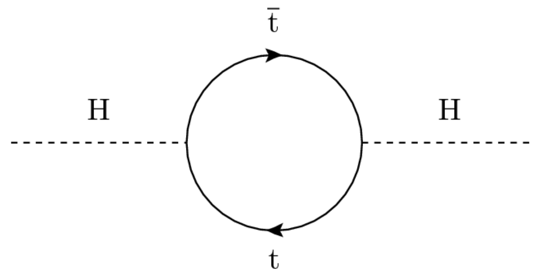

Figure 2.2.5: One-loop corrections to m_H^2 due to the top.

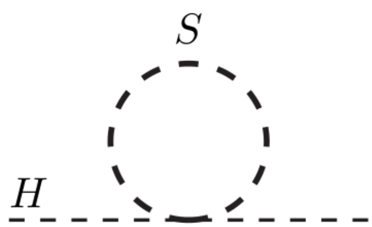

Figure 2.2.6: One-loop correction to m_H^2 due to a scalar.

to as the *hierarchy problem*.

The one-loop Feynman diagram in Figure 2.2.5 yields the correction:

$$\Delta m_H^2 \,|_{\mathrm{top}} = \left(-\frac{3y_t^2}{8\pi^2}\right)\left[a\Lambda_{UV}^2 - 6m_t^2 \ln\left(\frac{\Lambda_{UV}}{m_t}\right)\right], \tag{2.2.10}$$

where the factor of three takes account of the possible colours and $a = 1$ for a Pauli-Villars regularisation and $a = 0$ if one uses dimensional regularisation. Rejecting a physical interpretation for the cut-off ($a = 0$), it remains difficult to understand why m_H is so small, but the level of cancellation is more natural.

When a scalar S couples to the Higgs with a term in the Lagrangian $-\lambda_S \left|H\right|^2 \left|S\right|^2$ (see Figure 2.2.6) the correction to m_H^2 is:

$$\Delta m_H^2 \,|_{\mathrm{scalar}} = \left(\frac{\lambda_S}{16\pi^2}\right)\left[a\Lambda_{UV}^2 - 2m_S^2 \ln\left(\frac{\Lambda_{UV}}{m_S}\right) + ...\right]. \tag{2.2.11}$$

Considering two scalars for every Dirac fermion with the couplings respecting $\lambda_S = \left|\lambda_F\right|^2$, the quadratic divergences are erased. In order to evaluate the total one-loop

Figure 2.2.7: Two-loops corrections to m_H^2 due to a heavy fermion.

logarithmic correction one must consider the tri-linear mass term $m_S |S|^2 (H + H^\dagger)$. The logarithmic sensitivity remains and depends on the scalar and fermion masses but is zero when $m_S = m_F$.

Two-loop corrections to m_H^2 coming from heavy fermions F (see Figure 2.2.7) are of the form

$$\Delta m_H^2 = C_H \left(\frac{g^2}{16\pi^2}\right) \left[a\Lambda_{UV}^2 + 24 m_f^2 \ln\left(\frac{\Lambda_{UV}}{m_f}\right) + ...\right] \tag{2.2.12}$$

where C_H is the quadratic Casimir invariant of H and g is a gauge coupling (electroweak or unknown).

Summarising: contributions to m_H^2 come from Feynman diagrams with N-loops, where $N = 1, ...\infty$, involving the SM particles appearing in the diagram when new physics is assumed at the energy scale Λ_{UV}. The Higgs mass ($m_H \simeq 125$ GeV) is too small compared to the Planck or GUT scales and the miraculous cancellations are expected to have a physical reason instead to be the result of an unnatural fine-tuning as described in Section 2.3.6. SUSY provides an elegant solution to this issue by associating two scalar d.o.f. for every fermion of the SM (as discussed in Section 2.3.1). In such a way all the quadratic divergences are erased at every loop of the perturbative theory.

2.2.3 Grand Unified Theory

Every subgroup of the SM describes a renormalizable QFT and the couplings are a function of the energy. The unification of the three gauge interactions into a single force is the fascinating Grand Unified Theory (GUT). The SM does not provide a perfect unification of the couplings at the GUT scale. The beta functions, describing the dependence of the coupling parameters on the energy scale, satisfy the one-loop RG equations

$$\beta\left(g_i\right) \equiv \frac{d}{dt} g_i = \frac{1}{16\pi^2} b_i g_i^3, \qquad t = \ln\left(\frac{M}{M_0}\right) \tag{2.2.13}$$

where M is the RG scale, $M_0 = M_{GUT}$ for example, and b_i are constant coefficients with $i = 1, 2, 3$. The normalisations for $g_1 = \sqrt{5/3}\, g_Y$, $g_2 = g_W$ and $g_3 = g_S$ are chosen to agree with the canonical covariant derivative of the group $SU(3)_C \times SU(2)_L \times U(1)_Y$ into $SU(5)$. Usually the reciprocals of the quantities $\alpha_i = g_i^2/4\pi^2$ are represented, because at one-loop order they run linearly

$$\frac{d}{dt}\alpha_i = -\frac{b_i}{2\pi}. \tag{2.2.14}$$

The coefficients b_i are larger for supersymmetric models with respect to the SM because of the contributions of the extra particles in the loops. Comparing the SM with its minimal supersymmetric extension at the one-loop level one has the values:

Model	b_1	b_2	b_3
SM	$41/10$	$-19/6$	-7
MSSM	$33/5$	1	-3

Figure 2.2.8 shows the two-loop renormalisation group evolution of α_i^{-1} in SM and MSSM with sparticle masses treated as a common threshold between 500 GeV and 1.5 TeV.

2.3 Supersymmetry

Supersymmetry (SUSY) [24–33] is a popular and well-motivated theory capable of providing a solution for the hierarchy problem, the unification of the gauge couplings and a suitable DM candidate (when R-parity is conserved, see Section 2.3.2). In this

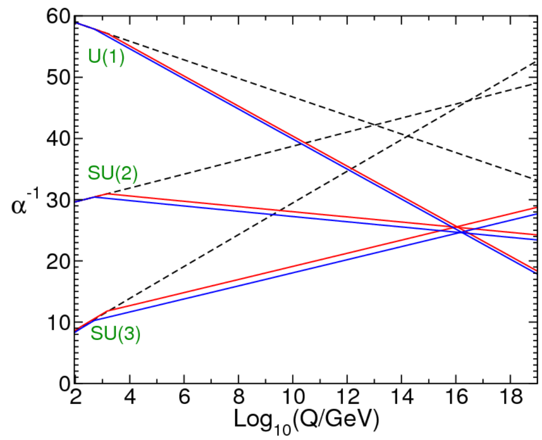

Figure 2.2.8: Two-loop renormalisation evolution of the gauge couplings in the SM (dashed lines) and the MSSM (solid lines). Figure from [23].

section, the writer discusses the ordinary $N = 1$ supersymmetry, where N refers to the number of supersymmetries. Being the focus of the proposed analyses in this thesis and, in recent years, of a large proportion of SUSY searches at the LHC, some aspects of the Minimal Supersymmetric Standard Model (MSSM) are described, with a particular focus on the phenomenological implications[10].

2.3.1 Introduction to SUSY

Supersymmetry refers to an invariance under generalised space-time transformations relating bosons and fermions. From the Coleman-Mandula theorem [35], an extension of the relativistic invariance is possible by introducing anticommuting spinorial generators, as described by the Haag–Łopuszański–Sohnius generalisation [36]. The supersymmetric spin-$\frac{1}{2}$ operator Q, and its hermitian conjugate $\bar{Q}$[11], transforms a bosonic state $|B\rangle$ in a fermionic state $|F\rangle$ and vice versa

$$\begin{aligned} Q\,|B\rangle &= |F\rangle \\ Q\,|F\rangle &= |B\rangle \end{aligned} \quad . \tag{2.3.1}$$

[10] This section closely follows prescriptions taken from [23, 34].

[11] The hermitian conjugate of a Weyl spinor is traditionally labelled with a bar ($-$) in the superfields nomenclature. The same conventions as in Section 2.1.8 are otherwise used.

From a geometrical perspective, alongside the four canonical space-time coordinates, one introduces four space coordinates θ respecting Grassmannian algebra. In such a way one defines a *superspace* with eight dimensions

$$x^{\mu},\ \theta^{\alpha},\ \bar{\theta}_{\dot{\alpha}}, \tag{2.3.2}$$

where α runs on two spinorial indexes. As a particle-quantum field is a representation of the Poincaré group, a generic scalar superfield

$$S\left(x,\theta,\bar{\theta}\right) = \phi + \theta\xi + \bar{\theta}\bar{\chi} + \theta^2 M + \bar{\theta}^2 N + \theta\sigma^{\mu}\bar{\theta}A_{\mu} + \theta^2\bar{\theta}\bar{\lambda}_1 + \bar{\theta}^2\theta\lambda_2 + \theta^2\bar{\theta}^2 D \tag{2.3.3}$$

represents the super-Poincaré group, where on the right side of Eq. 2.3.3 one specifies the complete Taylor series with respect to the fermionic coordinates. The idea is to construct a super-lagrangian Λ, function of the superfields, and an action A given by the expression

$$A = \int d^4x \int d\theta^2 d\bar{\theta}^2 \Lambda(S_i\left(x,\theta,\bar{\theta}\right)) = \int d^4x\ \mathcal{L}_{\mathrm{SUSY}}. \tag{2.3.4}$$

The Lagrangian can be obtained by integrating Λ over only the Grassmannian coordinates. The result of such integrations lives only the terms proportional to the maximum expansion in θ and $\bar{\theta}$.

Defining the supercharges explicitly as

$$\begin{cases} Q_{\alpha} & = -i\partial_{\alpha} - \left(\sigma^{\mu}\right)_{\alpha\dot{\beta}}\bar{\theta}^{\dot{\beta}}\partial_{\mu} \\ \bar{Q}^{\dot{\alpha}} & = i\bar{\partial}^{\dot{\alpha}} + \theta^{\beta}\left(\sigma^{\mu}\right)_{\beta}^{\ \dot{\alpha}}\partial_{\mu} \end{cases}, \tag{2.3.5}$$

the SUSY transformation is equivalent to a translation in superspace. The resulting Gol'fand-Likhtman (Poincaré) superalgebra gives the non-trivial anticommutator and commutators

$$\begin{aligned} \left\{Q_\alpha, \bar{Q}^{\dot{\alpha}}\right\} &= 2\left(\sigma_{\mu\nu}\right)_\alpha^{\ \dot{\alpha}} P_\mu \\ \left[M_{\mu\nu}, Q_\alpha\right] = -\left(\sigma_{\mu\nu}\right)_\alpha^{\ \beta} Q_\beta, &\quad \left[M_{\mu\nu}, \bar{Q}^{\dot{\beta}}\right] = -\left(\bar{\sigma}_{\mu\nu}\right)_{\dot{\beta}}^{\ \dot{\alpha}} \bar{Q}^{\dot{\beta}} \end{aligned} \tag{2.3.6}$$

where P_μ is the four-momentum and $M_{\mu\nu} = x_\mu P_\nu - x_\nu P_\mu$ generators of $SO(1,3)$.

Supersymmetric transformations of the superspace coordinates need the introduction of covariant derivatives defined as

$$\begin{cases} D_\alpha &= \partial_\alpha + i\left(\sigma^\mu\right)_{\alpha\dot{\beta}} \bar{\theta}^{\dot{\beta}} \partial_\mu \\ \bar{D}^{\dot{\alpha}} &= \bar{\partial}^{\dot{\alpha}} - i\theta^\beta \left(\sigma^\mu\right)_{\beta}^{\ \dot{\alpha}} \partial_\mu \end{cases} \tag{2.3.7}$$

anticommuting with the supercharges and with non zero torsion. The irreducible representations of the superalgebra are *chiral* superfields Φ obtained by imposing the covariant constraint

$$\bar{D}_{\dot{\alpha}} S\left(x, \theta, \bar{\theta}\right) = 0. \tag{2.3.8}$$

Conventionally, one introduces new bosonic coordinates

$$y^\mu \equiv x^\mu + i\theta\sigma^\mu\bar{\theta} \quad \bar{D}_{\dot{\alpha}} y^\mu = 0 \tag{2.3.9}$$

in such a way that the left-handed chiral superfield is not a function of $\bar{\theta}$ anymore and it can be written via a Taylor expansion as

$$\Phi\left(y, \theta\right) = \phi\left(y\right) + \sqrt{2}\theta\psi\left(y\right) + \theta^2 F\left(y\right). \tag{2.3.10}$$

Similarly, one can define an anti-chiral superfield $\Phi^\dagger\left(y^\dagger, \bar{\theta}\right)$.

Expanding the superfields on the bosonic coordinates, one can construct the Lagrangian combining a superpotential $W(\Phi)$, an holomorphic function of a chiral (or anti-chiral) superfields and a Kähler potential $K\left(\Phi^\dagger\Phi\right)$ and integrating on the fermionic coordinates as expressed by the Eq. 2.3.4.

The Wess-Zumino model introduces a Lagrangian composition of the quadratic and cubic terms of W and the simple form of the Kähler potential $K = \Phi^\dagger\Phi$ as in the expression

$$L_{WZ} = \int d\theta^2 d\bar{\theta}^2 \Phi^\dagger\Phi + \int d\theta^2 \frac{1}{2} m\Phi^2 + \frac{\lambda}{3}\Phi^3 + h.c. \tag{2.3.11}$$

The other class of superfields fundamental in order to describe SUSY gauge theories are the real or vector superfields $V = V^*$ satisfying the reality condition

$$S^\dagger\left(x, \theta, \bar{\theta}\right) = S\left(x, \theta, \bar{\theta}\right). \tag{2.3.12}$$

In the MSSM bosons and fermions are *superpartners* of each other and organised in such irreducible representations or *supermultiplets*. Respecting the superalgebra given by the expressions in Eq. 2.3.6, each of these superfields has the same number of bosonic and fermionic d.o.f. and all the single particle states populating the same supermultiplet have the same mass, colour, weak isospin, and hypercharge.

The gauge fields of the SM populate vector or gauge superfields, while Weyl fermions populate chiral supermultiplets. The superpartners of the gauge bosons are spin-$\frac{1}{2}$ fermions called gaug*inos*, while the superpartners of the Weyl fields are scalars referred to as *s*quarks and *s*leptons. SUSY models need two Higgs supermultiplets with $Y = \pm 1$, both to solve gauge anomalies and to give masses to the quarks of up and down-type. The superpartners of the Higgs bosons are called Higgs*inos* and populate chiral supermultiplets.

Gauge and chiral superfields are shown in Tab. 2.1 and Tab. 2.2 and as in the literature, the superpartners are denoted as the state of the SM, but with an upper tilde ($\sim$). Squarks and sleptons are scalars hence their left or right-handedness refers to the their SM superpartners; nevertheless only left-handed and anti-right-handed scalar fields interact weakly.

Φ	spin-0	spin-$\frac{1}{2}$	$SU(3)_C,\, SU(2)_L,\, U(1)_Y$
	squarks	quarks	
Q	$(\tilde{u}_L\, \tilde{d}_L),\, (\tilde{c}_L\, \tilde{s}_L),\, (\tilde{t}_L\, \tilde{b}_L)$	$(u_L\, d_L),\, (c_L\, s_L),\, (t_L\, b_L)$	$(\mathbf{3},\, \mathbf{2},\, \frac{1}{6})$
U	$\tilde{u}^* = \tilde{u}^*_R,\, \tilde{c}^*_R,\, \tilde{t}^*_R$	$u^\dagger_R,\, c^\dagger_R,\, t^\dagger_R$	$(\bar{\mathbf{3}},\, \mathbf{1},\, -\frac{2}{3})$
D	$\tilde{d}^*_R,\, \tilde{s}^*_R,\, \tilde{b}^*_R$	$d^\dagger_R,\, s^\dagger_R,\, b^\dagger_R$	$(\bar{\mathbf{3}},\, \mathbf{1},\, \frac{1}{3})$
	sleptons	leptons	
L	$(\tilde{\nu}_e\, \tilde{e}_L),\, (\tilde{\nu}_\mu\, \tilde{\mu}_L),\, (\tilde{\nu}_\tau\, \tilde{\tau}_L)$	$(\nu_e\, \tilde{e}_L),\, (\nu_\mu\, \tilde{\mu}_L),\, (\nu_\tau\, \tau_L)$	$(\mathbf{1},\, \mathbf{2},\, -1)$
E	$\tilde{e}^*_R,\, \tilde{\mu}^*_R,\, \tilde{\tau}^*_R$	$e^\dagger_R,\, \mu^\dagger_R,\, \tau^\dagger_R$	$(\mathbf{1},\, \mathbf{1},\, 1)$
	Higgs	Higgsinos	
H_u	$(H^+_u\, H^0_u)$	$(\tilde{H}^+_u\, \tilde{H}^0_u)$	$(\mathbf{1},\, \mathbf{2},\, \frac{1}{2})$
H_d	$(H^0_d\, H^-_d)$	$(\tilde{H}^0_d\, \tilde{H}^-_d)$	$(\mathbf{1},\, \mathbf{2},\, -\frac{1}{2})$

Table 2.1: Chiral supermultiplets in the MSSM.

V	spin-$\frac{1}{2}$	spin-1	$SU(3)_C,\, SU(2)_L,\, U(1)_Y$
g	$\tilde{g}$ gluino	g gluon	$(\mathbf{8},\, \mathbf{1},\, 0)$
W	$\tilde{W}^+,\, \tilde{W}^0,\, \tilde{W}^-$ winos	$W^+,\, W^0,\, W^-$ W-bosons	$(\mathbf{1},\, \mathbf{3},\, 0)$
B	$\tilde{B}^0$ bino	B^0 B-boson	$(\mathbf{1},\, \mathbf{1},\, 0)$

Table 2.2: Gauge supermultiplets in the MSSM.

The SUSY Lagrangian for the MSSM can be written in a compact form as

$$\begin{array}{c} L^{\mathrm{MSSM}}_{SUSY} = \int d\theta^2 d\bar{\theta}^2 \sum_{chiral} \Phi^\dagger e^{\sum_a g_a V_a} \Phi + \int d\theta^2 \mathrm{Tr}\left(\frac{1}{4g_a^2} W_a^\alpha W_{a\alpha}\right) + h.c. \\ + \int d\theta^2 \mu H_u H_d + \mathbf{y}_u QUH_u - \mathbf{y}_d QDH_d - \mathbf{y}_l LEH_d + h.c. \end{array}, \tag{2.3.13}$$

where the first term is the gauge and SUSY invariant kinetic term and the W_α are the supersymmetric generalisation of the strength tensors: a chiral superfield constructed as $-1/4\bar{D}^2 D_\alpha V$ for the Abelian and $-1/8\bar{D}^2 e^{-2V} D_\alpha e^{2V}$ for the non-Abelian case. The second line in Eq. 2.3.13 represents the superpotential for the MSSM and by convention has the signs such to reproduce a positive sign for the masses of the fermion of the SM when the two Higgs doublets get VEVs.

2.3.2 R-parity

The minimal superpotential in Eq. 2.3.13 can be enriched by other gauge-invariant terms violating lepton number (L) and individual flavour number by one unit

$$W_{L-\text{violating}} = \frac{1}{2}\lambda_1 LLE + \lambda_2 LQD + \lambda_3 LH \tag{2.3.14}$$

and baryon number (B) by one unit

$$W_{B-\text{violating}} = \frac{1}{2}\lambda_4 UDD, \tag{2.3.15}$$

with λ_4^{ijk} antisymmetric in the last two flavour indexes related to the down-type superfields ($j \neq k = 1, 2, 3$).

The low energy phenomenology of several processes and relative measurements places strong constraints on the violation of lepton and baryon number. For example, proton stability[12] demands the suppression of at least one of the possible B and L-violating terms. Figure 2.3.1 shows two example processes that could lead to the proton decay.

[12] An experimental lower limit for the proton lifetime ($\tau_p > 2.3 \times 10^{33}$ years) is set by the Super-Kamiokande collaboration for the decay channel $p \rightarrow K^+\bar{\nu}$ [37].

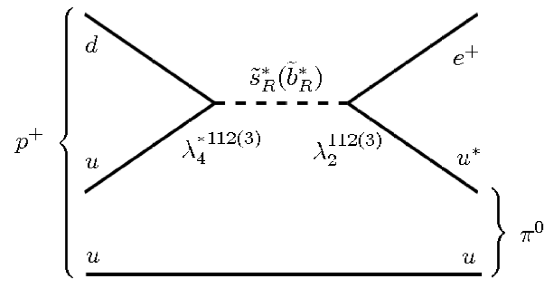

Figure 2.3.1: Feynman diagram for proton decay ($p \to \pi^0 e^+$) mediated by a strange (bottom) squark.

The conservation of a discrete $\mathbb{Z}_2$ symmetry called R-parity defined as:

$$R_P = (-1)^{3(B-L)+2s} \tag{2.3.16}$$

is assumed in the minimal extension of the SM. The particles of the SM and the other Higgs bosons have $R_P = 1$, while the superpartners are R-parity odd. R-parity conservation demands no particle-sparticle mixing and hence every interaction vertex has an even number of supersymmetric particles or none.

From a phenomenological perspective at collider experiments, R-parity conservation implies the production of an even number of superparticles, each decaying to an odd number of superparticles until the lightest stable supersymmetric particle is created. Final states are populated by an even number of LSPs, likely two, undetected by the experiments when not interacting strongly and/or electromagnetically. Several scenarios predict a neutral LSP whose properties compatible with dark matter phenomenology.

2.3.3 SUSY breaking and soft Lagrangian

SUSY cannot exist at the energy scale in which human beings live. A selectron not respecting the exclusion Pauli principle, but in all the other aspects identical to the electron, would implicate a completely different chemistry. None of the supersymmetric partners of the SM has been discovered so far, hence a realistic phenomenological model must contain a spontaneous supersymmetry breaking resulting in a SUSY mass spectrum around the TeV scale or above.

Comparing Eq. 2.2.9 and Eq. 2.2.11 in Section 2.2.2 one has shown how the vanishing of the quadratic divergences (Λ_{UV}^2) in the Higgs mass occurs when there are the same number of bosonic and fermionic d.o.f. and the dimensionless couplings respect the relation $\lambda_S = |\lambda_F|^2$. Consequently, an unbroken supersymmetry naturally maintains a hierarchy between the electroweak scale and a large (Planck or GUT) scale deleting also the logarithmic divergences proportional to the squared masses due of the degeneracy for the superparticle-particle masses.

Broken supersymmetry must still provide the solution for the hierarchy problem and so the cancellation for the quadratic divergences. This is referred to as $soft$ supersymmetry breaking. The effective Lagrangian can be written as

$$\mathcal{L} = \mathcal{L}_{\text{SUSY}} + \mathcal{L}_{\text{soft}}, \tag{2.3.17}$$

where $\mathcal{L}_{\text{SUSY}}$ contains terms conserving the supersymmetry while $\mathcal{L}_{\text{soft}}$ contains contributions violating the supersymmetry, but not dimensionless terms.

If one refers to m_{soft} as the mass scale associated with the terms in $\mathcal{L}_{\text{soft}}$, the corresponding corrections to the Higgs mass are of the form

$$\Delta m_H^2 = m_{\text{soft}}^2 \left[\frac{\lambda}{16\pi^2} \ln \left(\frac{\Lambda_{UV}}{m_{\text{soft}}} \right) + \dots \right], \tag{2.3.18}$$

with λ the general dimensionless coupling. The value of m_{soft} is responsible for the splitting between the SM and the SUSY spectrum. Once again, large contributions from m_{soft} provide large corrections for the Higgs mass which unnaturally sum to the value ~125 GeV. This implies, for example, an expected MSSM mass spectrum not much higher than the TeV scale. The introduction of a similar, but more moderate, fine tuning is referred to as *little hierarchy problem.*

The typical mechanism for SUSY breaking assumes a *hidden* sector communicating to the *visible* sector, such as the MSSM, via some mediator. Three major classes arise depending on the mediator:

- gravity mediated or Planck-scale mediated
- gauge mediated
- extra dimension and anomaly mediated

They can result in different scenarios and phenomenology of the visible sector. Analogously to EWSB, the vacuum is not invariant under a SUSY transformation and when broken has a positive energy. The SUSY generators are fermionic operators, hence the Nambu-Goldstone particle is the massless neutral *goldstino*. This would populate the longitudinal components of the last particle of the MSSM called the gravitino: the $^3/_2$ spin superpartner of the graviton. Depending on the procedure, the gravitino could be the LSP. This is the case for gauge or anomaly mediated MSSM.

Supersymmetry can be spontaneously broken only when a D or a F-term appearing in Eq. 2.3.3 and 2.3.10 has an expectation value not zero in the vacuum state. The two mechanisms are referred to as Fayet-Iliopoulos [38] or O'Raifeartaigh [39] respectively and provide different phenomenology. In MSSM the only D-term can not provide the masses for the sfermions.

Independently from the procedure, one can write a soft Lagrangian with positive mass dimension terms that explicitly breaks SUSY. For the MSSM such a generic Lagrangian assumes the expression given by

$$\begin{aligned} L_{soft}^{\mathrm{MSSM}} = & -\tfrac{1}{2}\left(M_3\tilde{g}\tilde{g} + M_2\tilde{W}\tilde{W} + M_1\tilde{B}\tilde{B} + c.c.\right) \\ & -\left(\tilde{U}\mathbf{a_u}\tilde{Q}H_u - \tilde{D}\mathbf{a_d}\tilde{Q}H_d - \tilde{E}\mathbf{a_e}\tilde{L}H_d + c.c.\right) \\ & -\tilde{Q}^\dagger\mathbf{m_Q^2}\tilde{Q} - \tilde{L}^\dagger\mathbf{m_L^2}\tilde{L} - \tilde{u}^*\mathbf{m_u^2}\tilde{u}^{*\dagger} - \tilde{d}^*\mathbf{m_d^2}\tilde{d}^{*\dagger} - \tilde{e}^*\mathbf{m_e^2}\tilde{e}^{*\dagger} \\ & -m_{H_u}^2 H_u^* H_u - m_{H_d}^2 H_d^* H_d - (bH_uH_d + c.c.) \end{aligned} \quad . \tag{2.3.19}$$

The first line consists of the gaugino masses, the second contains the corresponding three scalar couplings of the Yukawa terms in the superpotential in Eq. 2.3.13, the third line contains the scalar masses and the fourth contributions to the Higgs potential. A total of 105 new independent parameters can be obtained counting the masses, phases and mixing angles.

2.3.4 CMSSM

2.3.4.1 Flavour and phase constraints

Flavour physics measurements constrain the potential supersymmetric terms in the L_{soft}^{MSSM}, suppressing unwanted flavour mixing and CP violating contributions.

For example, an off-diagonal slepton mass term in Eq. 2.3.19 can result in the flavour mixing $\mu \to e\gamma$, and similarly $\tau \to e\gamma$ and $\tau \to \mu\gamma$, arising from the one-loop diagram involving the right-handed sleptons and the Bino [40], which in typical gravity mediated models can be approximated with the mass eigenstate of the LSP. The likelihood of smuon-selectron conversion should be compared with the experimental upper limit of $BR\,(\mu \to e\gamma) < 4.2 \times 10^{-13}$ at 90% of confidence level [41]. Other diagrams could involve left-handed sleptons and Winos or left and right-handed scalar leptons due to the tri-linear coupling with the VEVs of the Higgs.

Similarly for the squark mass terms, tight constraints come from the measurements of the oscillation of the neutral Kaon $K^0 \leftrightarrow \bar{K}^0$ suppressing the mixing between down and strange squarks, and weaker constraints on flavour violation arise from the systems $D^0 \leftrightarrow \bar{D}^0$ and $B^0 \leftrightarrow \bar{B}^0$. A large class of phenomena involve rare meson decays with flavour mixing via the parton level processes $b \to sll$, $c \to ull$ and $s \to dll$.[13] Moreover, the B-factory measurements [42, 43] of the branching fraction for the beauty meson decay via $b \to s\gamma$ place stringent indirect constraints for massive SUSY particles in the loop corrections.

[13] Here ll represents a pair of leptons.

Other strict constraints for the CP violating phases arise from limits on the electric dipole moments of the electron and neutron [44].

The idea is to constrain SUSY adopting a so-called s*oft supersymmetry breaking universality* hypothesis, or a weaker version, in which the matrices for the slepton and squark masses are diagonal as well as the three-scalar coupling matrices. These are set proportional to the Yukawa couplings matrices via three A_{0i} coefficients and all the CP-violating phases different from the SM CKM contribution are set to zero.

2.3.4.2 EW breaking in the MSSM

Two complex Higgs doublets complicate EWSB in the MSSM. The important terms in the classical potential are related to the neutral Higgs components and are F and D terms plus contributions from $\mathcal{L}_{soft}$, while the terms relative to the charged Higgs can be set to zero by performing a gauge transformation

$$\begin{aligned} V_{H^0}^{\rm MSSM} = \; & \left(|\mu|^2 + m_{H_u}^2\right)|H_u^0|^2 + \left(|\mu|^2 + m_{H_d}^2\right)|H_d^0|^2 - (bH_u^0 H_d^0 + c.c.) \\ & + \tfrac{1}{8}\left(g^2 + g'^2\right)\left(|H_u^0|^2 - |H_d^0|^2\right)^2 . \end{aligned} \tag{2.3.20}$$

The D-terms in the second line combine in a contribution always positive which stabilise the potential. In the D-flat direction, where the quartic contribution in the Higgs fields is set to zero ($|H_u^0| = |H_d^0|$), one can show that V has a minimum when

$$2b < 2\left|\mu^2\right| + m_{H_u}^2 + m_{H_d}^2. \tag{2.3.21}$$

In order to have EWSB one must provide a negative mass term for a linear combination of H_u^0 and H_d^0 and the following relation must be satisfied

$$b^2 > \left(|\mu|^2 + m_{H_u}^2\right)\left(|\mu|^2 + m_{H_d}^2\right). \tag{2.3.22}$$

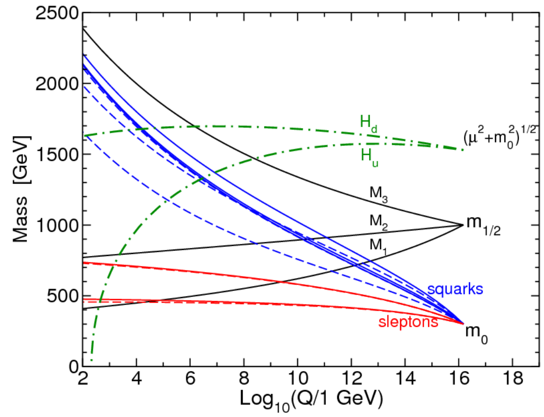

Figure 2.3.2: RG evolution of gauginos and scalar masses in the MSSM with mSUGRA boundary conditions imposed at $Q_0 = 1.5 \times 10^{16}$ GeV. Figure from [23].

Traditionally, one defines the ratio between the vacuum expectation values of the two Higgs as

$$\tan\beta \equiv \frac{v_u}{v_d} = \frac{\langle H_u^0 \rangle}{\langle H_u^d \rangle}, \tag{2.3.23}$$

which is related to the mass of the Z boson and electroweak couplings by the relation given in Eq. 2.1.38, with $v^2 = v_u^2 + v_d^2$. The conditions for the potential to have a minimum are

$$\begin{aligned} |\mu|^2 + m_{H_u}^2 - b\cot\beta - \tfrac{1}{2}M_Z^2\cos 2\beta &= 0 \\ |\mu|^2 + m_{H_u}^2 - b\tan\beta + \tfrac{1}{2}M_Z^2\cos 2\beta &= 0 \end{aligned} \tag{2.3.24}$$

and the two parameters b and $|\mu|$ can be substituted for $\tan\beta$ and the sign of the Higgsino mass. The RG evolution equations from the *visible* scale of the SUSY mass spectrum up to the SUSY-breaking scale unify the masses for the scalars and gauginos as shown in Figure 2.3.2.

Combining the principles of supersymmetry and general relativity, the theoretical framework referred to as minimal supergravity (mSUGRA) is defined by four parameters and a sign: the scalar superpartners have a common mass at the SUSY-breaking scale called m_0 while the gaugino masses unify in a parameter denoted $m_{1/2}$; the universal tri-linear scalar coupling is labelled A_0, the ratio of the vacuum expectation values of the two Higgs boson fields is $\tan\beta$, and finally, the sign of the Higgsino mass parameter μ

Gauge eigenstates	Mass eigenstates	Names
$\tilde{B}^0,\quad \tilde{W}^0,\quad \tilde{H}_u^0,\quad \tilde{H}_d^0$	$\tilde{\chi}_1^0,\quad \tilde{\chi}_2^0,\quad \tilde{\chi}_3^0,\quad \tilde{\chi}_4^0$	Neutralinos
$\tilde{W}^+,\quad \tilde{W}^-,\quad \tilde{H}_u^+,\quad \tilde{H}_d^-$	$\tilde{\chi}_1^\pm,\quad \tilde{\chi}_2^\pm$	Charginos
$\tilde{t}_L,\quad \tilde{t}_R$	$\tilde{t}_1,\quad \tilde{t}_2$	Stops
$\tilde{b}_L,\quad \tilde{b}_R$	$\tilde{b}_1,\quad \tilde{b}_2$	Sbottoms
$\tilde{\tau}_L,\quad \tilde{\tau}_R$	$\tilde{\tau}_1,\quad \tilde{\tau}_2$	Staus

Table 2.3: The mass eigenstates of supersymmetric particles as the result of the mixing of the gauge eigenstates in the MSSM.

remains undetermined.

The same parameters together with constraints provided by experimental measurements describe the Constrained Minimal Supersymmetric Standard Model (CMSSM) scenario for soft terms, which has been the target of a large proportion of SUSY searches in the last years.

2.3.4.3 Eigenstates of mass

For fixed sign(μ), every point in this four-dimensional space of parameters in CMSSM is *per se* a supersymmetric scenario. The evolution of nearby points down to the electroweak scale can provide different mass spectra, allowing or prohibiting specific decay modes, resulting in a completely different phenomenology at collider experiments.

When the electroweak symmetry is broken, the superpartners described in Tables 2.1 and 2.2, are not necessarily the mass eigenstates of the theory.

Three of the eight real scalar degrees of freedom associated to the Higgs doublets, are the would-be Nambu-Goldstone bosons G^0 , $G^\pm$, which become the longitudinal modes of the massive vector bosons. The remaining five mass eigenstates consist of two CP-even neutral h^0 and H^0, one CP-odd neutral A^0, and two charged $H^\pm$ Higgs scalar fields. Hence, alongside the SM-like Higgs (h^0) two other neutral and two charged scalar particles are assumed to exist.

Electroweakinos are linear combinations of the fermionic partner of the gauge bosons and the two Higgs bosons. Neutral Higgsinos and gauginos mix to form four eigenstates of mass called neutralinos ($\tilde{\chi}_i^0$ with $i = 1, 2$, 3 or 4) while charged winos and Higgsinos form two eigenstates of mass referred to as charginos ($\tilde{\chi}_i^{\pm}$ with $i = 1$ or 2) .

For the supersymmetric scalar sector, the amount of mixing is proportional to the corresponding Standard Model partner mass and is hence dominant for the third generation. Left and right-handed stops mix to form two eigenstates of mass $\tilde{t}_1$ and $\tilde{t}_2$ and similarly for the sbottom and stau.

The mixing for the SUSY particles is summarised in Table 2.3 while the other eigenstates of gauge correspond to the eigenstates of mass assuming a negligible mixing. Typically, the $\tilde{t}_1$ is the lightest squark, predominantly right-handed. Nevertheless, a light $\tilde{b}_1$ is expected because of the similarity of the RGE for the third generation of squarks and the mixing is larger with increasing $\tan\beta$.

2.3.4.4 Other constraints on the MSSM

Alongside flavour mixing processes associated with meson decays, indirect constraints are set for example by the precision measurements provided by LHCb [45] for the two rare beauty decays $B^0_{(s)} \to \mu^+\mu^-$. Once again, heavy superparticles could contribute in the loop corrections. For the same reason, the anomalous magnetic moment of the muon [46], $g-2$, is a low-energy phenomenon with important implications for the mSUGRA parameter space [47]. The mass of the W boson is another electroweak precision observable.

The recent results of the Higgs physics, from the mass, production and decay rates and coupling strengths measurements at the LHC experiments, provide additional information to constrain the MSSM.

Searches for the production of supersymmetric particles at LEP, Tevatron and LHC experiments set tight limits on the parameter space of CMSSM. In the next chapter, more details are presented for proton-proton collisions.

Other constraints arise from indirect searches due to the products from the annihilation of LSPs at the freeze-out time and direct searches setting limits on the DM nature in the mass - cross section plane.

The compatibility of SUSY models with the observed DM relic density is the most important astrophysical constraint. While the CMSSM is not required to provide the whole amount of the DM in the universe, many scenarios predict too high a relic density due to a small annihilation cross section at the freeze-out time due to a large LSP mass or a small coupling or both. For the WIMP miracle, the lightest neutralino can reproduce the right relic density until its mass is not too large $M_{\tilde{\chi}_1^0} \sim \mathcal{O}(100\text{ GeV})$, while the gravitino couples too weakly.

Four major mechanisms can reduce the DM relic density and allow for larger values of the mass of the LSP. Regions of the SUSY parameter space with a small mass difference between a superpartner of a fermion and the LSP are referred to as *sfermion co-annihilation* regions. During the freeze-out, a comparable number between one, or more sfermion species and the LSP could have contributed to reducing the DM relic density. For fixed $\tan\beta$, A_0 and $\text{sign}(\mu)$, for example in a way to reproduce the Higgs mass, these regions are located in the m_0-$m_{1/2}$ plane above the charged LSP region. For a bino-like LSP a "bulk region" with small values of m_0 and $m_{1/2}$ requires a not too heavy slepton exchange in the t-channel. Such models are strongly disfavoured by recent results from LHC searches. An A-funnel or H-funnel region refers to Higgs resonant processes due to a special proportion for the masses $2M_{\tilde{\chi}_1^0} \sim m_{A^0}, m_{h^0}, m_{H^0}$. The most efficient case is an s-wave annihilation with an A^0 resonance, requiring a large value for $\tan\beta$. Finally, heavier gauginos can contribute to the annihilation of the LSP via a co-annihilation process or through exchange in the t-channel if a significant wino or Higgsino mixing occurs. In the *focus point,* with a large m_0 and relative small

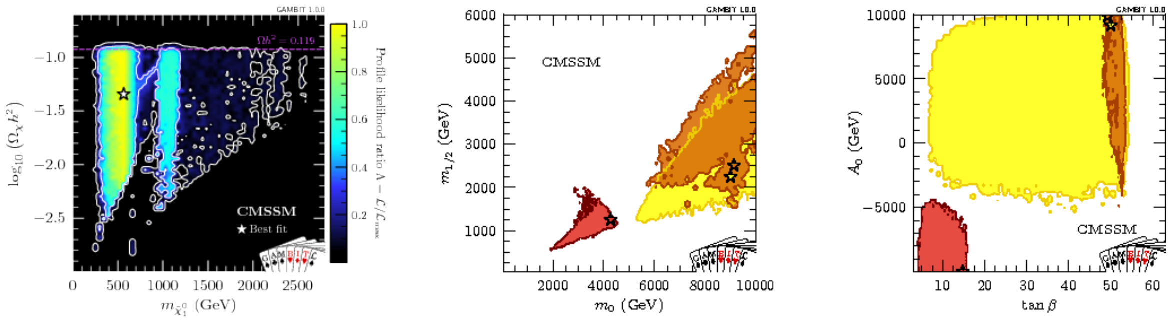

(a) (b) (c)

Figure 2.3.3: The profile likelihood ratio for the CMSSM with 68% and 95% CL contour lines, in terms of $M_{\tilde{\chi}_1^0}$ and the relic abundance of the lightest neutralino 2.3.3a. Confidence regions (within the 95% CL) in the m_0-$m_{1/2}$ parameter plane 2.3.3b and $\tan\beta - A_0$ parameter plane 2.3.3c with $\mu > 0$ for chargino co-annihilation (yellow), resonant annihilation via the A^0, H-funnel (brown) and stop co-annihilation (red). Fit from the GAMBIT collaboration [48].

$|\mu|$, heavy squarks and sleptons can be allowed assuming an LSP with a large Higgsino component.

At the current time, in the CMSSM context, the $\tilde{\chi}_1^0$ relic density does not exceed the measured value in confined parameter regions either through $\tilde{\chi}_1^\pm$ co-annihilation, resonant annihilation via the A^0, H-funnel, or $\tilde{t}_1$ co-annihilation. These regions are shown in Figure 2.3.3 for $M_{\tilde{\chi}_1^0} < 3$ TeV, together with the profile likelihood of the CMSSM in the $M_{\tilde{\chi}_1^0}$ - $\log(\Omega_{\tilde{\chi}_1^0} h^2)$ plane.

Extensions of the MSSM can result in a completely different thermal relic abundance prediction, sometimes with negligible changes to the collider phenomenology.

2.3.5 Decay phenomenology

Assuming R-parity conservation at pp collider experiments, the production of a pair of LSPs could be investigated with the monojet analysis [49]. Most of the scenarios assume a bino-like $\tilde{\chi}_1^0$, or a gravitino, as the LSP of the theory and in such a case the typical cross section for the production of the two LSPs is too small compared to the

SM background, or to generate any event in the LHC lifetime.

The production of superparticles heavier than the lightest one results in a final state topology and phenomenologies related to the mass spectrum and branching fractions for the different channels. In this section, a description of the SUSY decay modes is presented. Herein, one uses the generic labels l, ν and q for charged leptons, neutrinos and quarks and $\tilde{l}$, $\tilde{\nu}$ and $\tilde{q}$ for the respective scalar partners.

Neutralino decays

Probably the richest for the channel phenomenology, the decay of heavy neutralinos can be summarised by the expression

$$\tilde{\chi}_j^0 \to Z\tilde{\chi}_k^0,\ W^\pm\tilde{\chi}_i^\pm,\ h^0\tilde{\chi}_k^0,\ l\tilde{l},\ \nu\tilde{\nu},\ A^0\tilde{\chi}_k^0,\ H^0\tilde{\chi}_k^0,\ H^\pm\tilde{\chi}_i^\pm,\ q\tilde{q} \tag{2.3.25}$$

with $j > 1$ and $k < j$. The first five modes are dominant when allowed in the majority of SUSY models. If all the two body decays are prohibited, the three-body decays via off-shell W, and Z or h^0 bosons, depending on the nature of the neutralinos, are the dominant ones in most SUSY models.

Chargino decays

For the charginos, typically the two body-decay modes follow a trend with increasing likelihood from left to right

$$\tilde{\chi}_j^\pm \to W^\pm\tilde{\chi}_i^0,\ Z\tilde{\chi}_1^\pm,\ h^0\tilde{\chi}_1^\pm,\ l\tilde{\nu},\ \nu\tilde{l},\ A^0\tilde{\chi}_1^\pm,\ H^0\tilde{\chi}_1^\pm,\ H^\pm\tilde{\chi}_i^0,\ q\tilde{q}', \tag{2.3.26}$$

with the squark and the quark different in flavour. Similarly to the neutralino case, when all the two body decays are prohibited the three-body decays via W, and Z or h^0 bosons are dominant. Particularly interesting is the case $\tilde{\chi}_1^\pm \to W^\pm\tilde{\chi}_1^0$ via an on- or off-shell W boson, being probably the most favourite mode in the entire electroweak sector.

Slepton decays

When kinematically allowed the decay channels are quite simple:

$$\tilde{l} \to l\tilde{\chi}_i^0,\ \nu\tilde{\chi}_1^{\pm}, \tag{2.3.27}$$

$$\tilde{\nu} \to l\tilde{\chi}_i^0,\ l^{\mp}\tilde{\chi}_1^{\pm}. \tag{2.3.28}$$

Right-handed sleptons typically decay to a bino-like LSP $\tilde{\chi}_1^0$, while left-handed sleptons may prefer modes mediated by heavier wino-dominated electroweakinos.

Squark decays

The squark decay modes can be summarised by

$$\tilde{q} \to q\tilde{g},\ q\tilde{\chi}_i^0,\ q'\tilde{\chi}_1^{\pm}. \tag{2.3.29}$$

The first mode is dominant when allowed because of the QCD strength of the vertex. Similar to the slepton case, right-handed squarks likely decay directly in the LSP, while left-handed squarks may prefer intermediate wino-like charginos or neutralinos and provide a richer final state.

Only the third generation of squarks is likely to decay to Higgsino-dominated electroweakinos due to the larger Yukawa coupling with respect to the other two families.

The phenomenology for the cascade decay of the lightest stop is worth noting. Reducing progressively the mass splitting $M_{\tilde{t}_1} - M_{\tilde{\chi}_i^0}$, when allowed, the dominant modes follow the trend

$$\tilde{t}_1 \to t\tilde{\chi}_i^0,\ b\tilde{\chi}_1^{\pm},\ bW\tilde{\chi}_i^0,\ c\tilde{\chi}_i^0,\ bW^*\tilde{\chi}_i^0. \tag{2.3.30}$$

For the last two channels, it may be the case that the scalar top has a lifetime long enough to hadronise in a jet in a similar way to the partons of the Standard Model.

Gluino decay

The gluino decay is the simplest one, because it can only occur through a real or virtual squark:

$$\tilde{g} \to q\tilde{q}^{(*)}. \tag{2.3.31}$$

In many SUSY scenarios the light stop and sbottom are assumed to be the lightest coloured superparticles and if no other two-body decay is allowed, the modes through $\tilde{t}_1$ and $\tilde{b}_1$ will dominate.

The gravitino LSP

This paragraph briefly treats the phenomenology for the fermionic partner of the graviton and possible decays channels of heavier superparticles to $\tilde{G}$. In gravity mediated models the lightest neutralino ($\tilde{\chi}_1^0$) is the most favoured LSP candidate, while the lightest sneutrino is practically ruled-out. Gauge mediated and "no-scale" SUSY models predict a gravitino LSP. It does not interact weakly making its hunting non-feasible in direct searches.

At a *pp* collider experiment the typical phenomenological study assumes the $\tilde{\chi}_1^0$ as the next-to-lightest supersymmetric particle NLSP when the gravitino is the LSP. There are two main possibilities. When the half-life for the $\tilde{\chi}_1^0$ is long enough and the decay $\tilde{\chi}_1^0 \to \gamma\tilde{G}$ (which is supposed to be the dominant one) occurs outside the detector or when the mass difference between the two superpaticles is very small (less or $O(10\text{ GeV})$) the missing transverse momentum ($\not{E}_T$) can be simply approximated by the sum of transverse momentum of the two $\tilde{\chi}_1^0$. When the mass difference is larger and the $\tilde{\chi}_1^0$ lifetime short enough, a peculiar signature appears with two high energy photons and $\not{E}_T$ [50].

In the MSSM, sleptons are also likely to be the NLSP with a gravitino LSP. In such a case, depending on the value of $\tan\beta$, one can have a slepton co-NLSP scenario or a stau-NLSP scenario. For long-lived sleptons a track with high ionisation can be measured in the detector.

2.3.6 Theoretical guidelines

The mere philosophical argument, when extremely simplified as a battle between naturalness and the anthropic principle, can be misleading for the scientific method. A weak version of the anthropic principle is the following:

> *The observed values of all physical and cosmological quantities are not equally probable but they take on values restricted by the requirement that there exist sites where carbon-based life can evolve and by the requirements that the universe be old enough for it to have already done so.*
>
> Barrow and Tipler

When applied to the hierarchy problem it seems to suggest that human beings experience the mass of the Higgs ∼125 GeV almost by an accident in an infinite number of possible universes (the multiverse).

On the other hand, taking naturalness too rigorously can be misleading as well. At the present time, there are no observed SUSY signatures at the LHC in the CMSSM context and many natural models were already excluded from LEP searches as shown in Figure 2.3.4. In any case, often naturalness has guided the formulation of theoretical models which have been later proved correct.[14]

[14] Here correct or right (wrong) refers to the capacity for the theoretical model to explain (not explain) experimental results.

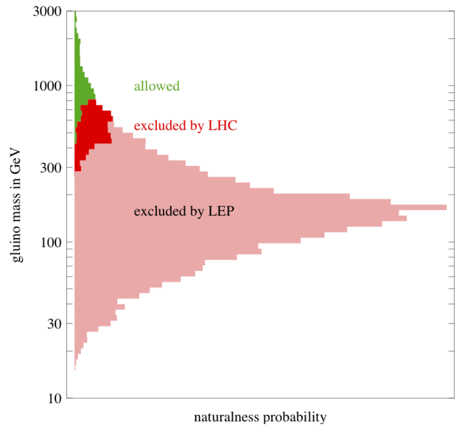

Figure 2.3.4: The distribution of the "Naturalness probability" for the gluino mass in the mSUGRA paradigm. The current LHC data allow a still more restricted region in the tail of the distribution. Figure from [51] (2011).

> *The appearance of fine-tuning in a scientific theory is like a cry of distress from Nature, complaining that something needs to be better explained.*
>
> Weinberg

> *Everything should be made as simple as possible but not simpler.*
>
> Einstein

These statements suggest that unnatural BSM theories are likely wrong and the further one deviates from the SM the more likely the theory is wrong. Is natural SUSY ruled out? It should be clear that supersymmetry is a large framework and not a simple model.

From a pragmatic point of view there are only three possibilities:

- Supersymmetry is wrong.
- Supersymmetry is right, but the energies achieved by the experiments are too low and it cannot be discovered yet.

- Supersymmetry is right with a visible sector at the weak scale, but it eludes the experiments for some reasons.

Betting on the third option, there are two main possible strategies to pursue. Consider extensions of the MSSM that can produce unique signatures at collider experiments. Parametrise our ignorance in the phenomenological MSSM (pMSSM) framework assuming the hints of organisation described in Section 2.3.4.1.

In the second case, one could scan the 19 weak-scale parameters with a rigorous statistical investigation or make some assumptions on the available sparticle phase space and take a subclass of these parameters, consider restrictions in which only a small number of processes can contribute, and look in regions of phase space that are particularly challenging to probe in experiments. In particular, the latter is the core of this thesis and described in the next chapter with more details.

Following the Einstein and Weinberg suggestions, it is better to consider fine-tuning quantitatively, since naturalness is a deep underlying motivation for weak-scale SUSY. The expansion of the MSSM Higgs potential $V_{Higgs} = V_{Tree} + \Delta V$, with V_{Tree} given in Eq. 2.3.20, for large $\tan\beta$ can be written in the form

$$\frac{M_Z^2}{2} = -\left|\mu\right|^2 + \frac{\left(m_{H_d}^2 + \sum_d\right) - \left(m_{H_u}^2 + \sum_u\right)\tan^2\beta}{\tan^2\beta - 1}. \tag{2.3.32}$$

Traditionally there are three classes or ways to evaluate fine tuning [52, 53]:

- The Barbieri-Giudice (BG) measure $\Delta_{BG} = \max|A_i| = \max\left|\frac{\partial \ln M_Z^2}{\partial a_i^2}\right|$.
- The High-Scale (HS) measure $\Delta_{HS} = \max_i \frac{|B_i|}{\left(M_Z^2/2\right)}$ with B_i containing $\log\Lambda$ dependencies.
- The Electroweak scale (EW) measure $\Delta_{EW} = \max_i \frac{|C_i|}{\left(M_Z^2/2\right)}$ with C_i defined at weak scale.

The value of fine-tuning is not only model-dependent but also evaluation-dependent with generally $\Delta_{EW} \lesssim \Delta_{BG} \lesssim \Delta_{HS}$. The simpler and unambiguous way to compute the fine-tuning is to take the EW version. All the terms on the right in Eq. 2.3.32 must be of order ${M_Z^2}/{2}$ to avoid fine-tuning, with the contributions $\sum_d$ and $\sum_u$ deriving from derivatives of $\triangle V$ evaluated at the minimum.

At tree level, the key observation that is relevant for SUSY collider phenomenology is that Higgsinos must be light because their masses are directly controlled by the μ term. At one-loop the main contribution to $\sum_u$ comes from the stop. At the same time, the stop cannot be too light since $M_h \sim M_Z\,|\cos 2\beta|$ at tree level, hence many natural SUSY models require large $\tan\beta$. Also the wino is involved in the one-loop corrections and for a similar reason its mass is expected to be below or at the TeV scale. From the two-loop corrections the gluino mass must be limited depending on the mass of the stops.

Assuming a maximum tuning of 10% ($\Delta_{EW} \lesssim 10$) natural inspired MSSMs suggest that the charginos and neutralinos, depending on their nature, are around $\sim \mathcal{O}$(100 GeV) when more Higgsino-like, and $\sim \mathcal{O}$(TeV) when wino-like. Stops are expected to be around the TeV scale or below $m(\tilde{t}_1)$, $m(\tilde{t}_2) \lesssim 1.5$ TeV depending on the mixing. The left-handed sbottom is part of the doublet with $\tilde{t}_L$, and due to the evolution of the masses described by the RGEs, sbottoms are expected to be not too much heavier than the stops with the light sbottom limited to $m(\tilde{b}_1) \lesssim 1.5$ TeV. Finally, depending on the mass of the light stop, the gluino mass is expected to be limited to $m\left(\tilde{g}\right) \lesssim 3 - 4.5$ TeV.[15]

At collider experiments, some natural MSSM scenarios are challenging due to the mass spectrum. For instance, when the electroweakino sector is compressed, due to a bunch of Higgsino-dominated eigenstates of mass, light stops and sbottoms can decay more or less democratically via involved cascade decays through charginos and neutralinos, evading SUSY search limits. At the same time, the cross sections for the electroweakino pair-production could be too small (see Figure 3.5.2) for discovery.

[15] Evaluating a la Barbieri-Giudice $\Delta_{BG} = 10$, the constraints beyond the tree level are more severe: $|\mu|^2 \lesssim 200$ GeV, $m\left(\tilde{t}_1\right) \lesssim 400 - 500$ GeV, $m\left(\tilde{g}\right) \lesssim 800 - 1000$ GeV.

A vast class of extensions of the MSSM paradigm make SUSY still natural altering significantly the considerations for the masses described so far. For example, the "Minimal Composite Higgs" symmetry breaking [54] provides heavy Higgsinos and hence a potentially heavy LSP. In the next chapters one describes that experimental analyses have low sensitivity for compressed spectra.

To conclude, suggestions related to naturalness are taken as a guideline for prospective SUSY discovery and not as a no-lose theorem. In this thesis, the astrophysical constraint due to the DM relic density is considered in a way that one assumes R-parity conservation and that the lightest neutralino ($\tilde{\chi}_1^0$) is the LSP of the theory. Motivated by the naturalness-inspired MSSM (or extensions of the MSSM), special investigations for compressed spectra in the electroweak sector and between the LSP and coloured sparticles are performed with particular focus on gluino pair-production. The third generation of squarks is treated separately with a particular interest in the sbottom, with the typical mode $\tilde{b}_1 \rightarrow b\tilde{\chi}_1^0$ being much more plausible with respect to different possible combinations of the stop decay channels (see Eq. 2.3.30 and Eq. 2.3.29).

Chapter 3

BSM at proton-proton collider experiments

3.1 Introduction

Several experiments all around the world are designed to search for BSM physics. Searches for dark matter can be categorised into three possible types as shown schematically in Figure 3.1.1 resulting in a complementarity for its detection.

Indirect searches, based for example on probing DM annihilation to γ-rays, are performed by experiments like Pamela [55], AMS [56] and Fermi-LAT [57]. Underground experiments such as LUX [58] and Xenon1T [59] search for the direct interaction of DM resulting in liquid Xenon nuclei recoils.

The detection of DM, together with a deep understanding of its phenomenology at collider experiments, presupposes the possibility to produce the on-shell particle from SM particles. The energy density achievable by the machine is a very important indicator of the discovery potential. According to the Einstein formula (here rewritten in natural units)

$$E = m \tag{3.1.1}$$

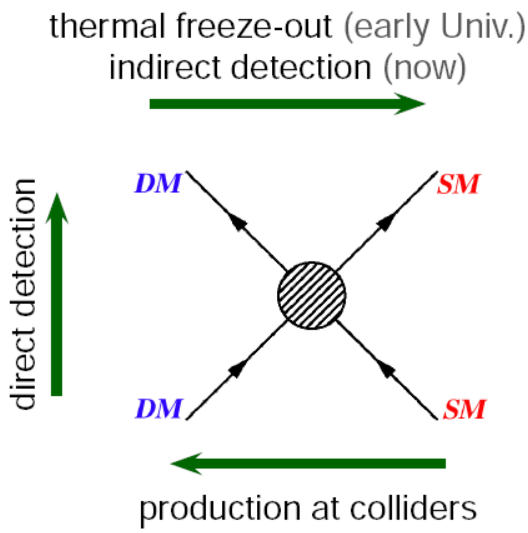

Figure 3.1.1: Searching for dark matter.

a particle of mass m could be produced only in the case of enough energy E being carried by the colliding SM particles. Whenever a particle can be produced its detection presupposes the ability to separate its phenomenology with respect to the background noise. The key to any search is the capacity to discriminate signal-like events from background-like events and a fundamental quantity to be considered is the ratio between the number of events of the two types:

$$r = \frac{S}{B}. \tag{3.1.2}$$

The number of events for the given process expected to be seen by a detector can be summarised by the following relation

$$N = \sigma \times BR \times \epsilon \times \int \mathrm{d}t\mathcal{L} \tag{3.1.3}$$

where σ is the cross section, BR is the factor related to the branching fractions of the channels, as described in the previous chapter, ϵ takes care of all the efficiencies and acceptances for the reconstruction of the objects in the final states as discussed in

Section 3.4.2 and $\int \mathrm{d}t\mathcal{L}$ is the luminosity integrated in time.[1]

The modern experimental setup of particle colliders involves two beams of SM particles of some kind accelerated and collided at an interaction point inside the detector. Contrary to the fixed target setup, all the energy of the beams can be converted into the mass of new particles. Hadrons must be preferred to lighter particles in synchrotrons due to the energy loss of charged particles moving along a curved trajectory

$$\frac{dE}{dt} \propto \frac{E^4}{m^4 R}, \tag{3.1.4}$$

with R the radius of curvature and E and m the particle's energy and mass. Easy to get from hydrogen, protons can be accelerated and brought together for head-on collisions by electromagnetic fields.

Protons cannot be approximated to point-like particles at the small distance scales probed at the LHC. The parton model is the theoretical framework [60] describing the interactions between the constituents of the two hadrons (A and B) as schematically shown in Figure 3.1.2a. At a hadron collider, a fraction of the momentum of the hadron x is carried by the valence and sea quarks and gluons of protons and neutrons.

The inclusive cross section for the production of the final state X from two protons $p_1$and p_2 is written with the factorisation

$$\sigma_{p_1 p_2 \to X} = \sum_{a,b\epsilon\{q,g\}} \int dx_a \int dx_b f_a^{p_1}\left(Q^2, x_a\right) f_b^{p_2}\left(Q^2, x_b\right) \sigma_{ab\to X}\left(Q^2\right), \tag{3.1.5}$$

where $\sigma_{ab}\left(Q^2\right)$ is the partonic cross section. The Parton Distribution Functions (PDFs) $f_{a(b)}^{P}$ describe the probability for a given parton of flavour a (b) to have a particular x value for a transferred momentum Q as how in Figure 3.1.3. Figure 3.1.2b shows the Standard Model cross sections as a function of the centre-of-mass energy achieved by the collider.

[1] Often in this thesis, the integrated luminosity is referred to simply as $\int \mathcal{L}$, omitting the time integration.

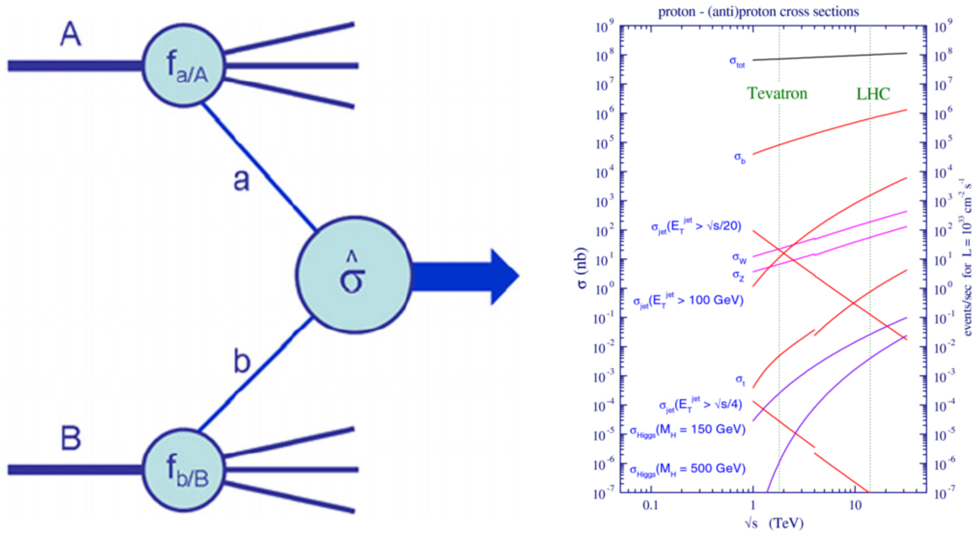

(a) (b)

Figure 3.1.2: Schematic diagram of a hard scattering process based on the parton model (3.1.2a). MSTW 2008 NLO Standard Model process cross sections as a function of collider energy (3.1.2b). Figures from [61].

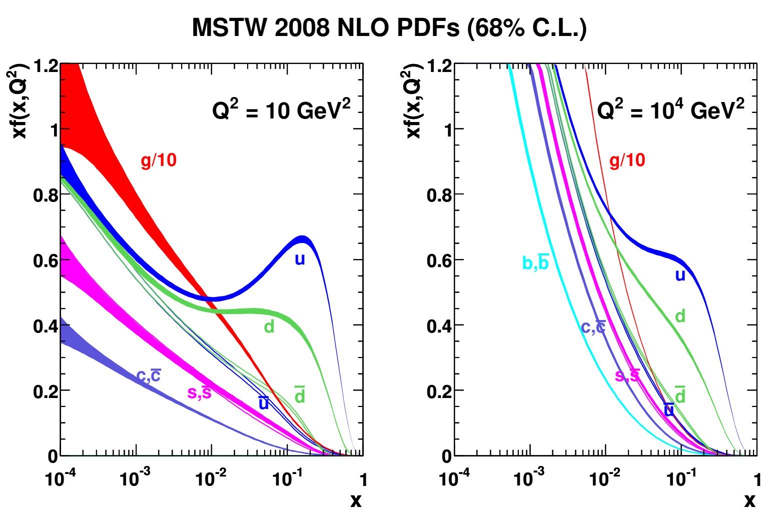

Figure 3.1.3: MSTW 2008 NLO parton distribution functions at Q^2=10 GeV^2 (left) and Q^2=10^4 GeV^2 (right). Figure from [61].

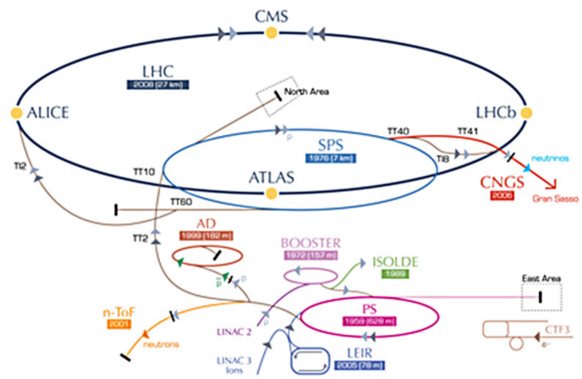

Figure 3.2.1: The CERN accelerator complex. Figure from [63].

3.2 LHC

Located in Geneva, at the Franco-Swiss border, the Large Hadron Collider (LHC) [62] is the world's largest particle accelerator designed to collide protons and lead ions at higher energies than any other existing experiment. Installed in the 27 km LEP tunnel, at CERN, the two-ring superconducting hadron collider is the final step of a number of accelerating structures used to boost the energy of the particles along the way as shown in Figure 3.2.1.

A gas bottle supplies hydrogen atoms. An electric field removes the electrons and the protons are accelerated by linear and synchrotron apparatus to energy of 450 GeV. The beam is then split in two and each part is accelerated in opposite directions around the LHC in two ultra-high vacuum pipes. Operating with a peak magnetic field of 8 T, superconducting dipole and focusing de-focusing quadrupole magnets accelerate and guide the protons in a close orbit and constraint the beams in transverse directions. The two beams, travelling close to the speed of light, are forced to collide with the nominal centre-of-mass energy for the two protons of $\sqrt{s} = 14$ TeV[2] at four interaction points corresponding to the locations of the four main experiments ALICE, ATLAS, CMS and LHCb.

[2] At the current time the LHC is operating at $\sqrt{s} = 13$ TeV.

3.2.1 Luminosity

The last term in Eq. 3.1.3 is the integral in time of the machine instantaneous luminosity and can be written as

$$\mathcal{L} = \frac{N_b^2 n_b f_{rev} \gamma_r}{4\pi \epsilon_n \beta^*} F \tag{3.2.1}$$

where N_b is the number of particles per bunch, n_b the number of bunches per beam, f_{rev} the revolution frequency, γ_r the relativistic gamma factor, ϵ_n the normalised transverse beam emittance, β^* the beta function at the collision point, and F a geometric reduction factor due to the non-zero crossing angle between the beams at the interaction point [62].

The quadratic dependence on N_b cannot be fully exploited in proton-antiproton colliders due to the difficulty in achieving the necessary antiproton beam intensity, while, on the other hand, too many particles per bunch can increase the noise due to the simultaneity of multiple interactions.

The nominal instantaneous luminosity of the LHC machine is $\mathcal{L} = 10^{34}\text{cm}^{-1}\text{s}^{-1}$. For the purposes of this thesis, fixed values will be assumed for the integrated luminosity as projections for the proposed analyses.

3.2.2 Event structure

A single LHC event is the result of a combination of physics phenomena as schematically summarised in Figure 3.2.2.

The two beams of ultra-relativistic protons are squeezed together and made to cross at the interaction point inside the detector. Protons can interact as a whole object with a small transferred momentum in a so called *soft* process. More interesting for the discovery prospects of BSM physics are processes in which the proton reveal their inner structure and the partons collide in a *hard* interaction. Multiple proton-proton interactions in a single bunch crossing referred as *in-time pileup* can occur producing

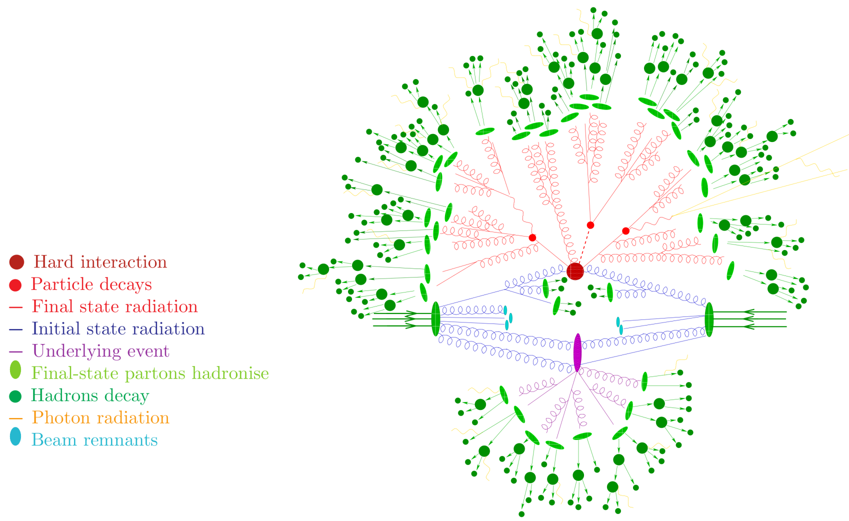

Figure 3.2.2: Pictorial representation of $pp \to t\bar{t}h \to$ hadrons event as produced by the generator SHERPA 1.1. Figure from [64].

an inconvenient background of mainly soft hadronic activity. *Out-of-time pileup* refers to the same phenomenon occurring in different bunches and can constitute a problem when the time response of the detector hardware is comparable to the time between two consecutive bunch crossings.[3] *Multi-parton interactions* (MPI) refer to the cases involving more than one parton of each proton in a hard process, while if only one parton interacts hardly, the soft processes related to the interaction involving the remnant of the proton are referred as *underlying events* (UE). Perturbative effects named *initial state radiation* (ISR) and *final state radiation* (FSR) are due to electromagnetic and strong emissions before or after the hard interaction. Finally, before they reach the detector, coloured particles hadronise in a jet of mesons and baryons due to confinement. The one exception is the top quark, as described in the next section.

[3]At $\sqrt{s}$=14 TeV, a time response of $\mathcal{O}(10 \text{ ps})$ would be necessary to resolve between a reasonable average number of interactions per crossing of ~ 50 (average in-time pileup).

3.3 Detectors

3.3.1 Multi-detector

The ATLAS and CMS machines are complex multi-detectors designed for general purpose experiments ranging from high precision Standard Model measurements to searches for new physics.

Conventionally, one uses a right-handed coordinate system, with the origin at the nominal interaction point. The x-axis points to the centre of the LHC ring, the y-axis points upward (perpendicular to the LHC plane), and the z-axis points along the anticlockwise beam direction. As the partons involved in the hard interaction can carry different fractions of the proton momenta it is possible for there to be an asymmetry in the collision and hence the centre-of-mass (CM) frame undergoes a Lorentz boost in the z-direction. The detector does not have full azimuthal coverage near to the beam axis, hence such an overall longitudinal boost is not known.

The spherical coordinate system has a polar angle (θ) measured from the positive z-axis and the pseudorapidity (η) defined in term of θ as $\eta = -\ln\left(\tan {}^{\theta}/_{2}\right)$ which corresponds to the rapidity $y = -\ln \frac{E+p_z}{E-p_z}$ for massless objects. Cylindrical coordinates are used in the transverse plane (r, ϕ) where r is the radius denoting the distance from the z-axis and ϕ the azimuthal angle measured from the positive x-axis. A really useful angular distance (ΔR) in the $\eta - \phi$ space is used to isolate different reconstructed "particle objects" and is defined as $\Delta R = \sqrt{\Delta\eta^2 + \Delta\phi^2}$. Pseudorapidity differences and ΔR are Lorentz invariants under longitudinal boosts.

The only stable Standard Model particles to directly interact with the detector are photons, muons and electrons. The Higgs boson, vector gauge bosons and τ-lepton decay leptonically or into quarks. Due to confinement, coloured particles cannot be detected as isolated objects, since they hadronise into mesons and baryons, reaching the detector as jets. The top quark, with a mean lifetime of 2.5×10^{-25} s, decays to a W-boson and a bottom quark before hadronisation. Finally, detectors are blind to weakly interacting neutrinos.

The general setup and characteristics of the two main detectors are quite similar. Built around the interaction point concentric cylindrical layers of sub-detectors cover a full azimuthal acceptance so as to extract a measure for the missing transverse momentum leveraging on the conservation of the momentum in the transverse plane. Depending on which sub-detector/s the particle interacts with, it can be identified as schematically shown in Figure 3.3.1. Exploiting the Lorentz law, charged particle trajectories in the inner detector are used for momentum reconstruction

$$p = Bqr, \tag{3.3.1}$$

with r the radius of the circular orbit in the magnetic field B. The resolution for the momentum has the dependence

$$\frac{dp}{p} \propto \frac{p}{Bl^2} \tag{3.3.2}$$

and can be improved increasing the magnetic field or the distance l.

Electromagnetic and hadronic calorimeters are used to stop photons-electrons, mesons and baryons respectively and measure their release of energy. They consist of layers of *passive* high-density material such as lead or steal interleaved with layers of an *active* medium. An excellent energy resolution is a fundamental characteristic for several analyses and is related to stochastic shower fluctuation a, readout electronic noise b and constant instrumental effects c following the formula [65]

$$\frac{\sigma}{E} = \frac{a}{\sqrt{E}} \oplus \frac{b}{E} \oplus c. \tag{3.3.3}$$

An outer sub-detector is used for the identification of the muons and the investigation of their kinematics. Another main feature in the design of the detectors is a good symmetric backward-forward coverage resulting from the combination of concentric cylinders around the beam axis referred to as the *barrel* detectors and plates called *endcap* disks

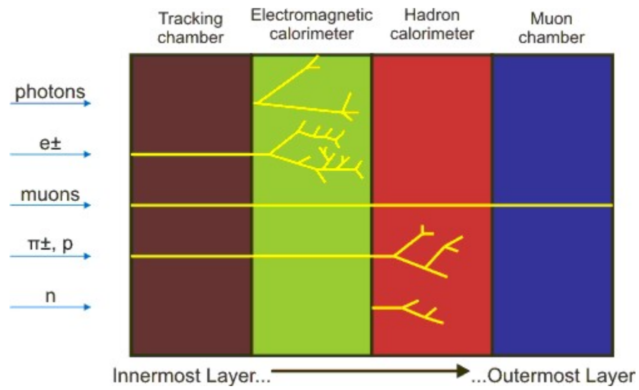

Figure 3.3.1: Schematic imprinting of the different particles in the sub-detectors of ATLAS and CMS. Figure from [66].

that cover the ends of the barrel. Moreover, the ability to find secondary vertices is particularly important for the identification of bottoms, charms and hadronically decaying τ-leptons.

3.3.2 ATLAS and CMS

The ATLAS detector [67], A Toroidal LHC ApparatuS, is a $\sim$ 7000 tonne machine constructed around one of the interaction points of the LHC ring as shown in Figure 3.3.2. Three large superconducting toroids together with a thin central superconducting solenoid dominate the apparatus design. The inner detector is located within a length of 5.8 m and a diameter of 2.56 m solenoid providing a 2T magnetic field. Closest to the pipe, it is responsible for the high precision measurements of position and momentum of charged particle tracks. It is subdivided into a silicon pixel detector (PIX), to which has recently has been added a new Insertable B-Layer (IBL) dedicated to the physics of the bottoms, a semiconductor tracker (SCT) making use of silicon strips, and the transition radiation tracker (TRT) which is a straw-tube tracking detector. Liquid argon scintillator (LAr) and plastic scintillator tiles are employed as the active medium in the calorimetry. The hadronic barrel calorimeter uses a tile scintillator while the EM barrel, EM and hadronic endcaps, and hadronic forward calorimeters employ LAr. The largest and outermost part consists of an array of detectors of the muon spectrometer

(MS) surrounding the toroidal magnet system. Four different technologies are employed: the Monitored Drift Tubes (MDT) and the higher granularity Cathode Strip Chambers (CSC) are used for measurements of the track bending respectively for smaller and larger pseudorapidity, while Resistive Plate Chambers (RPCs) are used in the barrel and Thin Gap Chambers (TGCs) are used in the endcaps for the trigger.

The Compact Muon Solenoid [68], (CMS) is the other main general-purpose detector at the LHC shown in Figure 3.3.3. The main feature is the superconducting solenoid designed to reach a 4 T magnetic field and operating at 3.8 T *in situ*. This provides an excellent momentum resolution when measuring charged particles with the silicon tracker as follow from Eq. 3.3.2. The silicon pixel detector is surrounded by silicon strip layers categorised in three subsystems: the Tracker Inner Barrel and Disks (TIB/TID) the Tracker Outer Barrel (TOD) and Tracker EndCaps (TEC). The Electromagnetic calorimeter ECAL, made up of a barrel and two endcap systems, employs active layers of lead tungstate crystal located between the tracker and the hadronic calorimeter. Covering different intervals of pseudorapidity and interaction depths, the barrel and endcap sampling HCALs are made of repeating layers of dense brass or steel absorber and tiles of plastic scintillator. Quartz fibers are used as the active medium in the forward hadronic calorimeter (HF) to increase the radiation resistance. A reversal of the curvature of the muon's trajectory is due to the opposite direction of the magnetic field passing from the solenoidal barrel to the *return yoke* sub-detectors. In order to track the particles' positions and provide a trigger one employs drift tubes (DTs) and cathode strip chambers (CSCs), while resistive plate chambers (RPCs) are dedicated only to the trigger. DTs and RPCs are arranged in concentric cylinder barrels around the beam axis whilst CSCs and RPCs, make up the endcap disks.

A much more detailed description of the two detectors can be found elsewhere [68, 69] together with their performances, objects combination-reconstruction, information for the electronics, trigger, data collection.[4] For the purpose of this thesis the specifics

[4]The acronyms used in this Section are typical of the ATLAS and CMS collaborations.

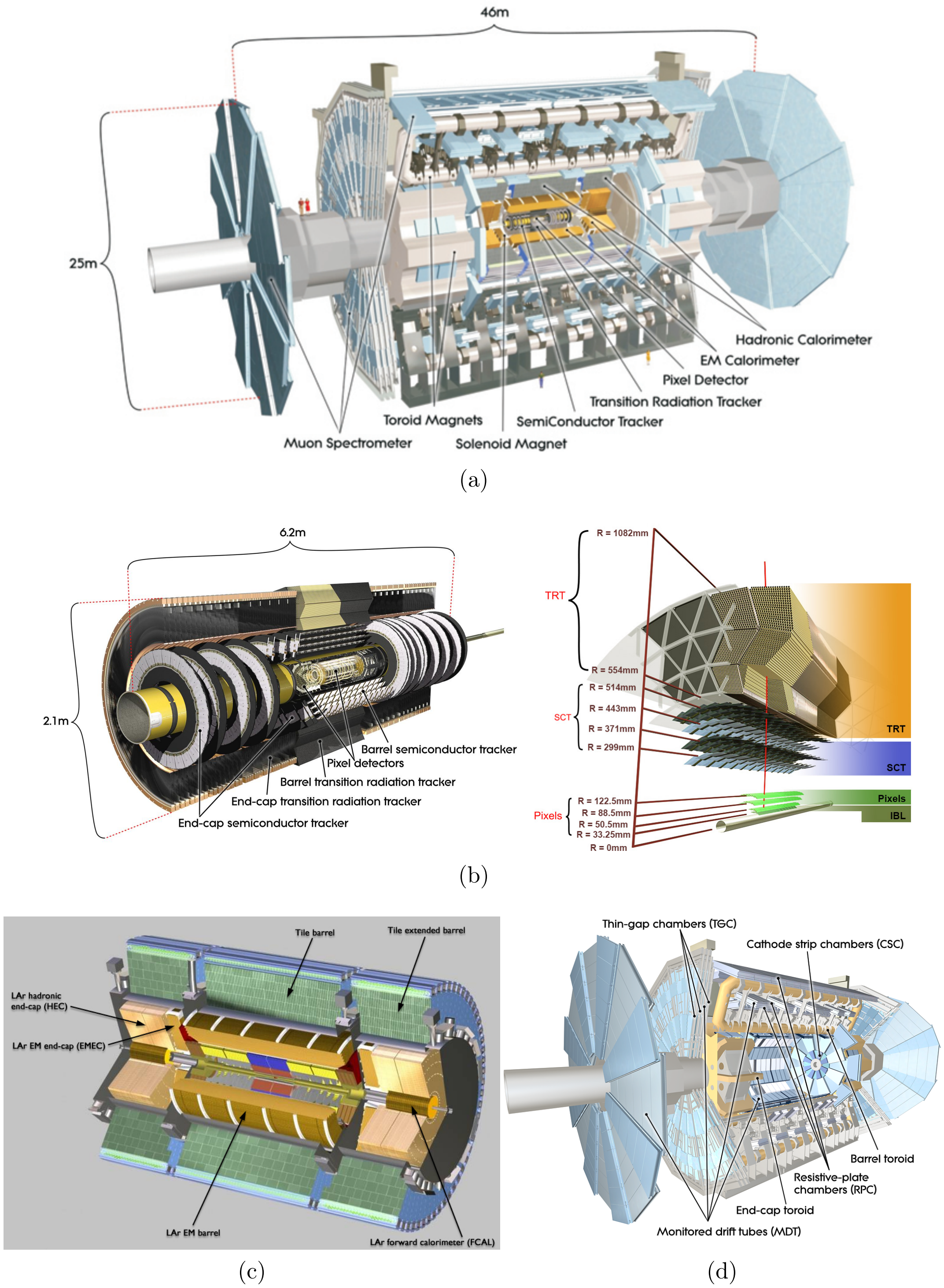

Figure 3.3.2: **The ATLAS detector**. The figures show schematic diagrams of: (a) the whole apparatus, (b) the inner detector (left) layout of the different sub-detectors of the inner detector in the barrel region (right), (c) calorimeter system and (d) muon spectrometer. Figures from [67].

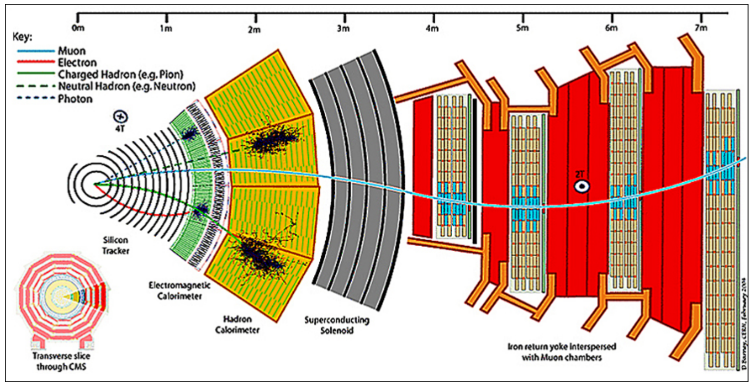

(a)

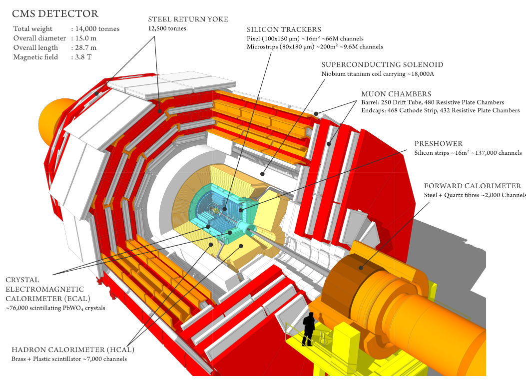

(b)

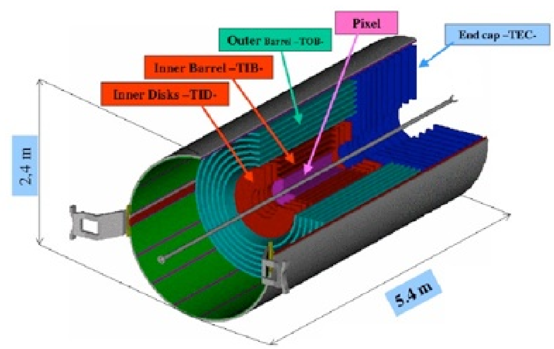

(c)

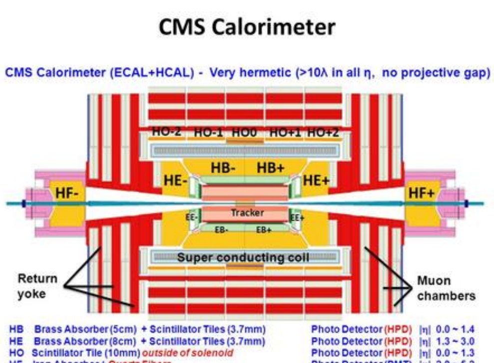

(d)

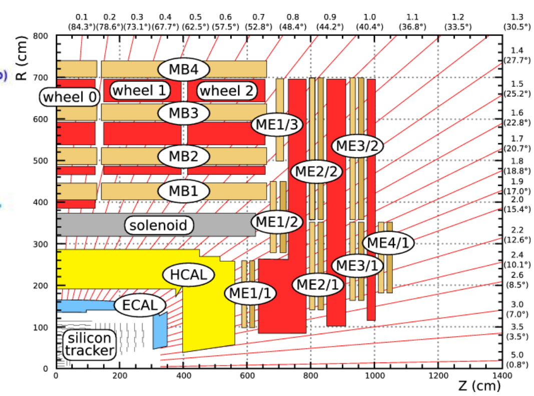

(e)

Figure 3.3.3: **The CMS detector**. The figures show schematic diagrams of: (a) the interaction of the particles with the sub-detectors in a transverse view of a CMS slide (b) the whole machine (c) the inner detector, (d) the calorimeter system and (e) a quadrant of the detector with the beam axis (z) horizontally and the radius (r) vertically with the muon stations in red. Figures from [68].

regarding the acceptances, isolation and efficiencies for the reconstruction of the objects are described in Section 3.4.2.

3.4 Monte Carlo simulation

The procedure used in this thesis presupposes Monte Carlo (MC) simulations for Standard Model background and signal samples. One considers each of the SM processes which are expected to constitute the dominant backgrounds to the SUSY signals as described in the Snowmass study [70]. These samples are proton proton collision at $\sqrt{s} = 14$ TeV generated with Madgraph 5 [71] using the default CTEQ6l1 PDF [72]. The parton shower is performed with Pythia 6 [73] followed by a detailed detector simulation with Delphes 3 [74] in which a parameterisation for the performances of the existing ATLAS and CMS experiments is implemented. The simulation procedure involves the generation of events at leading order in bins of the scalar sum of the generator level particles transverse momenta, with jet-parton matching and corrections for next-to-leading order (NLO) contributions. The SM background include all the processes described in Section 3.5.1 assuming the cross sections and k-factors in Ref. [75].

In this section some specifics of these tools are described. Because of the two extremes in the QCD behaviour, corresponding to asymptotic freedom and confinement of the partons, the generation of the events is separated into two parts.

Hard processes are characterised by a high value of Q^2 corresponding to a low value of the running α_S based on the renormalisation group equation [3]. The perturbative theory is used in the calculation of the different contributions and referred to as the matrix element (ME) method.

At lower energies non-perturbative effects such as hadronisation and UE, must be computed from QCD-inspired models. This is the case with soft-collinear emission, often referred to as the parton shower (PS).

3.4.1 Madgraph, Pythia, MLM matching

Madgraph 5 is the tool used for the generation of the hard processes, which are then matched with the PS generator, and for the cross section computations. A detailed description can be found elsewhere [71]. The parton level resulting from perturbative QCD corrections is interfaced with Pythia 6 [73] or Pythia 8 [76]. This latter general-purpose high-energy physics events generator is employed for the parton shower described as successive parton emissions and for the hadronisation.

In order to avoid overlap between the phase space explored by Madgraph and Pythia in the presence of extra partons in the generation a parton-jet matching procedure is required. The motivation to use both is related to the different QCD behaviour at high-low energies: the ME description diverges as partons become soft or collinear, while the PS description fails for high-momentum and widely separated partons. Two philosophies are the CKKW technique [77–79] based on a shower veto and event reweighting and the MLM method [80,81] based on event rejection. Three MLM schemes are implemented in Madgraph 5: the cone-jet, shower-p_T and k_T-jet MLM. The latter is used in the analyses and described in more details.

The Durham k_T algorithm is used to obtain the equivalent of the PS outcome for the final-state partons in each event generated by Madgraph 5. The clusterings corresponding to Feynman diagrams in the matrix element are kept while the others discarded. A cutoff scale *xqcut* is used as the minimum value required for the smallest k_T.

Events are passed to Pythia and the parton shower is implemented. The final-state partons are clustered to form jets once again using the k_T algorithm before the hadronisation and decays take place. A cutoff scale $QCUT$ is used for this second clustering. These jets are then compared to the partons: the *matching* is the case when the measure of k_T (parton, jets) is smaller than QCUT. In the case of each jet matched to a parton the event is kept except for the highest multiplicity sample, where extra jets are allowed below the k_T scale of the softest ME parton in the event. When partons are too close to generate a unique jet, or a single parton has too low transverse momentum

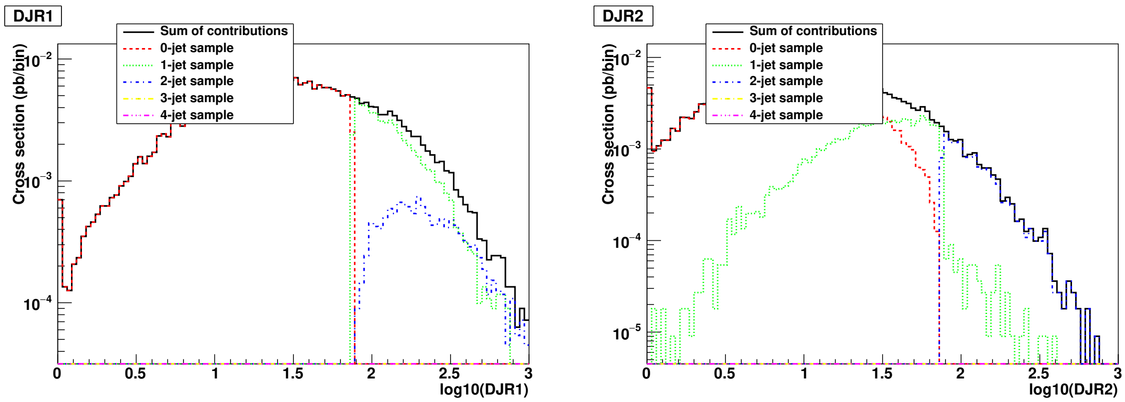

(a) (b)

Figure 3.4.1: Example of Differential Jet Rates (DJR1 (a) and DJR2 (b)) in the context of Madgraph + Pythia 6 matching. The sample is a chargino pair-production $pp \to \tilde{\chi}_1^+ \tilde{\chi}_1^-$, $pp \to \tilde{\chi}_1^+ \tilde{\chi}_1^- j$, $pp \to \tilde{\chi}_1^+ \tilde{\chi}_1^- jj$, with $M_{\tilde{\chi}_1^+} = M_{\tilde{\chi}_1^-} = 250$ GeV and j refers to additional partons hadronising in jets. Figure 3.4.1a shows log(DJR $0 \to 1$) and Figure 3.4.1b shows log(DJR $1 \to 2$) for xqcut=50 and QCUT =75. The passage from the red to the green curve (a) and from the green to the blue curve (b) results in a smooth transition at the merging scale for the distribution of the sum of contributions (black curve).

to be reconstructed as a jet, a non-matched event is the result.

The typical procedure is based on the generation of $N-1$ exclusive samples and one inclusive sample. When generating a sample with N additional partons, the generation of sub-samples with $\leq N-1$ partons proceeds by rejecting events containing more than the jet multiplicity required. The sub-sample with N additional partons is the inclusive one and additional jets from the PS are allowed as there will be no overlap. Usually the proposed analyses of this thesis assume next-to-leading order (NLO) contributions and matching or next-to-leading order and next-to-leading logarithmic (NLO+NLL) accuracy. Hence the generation assumes the tree level process plus one (or two) sub-processes with extra partons: $pp \to X$ and $pp \to X\ j$ (+ $pp \to X\ j\ j$).

Figures 3.4.1 and 3.4.2 show differential jet rates normalised to the cross section, for two examples of SUSY productions in the context of generation and matching Madgraph + Pythia. The differential jet rate is the scale at which the sample falls into a lower

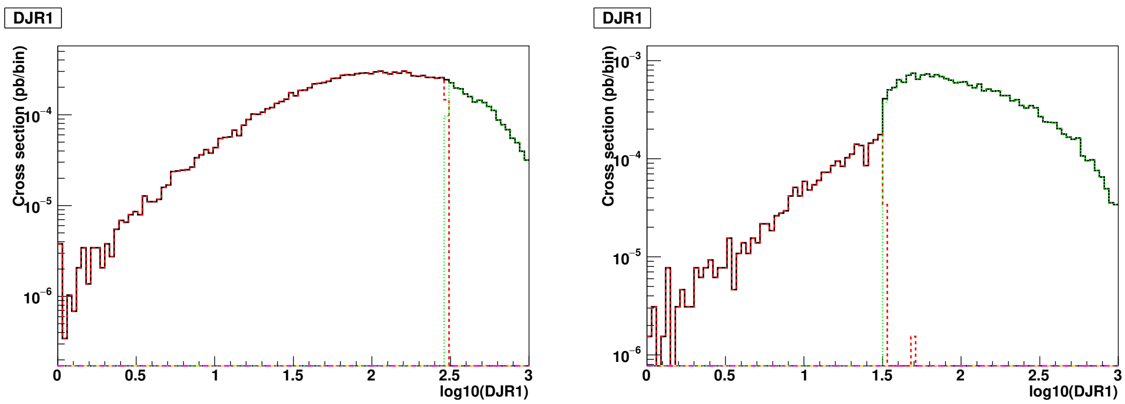

(a) xqcut=200, QCUT =300

(b) xqcut=30, QCUT =32

Figure 3.4.2: Example of differential jet rate (DJR1) in the context of Madgraph + Pythia 6 MLM matching. The SUSY sample corresponds to a sbottom pair-production with NLO corrections ($pp \to \tilde{b}_1\tilde{\bar{b}}_1$, $pp \to \tilde{b}_1\tilde{\bar{b}}_1 j$ with $M_{\tilde{b}} = 900$ GeV and j refers to one additional parton hadronising in a jet). Figure 3.4.2a and 3.4.2b show log(DJR $0 \to 1$) for xqcut=200 and QCUT =300 and for xqcut=30 and QCUT =32 respectively. Compare the transitions from the red to the green curves.

N-jet multiplicity based on the choices of QCUT and xqcut. The first example show the distribution of log(DJR $0 \to 1$) in Figure 3.4.1a and of log(DJR $1 \to 2$) in Figure 3.4.1b for the SUSY sample corresponding to a chargino pair-production with $M_{\tilde{\chi}_1^+} = M_{\tilde{\chi}_1^-} = 250$ GeV and NLO+NLL corrections. Their values must be independent of the cutoff scales chosen as these quantities do not have physical meaning.

The procedure consists of optimising the value for xqcut (and QCUT=1.5 xqcut for example) in a way to make the transitions between the 0 and 1 (and between 1 and 2) additional jet samples at the cutoff as smooth as possible. In addition one could check the transverse momentum of the leading and sub-leading jet and tune the QCUT/xqcut values in a way to stabilise the production cross section.

Figures 3.4.2a and 3.4.2b show distributions of DJR1 for a sbottom pair-production sample with $M_{\tilde{b}} = 900$ GeV and two possible QCUT/xqcut combinations. A smoother transition at the merging scale results choosing xqcut=200 and QCUT=300 than xqcut=30 and QCUT=32.

Typical values used for the generation of the SUSY samples are xqcut between $1/6$ and

1/3 of the hard scale, identified with the mass of the superparticle parent produced, and QCUT 50% larger.

3.4.2 Delphes and the definition of the physical objects

Final state events are passed to Delphes 3 [74] to simulate a fast detector response. Signal and background samples are generated with no-pileup at the pp centre-of mass collision of $\sqrt{s} = 14$ TeV and assuming a detector parametrisation based to the Snowmass study. The acceptances and efficiencies for the reconstruction of the different objects are in between the ATLAS and CMS responses or close to the best performance.

The tool simulates the response of the detector in reconstructing the tracking of charged particle. The electromagnetic and hadronic energy deposits are independently smeared by a log-normal distribution from Eq. 3.3.3. Two algorithms referred to as particle-flow tracks and particle-flow towers are used as input for reconstructing high resolution jets and missing transverse momentum. In this section a brief description of the efficiencies for the reconstruction of the objects together with the explanation of some physical key features is presented.

Isolation of electrons, muons and photons

The isolation is a fundamental feature in order to reject contributions due to jet backgrounds and accept *prompt* leptons reconstructed from the primary vertex, produced for example from the decay of on-shell vector bosons. In Delphes 3 each reconstructed electron, muon, or photon ($P = e, \mu, \gamma$) is defined to be isolated if the ratio collecting the activity of the i particles in its vicinity

$$I(P) = \frac{1}{p_T(P)} \left[\sum_{i \neq P}^{\Delta R < R,\, p_T(i) > p_T^{min}} p_T(i) \right] \tag{3.4.1}$$

is smaller than a fixed value I^{min}. One uses the values I^{min} =0.1, R=0.3 and p_T^{min} = 0.1 GeV.

In the detector, any other source different from isolated photons, electrons and muons is referred to as *fake*. A fake lepton includes in-flight decays of light or heavy hadrons or hadrons mimicking lepton signatures. Converted photons can be reconstructed as electrons. The neutral pion via the process $\pi^0 \to \gamma\gamma$ could mimic the signature of an high energy isolated photon. At this regard, ATLAS employs an highly segmented first ECAL compartment while CMS has a pre-shower detector in the endcap regions, where the angle between the two emerging photons is likely to be small enough to cause this problem. A simulation for the *fake* rate for electrons, muons and photons requires a detailed input from the experimental collaborations and is not implemented in Delphes 3.

3.4.2.1 Photon object

True photons and electrons with no reconstructed track reaching the electromagnetic calorimeter are identified as photons in Delphes 3 when isolated, with transverse momentum $p_T > 10$ GeV and efficiency:

- $\epsilon = 0.9635$, for $|\eta| \leq 1.5$ and $\epsilon = 0.9624$, for $1.5 < |\eta| \leq 2.5$

In SUSY analyses they are important, for instance, in the GMSB framework where the gravitino is the LSP and a possible signature with two high energy photons occur with a $\tilde{\chi}_1^0$ next-to-LSP.

3.4.2.2 Electron object

The electron object is defined when isolated, with transverse momentum $p_T > 10$ GeV and efficiency:

- efficiency: $\epsilon = 0.98$, for $|\eta| \leq 1.5$ and $\epsilon = 0.90$, for $1.5 < |\eta| \leq 2.5$

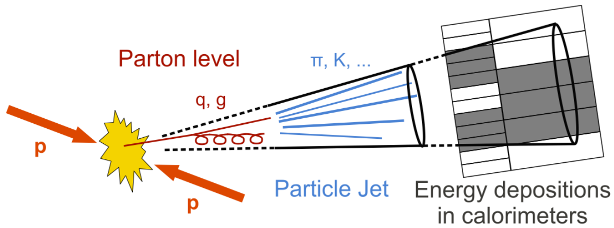

Figure 3.4.3: Schematic diagram for the production, parton shower, hadronisation and measurement of a jet. Figure from [82].

The electron energy resolution is a combination of the ECAL and tracker resolution: at low energy, the tracker resolution dominates and vice versa at high energy.

3.4.2.3 Muon object

Muons are the only SM particles to reach and interact with the outer layers of the CMS and ATLAS detectors. In Delphes the Snowmass parametrisation is obtained with an isolated muon candidate with $p_T > 10$ GeV and efficiency

- $\epsilon = 0.98$, for $|\eta| \leq 1.5$ and $\epsilon = 0.90$, for $1.5 < |\eta| \leq 2.5$

The final muon momentum is obtained by a Gaussian smearing of the initial four-momentum vector. The resolution is parametrised as a function of the transverse momentum and pseudorapidity.

3.4.2.4 Jet objects

What is a jet?

Coloured gluons and quarks do not interact directly with the detector due to QCD confinement. In a collision event, partons shower and hadronise in collimated jets releasing energy in the hadronic calorimeter as shown in Figure 3.4.3.

A parton jet equivalence is not exact: strictly speaking the concept of a parton is not valid beyond the tree level. In Section 3.2.2 one illustrates all the complications due to

QCD and the physical phenomena combined in a single event. A jet is the result of a *jet-finding* algorithm and depends on these phenomena.

In QCD ultraviolet (UV) divergences are reabsorbed into the parameters of the Lagrangian (being the theory renormalizable at high energy) and IR divergences in the initial state are reabsorbed into the PDFs via the DGLAP equations [83]. In the final state IR collinear and soft divergences can be seen from the amplitude describing the splitting of the n-th parton into two ($q \to qg$, $g \to qg$ $g \to q\bar{q}$). In the limit of massless objects the amplitude for the single QCD splitting in the parton shower can be written:

$$|\mathcal{M}_{n+1}|^2 = |\mathcal{M}_n|^2 \frac{\alpha_s}{2\pi} \frac{d\theta^2}{\theta^2} P\left(z\right) dz \tag{3.4.2}$$

where z, $(1-z)$ are the fractions of momenta of the two partons relative to the original one and θ the splitting angle. At leading logarithmic order the DGLAP splitting factors $P\left(z\right)$ have the dependence

$$P\left(z\right) \propto \frac{1}{z}, \tag{3.4.3}$$

for $z \ll 1$. From Eq. 3.4.2 one expects collimated jets in a parton final state resulting from a *pp* event collision with quarks and/or gluons. For the Kinoshita–Lee–Nauenberg theorem the collinear ($\theta \to 0$) and soft ($z \to 0$) divergences cancel between real and virtual diagrams at all orders of the perturbation theory. As a consequence the jet-finding algorithm must be such that the observable is infrared and collinear safe.

The anti-k_T algorithm [84] provides infrared and collinear safe jets by comparing the distances

$$\begin{gathered} d_{ij} = \min\left(p_{\mathrm{T},i}^{-2}, p_{\mathrm{T},j}^{-2}\right)\left(\Delta y_{ij}^2 + \Delta\phi_{ij}^2\right) \\ d_{iB} = p_{\mathrm{T},i}^{-2} R^2 \end{gathered} \tag{3.4.4}$$

where $p_{\mathrm{T},i}$, y_i and ϕ_i are the transverse momentum, rapidity and azimuthal angle of the particle i. From all the objects the method defines the two distances d_{ij} and d_{iB} and finds the minimal between the two. When the minimal distance is d_{ij} the two objects are combined into a $k = i + j$ object and the procedure is repeated until the minimum is d_{kB}. When the resulting transverse momentum is larger than a minimal value chosen the object is defined as a jet.

Different choices for the value of the radius of the cone produce a different average deviation between the transverse momentum of the jet and that of the original parton:

$$\langle \delta p_{\mathrm{T}} \rangle = \langle p_{\mathrm{T},jet} - p_{\mathrm{T},parton} \rangle \sim f(p_{\mathrm{T},parton}, R). \tag{3.4.5}$$

The R dependencies for $\langle \delta p_{\mathrm{T}} \rangle$ due to the physical phenomena described in Section 3.2.2 are $\sim -\log \frac{1}{R^2}$ for FSR, $\sim R^2$ for ISR and UE and $-R^{-1}$ for hadronisation, but the latter is important only for small values $R \lesssim 0.2$.

Though a jet-parton equivalence is not perfect, the jet multiplicity and their transverse momenta are main features in the analysis of any hadronic final state topology in addition to the jet *category.*

light-jet object

In Delphes 3 *Particle-flow Jets* are the result of clustering the *particle-flow tracks* and *particle-flow towers.* The FastJet package [85] is integrated and the writer employs the anti-k_T algorithm with p_T>20 GeV and $R = 0.5$.

A jet with $|\eta| < 5$ and no tag, as explained in the following paragraphs, is assumed to come from the fragmentation of a light quark or a gluon and referred to as a light jet or simply as a jet.

b-jet object

With the exception of the top, the quarks hadronise before they interact with the detector. The bottom quark forms bound states in which a single B or D meson carries most of the energy. *Beautiful* hadrons, and in particular the $b\bar{b}$ meson variety bottomonium, are rather unique in elementary particle physics and fundamental in

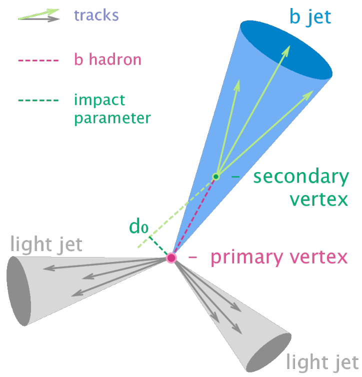

Figure 3.4.4: Schematic diagram of two light jet and a b-decay within a jet.

investigations of QCD, CP-violation, and BSM physics. They have large masses (5-10 GeV), a long life-time travelling on average 450 μm before decaying leptonically or hadronically via a D-meson and they produce a jet with an high number of charged particles and likely one or more in-flight leptons. A secondary vertex (or two) with some tracks displaced from the interaction point is often reconstructed together with nearby leptonic activity. The transverse impact parameter d_0 defined as the transverse component of the distance of closest approach of the track to the primary vertex point is used as well in the identification algorithm. Modern techniques use decay chain multi-vertex reconstruction or multivariate machine learning methods.

In Delphes 3 the algorithm for the identification of bottoms or hadronically decaying τ leptons consists of defining a potential candidate whenever a generated b or τ is in a nearby ΔR range from the jet axis. The parametrisation for the b-jet tagging corresponds to a tight[5] working point with efficiency

- $\epsilon = 0.7\tanh(0.01317 p_T - 0.062)$ for $|\eta| \leq 1.2$ and $\epsilon = 0.6\tanh(0.0105 p_T - 0.101)$ for $1.2 < |\eta| \leq 2.5$

and inefficiency for the misidentification of charm quark

- $i = 0.1873\tanh(0.0183 p_T - 0.2196)$ for $|\eta| \leq 1.2$ and $i = 0.1898\tanh(0.00997 p_T - 0.143)$ for $1.2 < |\eta| \leq 2.5$.

[5]When not specified in the analyses this tight b-tagging is assumed.

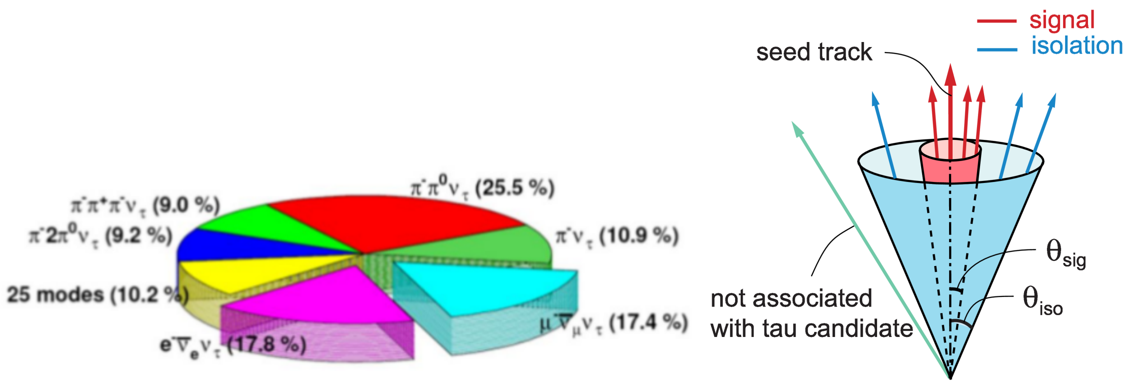

Figure 3.4.5: Branching fraction of the τ-lepton (left) and typical hadronic τ candidate phenomenology (right).

and otherwise i =0.001 for light jets. While a loose working point assumes the following parametrisation

- $\epsilon = 0.75\tanh(0.01317p_T - 0.062)$ for $|\eta| \leq 1.2$ and $\epsilon = 0.69\tanh(0.0105p_T - 0.101)$ for $1.2 < |\eta| \leq 2.5$
- $i = 0.29\tanh(0.0183p_T - 0.2196)$ for $|\eta| < 1.2$ and $i = 0.29\tanh(0.00997p_T - 0.143)$ for $1.2 < |\eta| \leq 2.5$

A parametrisation for the identification of jets resulting from the hadronisation of charm quarks is not implemented.

τ-jet object

Travelling on average 85 μm, the τ-lepton decays leptonically with two neutrinos or, roughly two thirds of the time, to light quarks with an extra neutrino before being detected. Hadronic τs result in collimated jets predominantly with one or three charged pions and often with one neutral pion producing a large electromagnetic component $\pi^0 \rightarrow \gamma\gamma$. The experimental identification is based on the reconstruction of the tracks associated to some $\Delta R < R$ cone around the axis of a τ-jet-candidate and the production vertex. These few prongs tracks, compared to a typical track multiplicity of a gluon or quark, are expected to provide an invariant mass smaller than 1.8 GeV.

In Delphes 3 the hadronic τ identification is based on the same procedure as the b-jet one. The parametrisation assumes a flat identification efficiency of 65% and a misidentification rate of 4%.

fat-jet object

Boosted Higgs, vector bosons and top quarks can decay hadronically in 2-3 quarks resulting in 2-3 pronged sub-jet cores clustered in a massive overall jet. The phenomenology for the parton shower of QCD jets follows Eq. 3.4.3: they have mostly a single hard core surrounded by soft radiation. Several techniques referred to as *grooming, filtering/trimming* [86, 87] and *pruning* [88] are used for the identification of these heavy candidates with jet sub-structure. Other possible investigations are based on constrain radiation patterns in the jet exploiting the different colours of the *sub-jets mother particles*; for example comparing a W boson with respect to a gluon splitting in a $q\bar{q}$ pair.

In the analyses, one defines a *fat-jet* object as a jet with mass $M > 60$ GeV, which is a candidate for heavy SM particles. Such a simple tagged jet is sometimes used to distinguish light quarks from supersymmetric decay objects or ISR candidates from jets produced via the decay of boosted h, W, Z and t-quarks.

3.4.2.5 Missing transverse momentum

Experimentally the x and y components of the missing transverse momentum are defined as

$$E^{\text{miss}}_{x(y)} = E^{\text{miss},\gamma}_{x(y)} + E^{\text{miss},e}_{x(y)} + E^{\text{miss},\mu}_{x(y)} + E^{\text{miss},\tau}_{x(y)} + E^{\text{miss},jets}_{x(y)} + E^{\text{miss,soft}}_{x(y)}. \tag{3.4.6}$$

Due to their particular mix of charged and neutral pions in a narrow cone, hadronic τs have their own energy calibration and associated missing momentum term, while the soft terms correspond to clusters of energy in the calorimeters matching tracks associated to the primary vertex but not reconstructed to high p_T objects. In the first approximation its resolution follows the calorimeter resolution.

In Delphes 3 particle-flow tracks and particle-flow towers are the input for the definition of the missing transverse momentum computed as

$$\vec{\not{E}}_T = -\sum_i \vec{p}_T(i). \tag{3.4.7}$$

The absolute value of this quantity is a key observable to distinguish models with DM candidates from the SM. In this thesis the two degrees of freedom associated to the modulus and the polar angle of the missing transverse momentum are exploited as described in Chapter 4.

3.4.2.6 Shortcomings of simulated samples

One of the issue with simulated samples is a lack of coverage for low-momentum objects. This is particularly problematic for compressed scenarios studied in this work. The minimum lepton momentum of 10 GeV and jet momentum of 20 GeV is insufficient to cover the extreme compressed region probed by the experiments (see for instance [89]). While this prevents demonstrating the power of the method shown in this thesis in certain regions of phase space, we would anticipate that with suitable object identification the conclusions of this work would hold in this extreme regime.

3.5 Typical strategy: how to discriminate the signal from the background

3.5.1 The SM background and the signal

A deep understanding and control of the Standard Model backgrounds is a *sine qua non* condition for the discovery of different physics. The four-vectors of electron, muon, photon and jets *objects* are measured at collider experiments. These known degrees of freedom, in concert with the two resulting from the conservation of the transverse momentum, plus the identification of the particles and the jet category are all the information from the final state experimentalists can leverage on. In high energy physics these quantities and their combinations are experimental observables.

Whenever produced at the LHC, new particles with electromagnetic or colour charge and lifetime long enough to interact with the detector can provide characteristic BSM signatures. Heavy particles not belonging to the SM paradigm can decay to a pair of leptons, photons or quarks and resonances could be observed appearing as bumps on an otherwise smooth invariant mass distribution. The conservation of a discrete $\mathbb{Z}_2$ symmetry of some type, such as R-parity for SUSY described in Section 2.3.2, is assumed to solve some of the shortcomings of the SM. In cases with a weakly interacting LSP, all the game is based on the ability to separate the object kinematics of background-like events from the signal-like events.

Figure 3.5.1 shows the cross sections of various SM processes for different values of the pp centre-of-mass collision energy. The multi-jet processes, except for the top-quark production, are colloquially referred to as QCD backgrounds and typically they result in a final state with low missing transverse momentum. Prompt mesons such as charmonium and bottomonium can provide pairs of opposite-sign leptons with low invariant mass ($\lesssim$ 10 GeV). They are typical products of charm and bottom fragmentation and they can rarely provide isolated leptons. All these processes of hadronic nature can constitute a problem in the case of fake contributions due to the huge cross sections compared to the rare signal events. Data-driven analyses are often employed to suppress such contributions and specific investigations lie outside of the purpose of this phenomenological thesis.

For the signal, as in a large proportion of the ATLAS and CMS searches for supersymmetry, one assumes the benchmark of a simplified topology [91, 92]. The idea is to impose restrictions on the available sparticle phase space, namely on the few masses of

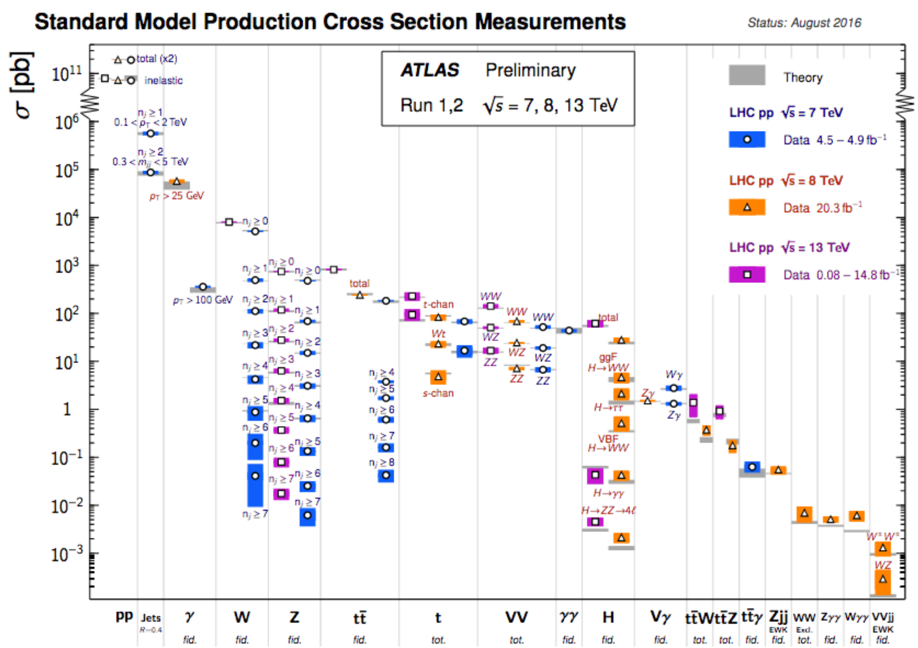

Figure 3.5.1: Theoretical and measured cross sections for SM processes at $\sqrt{s} = 7, 8, 13$ TeV. Figure from [90].

the superparticles investigated, such that only a small number of processes contribute. Most of the proposed analyses focus on one or few topologies and hence on a specific or few final states. The benefit of this strategy is an unambiguous interpretation of the results. The results could be then re-interpreted for more complicated models, for example, by taking linear combinations of the signal and backgrounds yields of several simplified models and assigning each different production cross sections and branching ratios. In any case, the method treated in this thesis can be extended to less exclusive topologies such as the case of compressed scenarios as described in Chapters 5 and 6.

The number of signal events are related to the cross section for the production of a pair of superparticles as described in the general expression given in Eq. 3.1.3. Figure 3.5.2 shows the SUSY cross sections at $\sqrt{s}$=8 TeV and the number of signal events expected to be produced by the LHC for an integrated luminosity of 20 fb^{-1} as a function of the mass of the supersymmetric particles.

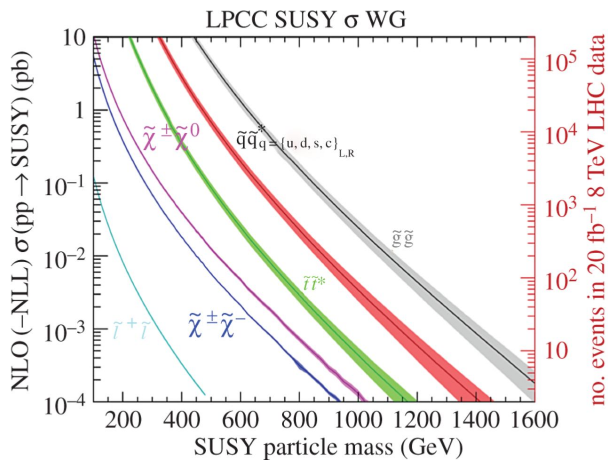

Figure 3.5.2: Cross sections as a function of the mass for SUSY productions at $\sqrt{s}$=8 TeV. Figure from [93].

The SM backgrounds topologically similar to the SUSY signal include the production of heavy bosons, top and additional jets and any combination of these. The phenomenology of these processes will be described analysis-by-analysis with a focus on the main background contributions. The trend shown in Figure 3.5.1 is that a higher multiplicity of final state objects or the production of heavy SM particles lowers the cross section.

The Snowmass study assumes the generation of the orthogonal background processes categorised in Table 3.1. The processes follow the increasing in cross section trend (equivalent of the left to right trend of Figure 3.5.1) and the "+ jets" indicates the fact that the QCD radiation of generator-level jets is allowed up to a total of four final state partons for each category.

Searching for new physics requires collection of sufficient data and application of selection criteria on experimental observables such to provide a statistical significance for the signal-to-background ratio in Eq. 3.1.2. This requires to minimise as much as possible the systematic uncertainties and the canonical procedure consists in defining orthogonal control and validation regions (based for example on a different multiplicity of one of the objects) in order to estimate the SM background in the signal region carefully. A typical cut and count analysis is based on a likelihood defined as a Poissonian $\mathcal{P}$ distribution with the average number of events assumed to be $\lambda = S + B$ and O the

Category	Snowmass label (sub-categories description)
Boson+jets	BJ-B-LL (Vector Boson + jets, off-shell V in di-lepton + jets)
$t\bar{t}$	TT-TB (top pair + jets-top pair (off shell $t^* \to Wj$) + jets)
Single-top	TJ (single top + jets)
di-boson	BB-BLL (Di-Vector + jets, off-shell Di-Vector in di-lepton +jets)
BJJ	Vector boson fusion (V and H) + jets
H	Higgs (gluon fusion plus jets)
$t\bar{t}$+V	TTB (top pair plus bosons, $t\bar{t}$+Z, $t\bar{t}$+W and $t\bar{t}$+h + jets)
tri-boson	BBB (tri-Vector +jets, Higgs associated +jets)

Table 3.1: Eight categories summarising all the main Standard Model backgrounds as part of the Snowmass study.

number of observed events

$$L = \frac{e^{-\lambda}\lambda^{O}}{O!}. \tag{3.5.1}$$

The several background and signal systematic uncertainties are summed in quadrature with the likelihood weighted by a Gaussian distribution.

In the proposed analyses of this thesis one cannot define *observed* discovery reach or exclusion limit. Monte Carlo simulations of signal and background samples are the Madgraph + Pythia + Delphes output of pp collisions at $\sqrt{s} = 14$ TeV as described in this chapter. Once generated, all the SM background samples are scaled using the procedure outlined in [75] applying the input cross sections and k-factors provided therein and choosing a value for the integrated luminosity. The same procedure is applied for the signal samples and the cross sections will be described in the relative analyses.

The results of the strategies developed for the proposed analyses will be expressed by the Z-value (or standard score) representing the significance of a given signal measured in standard deviations in the presence of a background hypothesis. The simple metrics $Z_{SB} = \frac{S}{\sqrt{B}}$ and $Z_{SSB} = \frac{S}{\sqrt{B+S}}$ are often used to give a significance for the ratio in Eq. 3.1.2.

The more conservative metric Z_{Bi} (Z binomial), particularly in the case of a low number of background events, is used in this thesis and described in Ref. [94]. In a frequentist approach, the relative background uncertainty is treated as being due to an auxiliary or sideband observation, equivalent to an experimental control region in HEP with no signal. The Likelihood is the product of two Poissonians distributed around $S+B$ and τB

$$L(x, y|S, B, \tau) = P(x|S+B)P(y|\tau B) \tag{3.5.2}$$

where τ is the ratio of the expected means under the background-only hypothesis H_0. The BG mean is assumed to have a normal statistics and τ assume the expression given by

$$\tau = \frac{\hat{\mu}_B}{\sigma_B^2} = \frac{1}{f^2 \hat{\mu}_B} \tag{3.5.3}$$

with $\hat{\mu}_B$ the estimate mean of the null hypothesis and the standard deviation σ_B assumed a fraction f of the background yield ($\hat{\mu}_B = B$). The expression in Eq. 3.5.2 can be rewritten as the product of a single Poisson probability with mean $S+B+\tau B$ and a binomial probability with

$$\rho = \frac{1}{1+\tau}. \tag{3.5.4}$$

The binomial p-value p_{Bi} is the one-tailed probability for the test of H_0 and can be computed as the ratio of incomplete and complete beta functions

$$p_{\mathrm{Bi}} = \frac{\mathcal{B}(\rho, B+S, 1+\tau B)}{\mathcal{B}(B+S, 1+\tau B)} = \frac{\int_0^\rho u^{B+S-1}(1-u)^{\tau B} du}{\int_0^1 v^{B+S-1}(1-v)^{\tau B} dv}. \tag{3.5.5}$$

Its value can be given by specifying the corresponding Z-score: the number of standard deviations in a one-tailed test of a Gaussian variate

$$Z_{\mathrm{Bi}} = \Phi^{-1}(1 - p_{\mathrm{Bi}}) = -\Phi^{-1}(p_{\mathrm{Bi}}), \tag{3.5.6}$$

where Φ has the form

$$\Phi(Z) = \frac{1}{2\pi} \int_{-\infty}^{Z} e^{-x^2} dx = \frac{1}{2} \left[1 + \mathrm{erf}(Z/\sqrt{2})\right], \tag{3.5.7}$$

and one has the expression given by

$$Z_{\mathrm{Bi}} = \sqrt{2}\mathrm{erf}^{-1}(1 - 2p_{\mathrm{Bi}}). \tag{3.5.8}$$

Hence the binomial Z-value takes as inputs the signal and the overall Standard Model background yields, and a systematic uncertainty for the background, usually assumed to be flat across the SUSY parameter space.[6]

A perfect comparison with current experimental results is not possible with the same assumed integrated luminosity. At the current time, the LHC is operating at $\sqrt{s} = 13$ TeV and the parametrisation implemented by Delphes is in between the ATLAS and CMS performances. Finally, a deep understanding and control of the systematics must be based on SM *candles* and is an experimental prerogative.

3.5.2 The jungle: an overview of the main observables

The ability to distinguish the kinematics of signal-like events from the SM ones requires carefully designed variables. Herein an incomplete list of experimental observables used for searches of BSM physics, in particular in supersymmetry is presented. A much more detailed description can be found elsewhere in the literature [96–107].

$\not{E}_T$ or E_T^{miss} (or MET) is defined experimentally in Eq. 3.4.6. For a perfect response of the detector it corresponds to $\sqrt{(\sum_w p_x)^2 + (\sum_w p_y)^2}$ where the sum is extended to all the weakly interacting particles in the final state.

$\not{H}_T$ or H_T^{miss} is the equivalent of $\not{E}_T$ considering only the response of the hadronic calorimeter. In most analyses it is defined only with the jets:

$$H_T^{\mathrm{miss}} = \left| \sum_{jets} \vec{p}_T^{\,jet} \right| \tag{3.5.9}$$

[6]From practical purposes, one can use the *BinomialExpZ*(S, B, f) method implemented in ROOT [95] with S the signal yield, B the background yield and f the relative background uncertainty.

with ($p_T^{jet} > p_T^{min}$) and p_T^{min} is the value assumed in the anti-k_T algorithm. In practice this is found not to be useful.

H_T is the scalar sum of the transverse momentum of the jets $H_T = \sum_{jets} p_T$, with ($p_T^{jet} > p_T^{min}$) . Often p_T^{min} is chosen larger than the minimal transverse momentum used for the anti-k_T algorithm. A similar observable can be defined with leptons.

m_{eff} is defined in different ways. It can include all the jets $m_{\text{eff}}^{inc} = \sum_{jets} p_T + \not{E}_T$ or only the the first n leading jets

$$m_{\text{eff}} = \sum_{jets}^{n} p_T + \not{E}_T \tag{3.5.10}$$

or all the jets with $p_T^{jet} > p_T^{min}$. A similar observable can be defined with the leptons or including all the visible objects in the final state. This simple scale variable gives information of the overall energy of the hard collision.

$\frac{\not{E}_T}{\sqrt{H_T}}$ and $\frac{\not{E}_T}{m_{\text{eff}}}$ are a measure of $\not{E}_T$ weighted by the hadronic activity H_T. They give information on the *genuineness* of the missing transverse momentum: since the intrinsic calorimeter resolutions scale approximately as $\sqrt{E}$, the factor $1/\sqrt{H_T}$ is appropriate for an approximate significance measure ($\frac{\not{E}_T}{\sqrt{H_T}}$).

p_T^{obj} is the transverse momentum of an object $\sqrt{p_x^2 + p_y^2}$. Analysis strategies based on selection criteria applied in particular to the leading jet(s) transverse momenta are often used to define signal regions.

$\Delta\phi\left(obj, \vec{\not{E}}_T\right)$ is the polar angle between the direction of an object and E_T^{miss}. In particular $\Delta\phi\left(jet, \vec{\not{E}}_T\right)$ is used to control the QCD/multi-jet backgrounds measuring the angular deviation of the leading and sub-leading jets (or more) with $\vec{\not{E}}_T$ and rejecting the events in cases in which one of the two satisfies $\Delta\phi < \Delta\phi^{min}$.

M_{oo} is the invariant mass between two objects of the same kind (l, γ, b-jets, τ-jets, light jets) and it is useful to discover/reject resonances. For two particles 1 and

2, it is defined as

$$M_{12}^2 = [E_T(1) + E_T(2)]^2 - [\vec{p}_T(1) + \vec{p}_T(2)]^2 \tag{3.5.11}$$

N_o is the multiplicity of the objects of a specific kind, useful in any analysis.

M^{jets} is the sum of the jet masses $\sum_{jet} M^{jet}$ with ($p_T^{jet} > p_T^{min}$ or $M^{jet} > M^{min}$) and it can be used to have information about the number of boosted objects.

M_T is the transverse mass defined for the two particles 1 and 2 as

$$M_T^2 = [E_T(1) + E_T(2)]^2 - [\vec{p}_T(1) + \vec{p}_T(2)]^2 \tag{3.5.12}$$

and in the limit of massless objects corresponds to $M_T^2 = 2p_T(1)\,p_T(2)\,(1 - \cos\phi_{12})$. It can be defined also between an object and $\vec{\not{E}}_T$. It is invariant under longitudinal boosts.

α_T is constructed to observe deviations from a di-jet event: $\alpha_T = \frac{E_T^{j2}}{M_T}$, where the numerator is the energy of the second jet in p_T. In the massless limit, the variable is one half for a perfect measured di-jet event. Lower values depend on jets resulting from the hadronisation of bottom or charm with collinear neutrinos or mis-measurement while values significantly greater than 0.5 are observed when the two jets are not back-to-back and are recoiling against a genuine $\vec{\not{E}}_T$, or a jet that has not been reconstructed, typically in QCD events. The generalisation consists in defining two pseudo-jets as a combination of all the jets in the event

$$\alpha_T = \frac{H_T - \Delta H_T}{\sqrt{H_T^2 - \not{H}_T^2}}, \tag{3.5.13}$$

with ΔH_T the energy imbalance of the pseudo-dijet system.

M_{T2} is the *s*transverse mass, a generalisation of M_T constructed to probe final state events with two weakly interacting particles. Imagine two (super)particles of mass

M_P decaying to a massless visible particle V and an invisible object of mass M_χ. The parent sparticle mass is bounded from below by the transverse mass

$$M_P^2 = M_\chi^2 + 2\left[E_T^V E_T^\chi \cosh\left(\Delta\eta\right) - \vec{p}_T^{\,V} \cdot \vec{p}_T^{\,\chi}\right] \geq M_T \tag{3.5.14}$$

The transverse momentum of the single invisible object is unknown, hence the observable is based on a minimisation over under-constrained kinematic degrees of freedom associated with the weakly interacting particles and defined as

$$M_{T2}^2\left(M_\chi\right) = \min_{\vec{p}_T^{\,\chi 1} + \vec{p}_T^{\,\chi 2} = \vec{\not{E}}_T} \left\{\max\left[M_T^2\left(1\right), M_T^2\left(2\right)\right]\right\}. \tag{3.5.15}$$

with $M_T^2\left(M_\chi, \vec{p}_T^{\,V_{1(2)}}, \vec{p}_T^{\,\chi_{1(2)}}\right) = M_\chi^2 + 2\left(E_T^{V_{1(2)}} E_T^{\chi_{1(2)}} - \vec{p}_T^{\,V_{1(2)}} \cdot \vec{p}_T^{\,\chi_{1(2)}}\right)$ the transverse mass in each hemisphere (1 and 2) and $V_{1(2)}$ the massless visible particle in the hemisphere 1 (2). With the right test mass $M_{T2}\left(M_\chi\right)$ has a kinematic endpoint at the parent mass $M_{T2}^{\max}\left(M_\chi\right) = M_P$, while with the zero-test mass one can infer the information related to the mass splitting $M_{T2}^{\max}\left(0\right) = M_\Delta = \frac{M_P^2 - M_\chi^2}{M_P}$.

M_{CT} is the contrasverse mass defined with an opposite sign to the transverse mass

$$M_{CT}^2 = \left[E_T\left(1\right) + E_T\left(2\right)\right]^2 - \left[\vec{p}_T\left(1\right) - \vec{p}_T\left(2\right)\right]^2 \tag{3.5.16}$$

and hence for massless particles: $M_{CT}^2 = 2p_T\left(1\right)p_T\left(2\right)\left(1 + \cos\phi_{12}\right)$. This corresponds to the (1+2) dimension version of the contra-variant or Euclidean mass M_C which has the opposite space sign with respect to the invariant mass: $m_1^2 + m_2^2 + 2E_1E_2 + 2\vec{p}_1 \cdot \vec{p}_2$ and is invariant under contra-linear equal magnitude Lorentz transformations of the two particles. The observable M_{CT} is invariant under longitudinal boosts and the maximum is invariant under contra-linear Lorentz boosts: $M_{CT} \leq M_C \leq M_{CT}^{\max}$.

M_2 and other modifications of M_{T2}. For long chains M_{T2} (and M_{CT}) can be defined on several single decay steps or on the overall chain. The variable M_2 is a (1+3) dimension generalisation of M_{T2}

$$M_2(M_\chi) = \min_{\vec{p}^{\chi_1}+\vec{p}^{\chi_2}} \{\max[M_{P1}(1), M_{P2}(2)]\}. \tag{3.5.17}$$

In this case the minimisation is made on the three-momenta and one demands the constraint $\vec{p}_T^{\chi_1} + \vec{p}_T^{\chi_2} = \vec{\not{E}}_T$. Two other constraints can be required and the complete constraint observable is referred to as M_{2CC} demanding $M_{P1} = M_{P2}$ and $M_{R1} = M_{R2}$, namely the same mass for the two parents and the same mass for the relatives.

Modifications of M_{CT}. The contransverse mass is bounded from above by M_{T2}, and M_T^R: $M_{CT}^{\max} = M_\Delta$ in the limit of massless visible objects, but the endpoint is not invariant under Lorentz boosts of the CM system due to initial state radiation or something else extraneous to the heavy particle decays 1 and 2. Several attempts have been made to mitigate this problem and correct M_{CT} to be less than the endpoint. Maybe the simplest one is to look at the event only along an axis perpendicular to the boost [102]. Another possibility is to correct a la Polesello-Tovey [101], defining the x-axis parallel and the y-axis perpendicular to the boost and the quantities

$$\begin{aligned} A_x &= p_x(1)E_y(2) + p_x(2)E_y(1) \\ M_{Cy}^2 = M_{CT\perp}^2 &= [E_y(1) + E_y(2)]^2 - [\vec{p}_y(1) - \vec{p}_y(2)]^2 \end{aligned} \tag{3.5.18}$$

The variable $A_{x(lab)}$ and A_x' are the value of A_x evaluated in the Lab frame and after the boost in the positive $\hat{x}$ direction. One can define two velocities $\beta_1 = \frac{p_b}{E_{CM}}$ or $\beta_2 = \frac{p_b}{\hat{E}}$ with p_b the net transverse momentum of upstream objects and an upper and a lower bound of the energy of the two particles produced at the collider: E_{CM} is the proton-proton centre of mass energy while $\hat{E}$ is obtained summing the energies of the visible objects with the missing transverse momentum and it is equal to the true one for massless, co-linear weakly interacting particles moving in the transverse plane. The two velocities result in a low and a high value for A_x'

and the correction is one of the three following possibilities:

$$M_{CT}^{\mathrm{corr}} = \begin{cases} M_{CT} & \text{after boosting by } \beta_1, \text{ if } \quad A_{x(lab)} \geq 0 \quad \text{and} \quad A'_{x(lo)} \geq 0 \\ M_{CT} & \text{after boosting by } \beta_2, \text{ if } \quad A'_{x(hi)} < 0 \\ M_{Cy} & \text{if } \quad A'_{x(hi)} \geq 0 \end{cases} \tag{3.5.19}$$

R and M_R are the razor variables. A special treatment should be dedicated to these observables defined as

$$\begin{cases} R = & \frac{M_T^R}{M_R} \\ M_R^2 = & \left(E^{V_1} + E^{V_2}\right)^2 - \left(p_z^{V_1} + p_z^{V_2}\right)^2 . \\ M_T^R = & \frac{\sqrt{\not{E}\left[p_T^{V_1} + p_T^{V_2}\right]^2 - \vec{\not{E}}\cdot\left[\vec{p}_T^{V_1} + \vec{p}_T^{V_2}\right]^2}}{4} \end{cases} \tag{3.5.20}$$

It can be extended to multi-object final states by defining a collection of two pseudo-objects as in the case of two mega-jets originally introduced in the case of hadronic final states [108]. It is constructed to have an endpoint for M_T^R and a peak for M_R at M_Δ, while backgrounds with no real missing transverse momentum populate values of R close to zero. The super-razor observable M_Δ^R [104] can be considered as another correction to M_{CT}.

These variables have been used with success in order to measure Standard Model heavy particles and have been employed for probing BSM physics. Most of them have sensitivity to SUSY if the mass scale is larger than the SM scale. This results in a high correlation and redundancy in the information. Some of these variables give information on the masses, or mass splittings, but only for the endpoint configurations. They are thus colloquially referred to *singularity* observables: *"a singularity is a point where the local tangent space cannot be defined as a plane or has a different dimension than the tangent spaces at non singular point"* [109]. Moreover, a statistical issue follows due to the fact that signal events can be distinguishable from backgrounds only in the tail of the distributions: few signal events or none can populate this configuration. Finally, the impact of a variable like M_{T2}, constraining all the unknown d.o.f. in once, is compromised if the mass or mass-difference targeted is similar to a SM background process.

If selection criteria on the object multiplicity are necessary in any kind of analysis, an extreme optimisation based on only endpoint scale variables can compromise the discovery prospects. This is the case of an overestimation of the number of expected SUSY events S due to the simplified hypothesis assumption ($BR(\tilde{P} \to \tilde{C}) = 1$, with $\tilde{P}$ and $\tilde{C}$ the generic parent and child superparticle) or an overestimation of the production cross section. Philosophically similar it is a kind of optimisation based on the definition of too many signal regions in the phase space, such as the $M_{\tilde{P}}$ vs $M_{\tilde{C}}$ plane, that can be seen from an experimental point of view, as an exacerbation for the control of the systematics uncertainties. Furthermore, an extreme optimisation on endpoint observables excludes the possibility of discovery in cases with similar signal-background mass scale. For these reasons, the strategy employed in this thesis is based on the definition of few signal regions based on a moderate optimisation of mainly scaleless variables.

Depending on the final state topology, main SM backgrounds, sparticle/particle spin and masses, luminosity and so on, the experimental observables can have different impacts and provide different information. The natural question that follows is this: what is the best basis or combination of variables?

> "*The guiding principle we employ to create useful hadron-collider observables: we should place the best possible bounds on any Lorentz invariants of interest, such as parent masses or the centre-of-mass energy $\sqrt{\hat{s}}$, in any cases where it is not possible to determine the actual values of those Lorentz invariants due to incomplete event information.*" [110]

Chapter 4

Recursive Jigsaw Reconstruction

4.1 Introduction to RJR: some nomenclature and conventions

In this section, we introduce the Recursive Jigsaw Reconstruction (RJR) technique. In the subsequent sections, some specific examples are used to illustrate the method in more detail and to match the proposed studies described in the following chapters of this thesis. More information can be found elsewhere [111–116].

RJR is a method for probing open final state topologies at collider experiments. Hence it can be used to investigate theories beyond the Standard Model characterised by a discrete $\mathbb{Z}_2$ symmetry such as SUSY when R-parity conservation is assumed. Event-by-event the procedure consists of finding an approximation for the relevant inertial frames of reference after imposing a decay tree diagram that mimics the signal topology. As a result, we introduce a basis of kinematic variables that can discriminate between the BSM signal and the SM backgrounds.

The algorithm *reconstructs* the relevant reference frames using a series of *jigsaw* rules. Frame-to-frame these rules are specified by only the relevant d.o.f. related to the specific Lorentz transformation. The jigsaw rules are customisable and interchangeable (like a jigsaw puzzle) and are applied *recursively,* travelling through each step of the topology chains.

For each event, a complete basis of variables is obtained. These kinematic observables are *diagonalised* resulting in quantities with physical meaning that are referred to colloquially as either *scale* variables when sensitive to masses or mass splittings, *angular* variables when spin-sensitive, or *scaleless* when constructed as ratios of scale variables or as a dimensionless combination. Scale(less) and angular variables are sometimes referred to globally as RJR or simply jigsaw observables. Similar variables describe similar physical proprieties along the decay chains, while unique variables are sensitive to overall masses or angular relations between different chains.

The studies described in this thesis exploit the largely uncorrelated nature of the kinematic variables or, in other words, the independent information that can be extracted from their distributions. This orthogonality is the result of the philosophy used to specify the jigsaw rules as the outputs of *extremisations*[1] as will be clear in the following. Hence the purpose of the RJR method is to obtain a basis of variables containing all the useful information and avoiding redundancies. Finally, the basis is always well-defined or unambiguous: the jigsaw rules are never so over-constrained as to prevent real solutions.

At collider experiments, open final state topologies are characterised by visible and invisible objects. Conventionally in this chapter we label the visible objects as *phenomenological* ϕ particles, while the weakly interacting or invisible objects are called k particles when some of the *kinematic* d.o.f. are not measured. An upside-down particle decay tree is assumed to specify the jigsaw rules that assign four-momenta to the particles not interacting with the detector. The number of constraints to be imposed, corresponding to the number of unknown d.o.f., follows the general rule

$$N_c = 4n_k - 2 + N_{\text{comb}} \tag{4.1.1}$$

[1]We use "extremisation" as a term to refer to either minimisation or maximisation.

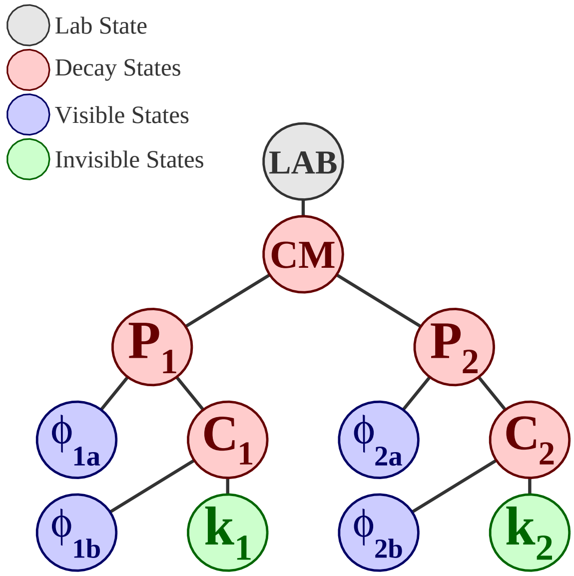

Figure 4.1.1: Decay tree for the prototype topology: the pair-production of the parents P_1 and P_2 in a final state with four visible and two invisible objects. The tree is generated using the RestFrames software package [117].

with n_k the number of weakly interacting particles. The two degrees of freedom for the vectorial sum of the transverse momenta of all of the invisible particles are constrained to be $\vec{\not{E}}_T$, while $N_{\text{comb}} = 0$ in the hypothesis of a trivial assignment of the visible objects reconstructed by the detector in each position in the decay tree: a final state event with exactly the same number of objects expected from the final state topology investigated and all distinguishable from each other with no ambiguity. The jigsaw rules are a recipe to assign the N_c constraints in Eq. 4.1.1.

In order to examine quantitatively the RJR algorithm the specific decay tree in Figure 4.1.1 is treated in detail. Two particle *parents* P are assumed to be produced at the collider experiment, each decaying to a *child* C and a visible state. Each child decays to a visible and an invisible particle. The decay tree specifies the systems of reconstructed (ϕ-states) and invisible (k-states) particles in the final state and the reference frames corresponding to each intermediate combination of these objects (C and P rest frames and the centre-of-mass of the two parents, CM-frame), which are considered decay states.

This *prototype* topology has all the essential ingredients to describe the RJR method in an exhaustive way for the prospect of SUSY discovery. In order to establish the jigsaw rules for this topology, two simpler physical examples are analysed in Sections 4.2 and 4.3. More complex topologies characterised by longer chains, an asymmetry of the two hemispheres, a higher multiplicity of visible or weakly interacting particles or additional phenomena such as ISR, can be substantially analysed with a rearrangement of the jigsaw rules treated herein. Some of these complications together with combinatoric issues are described in the other sections of this chapter.

As a convention, in this chapter we refer to the covariant four-momenta of the particle a in the reference frame F as $a^F_\mu = \left(E^F_a, -\bar{a}^F\right)$. The superscripts are often omitted when the frame of reference is the *Lab* frame and the absolute value of the three-momentum is written simply $\sqrt{\left(a^F_x\right)^2 + \left(a^F_y\right)^2 + \left(a^F_z\right)^2} = a^F$.

4.2 The two hemispheres and the weakly interacting mass

4.2.1 The contra-boost

Events with two identical, or similar, *hemispheres* are typical of a discrete $\mathbb{Z}_2$ symmetry phenomenology such as the case of a pair of superparticles produced at a collider, each decaying via the same particle cascade. In order to study these topologies, we describe the following example. Suppose a parent P particle decays to two identical children C_1 and C_2, each decaying to a visible ϕ particle and a kinematically invisible k particle as in Figure 4.2.1. At the collider experiment, this example is equivalent to assuming that the parent is at rest in the detector frame of reference.

The two children fly back-to-back in the $P = Lab$ frame and their masses, equal which

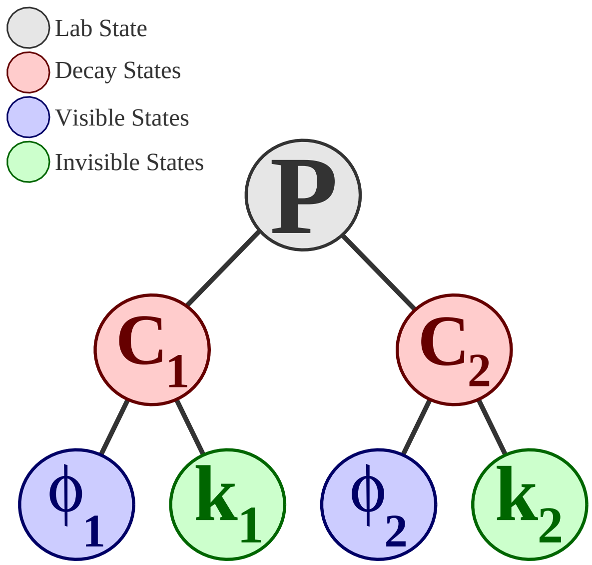

Figure 4.2.1: Decay tree: a parent P decays in two children C_1 and C_2. In each hemisphere (1 and 2) there is one visible ϕ and one invisible k particle.

one for identical particles ($M_{C_1} = M_{C_2} = M_C$), satisfy

$$M_C = E_{\phi_1}^{C_1} + E_{k_1}^{C_1} = E_{\phi_2}^{C_2} + E_{k_2}^{C_2}, \tag{4.2.1}$$

with the relations valid in each proper C_i frame.

The decay is symmetric with respect to ϕ and k when the relation $m_\phi = m_k$ is assumed. In this case the masses of the children satisfy the relation:

$$M_C = E_{\phi_1}^{C_1} + E_{\phi_2}^{C_2} = E_{k_1}^{C_1} + E_{k_2}^{C_2}. \tag{4.2.2}$$

The sum of the energies of the visible particles in their respective production frame is an estimate for M_C, independently of the invisible masses.

Consider the antisymmetric, or contra-linear, or contra-boost velocity $\bar{\beta}_c$ from P to C_1

$$\bar{\beta}_c \equiv \bar{\beta}(P \to C_1) = -\bar{\beta}(P \to C_2) \tag{4.2.3}$$

as the equal and opposite Lorentz boost associated with the estimate of the C_i rest frame.[2]

The first jigsaw rule is introduced as a result of an *extremisation*, a minimisation of M_C in Eq. 4.2.2 in this case, obtained via the following partial derivative:

$$\frac{\partial}{\partial \bar{\beta}_c}\left(E_{\phi_1}^{C_1} + E_{\phi_2}^{C_2}\right) = 0, \tag{4.2.4}$$

in order to chose $\bar{\beta}_c$ such that all the observables (like the visible energies in the C_i frame or the estimate of M_C) are independent of $\bar{\beta}_c$, or are contra-boost invariants. This principle is described in more detail in Section 4.2.5.

Suppose the two children fly back-to-back along the x-axis. A simple manipulation

$$\begin{aligned} 0 &= \frac{\partial}{\partial \beta_x}\left(E_{\phi_1}^{C_1} + E_{\phi_2}^{C_2}\right) \\ &= \frac{\partial}{\partial \beta_x}\left\{\gamma_x\left[E_{\phi_1}^{P} + E_{\phi_2}^{P} - \beta_x\left(\phi_{x_1}^{P} - \phi_{x_2}^{P}\right)\right]\right\} \\ &= \left[\frac{1}{\left(1-\beta_x^2\right)^{3/2}}\right]\left[-\beta_x^2\left(\phi_{x_1}^{P} - \phi_{x_2}^{P}\right) + \beta_x\left(E_{\phi_1}^{P} + E_{\phi_2}^{P}\right)\right. \\ &\qquad \left. - \left(\phi_{x_1}^{P} - \phi_{x_2}^{P}\right) + \beta_x^2\left(\phi_{x_1}^{P} - \phi_{x_2}^{P}\right)\right] \end{aligned} \tag{4.2.5}$$

gives

$$\beta_x = \frac{\phi_{x_1}^{P} - \phi_{x_2}^{P}}{E_{\phi_1}^{P} + E_{\phi_2}^{P}}. \tag{4.2.6}$$

The three-dimensional version is

$$\bar{\beta}_c = \frac{\bar{\phi}_1^{P} - \bar{\phi}_2^{P}}{E_{\phi_1}^{P} + E_{\phi_2}^{P}} \tag{4.2.7}$$

and is the guess for the contra-boost velocity for the reconstruction of the child frames of reference based on the hypothesis of symmetry between the two hemispheres.

The velocity $\bar{\beta}_c$ respecting Eq. 4.2.7, for visible and invisible massless particles $m_{k_1} = m_{k_2} = m_{\phi_1} = m_{\phi_2} = 0$ gives for M_C the minimum value

$$M_C = \left(2E_{\phi_1}^{P}E_{\phi_2}^{P} + 2\bar{\phi}_1^{P}\cdot\bar{\phi}_2^{P}\right)^{1/2} = \left[2\phi_1^{P}\phi_2^{P}\left(1+\cos\theta_{12}\right)\right]^{1/2} = M_E(0,0) \tag{4.2.8}$$

[2] They can be referred to also as $\bar{\beta}_{C_i}^{P}$

where $M_E(m_1 = m_2 = 0)$ is the Euclidean or contra-boost mass for two massless particles and a quantity that is itself contra-boost invariant by definition.

In general the contra-boost velocity can be described by the four-momenta of the visible and invisible particles via the following system of equations:

$$\begin{cases} \bar{\beta}(P \to C_1) = \frac{\bar{\phi}_1^P - \bar{\phi}_2^P}{E_{\phi_1}^P + E_{\phi_2}^P} & = \frac{\bar{\phi}_1^P + \bar{k}_1^P}{E_{\phi_1}^P + E_{k_1}^P} = \frac{\bar{C}_1^P}{E_{C_1}^P} \\ \\ \bar{\beta}(P \to C_2) = \frac{\bar{\phi}_2^P - \bar{\phi}_1^P}{E_{\phi_2}^P + E_{\phi_1}^P} & = \frac{\bar{\phi}_2^P + \bar{k}_2^P}{E_{\phi_2}^P + E_{k_2}^P} = \frac{\bar{C}_2^P}{E_{C_2}^P} \end{cases} . \tag{4.2.9}$$

Assuming the same mass for the two children $M_{C_1} = M_{C_2}$ the relation

$$E_{\phi_1}^P + E_{k_1}^P = E_{\phi_2}^P + E_{k_2}^P \tag{4.2.10}$$

is valid. Notice that for identical children Eq. 4.2.10 and Eq. 4.2.3 are equivalent. From now on the superscript (P) referring to the parent frame and coinciding with an ideal *Lab* frame is erased.

4.2.2 Bounding the weakly interacting mass

Supposing $m_{k_1} = m_{k_2} = 0$ and $m_{\phi_1} = m_{\phi_2} = m$, the visible and invisible squared masses are written $M_{\phi\phi}^2 = 2m^2 + 2E_{\phi_1}E_{\phi_2} - 2\bar{\phi}_1 \cdot \bar{\phi}_2 = M_E^2 - 4\bar{\phi}_1 \cdot \bar{\phi}_2$ and $M_{\chi\chi}^2 = 2E_{k_1}E_{k_2} - 2\bar{k}_1 \cdot \bar{k}_2 = 2k_1 k_2 (1 - \cos\theta)$. Introducing a normalisation factor N we can separately compare the numerator and the denominator in Eq. 4.2.9

$$\begin{cases} \bar{k}_1 & = & (N-1)\,\bar{\phi}_1 - N\bar{\phi}_2 \\ \bar{k}_2 & = & (N-1)\,\bar{\phi}_2 - N\bar{\phi}_1 \\ E_{k_1} & = & (N-1)\,E_{\phi_1} + NE_{\phi_2} \\ E_{k_2} & = & (N-1)\,E_{\phi_2} + NE_{\phi_1} \end{cases} . \tag{4.2.11}$$

Finally, imposing the condition that one of the invisible particles is massless we have

$$\begin{aligned}
m_{k_1}^2 = 0 &= (E_{C_1} - E_{\phi_1})^2 - \left(\bar{C}_1 - \bar{\phi}_1\right)^2 \\
&= (N-1)^2 E_{\phi_1}^2 + 2N(N-1) E_{\phi_1} E_{\phi_2} + N^2 E_{\phi_2}^2 \\
&\quad - \left[(N-1)\phi_1^2 - 2N(N-1)\bar{\phi}_1 \cdot \bar{\phi}_2 + N^2 \phi_2^2\right] \\
&= (N-1)^2 m^2 + N^2 m^2 + N(N-1)(2E_{\phi_1}E_{\phi_2} + 2\bar{\phi}_1 \cdot \bar{\phi}_2) \\
&= N^2 M_E^2 - N M_E^2 + m^2
\end{aligned} \tag{4.2.12}$$

and the same expression is valid for $m_{k_2}^2 = 0$. Solving for the normalisation factor

$$\Rightarrow N_{1,2} = \frac{1}{2} \pm \frac{1}{2}\left(\frac{M_E^2 - 4m^2}{M_E^2}\right)^{1/2} \tag{4.2.13}$$

with $N_2 = 1 - N_1$ and $N_{1,2} > 0$. We choose the positive sign, equivalent to N close to 1, motivated from the expectation $E_{\phi_1}^P + E_{\phi_2}^P \simeq E_{\phi_1}^P + E_{k_1}^P \simeq E_{\phi_2}^P + E_{k_2}^P$ for $m \to 0$ in Eq. 4.2.9:

$$N = \frac{1}{2} + \frac{1}{2}\left(\frac{M_E^2 - 4m^2}{M_E^2}\right)^{1/2} = \frac{1}{2} + \frac{1}{2}\left(\frac{M_C^2 - 2m^2}{M_C^2 + 2m^2}\right)^{1/2} \tag{4.2.14}$$

Using Eq. 4.2.11 we evaluate the invisible invariant mass

$$\begin{aligned}
M_{\chi\chi}^2 &= 2E_{k_1}E_{k_2} - 2\bar{k}_1 \cdot \bar{k}_2 \\
&= 2\left[(N-1)E_{\phi_1} + N E_{\phi_2}\right]\left[(N-1)E_{\phi_2} + N E_{\phi_1}\right] \\
&\quad -2\left[(N-1)\bar{\phi}_1 - N\bar{\phi}_2\right]\left[(N-1)\bar{\phi}_2 - N\bar{\phi}_1\right] \\
&= 2N(N-1)\left(2E_{\phi_1}E_{\phi_2} - 2\bar{\phi}_1 \cdot \bar{\phi}_2 + E_{\phi_1}^2 + E_{\phi_2}^2 + \phi_1^2 + \phi_2^2\right) \\
&\quad +2\left(E_{\phi_1}E_{\phi_2} - \bar{\phi}_1 \cdot \bar{\phi}_2\right)
\end{aligned} \tag{4.2.15}$$

and using Eq. 4.2.14 the following simple expression based on visible observables can be written:

$$\begin{aligned}
M_{\chi\chi}^2 &= M_{\phi\phi}^2\left(1 - \tfrac{2m^2}{M_E^2}\right) - 2m^2\left(\tfrac{2\phi_1^2 + 2\phi_2^2}{M_E^2}\right) \\
&= M_{\phi\phi}^2 - 2m^2 - 2m^2\left(\tfrac{M_{\phi\phi}^2 + 2\phi_1^2 + 2\phi_2^2}{M_{\phi\phi}^2 + 4\bar{\phi}_1 \cdot \bar{\phi}_2}\right) . \\
&= M_{\phi\phi}^2 - 4m^2\left[\tfrac{M_{\phi\phi}^2 + \left(\bar{\phi}_1 + \bar{\phi}_2\right)^2}{M_{\phi\phi}^2 + 4\bar{\phi}_1 \cdot \bar{\phi}_2}\right]
\end{aligned} \tag{4.2.16}$$

In proton-proton final state analyses an ideal detector with $Lab = P$ does not exist. We choose the mass of the weakly interacting particles M_w, as the smallest Lorentz invariant always bounding $M_{\chi\chi}|_{m_{k_1}=m_{k_2}=0}$ from above:

$$M^2_{\chi\chi}|_{m_{k_1}=m_{k_2}=0} \leq M^2_w = M^2_{\phi\phi} - 4m^2. \tag{4.2.17}$$

Notice $M^2_{\chi\chi}|_{m_{k_1}=m_{k_2}=0} = M^2_w$ when $\bar{\phi}_1 = \bar{\phi}_2$; in this case $M^2_{\phi\phi} - 4m^2 = 0$. A more detailed description is in Section 4.4, where we illustrate as every invariant smaller than $M^2_w = M^2_{\phi\phi} - 4m^2$ can potentially give tachyonic problems ($m^2_k < 0$). Indeed, in case of a real detector with $P \neq Lab$, the estimate of $M^2_{\chi\chi}$ is important for the reconstruction of the relevant frames of reference and we want to avoid that the rest frame of an invisible particle in the final state is reconstructed so to result in an imaginary value for the mass m_k.

The squared difference between the Lorentz invariant choice for the mass of the weakly interacting particles and the invariant mass is a positive quantity

$$M^2_w - M^2_{\chi\chi}|_{m_{k_1}=m_{k_2}=0} = \frac{4m^2\left(\bar{\phi}_1 - \bar{\phi}_2\right)^2}{M^2_{\phi\phi} + 4\bar{\phi}_1 \cdot \bar{\phi}_2} \tag{4.2.18}$$

giving a mass for k_1 and k_2 (see Sec. 4.2.4). On the other hand, assuming from the beginning $m_{k_1} = m_{k_2} = m_k \geq 0$ other invariants can be considered. This assumption will be interesting if we know m_k or want to use a test mass, or if each invisible particle is a combination of a multitude of weakly interacting particles with invariant mass larger than a known quantity. An exhaustive description of these cases can be found elsewhere [112], but eludes the purposes of this thesis.

4.2.3 A bit of asymmetry

Suppose $m_{\phi_1} = m_1 > m_{\phi_2} = m_2$. This could be the case with a more complex topology when each visible particle is substituted by a collection of visible observables. In this scenario we loose part of the symmetry between the two hemispheres.

There are two main possibilities: maintain or abandon the assumption of equal and opposite boosts.

For example, if we consider different masses for the two children, Eq. 4.2.10 and Eq. 4.2.3 are not valid anymore. In this case we can use a different normalisation such that

$$\begin{cases} \bar{k}_1 &= (N-1)\,\bar{\phi}_1 - N\bar{\phi}_2 \\ \bar{k}_2 &= (L-1)\,\bar{\phi}_2 - L\bar{\phi}_1 \\ E_{k_1} &= (N-1)\,E_{\phi_1} + NE_{\phi_2} \\ E_{k_2} &= (L-1)\,E_{\phi_2} + LE_{\phi_1} \end{cases} . \tag{4.2.19}$$

As a result the expressions for the masses of kinematic particles are

$$\begin{aligned} m_{k_1}^2 &= (N-1)^2 m_1^2 + N^2 m_2^2 + N(N-1)M_C^2 \\ m_{k_2}^2 &= (L-1)^2 m_2^2 + L^2 m_1^2 + L(L-1)M_C^2 \end{aligned} . \tag{4.2.20}$$

Imposing $m_{k_1} = m_{k_2} = 0$ we can write the expressions

$$N = \frac{1}{2} + \frac{1}{2}\frac{m_1^2 - m_2^2 + \sqrt{M_c^4 - 4m_1^2 m_2^2}}{m_1^2 + m_2^2 + M_c^2}, \tag{4.2.21}$$

$$L = \frac{1}{2} + \frac{1}{2}\frac{m_2^2 - m_1^2 + \sqrt{M_c^4 - 4m_1^2 m_2^2}}{m_1^2 + m_2^2 + M_c^2}, \tag{4.2.22}$$

where the difference is related to the mass squared difference of the phenomenological particles

$$N - L = \frac{m_1^2 - m_2^2}{M_{\phi\phi}^2 + 4\bar{\phi}_1 \cdot \bar{\phi}_2}. \tag{4.2.23}$$

The second possibility is physically more reasonable for the SUSY phenomenology. We maintain the equal contra-boost relation $\bar{\beta}(P \to C_1) = -\bar{\beta}(P \to C_2)$ assuming $M_{C_1} = M_{C_2}$, a direct consequence of C_1 identical to C_2. Clearly imposing $N = L$ the condition $m_{k_1} = 0$ in Eq. 4.2.20 gives $m_{k_2} \geq 0$:

$$m_{k_2}^2 = \left(m_1^2 - m_2^2\right) \frac{m_1^2 - m_2^2 + \sqrt{M_c^4 - 4m_1^2 m_2^2}}{m_1^2 + m_2^2 + M_c^2}. \tag{4.2.24}$$

Rewriting the relation for equal and opposite Lorentz boosts as

$$\frac{-\bar{\phi}_2 - \bar{k}_2}{E_{\phi_2} + E_{k_2}} = \frac{\bar{\phi}_1 - \bar{\phi}_2}{E_{\phi_1} + E_{\phi_2}} = \frac{\bar{\phi}_1 + \bar{k}_1}{E_{\phi_1} + E_{k_1}} \tag{4.2.25}$$

for $m_1 > m_2$ the normalisation factors can be rearranged such that:

$$\begin{cases} \bar{k}_1 & = & (N-1)\,\bar{\phi}_1 - L\bar{\phi}_2 \\ \bar{k}_2 & = & (L-1)\,\bar{\phi}_2 - N\bar{\phi}_1 \\ E_{k_1} & = & (N-1)\,E_{\phi_1} + LE_{\phi_2} \\ E_{k_2} & = & (L-1)\,E_{\phi_2} + NE_{\phi_1} \end{cases}. \tag{4.2.26}$$

The weakly interacting masses can be written

$$\begin{cases} m_{k_1}^2 & = E_{k_1}^2 - k_1^2 = \left[(N-1)\,E_{\phi_1} + LE_{\phi_2}\right]^2 - \left[(N-1)\,\bar{\phi}_1 - L\bar{\phi}_2\right]^2 \\ m_{k_2}^2 & = E_{k_2}^2 - k_2^2 = \left[(L-1)\,E_{\phi_2} + NE_{\phi_1}\right]^2 - \left[(L-1)\,\bar{\phi}_2 - N\bar{\phi}_1\right]^2 \\ M_{\chi\chi}^2 & = m_{k_1}^2 + m_{k_2}^2 + 2\left[(N-1)\,E_{\phi_1} + LE_{\phi_2}\right]\left[(L-1)\,E_{\phi_2} + NE_{\phi_1}\right] \\ & -2\left[(N-1)\,\bar{\phi}_1 - L\bar{\phi}_2\right]\left[(L-1)\,\bar{\phi}_2 - N\bar{\phi}_1\right] \end{cases}. \tag{4.2.27}$$

The system for the first two equations

$$\begin{cases} m_{k_1}^2 = (N-1)^2 m_1^2 + L^2 m_2^2 + L(N-1)M_C^2 \\ m_{k_2}^2 = (L-1)^2 m_2^2 + N^2 m_1^2 + N(L-1)M_C^2 \end{cases} \tag{4.2.28}$$

has no solutions. In any case, we can parametrise N and L in order to obtain the correct asymptotic behaviour for $\Delta M_k^2 = m_{k_2}^2 - m_{k_1}^2$ [3] and in analogy with Eq. 4.2.17

[3] Choosing $m_1 > m_2$ follows $m_{k_2} > m_{k_1}$.

we choose the lowest Lorentz invariant greater than or equal to $M^2_{\chi\chi}$

$$M^2_w = M^2_{\phi\phi} - 4m_1 m_2. \tag{4.2.29}$$

The Lorentz invariant in Eq. 4.2.29 is an educated guess for the mass of the weakly interacting system and can be extended in the more general cases of longer chains and higher multiplicity of the visible objects by substituting the masses of the phenomenological particles for the invariant masses of the hemispheres as described in Section 4.4.

4.2.4 Estimating the unknown d.o.f.

In order to assign reasonable values for N and L choosing M_w from Eq. 4.2.29 we exploit what we expect for the simpler case $m_1 = m_2 = m$ and $N = L$. Manipulating from Eq. 4.2.15 and 4.2.17 we find

$$N = \frac{1}{2} + \frac{1\left[(E_{\phi_1} + E_{\phi_2})^2 - 4m^2\right]^{1/2}}{2\left(E_{\phi_1} + E_{\phi_2}\right)} \tag{4.2.30}$$

and substituting in Eq. 4.2.12 the weakly interacting particles gain a mass

$$m^2_{k_1} = m^2_{k_2} = m^2 \frac{\left(\bar{\phi}_1 - \bar{\phi}_2\right)^2}{\left(E_{\phi_1} + E_{\phi_2}\right)^2}. \tag{4.2.31}$$

Note this squared mass is always positive being $M^2_w \geq M^2_{\chi\chi}|_0$ and the two invisible masses are the same assuming symmetry between the two hemispheres ($m_1 = m_2$).

When $m_1 \neq m_2$ we re-partition the weakly interacting d.o.f. with two weights a_1 and a_2 taking into account the mass difference

$$\begin{array}{rcl} a_1 & = & m_1^2 - m_2^2 + M_C^2 - 2m_1 m_2 \\ a_2 & = & m_2^2 - m_1^2 + M_C^2 - 2m_1 m_2 \end{array}. \tag{4.2.32}$$

Defining a common quantity contra-boost invariant

$$A = \frac{|a_1 m_1^2 - a_2 m_2^2| - 1/2\, |a_2 - a_1|\, M_C^2 + 1/2\, (a_1 + a_2)\, \sqrt{M_C^4 - 4 m_1^2 m_2^2}}{a_1^2 m_1^2 + a_2^2 m_2^2 + a_1 a_2 M_C^2} \tag{4.2.33}$$

where the modules can be omitted for $m_1 > m_2$ and

$$B = \frac{E_{\phi_1} + E_{\phi_2} + \sqrt{\left(\bar{\phi}_1 + \bar{\phi}_2\right)^2 + M_w^2}}{2\left(c_1 E_{\phi_1} + c_2 E_{\phi_2}\right)}, \tag{4.2.34}$$

with

$$\begin{array}{c} c_1 = \frac{1}{2}\left(1 + a_1 A\right) \\ c_2 = \frac{1}{2}\left(1 + a_2 A\right) \end{array}, \tag{4.2.35}$$

we write the normalisation factors as

$$\begin{array}{rcl} N & = & c_1 B \\ L & = & c_2 B \end{array}. \tag{4.2.36}$$

Notice when $m_1 = m_2 \to a_1 = a_2 = M_C^2 - 2m^2$, $c_1 = c_2 = 1$ and B takes the value in Eq. 4.2.30. In the limit $m_1, m_2 \to 0$ the asymptotic behaviour $B \to 1$ is satisfied.

Finally, the four-momenta of the two invisible particles are given by the expressions

$$\begin{array}{rcl} k_{1\mu} & = & \left[\left(N - 1\right) E_{\phi_1} + L E_{\phi_2},\ -\left(N - 1\right) \bar{\phi}_1 - L \bar{\phi}_2\right] \\ k_{2\mu} & = & \left[N E_{\phi_1} + \left(L - 1\right) E_{\phi_2}\ , -N \bar{\phi}_1 - \left(L - 1\right) \bar{\phi}_2\right] \end{array}. \tag{4.2.37}$$

As described in Section 4.5, this is the result of the *contra-boost invariant jigsaw rule* and the other invisible jigsaw rules, valid for symmetric ($m_1 = m_2$) and asymmetric ($m_1 > m_2$) hemispheres.

In this thesis reconstructions based on $M_{C_1} = M_{C_2}$ are assumed. Possible constraints include the assumption of the same mass for other particles along the decay chains, or the minimisation of the quantities $M_{C_1}^2 + M_{C_2}^2$ or $M_{C_1}^2 - M_{C_2}^2$ (see Eq. 4.2.23). A detailed description can be found in Ref. [112], where is shown as the $M_{C_1} = M_{C_2}$ approach yields the best mass-sensitive estimators and is the most suitable reconstruction for probing SUSY topologies.

4.2.5 The contra-boost invariants

By definition, it follows from Eq. 4.2.4 that M_C, evaluated as the sum of the visible energies, is independent of $\bar{\beta}_c$. Considering the same masses for the children, the equal and opposite boosts provide for the energies of the visible particles in each C_i frame:

$$\begin{array}{lll} E_{\phi_1}^{C_1} & = \frac{1}{(1-\beta_c^2)^{1/2}}\left(E_{\phi_1} - \bar{\beta}_c \cdot \bar{\phi}_1\right) & = \frac{2m_1^2+M_C^2}{2\left(m_1^2+m_2^2+M_C^2\right)^{1/2}} \\ E_{\phi_2}^{C_2} & & = \frac{2m_2^2+M_C^2}{2\left(m_1^2+m_2^2+M_C^2\right)^{1/2}} \end{array} . \tag{4.2.38}$$

These expressions are the same and are contra-boost invariants, since they depend only on $m_{\phi_1}^2 = m_{\phi_2}^2$ and M_C^2. Similarly, the absolute values of the visible and invisible particle three-momenta are contra-boost invariants in the C_i frame, given by

$$\begin{array}{lll} \phi_1^{C_1} = k_1^{C_1} & = \left[\left(E_{\phi_1}^{C_1}\right)^2 - m_1^2\right]^{1/2} & = \frac{1}{2}\sqrt{\frac{M_C^4-4m_1^2m_2^2}{m_1^2+m_2^2+M_C^2}} \\ \phi_2^{C_2} = k_2^{C_2} & = \left[\left(E_{\phi_2}^{C_2}\right)^2 - m_2^2\right]^{1/2} & = \frac{1}{2}\sqrt{\frac{M_C^4-4m_1^2m_2^2}{m_1^2+m_2^2+M_C^2}} \end{array} \tag{4.2.39}$$

and they are the same. All of these quantities are contra-boost invariants, while m_{k_1} and m_{k_2} are not. When the phenomenological particles are parents of other visible and invisible particles the contra-boost invariance becomes an inheritance of the "children" frames.

For the choice used when $m_1 \neq m_2$, the energies in Eq. 4.2.38 are generalised by the expressions

$$\begin{array}{ll} E_{\phi_1}^{C_1} & = \frac{2c_1m_1^2+c_2M_C^2}{2\left(c_1^2m_1^2+c_2^2m_2^2+c_1c_2M_C^2\right)^{1/2}} \\ E_{\phi_2}^{C_2} & = \frac{2c_2m_2^2+c_1M_C^2}{2\left(c_1^2m_1^2+c_2^2m_2^2+c_1c_2M_C^2\right)^{1/2}} \end{array} . \tag{4.2.40}$$

These quantities are obtained by simplifying the B^2 terms, appearing in quadratic terms in N and L, and they are still contra-boost invariants as well as $\phi_1^{C_1}$ and $\phi_2^{C_2}$.

The mass-squared difference ΔM_k^2 is not contra-boost invariant

$$\Delta M_k^2 = \quad m_{k_2}^2 - m_{k_1}^2 = \quad m_1^2\,(2N-1) + m_2^2\,(-2L+1) + M_C^2\,(L-N) \ , \tag{4.2.41}$$

but taking the limit $B \to 1$ (hence $N = c_1$ and $L = c_2$), it assumes the form given by

$$\Delta M_k^2 = \quad A\left[a_1 m_1^2 - a_2 m_2^2 + \tfrac{1}{2} M_C^2\,(a_2 - a_1)\right] \ . \tag{4.2.42}$$

For the definition given in Eq. 4.2.32 we write

$$\Delta M_k^2 \quad = \quad A\,(m_1^4 - m_2^4 + m_2^3 m_1 - m_1^3 m_2) = A\,(m_1 - m_2)\,(m_1^3 + m_2^3) \tag{4.2.43}$$

and $\Delta M_k^2 \to 0$ for $m_1 \to m_2$ and for $M_C \to \infty$ being the asymptotic value given by Eq. 4.2.33

$$A_{|M_C \to \infty} \sim M_C^{-2}. \tag{4.2.44}$$

Hence, the choices for the Eq. 4.2.32 and A, resulting from $m_{k_1} = 0$ in Eq. 4.2.28 and $N = c_1$ and $L = c_2$, are such that the difference ΔM_k^2, and consequently m_{k_2}, is as small as possible. The only non contra-boost invariant quantity is the B-term given by the Eq. 4.2.34, which has the behaviour $B \to 1$ in the limit of massless visible and invisible objects.

4.3 The transverse plane

Consider now a less ideal detector with $Lab \neq P$, but a much simpler topology as in Figure 4.3.1.

In the case of no full azimuthal coverage of the detector acceptance, the two unknown d.o.f. are the mass and the z-momentum of the invisible particle assuming that the constraints $\not{E}_x = k_x$ and $\not{E}_y = k_y$ are valid. For this topology the choices $m_k = 0$ and $k_z = \phi_z$ for a massless visible particle are simple to guess, but in this section we

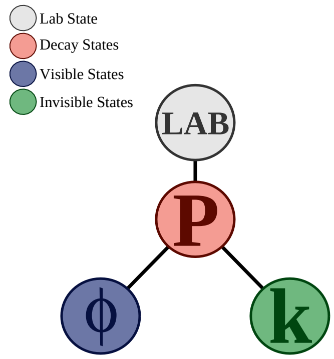

Figure 4.3.1: The decay tree: a particle P decays in a visible and an invisible object.

illustrate the motivations for this case and the implications for more complex topologies.

In order to boost our system from the *Lab* frame to P a longitudinal boost along the beam axis from the *Lab* to a *transverse* frame $\beta_z\,(Lab \to Tra)$ and a successive transverse boost from that frame to P: $\beta_T\,(Tra \to P)$ are necessary. In the true transverse frame of reference the relation $P_z^{Tra} = 0$ is valid.

We want to chose $\beta_z\,(Lab \to Tra)$ such that all the observables in the transverse frame and any frames that recursively follow from it are independent of the true value. With the same argument described for the contra-boost velocity we adopt a strategy based on the minimisation of the partial derivative:

$$\begin{aligned} 0 &= \frac{\partial E_\phi^{Tra}}{\partial \beta_z} \\ &= \left(1-\beta_z^2\right)^{-3/2}\left(\beta_z E_\phi - \phi_z\right) \end{aligned}, \tag{4.3.1}$$

and the resulting velocity is:

$$\beta_z = \frac{\phi_z}{E_\phi}. \tag{4.3.2}$$

This transverse frame is our guess for $P_z^{Tra} = 0$ and being the frame where $\phi_z^{Tra} = 0$ provides $k_z^{Tra} = 0$ independently from m_k.

In the true P frame the energy for the visible particle is

$$E_\phi^{P-\text{true}} = \frac{M_P^2 - m_k^2 + m_\phi^2}{2M_P} \tag{4.3.3}$$

Using once again an *extremisation* rule

$$\begin{aligned} 0 &= \frac{\partial E_\phi^P}{\partial \beta_T} \\ &= \left(1-\beta_T^2\right)^{-3/2}\left(\beta_T E_\phi^{Tra} - \bar{\beta}_T^{Tra} \cdot \bar{\phi}_T^{Tra}\right) \end{aligned} \tag{4.3.4}$$

we have a transverse boost velocity

$$\bar{\beta}_T = \frac{\hat{\beta}_T^{Tra} \cdot \bar{\phi}_T^{Tra}}{E_\phi^{Tra}} = \frac{\hat{\beta}_T \cdot \bar{\phi}_T}{E_\phi^{Tra}} \tag{4.3.5}$$

having $\hat{\beta}_T \cdot \bar{\phi}_T$ the same value in the Tra and Lab frames.

This quantity can be negative giving a velocity to k greater than the speed of light and imaginary values for m_k. In order to avoid tachyonic problems the smallest Lorentz invariant we can choose for the mass of the invisible particle is zero. In this case the transverse boost assumes the expression:

$$\bar{\beta}_T = \frac{\bar{\phi}_T + \bar{k}_T}{E_\phi^{Tra} + k_T}. \tag{4.3.6}$$

Considering the velocities in Eq. 4.3.2 and 4.3.6 and choosing $m_k = 0$ in Eq. 4.3.3 the following relation is valid

$$M_P = \left[m_\phi^2 + 2k_T\left(m_\phi^2 + \phi_T^2\right)^{1/2} - 2\bar{\phi}_T \cdot \bar{k}_T\right]^{1/2} \equiv M_T(0); \tag{4.3.7}$$

which is the transverse mass. As we have seen in Section 3.5.2 this expression is invariant for longitudinal boosts, depending only on the transverse components of the momenta and m_ϕ.

The procedure based on the factorisation of the problem in different jigsaw rules assigning only the d.o.f. relevant to the Lorentz transformation should now be clear. In the hypothesis of a more complicated tree, for example when the ϕ particle decays to other visible and/or invisible particles, any successive boost would be independent from the choice used for the longitudinal velocity, and only moderately dependent on

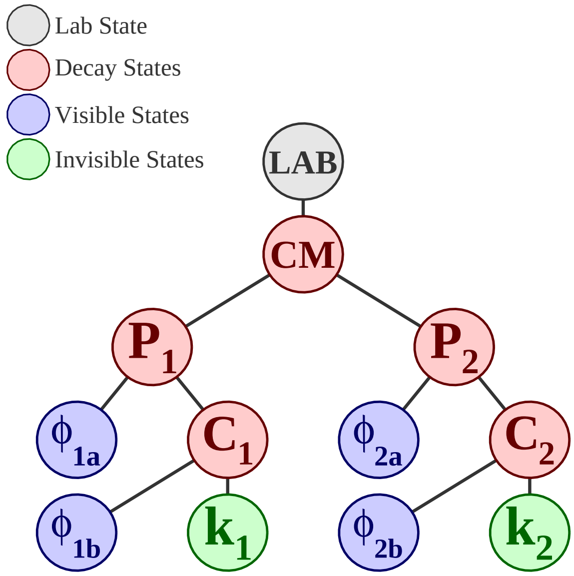

Figure 4.4.1: RJR tree for the prototype topology as in Figure 4.1.1: the pair-production of the parents P_1 and P_2 in a final state with four visible and two invisible objects.

the transverse velocity. The first one is based on longitudinal boost invariance and is a quantity that is wrong event-by-event but correct on average, independent of the estimation of M_P: the best estimate for the rapidity of the invisible particle is the rapidity of the visible one. This is the prototype of the *Set Rapidity* jigsaw rule. The transverse velocity is the approximated quantity in Eq. 4.3.6 and provides the transverse approximation $M_T(0)$ of M_P^{true}, hence reconstructing the true P frame for events populating the endpoint configuration for a massless invisible particle and a correct longitudinal boost.

4.4 RJR in practice

4.4.1 Choose the topology

We can now consider the decay tree in Figure 4.4.1. Two particle *parents* P are produced each decaying to a *child* C and a visible state, the children subsequently decay to a visible and an invisible state. The final states are characterised by four visible ϕ particles and two weakly interacting or invisible k particles.[4]

This topology has all the characteristics useful to treat the jigsaw rules in an exhaustive way. There are two hemispheres (labelled 1 and 2) and a two step decay. The symmetry between the two hemispheres is typical of a BSM physics model characterised by a $\mathbb{Z}_2$ discrete symmetry like SUSY in which $k = \tilde{\chi}_1^0$.

For convention, we define covariant four vectors $V_{1\mu} \equiv \phi_{1a\mu} + \phi_{1b\mu} = \left(E_{V_1}, -\bar{V}_1\right) = \left(E_{\phi_{1a}} + E_{\phi_{1b}}, -\bar{\phi}_{1a} - \bar{\phi}_{1b}\right)$, $V_{2\mu}$ describing the "*visible*" hemispheres 1 and 2 and $H_{1\mu} \equiv \phi_{1a\mu} + \phi_{1b\mu} + k_{1\mu} = \left(E_{\phi_{1a}} + E_{\phi_{1b}} + E_{k_1}, -\bar{\phi}_{1a} - \bar{\phi}_{1b} - \bar{k}_1\right) = \left(E_{H_1}, -\bar{H}_1\right)$, $H_{2\mu}$ describing the entire hemispheres.

4.4.2 Evaluation of the invisible particles four-momenta

The first assumption we make is $M_{P_1} = M_{P_2}$. The first transformation is a longitudinal boost $Lab \rightarrow Tra$ along the beam axis

$$\beta_L = \frac{V_{1z} + V_{2z}}{E_{V1} + E_{V2}}. \tag{4.4.1}$$

This is the best reconstruction of the transverse plane having no information from the z component of the missing energy. It is equivalent to setting the rapidity of the invisible objects equal to that of all the visible objects, and in the massless limit $k_{1z} + k_{2z} = V_{1z} + V_{2z}$. The minimisation of the energy of the visible particle in Eq. 4.3.1 is proportional to the minimisation in M_P and hence Eq. 4.4.1 is the analogue of Eq. 4.3.2 satisfying a minimisation of the energy of CM

$$\frac{\partial \sqrt{s_{par-par}}}{\partial \beta_L} \Rightarrow \beta_L = \frac{V_{1z} + V_{2z}}{E_{V1} + E_{V2}}. \tag{4.4.2}$$

We have reconstructed an approximation of the Tra frame and all the subsequent transformations are invariant under longitudinal boosts.

[4] The centre-of-mass frame (CM) of the two parents is often referred to as PP or simply to as S in the studies involving a supersymmetric system.

In order to perform the transverse boost in the PP centre-of-mass frame (CM) we need to guess the energy and so the invariant mass of the weakly interacting system M_w. The choice used is

$$M_w^2 = M_{V_1V_2}^2 - 4M_{V_1}M_{V_2} \tag{4.4.3}$$

where $M_{V_1V_2} = \sqrt{(E_{V_1}+E_{V_2})^2 - \left(\vec{V}_1+\vec{V}_2\right)^2} = \sqrt{E_{4\phi}^2 - \vec{P}_{4\phi}^2}$ is the invariant mass of all the phenomenological objects in the final state and $M_{V_1} = \sqrt{E_{V_1}^2 - \left(\vec{V}^1\right)^2}$, (M_{V_2}) is the invariant mass of the visible hemisphere 1 (2).

This choice, a generalisation of Eq. 4.2.29, does not use information other than the d.o.f. accessible in the event, and preserves the Lorentz invariance avoiding tachyonic problems: the masses of the decay products in the final state are preserved real.

The *transverse* energy of the weakly interacting system can be approximated as

$$E_w^2 = M_w^2 + \not{E}_T^2 \tag{4.4.4}$$

and we define a two-dimensional vector combining the transverse information of visible and invisible momenta

$$\bar{p}_T = \left(\not{E}_x + V_{1x} + V_{2x},\, \not{E}_y + V_{1y} + V_{2y}\right). \tag{4.4.5}$$

Using Eq. 4.4.4 and 4.4.5 it is possible to perform a boost in the transverse plane with the velocity

$$\bar{\beta}_T(Tra \to CM) = \frac{\bar{p}_T}{E_{4\phi} + E_w}. \tag{4.4.6}$$

A smaller Lorentz invariant than M_w can "over-boost" the CM-frame since the value in Eq. 4.4.3 is always greater than, or equal to, the true value. Smaller invariants can provide an approximation for $\bar{\beta}_T$ larger than the true value and produce unphysical results: m_{k_1} and m_{k_2} imaginary. In other words M_w^2 is the smallest invariant large enough to accommodate the subsequent contra-boost.

At this point, we have an approximation for the PP centre-of-mass frame and every four-momentum can be boosted into this frame. In the CM frame, we estimate the invisible four-momenta in order to partition the invisible system into the two hemispheres.

The equations in Section 4.2.4 can be rewritten with the substitutions $m_1 \to M_{V_1}$ and $m_2 \to M_{V_2}$ providing the final re-partition

$$\begin{array}{rcl} k_{1\mu}^{CM} & = & \left[(N-1)\,E_{V_1} + LE_{V_2},\, -(N-1)\,\bar{V}_1 - L\bar{V}_2\right] \\ k_{2\mu}^{CM} & = & \left[NE_{V_1} + (L-1)\,E_{V_2}\,, -N\bar{V}_1 - (L-1)\,\bar{V}_2\right] \end{array}. \tag{4.4.7}$$

4.4.3 Boosting the objects to the relevant frames of reference

The invisible four-momenta are now boosted back: $k_{1\mu}^{CM}$ and $k_{2\mu}^{CM}$ are calculated in the *Lab* frame using Lorentz transformations with velocities given by the Eq. 4.4.6 and 4.4.1, except for the opposite signs. We have estimated all the d.o.f. of the invisible objects and we can write the two hemispheres in the *Lab* frame:

$$\begin{array}{rcl} H_{1\mu} & = & \phi_{1a\mu} + \phi_{1b\mu} + k_{1\mu} \\ H_{2\mu} & = & \phi_{2a\mu} + \phi_{2b\mu} + k_{2\mu} \end{array}. \tag{4.4.8}$$

The velocity boosting the system to the CM frame is:

$$\bar{\beta}\,(Lab \to CM) \;\; = \;\; \frac{\bar{H}_1 + \bar{H}_2}{E_{H_1} + E_{H_2}}, \tag{4.4.9}$$

which corresponds to the composition of the longitudinal and transverse boosts (defined by the velocities in Eq. 4.4.1 and Eq. 4.4.5). This estimate of the CM-system velocity in the *Lab* frame is based on the constraint of two unknown d.o.f.: the assumption of the same rapidity for visible and invisible objects (a consequence of Eq. 4.4.2) and M_w

as the guess for the weakly interacting mass resulting from

$$\left.\frac{\partial M_P}{\partial \beta_c^{CM}}\right|_{M_{P_1}=M_{P_2}=M_P} \Rightarrow M_w. \tag{4.4.10}$$

We boost visible and invisible objects in the CM frame of reference.

From here, the velocities for the contra-boost transformations from the centre-of-mass frame to each parent rest frame are:

$$\begin{aligned} \beta(CM \rightarrow P_1) &= \frac{\bar{H}_1^{CM}}{E_{H_1}^{CM}} \\ \beta(CM \rightarrow P_2) &= \frac{\bar{H}_2^{CM}}{E_{H_2}^{CM}} \end{aligned} \tag{4.4.11}$$

and $\beta_c^{CM} \equiv \beta(CM \rightarrow P_1) = -\beta(CM \rightarrow P_2)$ by definition, being that the two parents identical. Finally, the velocity for the boosts from each P rest frame to each child rest frame can be expressed by

$$\begin{aligned} \beta(P_1 \rightarrow C_1) &= \frac{\bar{\phi}_{1b}^{P_1} + \bar{k}_1^{P_1}}{E_{\phi_{1b}}^{P_1} + E_{k1}^{P_1}} \\ \beta(P_2 \rightarrow C_2) &= \frac{\bar{\phi}_{2b}^{P_2} + \bar{k}_2^{P_2}}{E_{\phi_{2b}}^{P_2} + E_{k2}^{P_2}} \end{aligned}, \tag{4.4.12}$$

where the objects are evaluated in the approximate $P_{1(2)}$ frames. The remaining unknown degrees of freedom necessary to define the velocities in Eq. 4.4.11 and perform the transformation for the reconstruction of the $P_{1(2)}$ frames (and successive $C_{1(2)}$ frame) are the results of the repartition described in Section 4.2.4.

4.4.4 Construct the observables

Event-by-event a basis of experimental observables with a real physical meaning can be extracted. Imposing the decay tree in Figure 4.4.1, once the main frames of reference are reconstructed, the kinematic variables include:

Scale variables

- M_{PP} is a variable sensitive to the invariant mass of the two hemispheres, hence the overall mass scale. In the case of no other activity,[5] it corresponds to the estimate of centre-of-mass energy of the hard collision:

$$M_{PP} = E_{CM}^{CM} \equiv M_{CM} = \sqrt{s_{par-par}} = \sqrt{s x_a x_b} \tag{4.4.13}$$

where in the last expression x_a and x_b are the fractions of the proton momentum carried by the two interacting partons.

- $E_{\phi_{1a}}^{P_1}$, $E_{\phi_{2a}}^{P_2}$, $E_{\phi_{1b}}^{C_1}$ and $E_{\phi_{2b}}^{P_2}$, are variables sensitive to the mass splitting between parent and children particles in each hemisphere. They correspond to the energies of the visible objects in the P_i and C_i approximated rest frames described in this chapter. If the frames of reference could be reconstructed perfectly in each hemisphere, they would satisfy the relations as in Eq. 4.3.3:

$$\begin{cases} E_{\phi_a}^{P-\text{true}} = \frac{M_{P-\text{true}}^2 - M_{C-\text{true}}^2 + m_{\phi-\text{true}}^2}{2M_{P-\text{true}}} \\ E_{\phi_b}^{C-\text{true}} = \frac{M_{C-\text{true}}^2 - m_{k-\text{true}}^2 + m_{\phi-\text{true}}^2}{2M_{C-\text{true}}} \end{cases} . \tag{4.4.14}$$

- M_{P_1}, M_{P_2}, M_{C_1} and M_{C_2} are the masses associated with the $P(C)$ systems. Instead of the energies, the reconstructed masses of P and C systems can be used, being

$$\begin{cases} M_{C_i} = E_{\phi_b}^{C_i} + E_k^{C_i} \\ M_{P_i} = E_{\phi_{ia}}^{P_i} + E_{C_i}^{P_i} \end{cases} . \tag{4.4.15}$$

In the limit of massless visible and invisible objects they reduce to $M_{C_i} = 2p_{\phi_{ib}}^{C}$, $M_{P_i} = p_{C_i}^{P} + \sqrt{M_{C_i}^2 + \left(p_{C_i}^{P}\right)^2}$. These observables are particularly accurate in the case of massless weakly interacting particles, for example in SM final states involving neutrinos. As described in this chapter and for all the proposed analyses in this thesis, we use the RJR method assuming the $M_{P_1} = M_{P_2}$ approach.

[5] Other activity refers mainly to radiation or noise in the detector response.

Angular variables

- $\cos\theta_{PP}$ is the cosine of half of the angle between the two parents. It is evaluated as:
$$\cos\theta_{PP} = \hat{P}_1^{PP} \cdot \hat{\beta}_{PP}^{Lab} \tag{4.4.16}$$

- $\triangle\varphi_{P_1P_2}$ is the azimuthal angle between the decay planes of P_1 and P_2. It corresponds to
$$\triangle\varphi_{P_1P_2} = \triangle\varphi\left[\bar{\phi}_{1a}^{PP} \times \left(\bar{\phi}_{1b}^{PP} + \bar{k}_1^{PP}\right), \bar{\phi}_{2a}^{PP} \times \left(\bar{\phi}_{2b}^{PP} + \bar{k}_2^{PP}\right)\right] \tag{4.4.17}$$

- $\cos\theta_{P_1}$ ($\cos\theta_{P_2}$) is the cosine of the parent decay angle. It can be computed as
$$\cos\theta_{P_i} = \hat{\phi}_{ia}^{P_i} \cdot \hat{\beta}_{P_i}^{PP} \tag{4.4.18}$$

- $\cos\theta_{C_1}$ ($\cos\theta_{C_2}$) is the cosine of the child decay angle in the hemisphere 1 (2). It is:
$$\cos\theta_{C_i} = \hat{\phi}_{ib}^{C_i} \cdot \hat{\beta}_{C_i}^{P_i} \tag{4.4.19}$$

- $\triangle\varphi_{P_1C_1}$, ($\triangle\varphi_{P_2C_2}$) is the azimuthal angle between the first and second decay plane in the hemisphere 1 (2). It is evaluated as:
$$\triangle\varphi_{P_iC_i} = \triangle\varphi\left(\bar{\phi}_{ib}^{P_i} \times \bar{k}_i^{P_i}, \bar{\phi}_{ia}^{P_i} \times \bar{\beta}_{P_i}^{PP}\right) \tag{4.4.20}$$

Notice how $\triangle\varphi\left[\bar{\phi}_{ib}^{P_i} \times \bar{k}_i^{P_i}, \bar{\phi}_{ia}^{PP} \times \left(\bar{\phi}_{ib}^{PP} + \bar{k}_i^{PP}\right)\right]$ would be the angle between two quantities computed in different frames.

Scaleless variables

Angular observables are scaleless variables. In any case, this definition is used to refer to any non-trivial dimensionless combination of scale and angular variables. Scaleless observables are described analysis-by-analysis. In a two hemisphere topology, good scaleless observable are the simple relations

$$\gamma_c = \frac{M_{PP}}{2M_P} \qquad \text{or} \qquad 1-\beta_c^2 = \gamma_c^{-2} = \frac{M_{V_1}^2 + M_{V_2}^2 + M_c^2}{\left(E_{V_1}^{PP} + E_{V_2}^{PP}\right)^2} \tag{4.4.21}$$

with β_c the absolute value of the contra-boost velocity $\vec{\beta}_c = \vec{\beta}_{C_1}^{P_1} = -\vec{\beta}_{C_2}^{P_2}$. The last expression can be computed from Eq. 4.2.9 with $M_c = M_E\,(0,0)$ and $m_\phi \to M_V$. Notice that if the contra-boost velocity is identified correctly the boost factor γ_c satisfies $\gamma_c^{\text{true}} = \frac{M_{PP}^{\text{true}}}{2M_P^{\text{true}}}$ in the hypothesis of equal masses $M_{P_1} = M_{P_2} = M_P = M_P^{\text{true}}$, and $M_{PP}^{\text{true}} = \sqrt{s_{\text{par-par}}^{\text{true}}}$ in the absence of extra activity in the event.

In the case of the production of a resonant grandparent $pp \to G \to P_1P_2$, and otherwise identical tree, the scale observable M_{PP} corresponds to the estimate of M_G, $\cos\theta_{PP}$ corresponds to the cosine of the G decay angle $\cos\theta_G$ and another interesting angular observable would be the azimuthal angle between the G decay plane and the plane spanned by the beam axis and the boost from the laboratory frame to G:

$$\triangle\varphi_G = \triangle\varphi\left(\hat{\phi}_{P_1}^{G} \times \hat{\beta}_G^{Lab}, \hat{n}_z \times \hat{\beta}_G^{Lab}\right). \tag{4.4.22}$$

4.5 The jigsaw rules: customisable and interchangeable like a strange puzzle

4.5.1 More complex topologies

The jigsaw rules applied to the decay tree in Figure 4.5.1 assign the unknown degrees of freedom. In a final state with two invisible particles the relation $\bar{k}_{1,T} + \bar{k}_{2,T} = \vec{\not{E}}_T$ is assumed, and the observables summarised in the visible hemispheres V_i are used to define the rules. The rapidity of the invisible system is chosen be equal to the

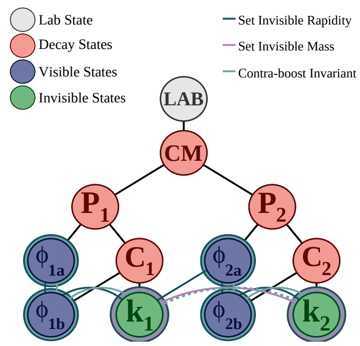

Figure 4.5.1: Decay tree and specific jigsaw rules for the weakly interacting particles.

visible one applying the rule *Set Invisible Rapidity*. The mass is chosen as in Eq. 4.4.3 via the *Set Invisible Mass* jigsaw rule. The remaining d.o.f. are assigned via the *Contra-boost Invariant* rule. The asymmetry due to different masses of the visible hemispheres results in a difference for the masses of the two invisible objects. In the case of perfect symmetry between the two hemispheres the jigsaw rules specifying four (8-4) d.o.f. assume the constraint for the weakly interacting transverse momentum, $M_{P_1} = M_{P_2}$ and the validity of the relation $m_{k_1} = m_{k_2}$, zero in the limit of massless visible hemispheres.

Final states with an higher multiplicity of visible or invisible particles can arise from a more complex topology maintaining a two hemispheres structure, typical of SUSY topologies, or by providing still more complicated and asymmetric ramifications. In the case of similar topologies with longer chains involving visible states, the jigsaw rules are the same with the visible hemispheres defined as the sum of the visible four-momenta on each side. The same goes for a larger multiplicity of invisible particles, except for cases when lower bound or test masses can be assumed for the invisible systems.

Whenever any node divides in two sub-branches, each one with visible and invisible particles, an additional *set invisible mass* rule must be applied to guess the node frame, and a *contra-boost invariant* jigsaw rule must be applied to reconstruct subsequent frames of reference. In the case of multiple weakly interacting particles in the same branch; for example for the SM process $\tau \to e\nu\nu$, the combination of the two neutrinos

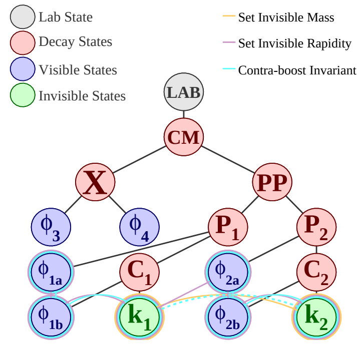

Figure 4.5.2: Decay tree: the two parent particles recoil against X.

can be summarised in a unique invisible object. In practice, this does not force the mass of the invisible system to resemble that one of a simple two-body decay ($\tau \to e\mathrm{I}$ with $M_{\mathrm{I}} = 0$), but instead the jigsaw rules allow the invisible system to gain a mass related to the kinematics of the visible objects in the final state and hence, event-by-event, to the number of WIMPs (see Eq. 4.2.31). Furthermore, in case of asymmetry between the two hemispheres this mass is larger for the invisible system collection of more invisible objects. For instance, for the SM $t\bar{t}$ production with $\bar{t} \to \bar{b}(W^-(e^-\nu))$ and $t \to bW^+(\nu\tau^+(e^+\nu\nu))$, the squared mass of the invisible system associated to the positron results larger of a quantity given by Eq. 4.2.41-4.2.43 with $m_1 \to M_{\bar{b}e^-}$ and $m_2 \to M_{be^+}$.

Suppose now that the PP system is boosted against something else X. This could be the case of another visible particle, an invisible one or a decay state. Suppose that it is a particle decaying to two visible objects as in Figure 4.5.2. A typical case could be SM $t\bar{t}$ production plus a boson decaying to two visible objects. Similarly, a pair of superparticles recoiling against some X or ISR; in this latter case the X state can be thought as an ISR-system composition of a non-specified number of visible objects.

For the decay tree considered, the main changes are as follows. The rapidity of the invisible system must to be set in the PP frame, hence set equal to the rapidity of the four visible decay products of the PP-system. The mass and the contra-boost invariant jigsaw rules must be defined with the same four objects. In practice a contra-boost must

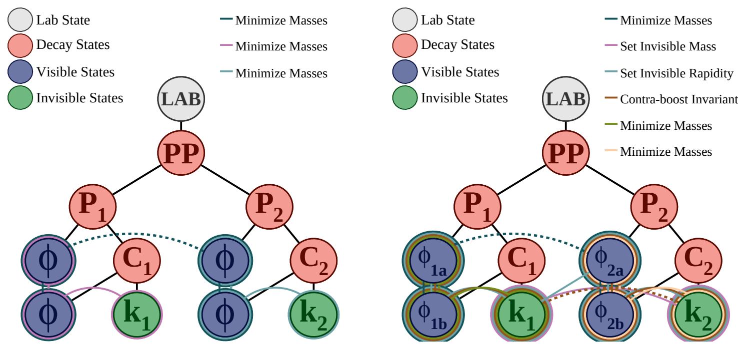

Figure 4.5.3: Minimisations of the masses to assign each visible object in the right position in the decay tree.

be performed to separate X from PP in the CM frame. Given that the X-system is fully reconstructed, namely all the decay products are visible, such as rule is trivial and not defined as a jigsaw rule. The same argumentation is valid for the contra-boost between $C_{1(2)}$ and $\phi_{1(2)a}$. Whenever both branches are not fully reconstructed an additional contra-boost invariant jigsaw rule must be applied, as is the case with invisible decay products in the X branch. The Set Invisible Mass and Rapidity rules will be defined with all the observable objects associated to the PP-system in the final state.

4.5.2 Combinatoric Jigsaw

In a real detector visible objects are not necessarily distinguishable from each other, in other words they have no label. Consider the worst scenario for the topology in Figure 4.5.3 where all the four phenomenological particles are identical objects (for example all jets coming from the fragmentation of light quarks). In this case, assigning every particle in the right position is a combinatoric challenge. Event-by-event there are twelve possible combinations for the assignment of each jet to the corresponding quark

$$N_{comb} = \frac{N_\phi!}{2} \tag{4.5.1}$$

given that the two hemispheres are identical.

We can categorise the twelve possible choices using the invariant mass of the potential hemispheres and another criteria to distinguish the first and second visible particle in each hemisphere. In the CM frame the two parents are back-to-back, so we use the minimum invariant mass between the three possible pair combinations

$$\min_{i=1,2,3}\left[V_{1\mu}(i)V_1^{\mu}(i)+V_{2\mu}(i)V_2^{\mu}(i)\right], \tag{4.5.2}$$

where $V_{1(2)\mu}(i)$ are the visible objects in the first (second) hemisphere introduced in Section 4.4.1. The invariant in Eq. 4.5.2 minimised in the *Lab* frame can be the first rule to be applied requiring simply the four-momenta of the visible objects. It is equivalent to minimising the visible $M_{P_{1(2)}}$.

We need to assign the first and second object in each hemisphere. Once again a minimisation is performed:

$$\begin{array}{c}\min\limits_{i\neq j=a,b}\left[\phi_{1i\mu}\phi_{1i}^{\mu}+\left(\phi_{1j}+k_1\right)_{\mu}\left(\phi_{1j}+k_1\right)^{\mu}\right]\\ \min\limits_{i\neq j=a,b}\left[\phi_{2i\mu}\phi_{2i}^{\mu}+\left(\phi_{2j}+k_1\right)_{\mu}\left(\phi_{2j}+k_1\right)^{\mu}\right]\end{array}, \tag{4.5.3}$$

where the second term in this minimisation corresponds to the two possible values of M_C^2, computed with one of the two phenomenological particles and the invisible one in each hemisphere. This minimisation is feasible because the estimation of the four-momenta of the invisible objects does not depend on the distinction between the first and second visible object in each hemisphere as in Eq. 4.2.37. In other words, the jigsaw rules described in the previous section depend only on the total visible hemisphere objects $V_{1(2)}$ and can be applied before the second minimisation. Once we have estimated the invisible four-momenta we can use their values in the *Lab* frame in order to take the minimum between the two possible invariants. This choice is independent of the mass spectrum and coherent with the Jigsaw philosophy: in the decay chain we use all, and only, the information relative to each step. Figure 4.5.3 on the right shows all the rules applied in the correct sequence: different concentric colours, ordered from outside to inside, surround the objects involved in the rule.

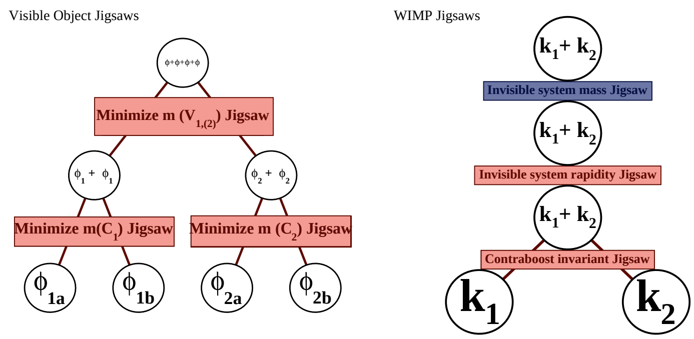

Figure 4.5.4: Combinatoric and invisible jigsaw rules for the decay tree in Figure 4.5.3.

Another way to see the jigsaw rules is to divide them in two categories. Combinatoric or visible rules are necessary to assign a label to the indistinguishable visible objects, while *WIMP* or invisible rules are used to assign a value for the unknown d.o.f. of the weakly interacting particles. Figure 4.5.4 shows the results for the visible rules based on minimisation of the masses as illustrated in Eq. 4.5.2 and Eq. 4.5.3, while all the three WIMP rules are necessary to guess the full four-momenta for the invisible particles.

Motivated by back-to-back kinematics of the decay products in the parent rest frame, the combinatoric jigsaw rules are the result of the minimisation of the masses. Any such minimisation can be considered a maximisation for the momentum of one of the two parts. For example, the minimisation of M_C in one of the two hemispheres in Eq. 4.5.3 is equivalent to maximise p for values of M_P and m_ϕ fixed, since

$$E_P^P \equiv M_P = E_C^P + E_\phi^P = \sqrt{M_C^2 + p^2} + \sqrt{m_\phi^2 + p^2} \tag{4.5.4}$$

with p the equal absolute three-momentum of the C and ϕ particles. It should now be clear the philosophy of the definition of a jigsaw rule as the result of an *extremisation* of a quantity related to the only d.o.f. relative to the transformation.

The last combinatoric challenge described in this section involves the presence of more visible objects in the final state than those expected from the topology. Typical is the case of high jet multiplicity for the phenomena described in Section 3.4.2.

Consider once again the decay tree in Figure 4.5.3 and suppose a final state with $n \geq 4$

indistinguishable jets. A veto for the events with more than four reconstructed jets is certainly too stringent a criterion. There are three main possible strategies for these scenarios.

- Select the four leading jets in p_T and use these for the definition of the jigsaw rules. This simple choice is driven from the expectation of large transverse momenta for the objects of interest.

- Take all the jets in the final states and treat every phenomenological state ϕ_i as a *pseudo-jet* or *mega-jet,* each one defined with at least one jet.[6] In this case the minimisation is the generalisation of the rules described in this section with an arbitrary number of jets ≥ 4. This choice, certainly useful in case of only FSR, has a bias in case of ISR, UE and multiple interactions. In particular, in the case of the production of heavy pairs PP, ISR is expected to have a large contribution due to the hard scale, while FSR is mostly collinear and expected to be collected inside the jet cone.

- The third procedure consists of dividing the study into two orthogonal regions: $n = 4$ and $n > 4$. For the first region, with exactly four jets, the decay tree and rules can be applied as illustrated. For the $n > 4$ region, an extra ISR-system with at least one jet can be required, then optional are minimisation of masses jigsaw rules performed to distribute all the remaining final state jets between the four visible decay products ϕ_{ij} and ISR.

The first and last options, together with b-jet combinatoric criteria, will be investigated in proposed analyses in Chapter 7 and Chapter 8.

[6]The combinatoric jigsaw rules can be defined with *exclusive* systems, namely requiring a specific number of objects in the state, or with *inclusive* systems, namely assuming a minimal number of objetcs.

4.5.3 Summary, and another example!

Non-trivial jigsaw rules constrain the unknown d.o.f. in the final state due to the combinatoric challenge of assigning indistinguishable visible objects in the right position in the tree or the lack of information from multiple weakly interacting particles. Once the jigsaw rules are applied we can estimate the four-momenta of the invisible objects and recursively reconstruct an approximation for the relevant frames of reference in the topology. The rules are never over-constraining so as to preserve real solutions and are the result of *extremisation* of quantities such as energies, masses and momenta considering the only known and unknown d.o.f. relevant to the Lorentz transformation or combinatoric choice in the assignment.

To summarise consider a final state with six phenomenological particles, four identical and two distinguishable, and two invisible particles as in the decay tree in Figure 4.5.5. A SM final state topology matching the tree is for example $t\bar{t} + h \to (t \to b\nu e^+,\ \bar{t} \to \bar{b}\nu\mu^-,\ h \to b\bar{b}) \to 4b$−jets + e^++ μ^-+$\vec{\not{E}}_T$ and conventionally the first hemisphere can be chosen as that one with the positron. In this way $e^+$and μ^- are assigned with no ambiguity in the tree.

To assign the four identical objects (b-jets) we need firstly a minimisation of the masses to separate those associated with $X = h$ from those assigned to $PP = t\bar{t}$. Then we could separate the other two b-jets in the two hemispheres $P_1 = t$ and $P_2 = \bar{t}$ performing a second combinatoric rule. Notice how the two minimisations of the masses can be performed before the WIMP rules and involve the two leptons four momenta together with $\vec{\not{E}}_T$, regulating an ambiguity $N_{comb} = 6 \times 2 = 12$. In this case h and $t\bar{t}$ are different systems and one of the six possibilities must be chosen to assign two b-jets in both. At this point, the second minimisation is roughly equivalent to associate each b-jet to the closer lepton in the $t\bar{t}$ system.

Then we can perform set invisible rapidity, set invisible mass and contra-boost invariant jigsaw rules and assign the weakly interacting degrees of freedom. Also in this case the minimisation can be generalised to the case of higher b-jet multiplicity requiring at least

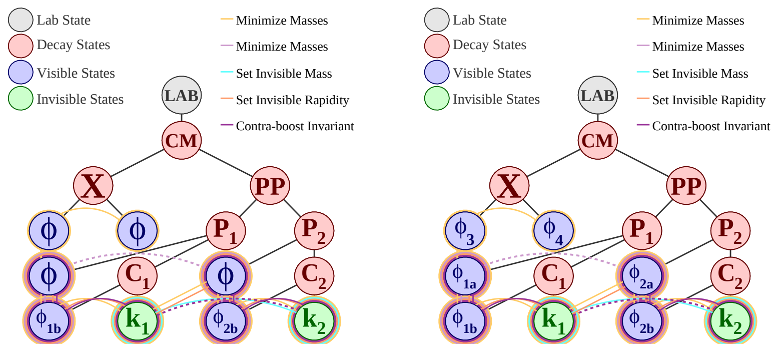

Figure 4.5.5: RJR decay tree for the analysis of $PP{+}X$.

one jet in each visible ϕ object.

Once the rules are specified, the frames are reconstructed recursively along the decay chains and a complete basis of variables can be extracted to probe the signal.

4.6 RJR for compressed spectra

4.6.1 Introduction to the compressed kinematics

In this section the RJR technique is described for compressed spectra of a generic supersymmetric topology. Herein a compressed scenario refers to a small supersymmetric spectrum mass-splitting, namely a small mass difference between the pair-produced parent superparticles $\tilde{P}$ and the LSPs $\tilde{\chi}$ [111].[7] In Section 2.3.6 it is described how compressed supersymmetric mass spectra in the EW-sector are quite common and how extensions of the MSSM can provide a heavy LSP and a compressed spectrum with coloured superparticles. A specific Recursive Jigsaw Reconstruction strategy is dedicated for such natural and not excluded scenarios.

[7] In this Section the general labels $\tilde{P}$ and $\tilde{\chi}$ are used to identify the parent sparticle and the lightest supersymmetric particle while in the specific analyses or examples conventional labels are used. The previous generic ϕ / k labels for visible/invisible objects in the final state would not be useful for compressed spectra.

4.6.1.1 The challenge

Supersymmetric final state topologies are challenging in the compressed regime. The challenge is due to the inefficiency of the detector to reconstruct low-momentum objects and the low impact of typical variables, such as the missing transverse momentum, exploited to separate signal-like events from the Standard Model backgrounds. For compressed scenarios the majority of the energy from sparticle decays that escapes detection is in the mass of the LSPs. This behaviour, specific to the compressed phenomenology, is now described more in detail.

Why low-transverse-momentum objects?

The product decay objects reconstructed by the detector and described in Section 3.4.2 have a momentum related to the mass-splitting of the overall supersymmetric mass spectrum associated to the event. The momentum of a massless object in the parent frame, as described in Eq. 4.3.3 is

$$p_o^{\tilde{P}} = \frac{M_{\tilde{P}}^2 - M_{\tilde{\chi}}^2}{2M_{\tilde{P}}}, \tag{4.6.1}$$

here rewritten for the parent sparticle $\tilde{P}$ decaying to a LSP $\tilde{\chi}$ and one SM object o. Consider the same mass for the two parent superparticles produced by the fusion of two partons.[8] The fraction of momentum of the two partons must be such that the energy of the collision $\sqrt{s_{par-par}}$ is greater than the production threshold $2M_{\tilde{P}}$. The events populate the tails of the parton distribution functions and in the absence of radiation from the initial state, the transverse momentum of the two interacting partons is negligible with respect to their z-momenta. In the limit of no ISR, for the conservation of momentum, the transverse momentum of the centre-of-mass of the parent frame $\tilde{P}\tilde{P}$ is negligible. In the $\tilde{P}\tilde{P}$ frame the two parents fly back-to-back with a momentum related to the difference between the collision energy of the two partons

[8] In this section we refer to the true masses.

and the threshold $\sqrt{s_{par-par}} - 2M_{\tilde{P}}$. With no ISR, it is likely that the two parent superparticles are produced not too far from the threshold and the result is a low transverse momentum of the parent sparticles in the detector frame.

For compressed scenarios the majority of the energy from sparticle decays provides the mass for the LSPs, quantified in the Eq. 4.6.1, resulting in a low transverse momentum for visible and invisible objects.

Why is the missing transverse momentum low?

In the limit of no initial state radiation the transverse momentum of the $\tilde{P}\tilde{P}$-system is negligible and in the $\tilde{P}\tilde{P}$ centre-of-mass frame, the two parent superparticles are back-to-back by definition. In the limit of nearly degenerate masses $M_{\tilde{\chi}} \sim M_{\tilde{P}}$ special relativity implies that $\vec{p}_{\tilde{\chi}} \sim \vec{p}_{\tilde{P}}$. The directions of the parent and child momenta are similar and in the $transverse\ Lab\ frame$ the two LSPs fly almost back-to-back. We have seen how the transverse momenta of all the objects are low and so for the LSPs, the vectorial sum is still lower. The result is a low value for the missing transverse momentum.

4.6.1.2 ISR to increase the momentum of the objects

For supersymmetric compressed mass spectra, the large absolute mass-scale of the LSPs could be distinctive from the typical Standard Model background scale, while the mass-splitting scale is certainly very similar if not smaller. While we cannot measure $M_{\tilde{\chi}}$ from $\vec{\not{E}}_T$, indirect sensitivity by observing the reaction of the LSP to a probing force can be gained.

The initial state radiation from interacting partons is the natural probe provided in the laboratory of a hadron collider. The ISR can provide large momentum to the sparticles produced in these reactions, in turn endowing their decay products with this momentum.

For compressed scenarios, in order to separate signal-like events from background-like events, the focus is on final states with ISR. Particularly for supersymmetric final state topologies with jets produced from heavy parent superparticles we focus on a high momentum of the ISR-system.

In Section 4, it is noted that detectors such as ATLAS and CMS provide no information about the z-component of the missing energy, and that the pseudorapidity rule addresses this issue. For compressed scenarios, the Recursive Jigsaw Reconstruction technique focuses on the transverse plane. This is performed by setting to zero all the z-component momenta as shown in the subsequent chapters. It is roughly the same as using special relativity with only two dimensions of space. All the momenta, energies, masses and frames should be labelled as transverse, nevertheless the subscript T is often omitted.

To be more precise, in the compressed regime, the RJR technique leverages cases with initial state radiation where the transverse momentum of the ISR-system causes the SUSY-system to recoil against it in the transverse plane, enhancing the transverse momenta of the visible and invisible decay products.

Compressed kinematics in the presence of ISR: first approximation

In the limit of nearly degenerate masses, $M_{\tilde{P}} \sim M_{\tilde{\chi}}$, a very rough approximation in the *Lab* frame can be computed [9]

$$\vec{p}_{\tilde{\chi}}^{\,Lab} \sim \frac{M_{\tilde{\chi}}}{M_{\tilde{P}}} \vec{p}_{\tilde{P}}^{\,Lab}. \tag{4.6.2}$$

With this approximation the missing transverse momentum and the transverse momentum of the ISR-system are related by a simple rule. Combining for the two LSPs

$$\vec{p}_{1\tilde{\chi}}^{\,Lab} + \vec{p}_{2\tilde{\chi}}^{\,Lab} \sim \frac{M_{\tilde{\chi}}}{M_{\tilde{P}}} \vec{p}_{1\tilde{P}}^{\,Lab} + \frac{M_{\tilde{\chi}}}{M_{\tilde{P}}} \vec{p}_{2\tilde{P}}^{\,Lab} \tag{4.6.3}$$

[9]The transverse view of the event implies all the momenta, reconstructed masses, energies and reference frames should be labelled transverse, but the subscript T is often omitted.

and assuming for the vectorial sum of the transverse momentum of the two $\tilde{\chi}$ the value $\vec{\not{E}}_T$ reconstructed by the detector, the relation

$$\vec{\not{E}}_T \sim -\frac{M_{\tilde{\chi}}}{M_{\tilde{P}}}\vec{p}_{T,ISR} \tag{4.6.4}$$

is valid in the absence of additional weakly interacting particles.

For compressed scenarios most of the transverse momentum of the ISR-system is expected to result in $\vec{\not{E}}_T$. In the presence of a non negligible transverse momentum of the ISR-system the absolute scale can be investigated (being that the ratio of the masses is roughly the ratio $\not{E}_T/p_{T,ISR}$).

Recent studies for probing supersymmetric topologies in the compressed regime have suggested exploiting this feature [118–120]. In these analyses, a kinematic selection is used to isolate events where a single, hard ISR jet recoils approximately opposite to $\vec{\not{E}}_T$ in the event transverse plane. One can then use various reconstructed proxies of $p_{T,ISR}$, such as the leading jet or $\sqrt{H_T}$, and use observables such $\not{E}_T/p_T^{\mathrm{lead-jet}}$ or $\not{E}_T/\sqrt{H_T}$ in order to be sensitive to the presence of massive LSPs [118, 119].

Alternatively, using assumed knowledge of the sparticle mass-splittings, one can attempt to sort non-ISR jets from radiative ones using, for example, the sum of jet energies in each class and multiplicities as discriminating observables [120].

Choosing the subset of events where the momentum of the ISR-system is carried predominantly by a single clean high-momentum jet radiated in the initial state limits the available event sample. For less restrictive event selections, the suggested observables become progressively less accurate estimators of $\not{E}_T/p_{T,ISR}$. Furthermore, low-momentum jets produced by other radiation or underlying events, such as pile-up, exacerbate the difficulty in the discrimination between the “ISR-jets” with respect to the “signal jets” when an *a priori* knowledge of the mass difference is used.

Compressed kinematics in the presence of ISR: a more careful examination

In the next section, the RJR technique for the compressed scenario is described. Here a more careful examination of the approximate relation given by Eq. 4.6.4 is shown.

Assume an ideal detector capable of reconstructing all of the visible objects and the sum of the invisible particle momenta with infinitesimal resolutions. Consider this detector blind to the longitudinal values of the momenta, or, in other words, we focus on the transverse view of the event. For such a detector, the *transverse* centre-of-mass frame, CM, of the $ISR + \tilde{P}\tilde{P}$ system coincides with the *Lab* frame. Assuming the case of two identical parent superparticles, $M_{\tilde{P}_1} = M_{\tilde{P}_2}$, each decaying to a visible particle and an invisible LSP, $\tilde{\chi}$, the expression

$$\vec{\not{E}}_T \cdot \hat{\beta}_{\tilde{P}\tilde{P}} = (\bar{p}_{\tilde{\chi}1} + \bar{p}_{\tilde{\chi}2}) \cdot \hat{\beta}_{\tilde{P}\tilde{P}}, \tag{4.6.5}$$

is satisfied in the *Lab* frame, where $\hat{\beta}_{\tilde{P}\tilde{P}}$ is the unit vector for the velocity defining the Lorentz boost from *Lab* to the $\tilde{P}\tilde{P}$ centre-of-mass frame: $\bar{\beta}_{\tilde{P}\tilde{P}} = \beta_{\tilde{P}\tilde{P}}\hat{\beta}_{\tilde{P}\tilde{P}}$.[10] Introduced in Eq. 4.2.3, the velocity for the Lorentz contra-boosts from $\tilde{P}\tilde{P}$ to each $\tilde{P}$ rest frame is here rewritten $\bar{\beta}^{\tilde{P}\tilde{P}}_{\tilde{P}_1} = \beta_c\hat{\beta}^{\tilde{P}\tilde{P}}_{\tilde{P}} = -\bar{\beta}^{\tilde{P}\tilde{P}}_{\tilde{P}_2}$ and Eq. 4.6.5 can be expressed as

$$\begin{aligned}
\vec{\not{E}}_T \cdot \hat{\beta}_{\tilde{P}\tilde{P}} &= \gamma_{\tilde{P}\tilde{P}}\beta_{\tilde{P}\tilde{P}}\left(E^{\tilde{P}\tilde{P}}_{\tilde{\chi}1} + E^{\tilde{P}\tilde{P}}_{\tilde{\chi}2}\right) + \gamma_{\tilde{P}\tilde{P}}\left(\bar{p}^{\tilde{P}\tilde{P}}_{\tilde{\chi}1} + \bar{p}^{\tilde{P}\tilde{P}}_{\tilde{\chi}2}\right)\cdot\hat{\beta}_{\tilde{P}\tilde{P}} \\
&= \gamma_{\tilde{P}\tilde{P}}\beta_{\tilde{P}\tilde{P}}\gamma_c\left(E^{\tilde{P}_1}_{\tilde{\chi}1} + E^{\tilde{P}_2}_{\tilde{\chi}2}\right) + \gamma_{\tilde{P}\tilde{P}}\beta_{\tilde{P}\tilde{P}}\gamma_c\beta_c\left(\bar{p}^{\tilde{P}_1}_{\tilde{\chi}1} - \bar{p}^{\tilde{P}_2}_{\tilde{\chi}2}\right)\cdot\hat{\beta}^{\tilde{P}\tilde{P}}_{\tilde{P}} \\
&\quad + \gamma_{\tilde{P}\tilde{P}}\left(\bar{p}^{\tilde{P}_1}_{\tilde{\chi}1} + \bar{p}^{\tilde{P}_2}_{\tilde{\chi}2}\right)\cdot\hat{\beta}_{\tilde{P}\tilde{P}} \\
&\quad + \gamma_{\tilde{P}\tilde{P}}\left(\gamma_c - 1\right)\left(\hat{\beta}_{\tilde{P}\tilde{P}}\cdot\hat{\beta}^{\tilde{P}\tilde{P}}_{\tilde{P}}\right)\left(\bar{p}^{\tilde{P}_1}_{\tilde{\chi}1} + \bar{p}^{\tilde{P}_2}_{\tilde{\chi}2}\right)\cdot\hat{\beta}^{\tilde{P}\tilde{P}}_{\tilde{P}}
\end{aligned}. \tag{4.6.6}$$

Since a perfect symmetry between the two hemispheres is assumed, with same masses for the two parent superparticles and for the two LSPs, the relation $E^{\tilde{P}_1}_{\tilde{\chi}1} = E^{\tilde{P}_2}_{\tilde{\chi}2} = E^{\tilde{P}}_{\tilde{\chi}}$ is satisfied and used in Eq. 4.6.6.

Furthermore, we can write $\bar{p}^{\tilde{P}_1}_{\tilde{\chi}1} = p^{\tilde{P}}_{\tilde{\chi}}\hat{p}^{\tilde{P}_1}_{\tilde{\chi}1}$ and $\bar{p}^{\tilde{P}_2}_{\tilde{\chi}2} = p^{\tilde{P}}_{\tilde{\chi}}\hat{p}^{\tilde{P}_2}_{\tilde{\chi}2}$, and in the limit of $p^{\tilde{P}}_{\tilde{\chi}} \ll M_{\tilde{\chi}}$,

[10] As usual, when not specified, the frame of reference is *Lab* and vectors are two-dimensional objects in the transverse plane.

the approximations $E_{\tilde{\chi}}^{\tilde{P}} \sim M_{\tilde{\chi}}[1 + \frac{1}{2}(\frac{p_{\tilde{\chi}}^{\tilde{P}}}{M_{\tilde{\chi}}})^2 + \ldots] \sim M_{\tilde{\chi}}$ and $\frac{p_{\tilde{\chi}}^{\tilde{P}}}{E_{\tilde{\chi}}^{\tilde{P}}} \sim [\frac{p_{\tilde{\chi}}^{\tilde{P}}}{M_{\tilde{\chi}}} - \frac{1}{2}(\frac{p_{\tilde{\chi}}^{\tilde{P}}}{M_{\tilde{\chi}}})^3 + \ldots] \sim \frac{p_{\tilde{\chi}}^{\tilde{P}}}{M_{\tilde{\chi}}}$ are valid. We substitute the contra-boost factor introduced in Eq.4.4.21, $\gamma_c = M_{\tilde{P}\tilde{P}}/2M_{\tilde{P}}$[11], and

$$\beta_{\tilde{P}\tilde{P}} = \frac{p_T^{ISR}}{E_{\tilde{P}\tilde{P}}} = \frac{p_T^{ISR}}{\sqrt{\left(p_T^{ISR}\right)^2 + M_{\tilde{P}\tilde{P}}^2}}, \qquad \gamma_{\tilde{P}\tilde{P}}\beta_{\tilde{P}\tilde{P}} = \frac{p_T^{ISR}}{M_{\tilde{P}\tilde{P}}} \tag{4.6.7}$$

in Eq 4.6.6. Neglecting $\mathcal{O}[(\frac{p_{\tilde{\chi}}^{\tilde{P}}}{M_{\tilde{\chi}}})^2]$ terms we have

$$\begin{aligned}\frac{\vec{\not{E}}_T\cdot\hat{\beta}_{\tilde{P}\tilde{P}}}{p_T^{ISR}} \sim \quad & \frac{M_{\tilde{\chi}}}{M_{\tilde{P}}} + \frac{p_{\tilde{\chi}}^{\tilde{P}}}{2M_{\tilde{P}}}\beta_c\left(\hat{p}_{\tilde{\chi}1}^{\tilde{P}_1} - \hat{p}_{\tilde{\chi}2}^{\tilde{P}_2}\right)\cdot\hat{\beta}_{\tilde{P}}^{\tilde{P}\tilde{P}} \\ & + \frac{p_{\tilde{\chi}}^{\tilde{P}}}{2M_{\tilde{P}}}\frac{\sqrt{\left(p_T^{ISR}\right)^2+M_{\tilde{P}\tilde{P}}^2}}{p_T^{ISR}}\gamma_c^{-1}\left(\hat{p}_{\tilde{\chi}1}^{\tilde{P}_1} + \hat{p}_{\tilde{\chi}2}^{\tilde{P}_2}\right)\cdot\hat{\beta}_{\tilde{P}\tilde{P}} \\ & + \frac{p_{\tilde{\chi}}^{\tilde{P}}}{2M_{\tilde{P}}}\frac{\sqrt{\left(p_T^{ISR}\right)^2+M_{\tilde{P}\tilde{P}}^2}}{p_T^{ISR}}\left(\frac{\gamma_c-1}{\gamma_c}\right)\left(\hat{\beta}_{\tilde{P}\tilde{P}}\cdot\hat{\beta}_{\tilde{P}}^{\tilde{P}\tilde{P}}\right)\left(\hat{p}_{\tilde{\chi}1}^{\tilde{P}_1} + \hat{p}_{\tilde{\chi}2}^{\tilde{P}_2}\right)\cdot\hat{\beta}_{\tilde{P}}^{\tilde{P}\tilde{P}}\end{aligned}, \tag{4.6.8}$$

where the second and forth contributions, with factors β_c and $\frac{\gamma_c-1}{\gamma_c}$ respectively, are expected to be relatively small, while the third contribution tends asymptotically to $\frac{p_{\tilde{\chi}}^{\tilde{P}}}{2M_{\tilde{P}}}$ for $p_T^{ISR} \gg M_{\tilde{P}\tilde{P}}$ except for a combination of unit vectors.

Indeed, in the extreme compressed regime ($M_{\tilde{\chi}} \sim M_{\tilde{P}}$), the asymptotic behaviours $\beta_c \to 0$, $\gamma_c \to 1$ and

$$\frac{\vec{\not{E}}_T\cdot\hat{\beta}_{\tilde{P}\tilde{P}}}{p_T^{ISR}} \sim \frac{M_{\tilde{\chi}}}{M_{\tilde{P}}} + \frac{p_{\tilde{\chi}}^{\tilde{P}}}{2M_{\tilde{P}}}\left[\frac{\sqrt{\left(p_T^{ISR}\right)^2 + M_{\tilde{P}\tilde{P}}^2}}{p_T^{ISR}}\left(\hat{p}_{\tilde{\chi}1}^{\tilde{P}_1} + \hat{p}_{\tilde{\chi}2}^{\tilde{P}_2}\right)\cdot\hat{\beta}_{\tilde{P}\tilde{P}}\right] \tag{4.6.9}$$

are expected, with the first contribution close to one and the second term non negligible for $p_T^{ISR} \ll M_{\tilde{P}\tilde{P}}$. The expression given in Eq. 4.6.8, and this last approximation, can be seen as the SUSY mass ratio first term plus corrections proportional to the momentum of the LSP in the parent sparticle frame and inversely proportional to the SUSY mass

[11] Here $\gamma_c = M_{\tilde{P}\tilde{P}}/2M_{\tilde{P}}$ refers to the ratio of the true masses, while Eq.4.4.21 refers to the the ratio of the observables reconstructed by the RJR technique event-by-event.

scale:

$$\frac{\left|\vec{\not{E}}_T \cdot \hat{p}_T^{ISR}\right|}{p_T^{ISR}} \sim \frac{M_{\tilde{\chi}}}{M_{\tilde{P}}} + \mathcal{O}\left(\frac{p_{\tilde{\chi}}^{\tilde{P}}}{2M_{\tilde{P}}}\right)\left(\frac{\sqrt{\left(p_T^{ISR}\right)^2 + M_{\tilde{P}\tilde{P}}^2}}{p_T^{ISR}}\right)\sin\Omega, \tag{4.6.10}$$

where $\hat{\beta}_{\tilde{P}\tilde{P}} = -\hat{p}_T^{ISR}$ is valid assuming a transverse view of the event. The quantity $\sin\Omega$ represents a function of dot products between the velocities relating the laboratory frame, the $\tilde{P}\tilde{P}$ frame, and $\tilde{P}$ rest frames and the directions of the LSP momenta in their respective production frames. For extreme compressed scenarios $\sin\Omega$ is independent of the contra-boost direction $(\hat{\beta}_{\tilde{P}}^{\tilde{P}\tilde{P}})$ and is expected to be zero on average when nontrivial spin correlations are absent.

4.6.2 The compressed RJR tree

In the compressed regime, the focus is on final state topologies with one or more additional radiations from the initial state. The Recursive Jigsaw Reconstruction technique is based on a simplified tree assuming a transverse decay view of the event.

The *compressed* decay tree specifies both the systems of relevant reconstructed objects and the *transverse* reference frames. The tree is simple and generic for any compressed topology as shown in Figure 4.6.1.

In the compressed decay tree CM represents the centre-of-mass system of the whole reaction S+ISR, ISR is the system assigned to the radiation from the initial state, and S is the signal or sparticle system decaying to visible and invisible products in the V and I systems. In each event, the missing transverse momentum is assigned to the I-system, while reconstructed objects are assigned to the V-system or to the ISR-system. The jigsaw rules specify those hypothesised to come from the decay of sparticles and assigned to the V-system as opposed to those identified as initial state radiation and associated with ISR.

For an ideal detector the *Lab* frame coincides with the CM frame, nevertheless herein we

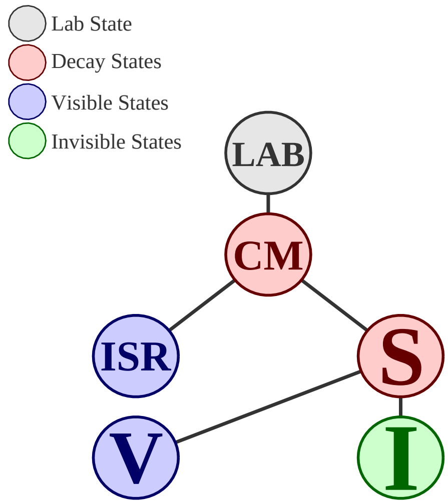

Figure 4.6.1: The compressed decay tree: Lab is the laboratory system, CM is the centre-of-mass system (S+ISR), ISR is the initial state radiation system, S is the signal or sparticle system, V is the visible system and I the invisible system.

emphasise the distinction because the final states of compressed topologies are expected to be rich in low momentum objects. The transverse momentum of the CM frame is not zero mainly due to the energy not reconstructed in the objects:

$$\vec{p}_T(\mathrm{CM}) = \vec{\not{E}}_T + \sum_i \vec{p}_T(o_i) \tag{4.6.11}$$

with i objects reconstructed from the detector in the event.

The full substructure of the SUSY topology is not defined and a basis of useful observables utilised for the analyses are defined in the CM frame as shown in the next section. The jigsaw rules associated to the compressed tree are simple. The transverse view of the event is equivalent to set all the z-momenta to zero $\vec{p}_z(o_i) = 0$. The mass of the invisible system is set to zero: all the weakly interacting particles are treated as a unique massless object. When identical objects, such as jets resulting from the fragmentation of light quarks, can be associated both to the V and the ISR-system a combinatoric rule is applied. The hadronic final state ambiguity due to the provenance of reconstructed jets, is addressed by a rule based on the minimisation of the masses, analogous to the one described in Section 4.5.2, to separate the ISR-system with respect to the SUSY system. Objects different from the light jets can be forced into the V-system, or assigned with a minimisation of the masses, or with a combination of the two strategies and the final resulting rule will be specified analysis-by-analysis for the topology investigated.

What do minimisations of the masses mean for the compressed tree?

Consider a final state with all identical objects and missing transverse momentum. In the true centre-of-mass frame the relation

$$M_{CM} = \sqrt{M_S^2 + p^2} + \sqrt{M_{ISR}^2 + p^2} \tag{4.6.12}$$

is valid and event-by-event, $M_{CM} \equiv E_{CM}$ is a fixed value, which for an ideal detector is equivalent to $E_{Lab} \equiv \sqrt{s_{par-par}}$. Minimising M_s and M_{ISR} means maximising the momentum p.

In the compressed tree the missing transverse momentum is a massless two-dimensional momentum object assigned to the I-system and so to the S-system, because I inherits from S. The other reconstructed objects are combined by minimising the invariant masses in a generalisation of Eq. 4.5.2 with at least one object assigned to the ISR-system. Assuming a transverse view of the event, the combinatoric rule, translates to a maximisation of the transverse momentum of the ISR or S-system ($\vec{p}^{\,\rm CM}_{\rm S,\it T} = -\vec{p}^{\,\rm CM}_{\rm ISR,\it T}$). The result of this jigsaw rule is equivalent to an estimate of the thrust axis in the CM frame.

4.6.3 Compressed variables

In this section a collection of kinematic observables which can be used to probe compressed scenarios is described. A detailed description is provided for the RJR observable used as a proxy for the ratio $\not{E}_T/p_T^{ISR}$. This scaleless variable is defined as follows:

$$R_{\text{ISR}} \equiv \frac{\left|\vec{p}_{\text{I},T}^{\,\text{CM}} \cdot \hat{p}_{\text{ISR},T}^{\text{CM}}\right|}{p_{\text{ISR},T}^{\text{CM}}}, \tag{4.6.13}$$

where subscripts indicate the system and superscripts the reference frame the momentum is evaluated in. It is the ratio between the projection of the transverse momentum of the invisible system to the S-system and the magnitude of the transverse momentum of the S-system, being $\vec{p}_{\text{ISR},T}^{\,\text{CM}} = -\vec{p}_{\text{S},T}^{\,\text{CM}}$. This is the same quantity given by the Eq. 4.6.10. For a realistic detector with the CM=ISR+$\tilde{P}\tilde{P}$ frame different from the laboratory reference frame and in the limit of a low-momentum of the LSP in the parent sparticle rest frame $p_{\tilde{\chi}}^{\tilde{P}}$ with respect to the parent sparticle mass $M_{\tilde{P}}$, the ratio R_{ISR} is

$$R_{\text{ISR}} \sim \frac{M_{\tilde{\chi}}}{M_{\tilde{P}}} + \mathcal{O}\left(\frac{p_{\tilde{\chi}}^{\tilde{P}}}{2M_{\tilde{P}}}\right)\left(\frac{\sqrt{\left(p_T^{ISR}\right)^2 + M_{\tilde{P}\tilde{P}}^2}}{p_T^{ISR}}\right)\sin\Omega. \tag{4.6.14}$$

The order one dot products between the velocities relating the CM frame, the $\tilde{P}\tilde{P}$ rest frame, and $\tilde{P}$ rest frames summarised by $\sin\Omega$ are zero on average in the absence of non-trivial spin correlations or efficiency dependence from decay product reconstruction and selection.

The behaviour expected is a distribution peaked at $\frac{M_{\tilde{\chi}}}{M_{\tilde{P}}}$ with a theoretical width of order $\mathcal{O}\left(\frac{p_{\tilde{\chi}}^{\tilde{P}}}{2M_{\tilde{P}}}\right)$ in the limit $p_T^{ISR} \gg M_{\tilde{P}\tilde{P}}$. The resolution of order $\mathcal{O}\left(\frac{p_{\tilde{\chi}}^{\tilde{P}}}{2M_{\tilde{P}}}\right)$ can be approximated for a parent sparticle decaying in a LSP and a Standard Model object with negligible mass to $\mathcal{O}(\frac{M_{\tilde{P}}^2 - M_{\tilde{\chi}}^2}{4M_{\tilde{P}}^2})$ using Eq. 4.6.1, while for a multi-body decay to $\mathcal{O}(\frac{M_{\tilde{P}}^2 - M_{\tilde{\chi}}^2 + m_{o_i}^2}{4M_{\tilde{P}}^2})$ with $m_{o_i}^2$ the invariant mass of the i objects.

In order to elucidate the behaviour of R_{ISR}, consider a case with no ambiguity between the ISR and S-systems. As an example, a pair of heavy neutralinos (for example $\tilde{\chi}_2^0$) are produced at a hadron collider with decays $\tilde{\chi}_2^0\tilde{\chi}_2^0 \to Z(l^+l^-)\tilde{\chi}_1^0, h(\gamma\gamma)\tilde{\chi}_1^0$. Two leptons and two photons are required to be reconstructed in each event and are assigned to the V-system, $\vec{\not{E}}_T$ to the I-system and one or more reconstructed jets are associated to the

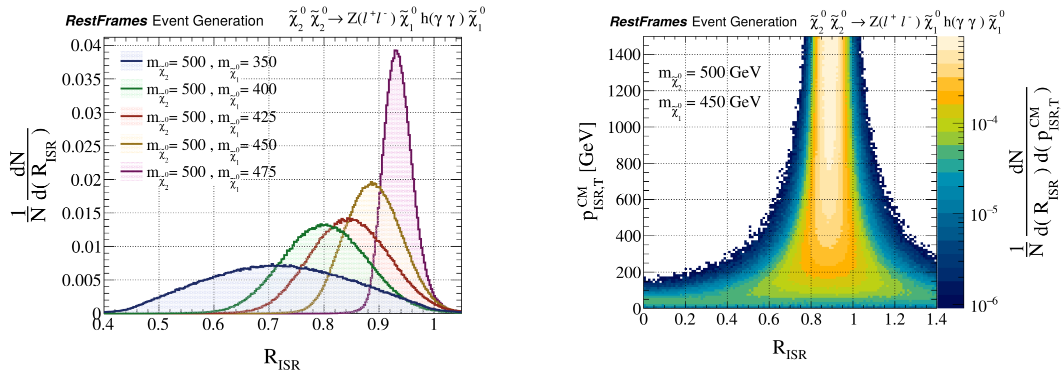

Figure 4.6.2: The left figure shows the normalised distribution of R_{ISR} for the production and decay of $\tilde{\chi}_2^0\tilde{\chi}_2^0 \to Z(l^+l^-)\tilde{\chi}_1^0, h(\gamma\gamma)\tilde{\chi}_1^0$ at the 13 TeV LHC for different masses of the LSP and $M_{\tilde{P}}$=500 GeV. The figure on the right refers to the two-dimensional distribution of $p^{\text{CM}}_{\text{ISR},T}$ as a function of the ratio for the sample with $\triangle M$= 50 GeV. Figures from [111]. Simulated *particle-level* events are generated and analysed using the RestFrames software package [117].

ISR-system.

As shown in Figure 4.6.2, the R_{ISR} distribution for these events scales with ratio $\frac{M_{\tilde{\chi}}}{M_{\tilde{P}}}$, as expected from Eq. 4.6.14, with increasingly fine resolution for progressively smaller mass-splittings between the two sparticle states. Similarly, the resolution of the kinematic feature improves with increasing ISR transverse momentum.

The absolute value of the transverse momentum of the ISR-system evaluated in the CM frame $p^{\text{CM}}_{\text{ISR},T}$ is another RJR observable. Its distribution is expected to be related to the hard scale of the process investigated. In particular, the heavier the parent superparticles produced at the proton collider (and hence the LSP for compressed scenarios) in the final state, the more the observables should discriminate SM backgrounds.

Other masses and angles constitute a basis of complementary observables. Different observables are useful for the investigation of different topologies and different hard scales.

The variables that can be extracted from all the compressed scenarios are the follow:

- $R_{\text{ISR}} = \frac{\left|\vec{p}^{\,\text{CM}}_{\text{I},T} \cdot \hat{p}^{\text{CM}}_{\text{ISR},T}\right|}{p^{\text{CM}}_{\text{ISR},T}}$: variable sensitive to the mass ratio parent/LSP.

- $p^{\text{CM}}_{\text{ISR},T}$: modules of the jets vector-sum transverse momentum of the ISR-system evaluated in the CM frame.
- M^{S}_T: transverse mass of the S-system (V+I).
- M^{V}_T: transverse mass of the V-system.
- $\Delta\phi_{\text{ISR,I}}$: opening angle between the ISR-system and the I-system, evaluated in the CM frame.
- $\Delta\phi_{\text{CM,I}}$: opening angle between the CM system and the I-system.

Once the ISR-system is separated from the S-system other more conventional and *system-related* variables can be used.

A specific example is once again useful to understand this concept. Consider a variation of the previous topology with an Higgs boson decaying to bottoms: $\tilde{\chi}^0_2\tilde{\chi}^0_2 \rightarrow Z(l^+l^-)\tilde{\chi}^0_1, h(bb)\tilde{\chi}^0_1$. Suppose that the separation between the ISR-system and the S-system is made forcing the leptons into V and assigning the jets minimising the masses; independently if tagged or not as bottom. The supersymmetric final state topology has two b-jets and hence, for signal events, the b-jets multiplicity in the V-system is expected to be higher than in the ISR-system. Different criteria based on the object multiplicities can be applied in the ISR and V systems in order to discriminate the SM backgrounds. In this example a b-jet veto in the ISR-system and a requirement of at least one b-jet in the V-system could be a reasonable choice.

These additional system-related handles are topology dependent. The possibilities are quite vast and can be summarised as follow:

- $N^{\text{V}}_{o_i}$: number of objects of type i in the V-system
- $N^{\text{ISR}}_{o_i}$: number of objects of type i in the ISR-system
- $p^{\text{V}}_{o_{ji},T}$: transverse momentum of the j-th object of type i in the V-system

- $p^{\mathrm{ISR}}_{o_{ji},T}$: transverse momentum of the j-th object of type i in the ISR-system
- $M^{\mathrm{V}}_{o_i o_j}$:invariant mass of the i-j objects in the V-system
- $\Delta\phi_{\mathrm{ISR},o_i}$: opening angle between the ISR-system and a specific object in the CM or Lab frame.
- $\Delta\phi_{\mathrm{I},o_i}$: opening angle between the I-system and a specific object in the CM or Lab frame.

The Standard Model objects o of different type i (o_i) are the same as described in Section 3.4.2.[12]

[12]The choice illustrated in the example considered would be $N^{\mathrm{V}}_{b-\mathrm{jet}} \geq 1$ and $N^{\mathrm{ISR}}_{b-\mathrm{jet}} = 0$.

Chapter 5

Sparticles in Motion

5.1 Introduction

This chapter is dedicated to the study "Sparticles in Motion - Analyzing compressed SUSY scenarios with a new method of event reconstruction" [111]. In this paper the approach for the analyses of supersymmetric compressed spectra is based on the generic RJR compressed tree described in Section 4.6.2. Compressed scenarios of squark and gluino pair-production topologies are investigated. The focus is on mass-splittings between parent super-particles and their lightest decay products between 25 and 200 GeV.

In the case of a final state topology with all the objects identifiable by their type and different from jets, there is no ambiguity: the reconstructed objects expected to come from sparticle decays are assigned to the V-system, while jets are assigned to the ISR-system. For final state topologies involving light jets a combinatoric rule is necessary to solve the ambiguity. When jets are tagged as b, τ or fat both strategies can be adopted and the choice depends on the multiplicity of the objects, efficiency and inefficiency for the detector to tag or mis-tag the object, the behaviour expected for the main backgrounds and so on.

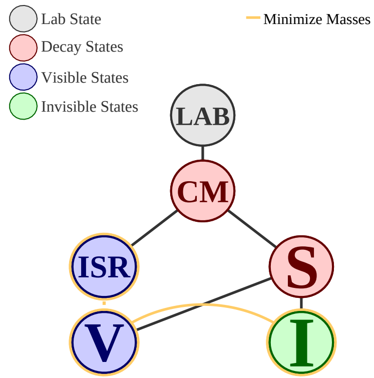

Figure 5.1.1: The compressed decay tree: Lab is the laboratory system, CM is the centre-of-mass system (S+ISR), ISR is the initial state radiation system, S is the signal or sparticle system, V is the visible system and I the invisible system. The visible objects are assigned between the ISR and V-system using a jigsaw rule based on the minimisation of the masses.

In this study, probably the *worst* scenario is considered: the final state topologies involve only identical light jets and missing transverse momentum and a complete ambiguity is due to the assignment of reconstructed jets. Figure 5.1.1 shows the compressed tree and the jigsaw rule used to distinguish between the ISR and V objects. Once $\vec{\not{E}}_T$ is assigned to the I-system the light jets are assigned to the appropriate system minimising the masses.

The samples of all major Standard Model backgrounds are proton-proton collisions simulated at 14 TeV as part of the Snowmass study. All signal and BG samples are generated-simulated using the same versions and data-cards of Madgraph + Pythia + Delphes with jet-parton matching and corrections for next-to-leading order (NLO) contributions. The specifics are described in Section 3.4.

The signal samples are the simplified topologies in Figure 5.1.2 generated within the mass ranges $0.5\,\text{TeV} \leq M_{\tilde{g}} \leq 1.4\,\text{TeV}$ and $0.5\,\text{TeV} \leq M_{\tilde{q}} \leq 1\,\text{TeV}$, with intervals of 100 GeV for the parent sparticle masses and with four mass splittings $\Delta M = M_{\tilde{P}} - M_{\tilde{\chi}} = 25, 50, 100$ and 200 GeV. The cross sections for gluino and squark pair-production with the other superparticles decoupled at $\sqrt{s}$=14 TeV can be found in Ref. [121].

All the signal and background samples are passed to the algorithm summarised by

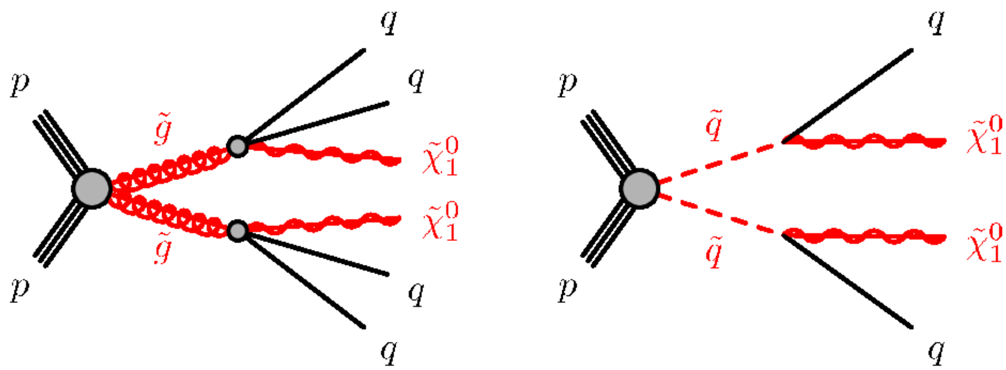

(a) Gluino pair-production in a final state with four light jets and MET.

(b) Squark pair-production in a final state with two light jets and MET.

Figure 5.1.2: Feynman diagrams for the simplified topologies of gluino and squark pair-production in final state with light jets and missing transverse momentum.

the compressed tree in Figure 5.1.1 and event-by-event the basis of RJR variables is extracted and analysed for a projection of $\int \mathcal{L} = 100\,\text{fb}^{-1}$.

In Section 5.2 the distributions of the main RJR observables used are described, while in Section 5.3 the necessity to focus on the high ISR-regime for this analysis is shown. In Section 5.4 the signal regions defined with the compressed RJR observables are described and in Section 5.5 the results obtained are shown.

5.2 Preselection criteria

In this section the distribution of the compressed RJR observables are shown for the events satisfying minimal preselection criteria. The signal final state topologies investigated are expected with no leptons and a veto is applied for electrons and muons. A minimal value for the missing transverse momentum is required: $\not{E}_T > 100$ GeV, while all the jets reconstructed from the detector with $p_T^{\text{jet}} > 20$ GeV are considered. No criteria are applied to fat or tau tagged jets, while a b-jet veto will be applied to all the jets in the final states.

The observables used in the analysis and described in the Section 4.6.3 are the generic

Category	Snowmass label (sub-categories description)
Boson + jets	BJ-BJJ (Vector boson + jets, vector boson fusion)
$t\bar{t}$ (+V)	TT, TTB (Top pair +jets, top pair plus bosons: $t\bar{t}$+Z, $t\bar{t}$+W and $t\bar{t}$+h + jets)
single top	TJ-TB (Single top + jets, top pair (off shell $t^* \to Wj$) + jets)
Di-/Tri-Boson	BBB-BB-BLL-B-LL (tri-Vector + jets, Di-Vector + jets, Drell-Yan in leptons)
Higgs	H(Gluon fusion + jets)

Table 5.1: Five categories summarizing all the main Standard Model backgrounds as part of the Snowmass study. The category name is indicative of the dominant sub-category backgrounds.

observables for the compressed tree [1] plus a couple of topology dependent variables.

Figures 5.2.1 and 5.2.2 show the distributions of the RJR observables sensitive to compressed scenarios for events that have satisfied the preselection criteria. All the Standard Model backgrounds are stacked together and categorised in five groups, while the overlaid dashed curves refer respectively to gluino and squark pair-production samples. The SM category names are explained in Table 5.1.

Figures 5.2.1a and 5.2.2a show the distributions of R_{ISR}. The variable provides little signal-to-background discrimination in the absence of more stringent selection criteria. The signal distributions are progressively closer to one for smaller mass splittings, while the $t\bar{t}$ background events tend to populate smaller values of the ratio with respect the other SM backgrounds. Notice that R_{ISR} cannot assume a value larger than one if all the objects are assigned minimising the masses.

Figures 5.2.1b and 5.2.2b show the distributions of $p^{\mathrm{CM}}_{\mathrm{ISR},T}$. The slopes are related to the hard scale, namely the mass of particles produced by the scattering of the two partons. They appear less severe for the signal samples , since $M_{\tilde{P}}$ is greater than the typical Standard Model mass scale.

The distributions of the jet multiplicities in the V-system are shown in Figures 5.2.1c

[1] Herein the transverse mass of the visible system M_T^{V} is not considered because the mass splitting scale is similar to typical Standard Model scales. Furthermore, the observable looses resolution when computed with jets momenta and particularly in cases of jets misassignment for signal events.

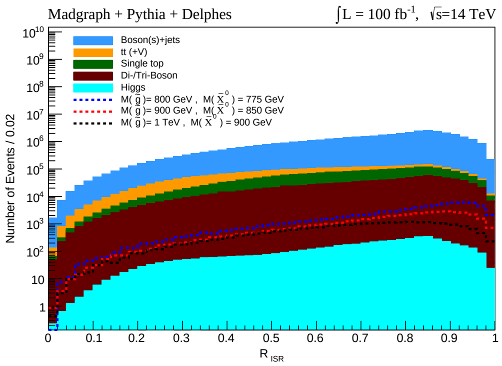

(a) Distribution of $R_{\text{ISR}} = \frac{|\vec{p}^{\,\text{CM}}_{\text{I},T} \cdot \hat{p}^{\text{CM}}_{\text{ISR},T}|}{p^{\text{CM}}_{\text{ISR},T}}$: variable sensitive to the mass ratio parent sparticle LSP

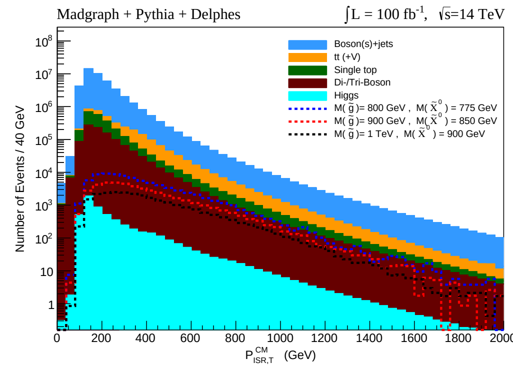

(b) Distribution of $p^{\text{CM}}_{\text{ISR},T}$: magnitude of the jets vector-sum transverse momentum of ISR-system evaluated in the CM frame

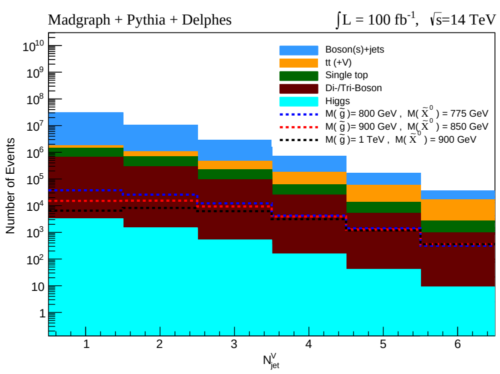

(c) Distribution of the $N^{\text{V}}_{\text{jet}}$: light jet multiplicity in the V-system.

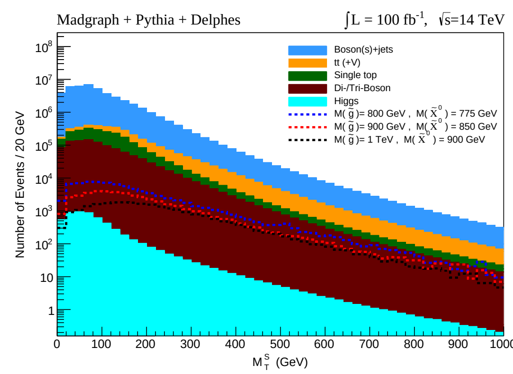

(d) Distribution of M^{S}_{T}: transverse mass of S-system (V+I).

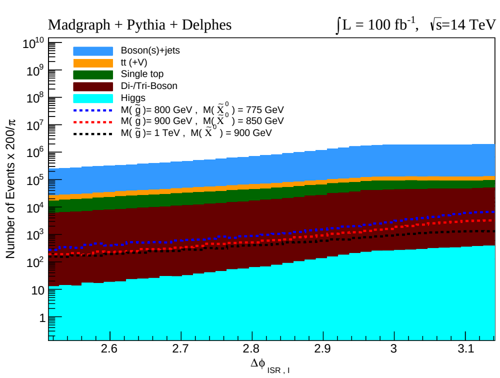

(e) Distribution of $\Delta\phi_{\text{ISR,I}}$: opening angle between the ISR-system and the I-system, evaluated in the CM frame.

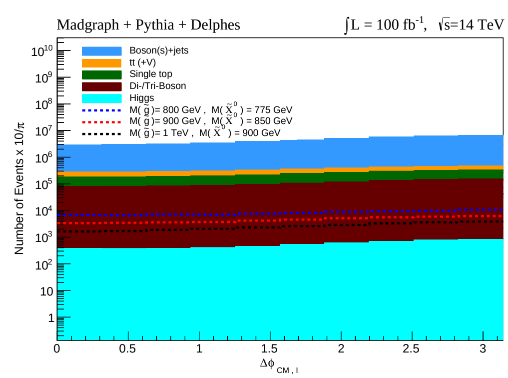

(f) Distribution of $\Delta\phi_{\text{CM,I}}$: opening angle between the CM system and the I-system.

Figure 5.2.1: Distribution of the RJR observables sensitive to compressed scenarios for events that have satisfied the preselection criteria (Table 5.2). Standard Model backgrounds are stacked together while the overlaid dashed curves refer to gluino pair-production samples. All the contributions are scaled with an integrated luminosity of 100 fb^{-1} at 14 TeV.

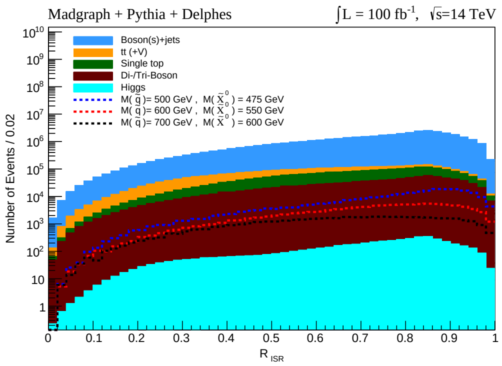

(a) Distribution of $R_{\text{ISR}} = \frac{|\vec{p}^{\,\text{CM}}_{\text{I},T} \cdot \hat{p}^{\text{CM}}_{\text{ISR},T}|}{p^{\text{CM}}_{\text{ISR},T}}$: variable sensitive to the mass ratio parent sparticle LSP

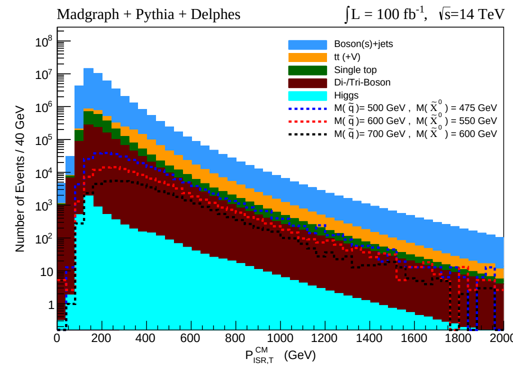

(b) Distribution of $p^{\text{CM}}_{\text{ISR},T}$: magnitude of the jets vector-sum transverse momentum of ISR-system evaluated in the CM frame

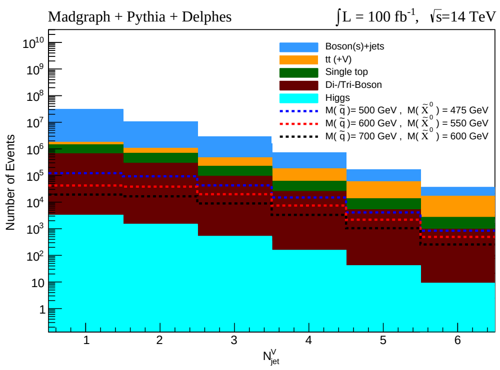

(c) Distribution of the N^{V}_{jet}: light jet multiplicity in the V-system.

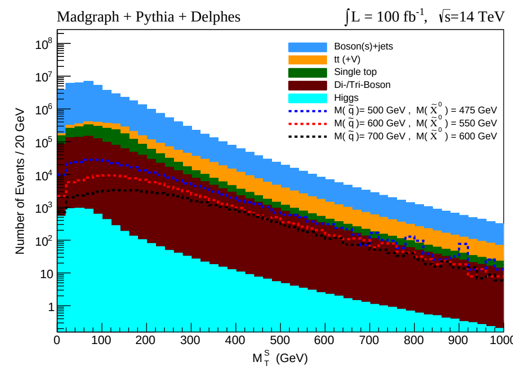

(d) Distribution of M^{S}_{T}: transverse mass of S-system (V+I).

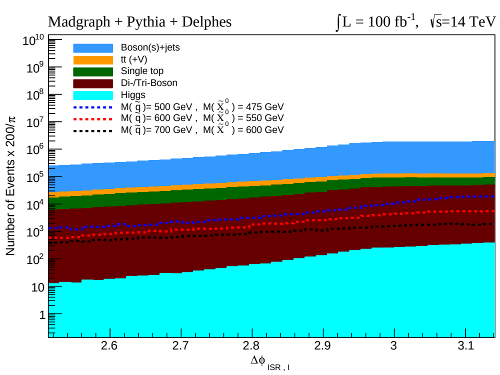

(e) Distribution of $\Delta\phi_{\text{ISR,I}}$: opening angle between the ISR-system and the I-system, evaluated in the CM frame.

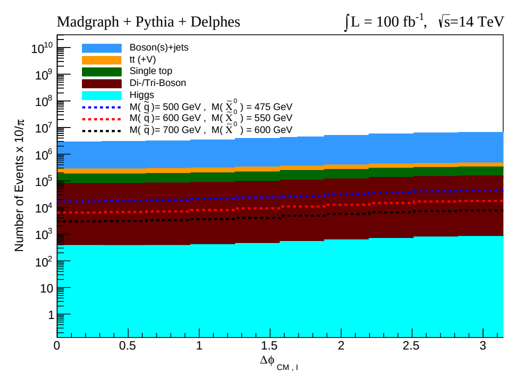

(f) Distribution of $\Delta\phi_{\text{CM,I}}$: opening angle between the CM system and the I-system.

Figure 5.2.2: Distribution of the RJR observables sensitive to compressed scenarios for events that have satisfied the preselection criteria (Table 5.2). Standard Model backgrounds are stacked together while the overlaid dashed curves refer to squark pair-production samples. All the contributions are scaled with an integrated luminosity of 100 fb^{-1} at 14 TeV.

and 5.2.2c. For the topologies investigated this observable is equivalent to the multiplicity of all the objects reconstructed in the V-system. The $t\bar{t}$ events tend to provide higher values than the other Standard Model backgrounds as expected.

Figures 5.2.1d and 5.2.2d are the distributions of M_T^{S} and little signal-to-background discrimination is provided in the absence of more stringent selection criteria. Signal distributions have a progressively more severe slope for smaller mass splittings: the observable is expected to have a higher discrimination impact for larger mass differences.

Figures 5.2.1e and 5.2.2e refer to the distributions of the opening angle between the ISR-system and the invisible system. Both signal and background distributions tend towards π, but the signal has a much stronger tendency to do so and this behaviour remains valid when more stringent criteria are required.

Finally, Figures 5.2.1f and 5.2.2f refer to the distributions of the opening angle between the CM system and the invisible system. This variable has no great impact for the topologies investigated. This is true both at the preselection level and after further selection criteria and will not be considered anymore.

5.3 High-ISR regime

In this section we focus on the high ISR regime, specifically $p_{\mathrm{ISR},T}^{\mathrm{CM}} > 800$ GeV. For the topologies investigated an high value of the transverse momentum of the ISR-system provides several advantages.

Firstly, in the study considered there is a complete ambiguity between the jets from the sparticle decay and those from the radiation in the initial state. The jigsaw rule, based on the minimisation of the masses, is progressively more efficient to distinguish the two jet categories increasing the minimal requirement on $p_{\mathrm{ISR},T}^{\mathrm{CM}}$.

Secondly, a high value for the transverse momentum of the ISR-system guarantees a focus on final states with real ISR as shown in the Feynman diagrams in Figure 5.3.1

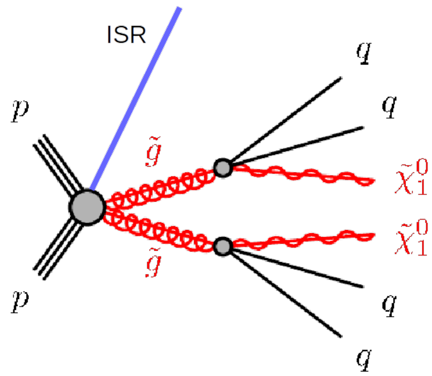

(a) Gluino pair-production in final state with light jets and $\not{E}_T$.

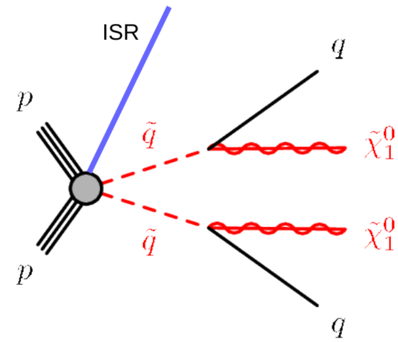

(b) Squark pair-production in final state with light jets and $\not{E}_T$.

Figure 5.3.1: Feynman diagrams for the simplified topologies of gluino and squark pair-production in final states with light jets and missing transverse momentum. To focus on final states with ISR we require a large value of $p^{\mathrm{CM}}_{\mathrm{ISR},T}$.

and the distributions of the RJR observables assume the behaviour expected for the signal samples.

Third, in the high ISR regime a moderate discrimination is provided by $p^{\mathrm{CM}}_{\mathrm{ISR},T}$: in Figures 5.2.1b and 5.2.2b we have seen how the slope of the distribution is less severe for the signal examples.

Finally, and most importantly, in the high ISR regime a peculiar feature appears due to the complementarity of $p^{\mathrm{CM}}_{\mathrm{ISR},T}$ with R_{ISR}. Figure 5.3.2 shows the distribution of $p^{\mathrm{CM}}_{\mathrm{ISR},T}$ as a function of the ratio R_{ISR} for a gluino (5.3.1a) and a squark (5.3.1b) sample. The behaviour is analogous to what we have seen in Figure 4.6.2. The resolution cannot be as good as that of a final state where all the objects in the V-system can be identified as products of the sparticle decays. This is due to the detector noise related to the physics of the jets, as discussed in Section 3.4.2, and the ambiguity in the assignment, particularly for jets from additional low-momentum radiation, between the V and ISR-system.

For the zero lepton Standard Model backgrounds the behaviour is completely different. Figure 5.3.3 shows how it is increasingly hard for the backgrounds to have a large value

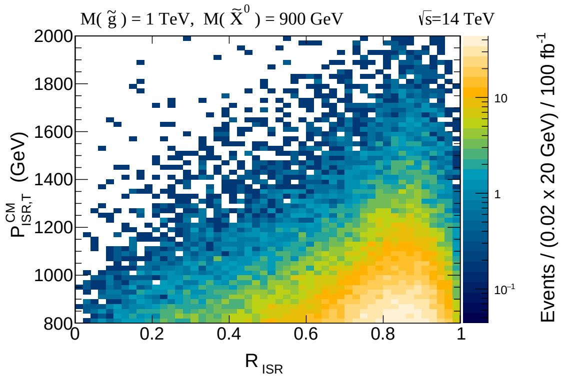

(a) Scatter plot R_{ISR} vs $p^{\mathrm{CM}}_{\mathrm{ISR},T}$ refers to the topology in Figure 5.3.1a with $M_{\tilde{g}} = 1$ TeV and $\Delta M = 100$ GeV.

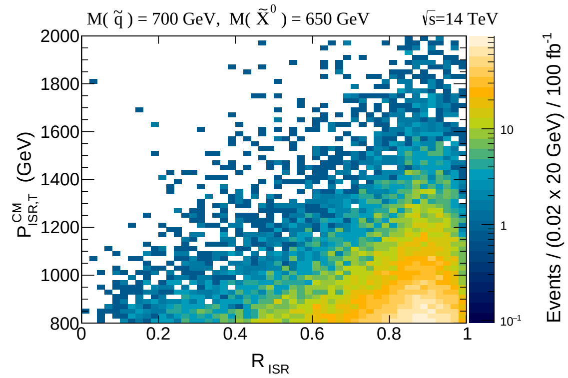

(b) Scatter plot R_{ISR} vs $p^{\mathrm{CM}}_{\mathrm{ISR},T}$ refers to the topology in Figure 5.3.1b with $M_{\tilde{q}} = 700$ GeV and $\Delta M = 50$ GeV.

Figure 5.3.2: Distribution of the $p^{\mathrm{CM}}_{\mathrm{ISR},T}$ as a function of R_{ISR} for gluino (a) and squark (b) signal samples. The two-dimensional histograms shows the number of events expected per bin for an integrated luminosity of 100 fb^{-1} satisfying the preselection criteria and $p^{\mathrm{CM}}_{\mathrm{ISR},T} > 800$ GeV.

of the ratio for higher values of $p^{\mathrm{CM}}_{\mathrm{ISR},T}$. In the high ISR regime the events for all the main backgrounds, vector boson + jets (Figure 5.3.3a) single top and $t\bar{t}$ (Figure 5.3.3b) and multi-bosons (Figure 5.3.3c), tend to populate low value of R_{ISR}.

For large values of $p^{\mathrm{CM}}_{\mathrm{ISR},T}$, the ratio R_{ISR} remains a proxy for the mass ratio parent sparticle to LSP and becomes an excellent discriminant between signal and background-like events.

The other compressed RJR observables are mainly orthogonal to the ratio R_{ISR}. This uncorrelation is shown in the two dimensional distributions in Figures 5.3.4-5.3.6 for the vector boson +jet, single top and tt and di-tri-bosons respectively. Figures 5.3.7 and 5.3.8 show the scatter plots of the RJR observables as a function of R_{ISR} for gluino and squark samples.

The complementarity of M_T^{S} with R_{ISR} is shown in Figures 5.3.4a-5.3.8a. When signal samples with larger mass-splittings are investigated the relaxation of the selection on R_{ISR} can be compensated by tightening the selection requirement on the transverse mass of the S-system.

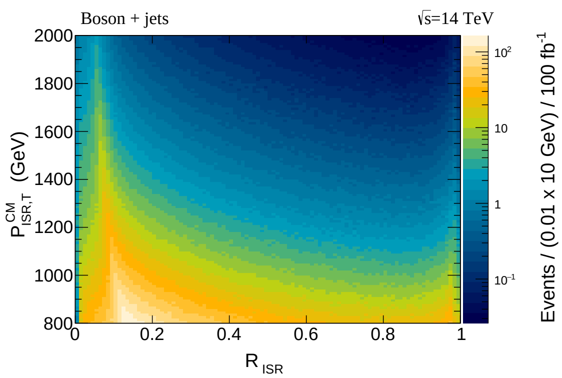

(a) The scatter plot R_{ISR} vs $p^{\text{CM}}_{\text{ISR},T}$ refers to the Standard Model background Boson (Z and W) + jets.

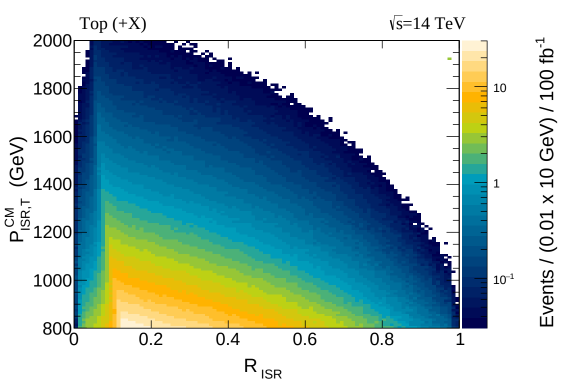

(b) The scatter plot R_{ISR} vs $p^{\text{CM}}_{\text{ISR},T}$ refers to the Standard Model backgrounds single top and $t\bar{t}$.

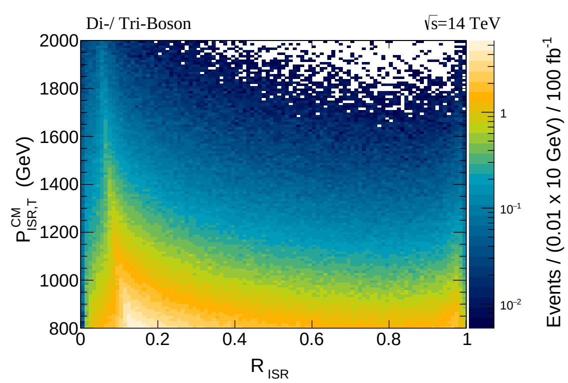

(c) The scatter plot R_{ISR} vs $p^{\text{CM}}_{\text{ISR},T}$ refers to the Standard Model background involving multi-bosons (Z and W).

Figure 5.3.3: Distribution of the $p^{\text{CM}}_{\text{ISR},T}$ as a function of R_{ISR} for boson + jet (a) single top and $t\bar{t}$ (b) di/tri bosons (c) samples. The two-dimensional histograms shows the number of events expected per bin for an integrated luminosity of 100 fb^{-1} satisfying the preselection criteria and $p^{\text{CM}}_{\text{ISR},T} > 800$ GeV.

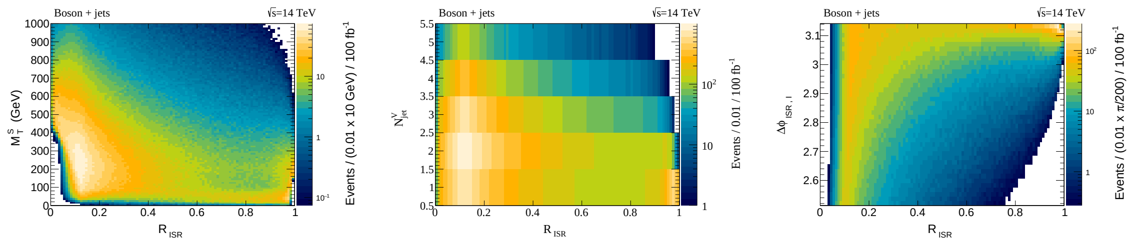

(a) The scatter plot: R_{ISR} vs M_T^{S}. (b) R_{ISR} vs $N_{\mathrm{jet}}^{\mathrm{V}}$. (c) R_{ISR} vs $\Delta\phi_{\mathrm{ISR,I}}$.

Figure 5.3.4: Distribution of M_T^{S} (a), $N_{\mathrm{jet}}^{\mathrm{V}}$ (b) and $\Delta\phi_{\mathrm{ISR,I}}$ (c) as a function of R_{ISR}. The two-dimensional histograms show the number of events expected for the vector boson + jets background per bin for an integrated luminosity of 100 fb^{-1} satisfying the preselection criteria and $p_{\mathrm{ISR},T}^{\mathrm{CM}} > 800$ GeV.

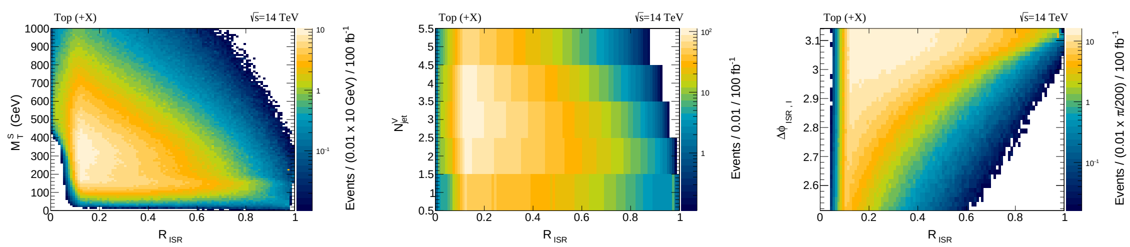

(a) The scatter plot: R_{ISR} vs M_T^{S}. (b) R_{ISR} vs $N_{\mathrm{jet}}^{\mathrm{V}}$. (c) R_{ISR} vs $\Delta\phi_{\mathrm{ISR,I}}$.

Figure 5.3.5: Distribution of M_T^{S} (a), $N_{\mathrm{jet}}^{\mathrm{V}}$ (b) and $\Delta\phi_{\mathrm{ISR,I}}$ (c) as a function of R_{ISR}. The two-dimensional histograms show the number of events expected for the $t\bar{t}$ and single top backgrounds per bin for an integrated luminosity of 100 fb^{-1} satisfying the preselection criteria and $p_{\mathrm{ISR},T}^{\mathrm{CM}} > 800$ GeV.

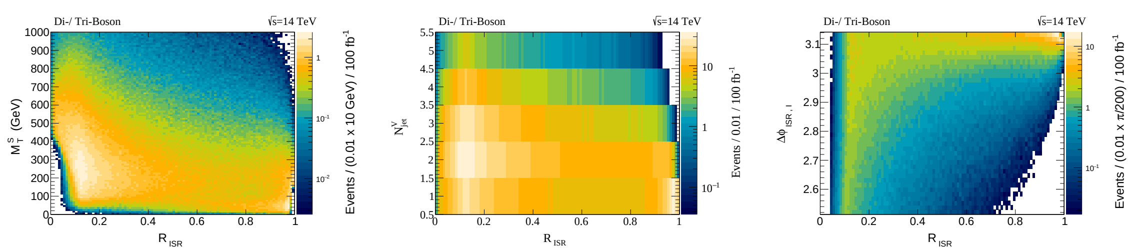

(a) The scatter plot: R_{ISR} vs M_T^{S}. (b) R_{ISR} vs N_{jet}^{V}. (c) R_{ISR} vs $\Delta\phi_{\mathrm{ISR,I}}$.

Figure 5.3.6: Distributions of M_T^{S} (a), $N_{\mathrm{jet}}^{\mathrm{V}}$ (b) and $\Delta\phi_{\mathrm{ISR,I}}$ (c) as a function of R_{ISR}. The two-dimensional histograms show the number of events expected for the Di-/tri-bosons background per bin for an integrated luminosity of 100 fb^{-1} satisfying the preselection criteria and $p_{\mathrm{ISR},T}^{\mathrm{CM}} > 800$ GeV.

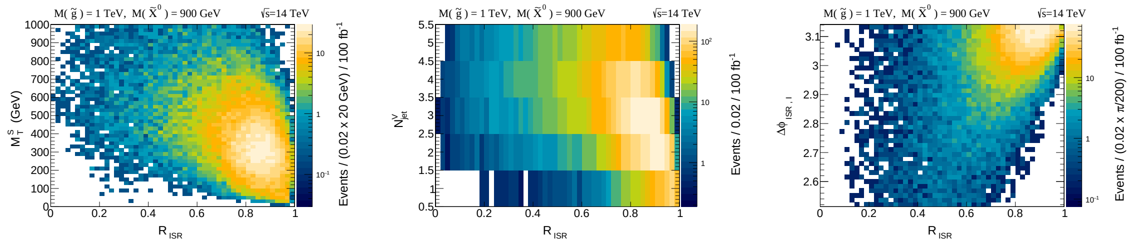

(a) The scatter plot: R_{ISR} vs M_T^{S} (b) R_{ISR} vs N_{jet}^{V}. (c) R_{ISR} vs $\Delta\phi_{\mathrm{ISR,I}}$

Figure 5.3.7: Distributions of M_T^{S} (a), $N_{\mathrm{jet}}^{\mathrm{V}}$ (b) and $\Delta\phi_{\mathrm{ISR,I}}$ (c) as a function of R_{ISR}.The two-dimensional histograms show the number of events expected for signal sample $M_{\tilde{g}}$ = 1 TeV, $M_{\tilde{\chi}_1^0}$ = 900 GeV per bin for an integrated luminosity of 100 fb^{-1} satisfying the preselection criteria and $p_{\mathrm{ISR},T}^{\mathrm{CM}} > 800$ GeV.

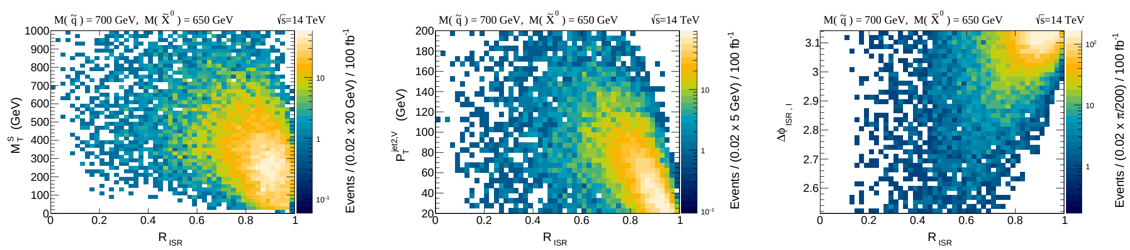

(a) The scatter plot: R_{ISR} vs M_T^{S}. (b) R_{ISR} vs $p_T^{\mathrm{jet2,V}}$. (c) R_{ISR} vs $\Delta\phi_{\mathrm{ISR,I}}$

Figure 5.3.8: Distributions of M_T^{S} (a), $p_T^{\mathrm{jet2,V}}$ (b) and $\Delta\phi_{\mathrm{ISR,I}}$ (c) as a function of R_{ISR}. The two-dimensional histograms show the number of events expected for signal sample $M_{\tilde{q}}$ = 700 GeV, $M_{\tilde{\chi}_1^0}$ = 650 GeV per bin for an integrated luminosity of 100 fb^{-1} satisfying the preselection criteria and $p_{\mathrm{ISR},T}^{\mathrm{CM}} > 800$ GeV.

The distribution of the jet multiplicity in the V-system as a function of R_{ISR} is shown in Figures 5.3.4b-5.3.7b for the main Standard Model backgrounds and the gluino sample $M_{\tilde{g}}$ =1 TeV $M_{\tilde{\chi}_1^0}$ =900 GeV. Notably, the large background contributions from boson+jets and di-boson in the high R_{ISR} region occur at $N_{\mathrm{jet}}^{\mathrm{V}} = 1$. These processes include the Z boson decaying invisibly with an additional jet associated to the V-system and $W \to \tau(\mathrm{had})\nu$.[2] These processes can be discriminated from the gluino signals requiring a minimum value of three or four for $N_{\mathrm{jet}}^{\mathrm{V}}$, while for the squark topology only two jets are expected in the V-system. Figure 5.3.8b shows the two-dimensional distribution of the second jet ordered in p_T as a function of R_{ISR} for the squark sample $M_{\tilde{q}}$ =700 GeV and $M_{\tilde{\chi}_1^0}$ =650 GeV. This is the second topology dependent observable used in concert with $N_{\mathrm{jet}}^{\mathrm{V}}$ in this study and it is largely uncorrelated with respect to the ratio.

Finally the scatter plots R_{ISR} vs $\Delta\phi_{\mathrm{ISR,I}}$ are shown in Figures c). The two variables are mostly independent for the signal samples and a criterion close to π can be used to improve the discrimination with respect to the Standard Model background events.

Similar features appear for all the other signal samples with the distribution of R_{ISR} scaling with ΔM as expected.

5.4 Signal regions

The RJR observables are used to define selection criteria resulting in signal regions targeting the four mass splittings investigated for gluino and squark pair-production. Figures 5.4.1 and 5.4.2 show distributions of the variables with greater impact to distinguish between signal-like events and background-like events when the respective N-1 requirements in Table 5.2 are applied.

Figures 5.4.1a and 5.4.1b show the distributions of R_{ISR} for the backgrounds, and for gluino and squark samples respectively, for the events respecting the criteria in Table

[2] No criteria for the τ tagging are applied in this study: the misidentification of an hadronically decay τ lepton in a light jet is high as described in Section 3.4.2.

5.2 column 3 and 2 respectively. In the high ISR regime the variable is the best signal-to-background discriminant: final state events for gluino and squark pair-production topologies tend to populate higher values than background-like events.

Figures 5.4.1b and 5.4.2b show the distributions of $p^{\mathrm{CM}}_{\mathrm{ISR},T}$ for some gluino and squark samples with ΔM =100 GeV and 50 GeV respectively. The discriminant impact is moderate and a common threshold value of 1 TeV is chosen representing the order of the hard scale investigated.

Figure 5.4.1c and 5.4.2c show the number of jets with transverse momentum higher than 20 GeV associated to the V-system. Four and two jets are expected as decay products of the gluino and squark topologies and roughly a smaller multiplicity can be attributed to the inefficiency of the detector to reconstruct low-momentum jets while a larger multiplicity is due to the presence of additional low radiation in the direction of the S-system. Notably, the distributions fall down on the 5th bin for the gluino samples and on the 3rd bin for squark samples.

In concert with the jet multiplicity an extra topology dependent variable can be used to improve the discovery prospects of such supersymmetric signals. Focusing on the 2nd and 3rd bin of $N^{\mathrm{V}}_{\mathrm{jet}}$ the transverse momentum of the corresponding jet can be investigated. Figures 5.4.1e and 5.4.2e show the distributions of these observables.

The transverse mass of the S-system is a scale variable related partially to the overall scale ($M_{\tilde{\chi}}$ for the signal) and mostly to the mass splitting scale (ΔM for the signal). It becomes a good discriminant for signal samples with a large value of the mass difference respect Standard Model processes involving real Z, W bosons or top assigned to the V-system with some source of missing transverse momentum. Figures 5.4.1e and 5.4.2e show the N-1 distributions of M^{S}_{T} for gluino and squark samples with $\Delta M = 200$ GeV.

Notably, from Figures 5.4.1f and 5.4.2f additional improvement can be made by tuning selection criteria on $\Delta\phi_{\mathrm{ISR,I}}$.

The *inclusive* signal regions targeting the four mass splittings are shown in Table 5.2. The word inclusive refers to the fact that the same signal regions are used to investigate

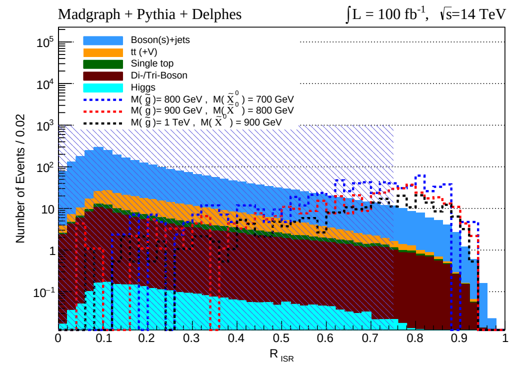

(a) The distribution of $R_{\rm ISR}$ for gluino signals with $\Delta M = 100$ GeV and SM backgrounds.

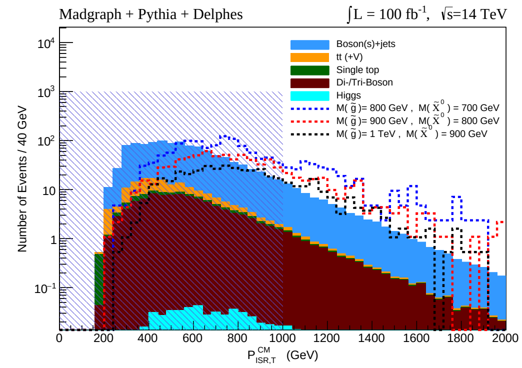

(b) The distribution of $p^{\rm CM}_{{\rm ISR},T}$ for gluino signals with $\Delta M = 100$ GeV and SM backgrounds.

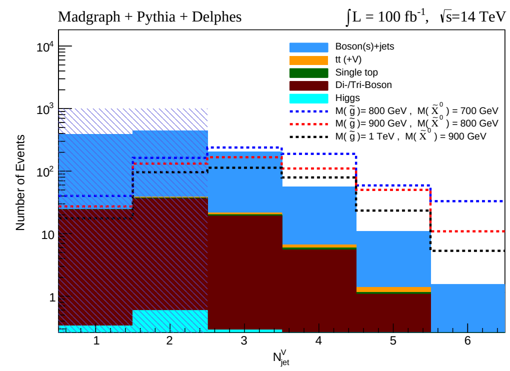

(c) The distribution of the $N^{\rm V}_{\rm jet}$ for gluino signals with $\Delta M = 100$ GeV and SM backgrounds after the application of the N-1 requirements in Table 5.2 column 3.

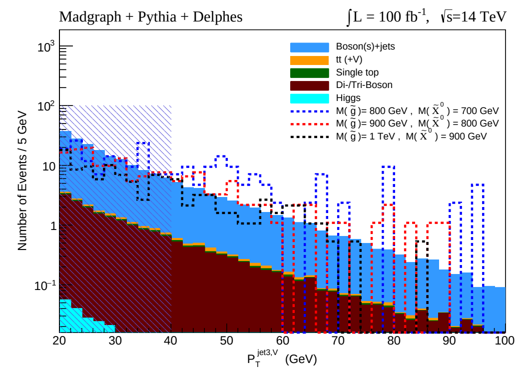

(d) The distribution of $p_T^{\rm jet3,V}$ for gluino signals with $\Delta M = 100$ GeV and SM backgrounds after the application of the N-1 requirements in Table 5.2 column 3 in final states with 3 jets in the V-system.

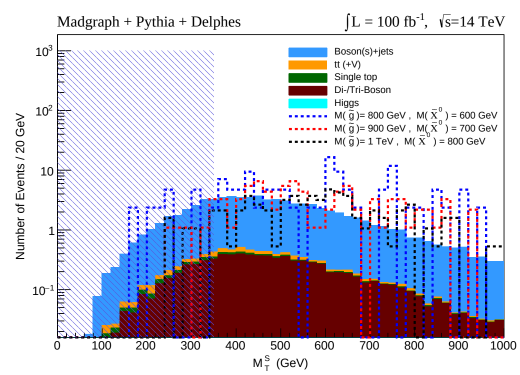

(e) The distribution of $M_T^{\rm S}$ for gluino signals with $\Delta M = 200$ GeV and SM backgrounds.

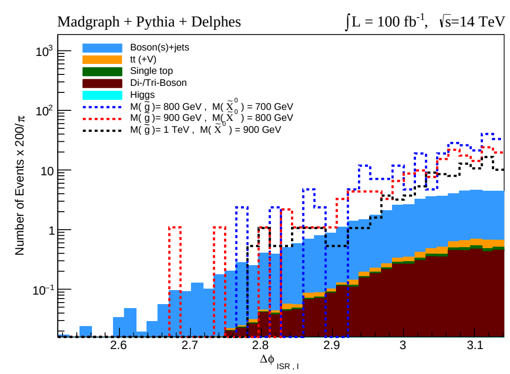

(f) The distribution of $\Delta\phi_{\rm ISR,I}$ for gluino signals with $\Delta M = 100$ GeV and SM backgrounds.

Figure 5.4.1: Distribution of the RJR observables sensitive to compressed scenarios for events that have satisfied all the selection criteria in Table 5.2 except the requirement on the variable that is displayed. Standard Model backgrounds are stacked together, while the overlaid dashed curves refer to gluino pair-production samples with $\Delta M = 100$ GeV and $\Delta M = 200$ GeV. All the contributions are scaled with an integrated luminosity of 100 fb^{-1} at 14 TeV.

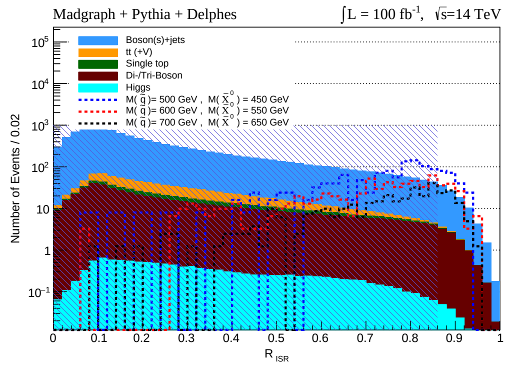

(a) The distribution of $R_{\rm ISR} = \frac{\left|\vec{p}^{\,\rm CM}_{{\rm I},T} \cdot \hat{p}^{\,\rm CM}_{{\rm ISR},T}\right|}{p^{\rm CM}_{{\rm ISR},T}}$ for gluino signals with $\Delta M = 50$ GeV and SM backgrounds.

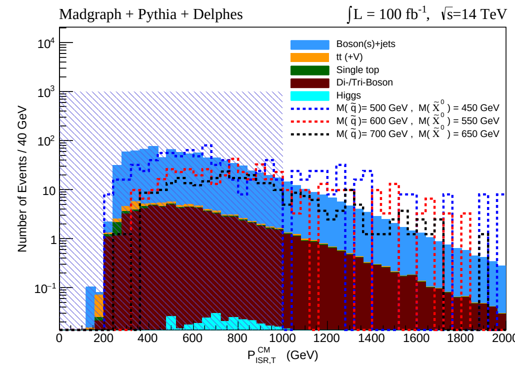

(b) The distribution of $p^{\rm CM}_{{\rm ISR},T}$ for gluino signals with $\Delta M = 50$ GeV and SM backgrounds.

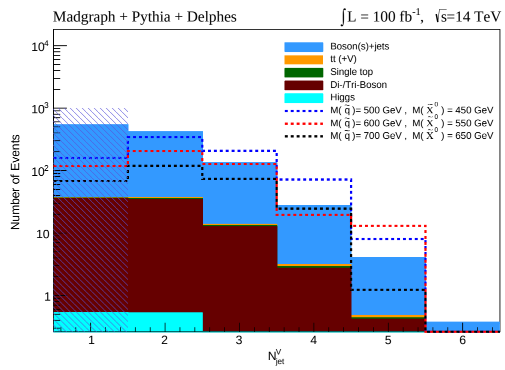

(c) The distribution of the $N^{\rm V}_{\rm jet}$ for gluino signals with $\Delta M = 50$ GeV and SM backgrounds after the application of the N-2 (no requirement on $p_T^{\rm jet2,V}$) selection criteria in Table 5.2 column 2.

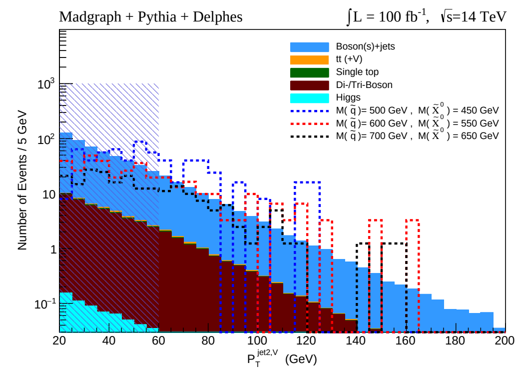

(d) The distribution of $p_T^{\rm jet2,V}$ for squark signals with $\Delta M = 50$ GeV and SM backgrounds after the application of the N-1 requirements in Table 5.2 column 2.

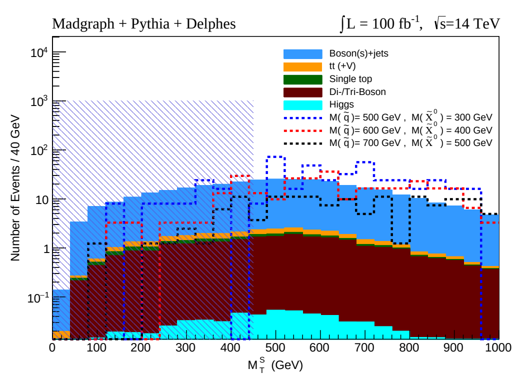

(e) The distribution of $M_T^{\rm S}$ for gluino signals with $\Delta M = 200$ GeV and SM backgrounds after the application of the N-1 requirements in Table 5.2 column 4.

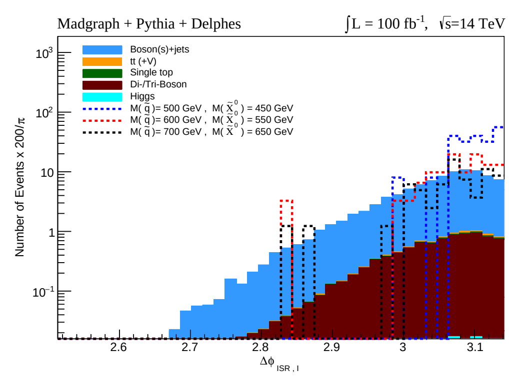

(f) The distribution of $\Delta\phi_{\rm ISR,I}$ for gluino signals with $\Delta M = 50$ GeV and SM backgrounds after the application of the N-1 requirements in Table 5.2 column 2.

Figure 5.4.2: Distribution of the RJR observables sensitive to compressed scenarios for events that have satisfied the selection criteria in Table 5.2. Standard Model backgrounds are stacked together while the overlaid dashed curves refer to squark pair-production samples. All the contributions are scaled with an integrated luminosity of 100 fb^{-1} at 14 TeV.

	Mass Splitting [GeV]			
Variable	$\Delta M = 25$	$\Delta M = 50$	$\Delta M = 100$	$\Delta M = 200$
Preselection criteria	Lepton (e and μ) and b-jet veto			
	$\not{E}_T > 100$ GeV, $p_T(jet) > 20$ GeV			
$p_{\mathrm{ISR},T}^{\mathrm{CM}}$ [GeV]	> 1000			
$R_{\mathrm{ISR}} = \frac{\lvert \vec{p}_{\mathrm{I},T}^{\,\mathrm{CM}} \cdot \hat{p}_{\mathrm{ISR},T}^{\mathrm{CM}} \rvert}{p_{\mathrm{ISR},T}^{\mathrm{CM}}}$	> 0.9	> 0.85	> 0.75	> 0.65
M_T^{S}	–	> 100	> 250	> 400
$N_{\mathrm{jet}}^{\mathrm{V}}$	$\geq 3(\geq 2)$		$\geq 4(\geq 2)$	
$p_T^{\mathrm{jet3(2),V}}$ [GeV]	$> 20(> 40)$	$> 30(> 60)$	$> 40(> 120)$	$> 50(> 160)$
$\Delta\phi_{\mathrm{ISR,I}}$	> 3			

Table 5.2: A conservatively optimised set of selection criteria for signal regions in the analysis of gluino (squark) pair-production. The selection assumes a sample of 100 fb^{-1} collected in proton-proton collisions with a centre-of-mass energy of $\sqrt{s} = 14$ TeV. The natural pattern is to loosen the scaleless criteria as the criteria with units GeV are tightened.

the gluino and squark topologies except the criteria applied to the two more topology dependent observables $N_{\mathrm{jet}}^{\mathrm{V}}$ and $p_T^{\mathrm{jeti,V}}$. For these two observables different requirements are applied to the gluino (squark) topologies. The natural pattern is related to the ΔM targeted as follow: the smaller the mass difference the tighter the criterion on R_{ISR}, while the *scale* selection criteria are progressively more relaxed.

The signal regions can be substantially modified and partially optimised adopting several strategies.

The two variables $N_{\mathrm{jet}}^{\mathrm{V}}$ and $p_T^{\mathrm{jeti,V}}$ are the only two model-dependent observables utilised in this study. Other possibilities could be the opening angle between the i-th jet in the V and the I-system or the ISR-system.

The requirement $p_{\mathrm{ISR},T}^{\mathrm{CM}} > 1$ TeV is common with a value in between the hard scales of the squark and gluino samples investigated. An optimisation can be made by tuning the value to $M_{\tilde{P}}$ using a smaller value for the squark samples with respect the gluino one or tightening the criterion when ΔM is larger and the R_{ISR} requirement is relaxed.

The criteria on R_{ISR} are mass-splitting related. Improvement can be made by using a careful examination of the relative mass splitting or the mass ratio for the different samples from the moment the distribution scales for the signal with $M_{\tilde{\chi}_1^0}/M_{\tilde{P}}$ (see Eq. 4.6.10). To extract the optimal significance for each signal point considered we could increase the number of signal regions matching the R_{ISR} requirement to the mass ratio parent sparticle to LSP.

Finally, the requirement for the distribution of $\Delta\phi_{\mathrm{ISR,I}}$ is not optimised at all. Tuning a selection criterion on this quantity means choosing a value between 3 and π. Nevertheless, data analysis can leverage the discriminant power provided by the distribution of this variable .

The purpose of this phenomenological study is not to obtain the best values for the significances, but rather show the power of the Recursive Jigsaw Reconstruction technique. The RJR technique is already used by the ATLAS collaboration in order to investigate the compressed regime [122].

5.5 Results and summary

The inclusive signal regions resulting from selection criteria of the RJR observables defined in Table 5.2 are applied to calculate projected sensitivities for the gluino and squark samples in the compressed regime.

Figures 5.5.1 and 5.5.2 show the value of Z_{Bi} calculated assuming the metric [94] with inputs the yields of each signal sample, the overall Standard Model background and assuming for this a systematic uncertainty of 15%. The Z-value represents the significance of a given signal expressed in standard deviations in the presence of a background hypothesis, as described in Section 3.5.1.

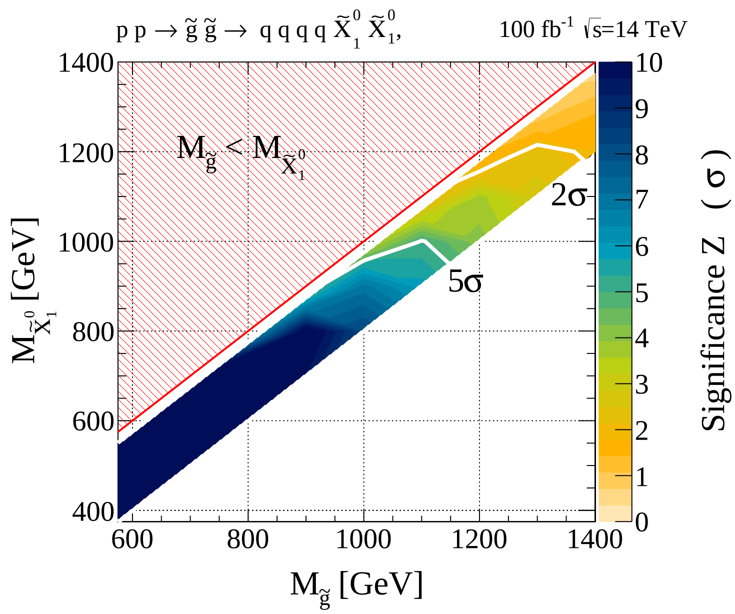

Figure 5.5.1: Projected exclusion and discovery reach for gluino pair-production in the compressed regions: 25 GeV $\leq \Delta M \leq$ 200 GeV

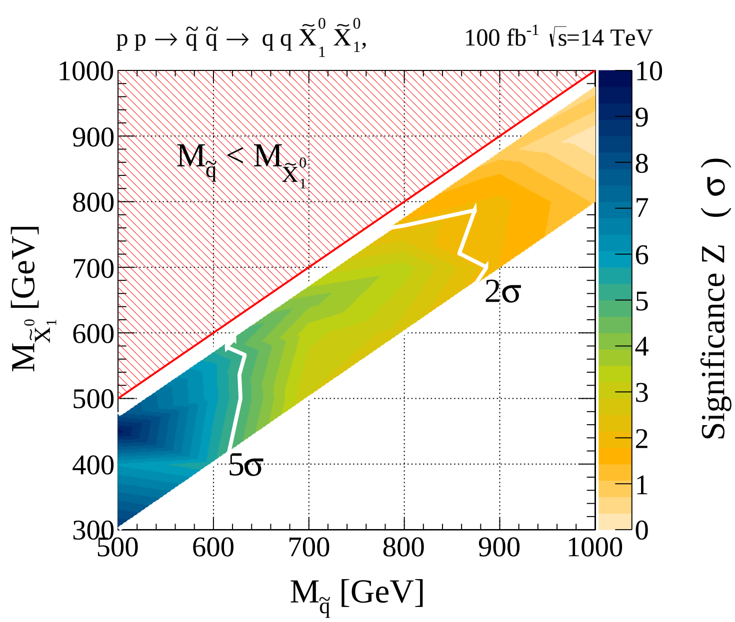

Figure 5.5.2: Projected exclusion and discovery reach for squark pair-production in the compressed regions: 25 GeV $\leq \Delta M \leq$ 200 GeV.

The results are the expected significances for the simplified topologies in Figure 5.1.2, in the compressed scenarios 25 GeV$\leq \Delta M \leq$200 GeV, in proton-proton collisions with a centre-of-mass energy of 14 TeV projected to an integrated luminosity of 100 fb^{-1}. The curves refer to the values 5σ and 2σ of significances and can be interpreted as benchmark lines for the discovery of potential supersymmetric signatures and exclusion at the 95% confidence level.

In the compressed regime gluinos would be discovered with masses above 1 TeV and excluded up to 1.4 TeV, while for squarks the 5σ contour line is above 600 GeV and the exclusion between 800 GeV and 900 GeV.

The Recursive Jigsaw Reconstruction technique provides excellent results for the discovery prospects of compressed spectra of gluino and squark pair-production in final states with light jets and missing transverse momentum. Leveraging on high ISR transverse momentum, the method, summarised by the compressed tree in Figure 4.6.1, assigns identical objects between the ISR and the V-system using a jigsaw rules based on the minimisation of the masses, equivalent to the maximisation of the transverse momentum of the ISR-system. The RJR technique provides a basis of complementary observables used to define inclusive signal regions. The guidelines for an optimisation of the selection criteria are given and can be used in the analysis of the experimental data in order to increase the potential signal to background yield ratio.

The RJR technique has already been used by the ATLAS collaboration in order to probe the sensitivity to these topologies. Details for this investigation can be found elsewhere [122].

The primary focus of this work has been on solely hadronic final states, in particular jets resulting from the hadronisation of light quarks. In principle, the same strategy can trivially be applied to any final state in order to study compressed regimes. In the next section we focus on the *opposite extreme*: final state topologies with no ambiguity between the ISR-system and the products from sparticle decays.

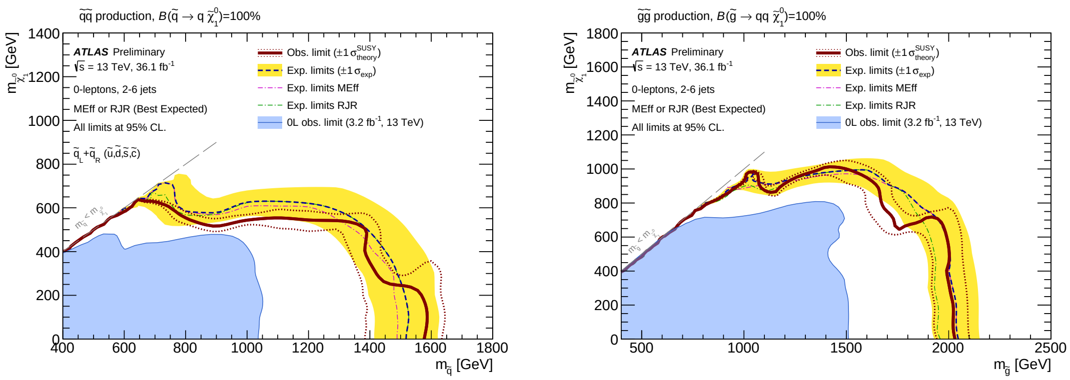

(a) (b)

Figure 5.5.3: Recent exclusion limits at the 95% CL from the ATLAS collaboration for the SUSY simplified topologies $pp \to \tilde{q}\tilde{q}(\tilde{q} \to q\tilde{\chi}_1^0)$ (a) and $pp \to \tilde{g}\tilde{g}(\tilde{g} \to qq\tilde{\chi}_1^0)$ (b). Figures from [122].

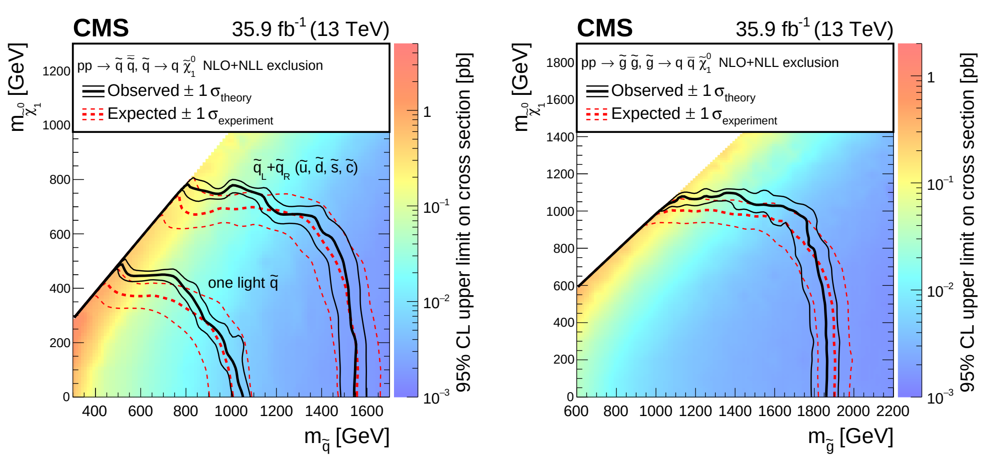

(a) (b)

Figure 5.5.4: Current results from the CMS collaboration for the SUSY simplified topologies $pp \to \tilde{q}\tilde{q}(\tilde{q} \to q\tilde{\chi}_1^0)$ (a) and $pp \to \tilde{g}\tilde{g}(\tilde{g} \to qq\tilde{\chi}_1^0)$ (b). Figures from [123].

Chapter 6

Probing the supersymmetric electroweak sector phenomenology for compressed mass spectra with RJR

6.1 Introduction to the topologies investigated

This section is dedicated to the study of supersymmetric compressed scenarios in the electroweak sector [115]. The production of charginos ($\tilde{\chi}_i^{\pm}$ with $i = 1$ or 2) and/or heavy neutralinos ($\tilde{\chi}_i^0$ with $i = 2$, 3 or 4) provides a plethora of final state topologies having the missing transverse momentum as a unique common denominator. Phenomenological studies involving compressed electroweakinos can be found elsewhere in literature [124–130].

Compressed scenarios involving electroweakinos are common in supersymmetric models as described in Section 2.3.6. Particularly, mass spectra with a $\tilde{\chi}_1^{\pm}$ and/or $\tilde{\chi}_2^0$ next-to-LSP and the resulting simplified assumption $\tilde{\chi}_1^{\pm} \to W^{\pm}\tilde{\chi}_1^0$ and $\tilde{\chi}_2^0 \to Z(h)\tilde{\chi}_1^0$ are well motivated. This is related to the light Higgsino-component and limited wino-component expected in naturalness-inspired models [52] appearing at the tree-level and one-loop

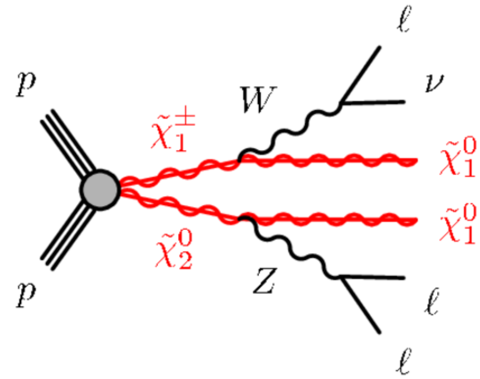

Figure 6.1.1: Feynman diagram for chargino-neutralino associated production in final states with three leptons and missing transverse momentum.

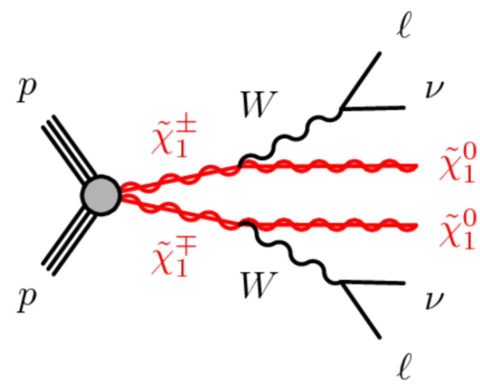

Figure 6.1.2: Feynman diagram for chargino pair-production in final states with two leptons and missing transverse momentum.

corrections to the Higgs mass respectively. Qualitatively, the smaller the mass splitting $\Delta M = M_{\tilde{P}} - M_{\tilde{\chi}}$, the less the opportunity to accommodate an additional superparticle with intermediate mass. At the current time, there are very low exclusion limits from CMS and ATLAS searches for charginos and neutralinos decaying via W and Z bosons to $\tilde{\chi}_1^0$. The challenge, aside from the main irreducible di-boson backgrounds, is once again related to the inefficiency of the detector in reconstructing low-momentum objects and the low value of the missing transverse momentum in the compressed regime.

Herein the focus is on the topologies in Figures 6.1.1 and 6.1.2. A specific analysis is dedicated to each topology: the lepton multiplicity in the final state is different, the expected Standard Model backgrounds differ, and the expected signal distributions of the RJR observables are different.

From the previous study focused on compressed RJR observables, and in particular $R_{\rm ISR} \equiv \frac{|\vec{p}^{\,\rm CM}_{\rm I,\mathit{T}} \cdot \hat{p}^{\rm CM}_{\rm ISR,\mathit{T}}|}{p^{\rm CM}_{\rm ISR,\mathit{T}}}$ discussed in Section 4.6.3, it is clear how the adjective *compressed* has a meaning relative to the mass of the parent superparticle. In this work, we probe electroweakino samples with masses in the range 100 GeV$\leq M_{\tilde{P}} \leq$ 500 GeV, while the mass splittings considered are 15 GeV$\leq \Delta M \leq$ 75 GeV; in other words the W and Z bosons are off-shell.

6.1.1 The golden channels

In principle, all the final states resulting from the different vector boson channels can be probed with the compressed RJR tree. Nevertheless, focusing on electrons and muons as supersymmetric visible decay products provides several advantages, which, when properly exploited, promote the branches of the topologies in Figures 6.1.1 and 6.1.2 as *golden* channels.

Firstly, from a simple pre-analysis based only on the object multiplicities, the ratio of signal-to-background events for the final states with the largest number of leptons is orders of magnitude higher with respect final states with W and/or Z bosons decaying hadronically. Secondly, the channels result in clean final states with high efficiencies for the reconstruction of leptons[1]. Finally, for our purposes all leptons are identifiable as reconstructed objects expected to come from sparticle decays and so they are assigned to the V-system, while all the jets can be placed into the ISR-system with no ambiguity. This allows us to avoid focusing on a high ISR regime in order to exploit the compressed RJR strategy.[2]

[1] In this study the conservative minimum value for the reconstructed leptons $p_T >$ 10 GeV is assumed. A recent effort by the ATLAS and CMS collaborations is dedicated to the improvement of the efficiency for the identification of $soft$ isolated electrons and muons (3-4 GeV$\lesssim p_T^{lep} \lesssim$ 10 GeV) [89].

[2] For the chargino pair analysis we define the substructure of the S-system in a more complete vision than the simplified S$\rightarrow$VI, but all the considerations of this section remain valid.

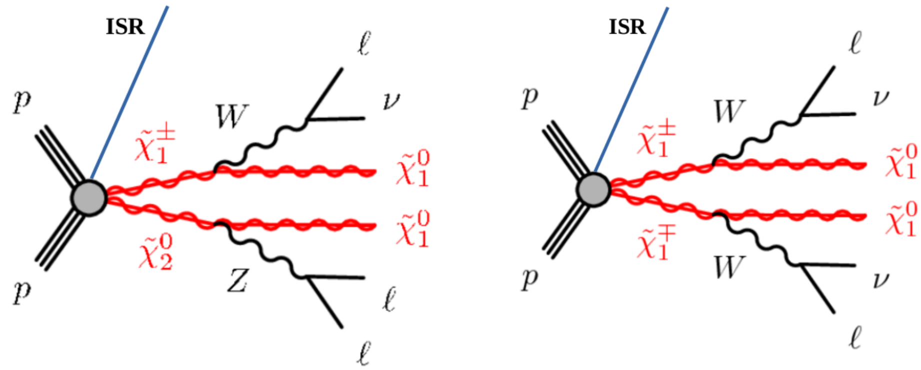

Figure 6.1.3: All the jets in the final state are assigned to the ISR-system: a minimal criterion on $p^{\mathrm{CM}}_{\mathrm{ISR},T}$ is required.

A minimal value of the transverse momentum of the ISR-system can produce some value for $\not{E}_T$ and give the leptons some transverse momentum. The compressed RJR variables can be used to probe supersymmetric spectra with small mass splittings. In the next sections, we demonstrate how R_{ISR} maintains its impact to discriminate the signal from the background: the lost of resolution in the low ISR regime is compensated for the lack of ambiguity in the assignment of the objects between the V and ISR-system.

On the other hand, the mass scales investigated are close to the typical scale of Standard Model backgrounds. For this reason $p^{\mathrm{CM}}_{\mathrm{ISR},T}$ is not expected to have a great impact in the discrimination, but rather to ensure a focus on final states with real jets radiated from the initial state as in the Figures 6.1.3. In this way we can leverage the impact of the RJR compressed observables without requiring a restrictive event selection based on a huge value of the ISR transverse momentum.

6.1.2 Validation of the cross sections and branching fractions for the simplified topologies

A careful examination of the number of signal and backgrounds events is a key feature in any search in particle physics. This section provides a brief description for the evaluation of the cross sections and branching fractions used for the investigation of the two topologies shown in the Feynman diagrams in Figures 6.1.1 and 6.1.2.

6.1.2.1 The cross sections

The cross sections for wino-like chargino pair-production and chargino-neutralino associated production at 13 TeV at next-to-leading logarithmic accuracy (NLL) can be found here [131, 132]. The writer has estimated the NLL cross sections for $\sqrt{s} = 14$ TeV as follows.

A wino-like parameter-card is used for the generation of the electroweakinos pair-production from proton-proton collisions at 13 TeV at next-to-leading order (NLO) with Madgraph. A $k-$factor is computed as the ratio of the NLL/NLO cross sections at 13 TeV

$$
\begin{aligned}
k_i &= \frac{\sigma_{i,\mathrm{NLL}}\left[pp\left(\sqrt{s}=13\ \mathrm{TeV}\right)\to\tilde{\chi}_1^{\pm}\tilde{\chi}_2^{0}\right]}{\sigma_{i,\mathrm{NLO}}\left[pp\left(\sqrt{s}=13\ \mathrm{TeV}\right)\to\tilde{\chi}_1^{\pm}\tilde{\chi}_2^{0}\right]} = \frac{\sigma_{i,\mathrm{LHC-SUSY}}}{\sigma_{i,\mathrm{Madgraph}}} \\
k_j &= \frac{\sigma_{j,\mathrm{NLL}}\left[pp\left(\sqrt{s}=13\ \mathrm{TeV}\right)\to\tilde{\chi}_1^{\pm}\tilde{\chi}_1^{\mp}\right]}{\sigma_{j,\mathrm{NLO}}\left[pp\left(\sqrt{s}=13\ \mathrm{TeV}\right)\to\tilde{\chi}_1^{\pm}\tilde{\chi}_1^{\mp}\right]} = \frac{\sigma_{j,\mathrm{LHC-SUSY}}}{\sigma_{j,\mathrm{Madgraph}}}
\end{aligned}
\tag{6.1.1}
$$

where i (j) refers to the different degenerate mass $M_{\tilde{\chi}_1^{\pm}} = M_{\tilde{\chi}_2^0}$ $(M_{\tilde{\chi}_1^{+}} = M_{\tilde{\chi}_1^{-}})$ samples investigated.

The NLO cross sections are computed at $\sqrt{s} = 14$ TeV with the same data_cards. The same k-factors as in Eq. 6.1.1 are assumed for the corrections:

$$
\begin{aligned}
\sigma_{i,\mathrm{NLL}}\left[pp\left(\sqrt{s}=14\ \mathrm{TeV}\right)\to\tilde{\chi}_1^{\pm}\tilde{\chi}_2^{0}\right] &= k_i\times\sigma_{i,\mathrm{NLO}}\left[pp\left(\sqrt{s}=14\ \mathrm{TeV}\right)\to\tilde{\chi}_1^{\pm}\tilde{\chi}_2^{0}\right] \\
\sigma_{j,\mathrm{NLL}}\left[pp\left(\sqrt{s}=14\ \mathrm{TeV}\right)\to\tilde{\chi}_1^{\pm}\tilde{\chi}_1^{\mp}\right] &= k_j\times\sigma_{j,\mathrm{NLO}}\left[pp\left(\sqrt{s}=14\ \mathrm{TeV}\right)\to\tilde{\chi}_1^{\pm}\tilde{\chi}_1^{\mp}\right]
\end{aligned}
\tag{6.1.2}
$$

The resulting NLL cross sections are shown in Figure 6.1.4 and used as inputs for the analysis of the simplified supersymmetric topologies in Figures 6.1.1 and 6.1.2.

At 13 TeV the values for the relative cross section uncertainties are in the range 4.5% $\lesssim \triangle\sigma \lesssim$ 9% for the samples studied [131, 132]. The procedure here described provides small corrections ($\lesssim$ 5%) from the k-factors and can be considered a check for the

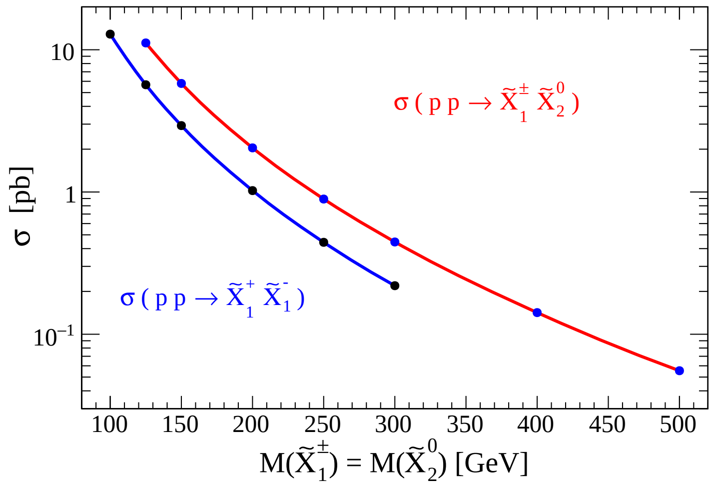

Figure 6.1.4: Estimated NLL cross sections for wino-like chargino pair-production (blue curve) and chargino-neutralino associated production (red curve) at $\sqrt{s} = 14$ TeV.

matched Madgraph cross sections and their potential dependences from the cutoff scales chosen.

6.1.2.2 The branching fractions

For the signal samples the number of events with highest lepton multiplicity is a small portion of the total number of events generated because of the low branching fractions of the W and Z bosons golden channels. As a consequence assuming the true W and Z branching fractions is inefficient requiring a large amount of time and storage capacity. In order to enhance the statistics for the lepton decay modes the complete topologies as in Figures 6.1.1 and 6.1.2 are generated. In this section a brief description of the method of re-weighting with the proper branching fractions is shown, along with a validation.

Section 3.4 shows how the number of events expected to be seen by a detector is expressed by the relation $N = \sigma \times BR \times \epsilon \times \int \mathrm{d}t\mathcal{L}$, where σ is the cross section, BR is the branching ratio of the channels, ϵ takes care of all the efficiencies and acceptances for the reconstruction of the objects in the final states as discussed in Section 3.4.2 and $\int \mathrm{d}t\mathcal{L}$ is the integrated luminosity.

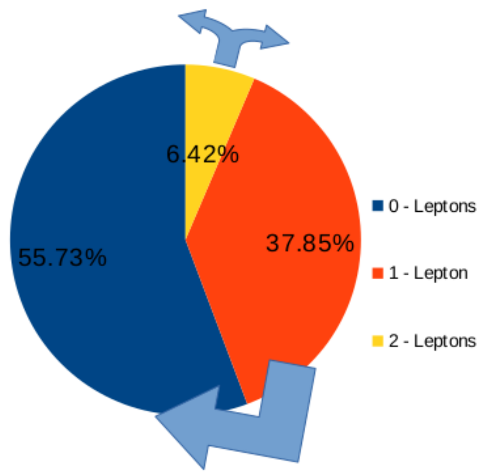

Figure 6.1.5: Branching fractions for the decay of two W-bosons to 0,1 and 2 leptons (electrons plus muons) independently from the number of jets. The arrows show the decrement of the higher lepton multiplicity statistics in advantage of the lower one due to the detector response (ϵ). An arrow with opposite direction can be interpreted as a fake contribution and can be neglected for the signal.

With $\sigma \times \int \mathrm{d}t\mathcal{L}$ held fixed from a Monte Carlo simulation point of view, the number of events is $N = BR \times \epsilon \times n$ where n is the number of events generated.[3] For our purposes we can categorize the branching ratios based on the lepton multiplicity, indeed the number of electrons plus muons in the final state.

Consider the chargino pair-production samples $pp \to \tilde{\chi}_1^{\pm}\tilde{\chi}_1^{\mp}$. The number of events with 0, 1 or 2 leptons is related to the BR of two Ws in different channels, while ϵ substantially decreases the higher multiplicity statistics increasing the 0 and 1 lepton cases as in Figure 6.1.5.

The decay of the W-boson is forced with equal probability (1/3) to electron, muon or tau leptons and the final number of events is re-weighted properly.[4] As a check, for some signal samples, the generation is performed for the two cases $pp \to \tilde{\chi}_1^{\pm}\tilde{\chi}_1^{\mp} \to W^*(\to \text{all})W^*(\to \text{all})\tilde{\chi}_1^0\tilde{\chi}_1^0$ and $pp \to \tilde{\chi}_1^{\pm}\tilde{\chi}_1^{\mp} \to W^*(\to L^+\nu)W^*(\to L^-\nu)\tilde{\chi}_1^0\tilde{\chi}_1^0$, where in

[3] To be more specific it is the number of events from the Madgraph-Pythia matching.

[4] The τ-lepton channel is considered due to the two additional neutrinos in the final state: the branching ratios are assumed 0.33 for the electron and muon channels and 0.34 for the tau channel.

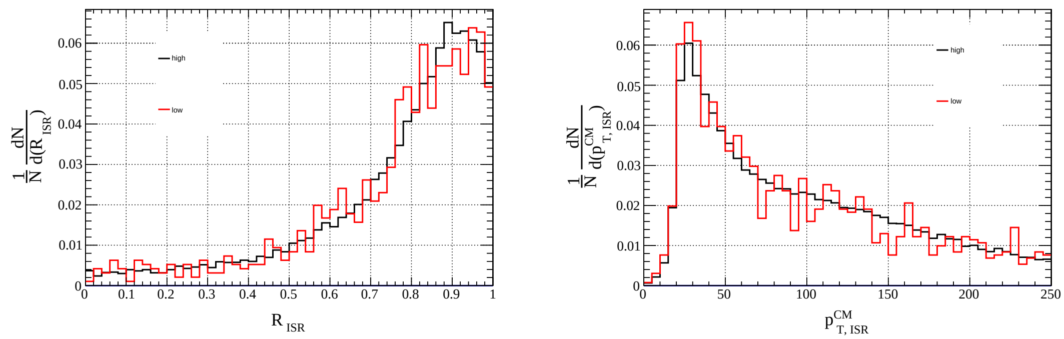

Figure 6.1.6: Normalised distributions of $R_{\rm ISR}$ and $p^{\rm CM}_{{\rm ISR},T}$ for high ($pp \to \tilde{\chi}^{\pm}_1\tilde{\chi}^0_2 \to W^*(\to L^+\nu)Z^*(\to l^-l^+)\tilde{\chi}^0_1\tilde{\chi}^0_1$ in black) low ($pp \to \tilde{\chi}^{\pm}_1\tilde{\chi}^0_2 \to W^*(\to all)Z^*(\to all)\tilde{\chi}^0_1\tilde{\chi}^0_1$ in red) statistics for the signal sample $M_{\tilde{\chi}^0_2} = M_{\tilde{\chi}^{\pm}_1} = 500$ GeV, $M_{\tilde{\chi}^0_1}$=425 GeV.

the first simulation the decay of the off-shell W boson is performed by Pythia, while in the second case the three body decay $\tilde{\chi}^{\pm}_1 \to L^{\pm}\nu\tilde{\chi}^0_1$ assumes equal probability for the different flavours $L = e, \mu, \tau$.

For the two cases, the number of events with two leptons can be schematically written as $N_l = BR_l \times \epsilon \times n_{all}$ and $N_h = BR_h \times \epsilon \times n_{Lep}$ with l =low and h=high statistics expected.

The same procedure is assumed for chargino-neutralino associated production focusing on final states with three leptons. In this case the off-shell Z is forced 50% to e^+e^- and 50% to $\mu^+\mu^-$, with the channels mediated by $\tau\tau$ being negligible.

The first check is to verify the ratio $BR_l/BR_h = N_l N_{\rm Lep}/N_h N_{\rm all}$ with the number of events generated and resulting final states with two (three) leptons. As a double check the RJR observables for high and low statistics are compared. Figure 6.1.6 shows the $R_{\rm ISR}$ and $p^{\rm CM}_{{\rm ISR},T}$ normalised distributions for a signal example.

The fractions of the number of events and the distributions are double checked for some signal samples and the values $w = BR_l/BR_h$ used to re-weight are the follow:

$$w(2\tilde{\chi}^{\pm}_1 \to 2l) = \frac{BR(2W \to 2l)}{(2/3 + 1/3 \times BR(\tau \to l))^2} \sim 0.105677 \tag{6.1.3}$$

$$w(\tilde{\chi}_2^0\tilde{\chi}_1^{\pm} \to 3l) = \frac{BR(ZW \to 3l)}{(1 - 1/3 \times BR(\tau \to l))} \sim 0.022017 \tag{6.1.4}$$

where $BR(2W \to 2l) = BR^2(W \to l) + 2BR(W \to l)BR(W \to \tau)BR(\tau \to l) + BR^2(W \to \tau)BR^2(\tau \to l)$, and $BR(ZW \to 3l) \sim BR(Z \to l^+l^-) \times [BR(W \to l) + BR(W \to \tau)BR(\tau \to l)]$ with l in short an electron or a muon.[5] The weights are computed using the branching fractions in [41].

To conclude, this procedure is simple and rigorous only for the highest lepton multiplicity case. In particular in the compressed regime it cannot be trivially used for the other cases. Indeed, the minimum value for the transverse momentum of isolated electrons and muons is chosen to be 10 GeV, and investigating mass splittings down to 15 GeV means approaching a regime with low efficiency ϵ for the reconstruction of the two (three) leptons. For example, for chargino pair-production the two lepton slice in Figure 6.1.5 is reduced towards mainly the 0 lepton category, with a progressively higher effect the smaller the mass difference studied. Final states with no leptons will be a mixture of different channels, with different weights, including topologies with no reconstructed leptons. If not properly re-weighted, the RJR observables can be biased and in such cases a generation including all the channels is preferable.

6.2 Chargino-neutralino associated pair-production in final states with three leptons

The signal samples are the simplified topologies as in Figure 6.1.1 generated within the mass ranges 125 GeV $\leq M_{\tilde{\chi}_1^{\pm}} = M_{\tilde{\chi}_2^0} \leq$ 500 GeV, with five mass splittings $\Delta M = M_{\tilde{P}} - M_{\tilde{\chi}} =$ 15, 25, 35, 50 and 75 GeV.

All the signal and background samples are passed to the algorithm summarised by the compressed tree in Figure 6.2.1[6]. Assuming a transverse view, event-by-event a basis of

[5] Notice in $BR(ZW \to 3l)$ the contribution of order $BR^2(\tau \to l)$ has been neglected.

[6] A more sophisticated reconstruction of the S-system could be applied where all the supersymmetric

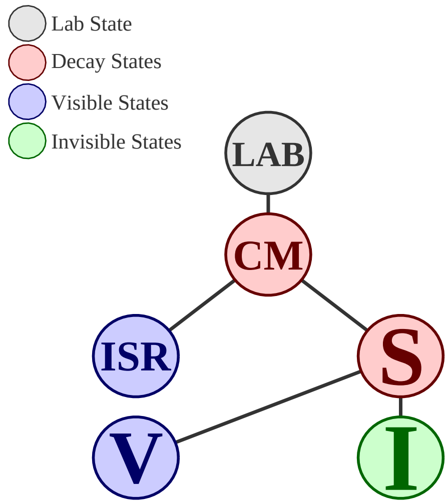

Figure 6.2.1: The compressed decay tree: LAB is the laboratory system, CM is the centre-of-mass system (S+ISR), ISR is the initial state radiation system, S is the signal or sparticle system, V is the visible system (the system associated with the three leptons) and I the invisible system.

RJR variables is extracted and analysed to probe compressed spectra for a projection of $\int \mathcal{L} = 300\,\text{fb}^{-1}$.

6.2.1 Compressed RJR observables-preselection criteria

In this section the distributions of the main RJR observables are described for the events satisfying minimal preselection criteria. Three leptons (electrons and muons) are required in the final state with $p_T > 10$ GeV, while at least one jet with $p_T > 20$ GeV is associated to the ISR-system. A minimal value for the missing transverse momentum is required $\not{E}_T > 50$ GeV. This choice guarantees a focus on the signal events of interest, and together with the three leptons requirement substantially reduces the backgrounds with no weakly interacting particles.

Figures 6.2.2 and 6.2.3 show the distributions of the main RJR observables sensitive to compressed scenarios for events that have satisfied the preselection criteria. All the

visible objects are assignable with no ambiguity. For this study the writer presents the performances of the RJR technique resulting from selection criteria of only the *transverse* observables associated to the simplified tree.

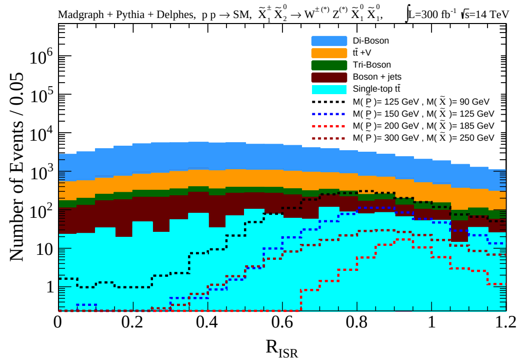

(a) Distribution of $R_{\text{ISR}} = \frac{\left|\vec{p}^{\,\text{CM}}_{\text{I},T} \cdot \hat{p}^{\,\text{CM}}_{\text{ISR},T}\right|}{p^{\text{CM}}_{\text{ISR},T}}$: variable sensitive to the mass ratio parent sparticle LSP.

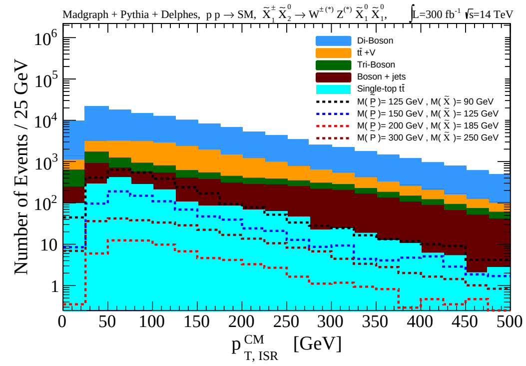

(b) Distribution of $p^{\text{CM}}_{\text{ISR},T}$: magnitude of the jets vector-sum transverse momentum of ISR-system evaluated in the CM frame.

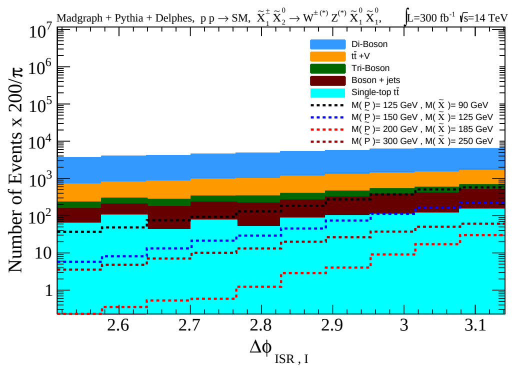

(c) Distribution of $\Delta\phi_{\text{ISR,I}}$: opening angle between the ISR-system and the I-system, evaluated in the CM frame.

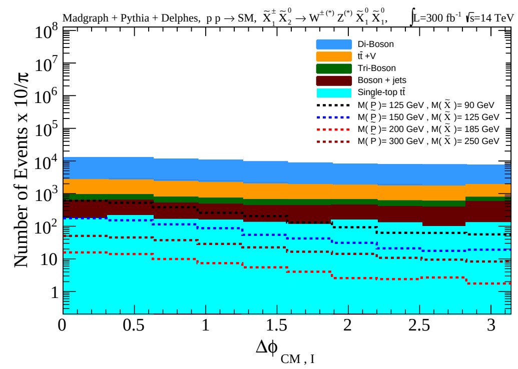

(d) Distribution of $\Delta\phi_{\text{CM,I}}$: opening angle between the CM system and the I-system.

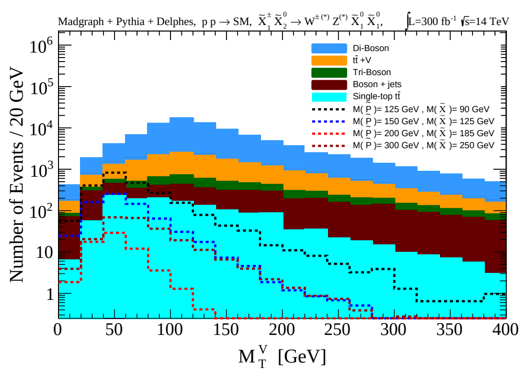

(e) Distribution of the M^{V}_{T}: transverse mass of the V-system.

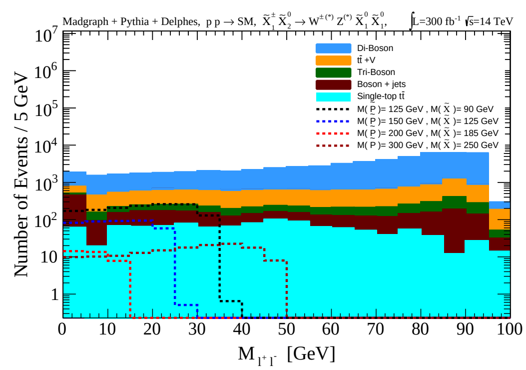

(f) Distribution of $M_{l^{+}l^{-}}$: transverse mass of the two same flavour leptons when the third lepton has different flavour.

Figure 6.2.2: Distributions of the RJR observables sensitive to compressed scenarios for events that have satisfied the preselection criteria. Standard Model backgrounds are stacked together while the overlaid dashed curves refer to four signal samples as in Figure 6.1.1. All the contributions are scaled with an integrated luminosity of 300 fb^{-1} at 14 TeV.

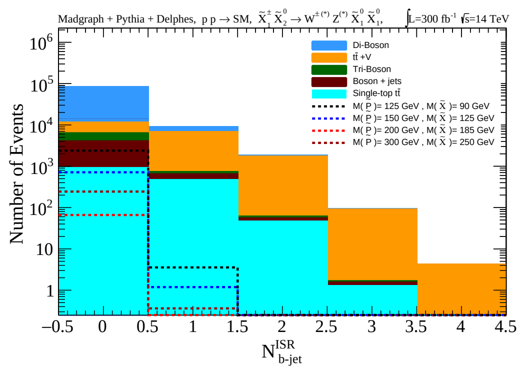

(a) Distribution of N^{ISR}_{b-jet}: number of b-jet in the final state.

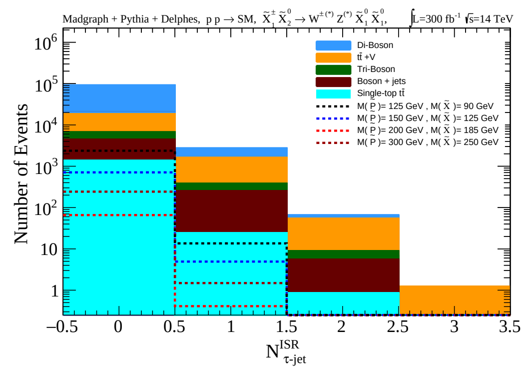

(b) Distribution of $N^{\mathrm{ISR}}_{\tau-jet}$: number of τ-jet in the final state.

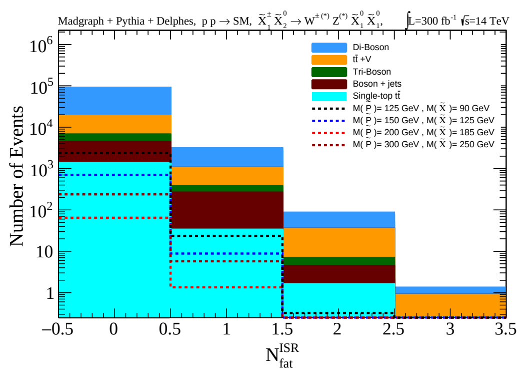

(c) Distribution of N^{ISR}_{fat}: number of fat-jet in the final state ($M(jet) > 60$ GeV).

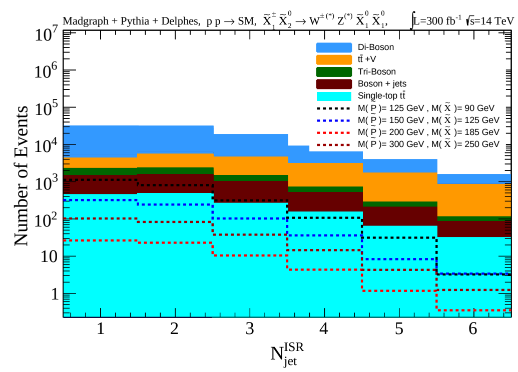

(d) Distribution of N^{ISR}_{jet}: number of light jet in the final state.

Figure 6.2.3: Distributions of the jet multiplicities for events that have satisfied the preselection criteria. Standard Model backgrounds are stacked together while the overlaid dashed curves refer to four signal samples as in Figure 6.1.1. All the contributions are scaled with an integrated luminosity of 300 fb^{-1} at 14 TeV.

Category	Snowmass label (sub-categories description)
Di-boson	BB-BLL (Di-boson + jets, off-shell Di-boson in di-lepton + jets)
$t\bar{t}$+V	TTB (top pair plus bosons, $t\bar{t}+Z$, $t\bar{t}+W$ and $t\bar{t}+h$ + jets)
Tri-boson	BBB (tri-vector-boson + jets, Higgs associated + jets)
Boson+jets	BJ-B-LL-BJJ (Vector Boson + jets, off-shell V in di-lepton, vector boson fusion)
Single-top $t\bar{t}$	TT-TB-TJ (top pair + jets, top pair (off shell $t^* \to Wj$) + jets, single top + jets)

Table 6.1: Five categories summarizing all the main Standard Model backgrounds as part of the Snowmass study. The category name is indicative of the dominant sub-category backgrounds.

Standard Model backgrounds are stacked together and categorised in five groups as in Table 6.1, while the overlaid dashed curves refer to the signal samples.

The main SM contributions are WZ boson associated production and $t\bar{t}$ processes with an additional vector boson.

The number of events passing the preselection criteria is smaller for the signal sample $M_{\tilde{\chi}_1^\pm} = M_{\tilde{\chi}_2^0}$=200 GeV, ΔM =15 GeV than the sample $M_{\tilde{\chi}_1^\pm} = M_{\tilde{\chi}_2^0}$=300 GeV, ΔM =50 GeV as can be seen from all the RJR observables. Since the electron and muon objects are assumed to have a minimal transverse momentum of 10 GeV, when the mass splitting approaches this regime the efficiency of the detector for the reconstruction of three leptons dramatically decreases. In order to probe this extreme phase space $\Delta M < 15$ GeV, a parametrisation for the efficiencies of soft leptons must be implemented [89].

Figures 6.2.2a shows the distributions of R_{ISR}. The variable provides great signal-to-background discrimination in the absence of more stringent selection criteria. The assignment of the different objects in the compressed tree is performed with no ambiguity and it is unnecessary to focus on the high ISR regime. Notice that R_{ISR} assumes values larger than unity when some objects are forced in the V-system. The signal distributions scale with the mass ratio LSP to parent sparticle: the observable is expected to be peaked for values greater than $M_{\tilde{\chi}}/M_{\tilde{P}}$ due to the additional contribution to $\not{E}_T$ coming from the neutrino. Since the hard scale is low, the mass ratio, rather than the absolute mass difference, will be considered for the R_{ISR} requirements.

Figure 6.2.2b shows the distribution of $p^{\mathrm{CM}}_{\mathrm{ISR},T}$. The hard scales for the signal and background samples are similar and the variable has no impact. In the absence of other requirements the slope for the signal is paradoxically more severe because of the background events with non radiative jets forced in the ISR-system. We have seen how a minimal requirement on $p^{\mathrm{CM}}_{\mathrm{ISR},T}$ is essential to exploit the RJR technique with multi-leptons final states. The requirement applied to this variable, being the only large scale observable in this study together with $\not\!\!E_T$, will be moderately tighter for large mass splittings, when the criterion on R_{ISR} is relaxed.

Figures 6.2.2c and 6.2.2d show the distributions of the opening angle between the ISR-system and the invisible system and between the CM system and the invisible system respectively. Both of the variables are useful to decrease the SM background yields. Once again, for $\Delta\phi_{\mathrm{ISR,I}}$, both signal and background distributions tend towards π, but the signal has a stronger tendency to do so. The distributions of $\Delta\phi_{\mathrm{CM,I}}$ for the signal samples are almost independent of ΔM.

Two transverse masses, one compressed and one topology dependent, are used in the analysis. Figure 6.2.2e shows the transverse mass of the visible system. Signal events tend to populate lower values than SM backgrounds events. This feature is expected, in particular in the low-ISR regime, since the variable is the transverse mass of the three leptons. The selection criteria applied to this scale observable will be an upper bound: a maximum, rather than a minimum value, will be required.

Figure 6.2.2f shows the transverse mass of two leptons when the third lepton in the final state has different flavour: the variable corresponds to $M_{T,\,e^+e^-}$ when the third lepton is a muon and $M_{T,\,\mu^+\mu^-}$ when the third lepton is an electron[7]. A pair of leptons with same flavour (SF) is expected from the off-shell Z boson produced from the $\tilde{\chi}^0_2$. The distribution for the signal samples has an end-point at the mass difference. A check on the electric charge is performed and the distribution refers to roughly half of the total

[7]The variable is simply labelled $M_{l^+l^-}$, avoiding to write the transverse subscript: M_{T,l^+l^-}

number of events.

Finally, Figure 6.2.3 shows the distributions for the b-jet, τ-jet, fat-jet and light jet multiplicities.[8] A veto is applied to the b-jets, helpful against $t\tilde{t}$ +V, while vetoing on fat and τ have no impact. For the light jet number an opposite strategy will be used. The Standard Model backgrounds are expected to have a higher jet multiplicity due to non-ISR jets, hence upper bounds will be applied in the signal regions.

This is a complete basis of $transverse$ observables: other possible general and topology dependent variables give redundant or no additional information. The scale variable M_T^{S} has no great impact since the hard scale and the mass-difference scale are too small for the signal. Other topology dependent variables such as the i-th lepton p_T are not exploited: M_T^{V}, in such a way, treats the three lepton transverse momenta and the relative angles in one. No additional information can be extracted from the distributions of $p^{\mathrm{V}}_{\mathrm{lep1},T}$, $p^{\mathrm{V}}_{\mathrm{lep2},T}$ or $p^{\mathrm{V}}_{\mathrm{lep3},T}$.

Additional handles could be extracted considering the whole supersymmetric tree restoring the three-dimensional view of the event. For this analysis we want to emphasize the performance of the RJR technique obtained exploiting only transverse observables.

6.2.2 Two-dimensional distributions

The transverse momentum of the ISR-system $p^{\mathrm{CM}}_{\mathrm{ISR},T}$ has a small impact on the discrimination of the SM backgrounds, but a minimal requirement ($>$ 50 GeV), together with $\not{E}_T$ >50 GeV, is a *sine qua non* condition in order to focus on the final states of interest and exploit the RJR technique for compressed scenarios. From now on this requirement, together with a veto on jets tagged as bottoms is applied.

The ratio R_{ISR}, sensitive to the the mass ratio $M_{\tilde{\chi}}/M_{\tilde{P}}$, has a high impact also in the low-ISR regime due to the unambiguity in the separation of the V and ISR systems. The

[8]The numbers of light jets, b-jets, τ-jets and fat-jets in the ISR-system are equivalent to the respective multiplicities in the final state, because no jets are assigned to the V-system.

visible system, corresponding to three leptons, is expected to provide a small transverse mass for the signal samples. An increment for the value of $p^{\mathrm{CM}}_{\mathrm{ISR},T}$ is expected to increase mainly the transverse momentum of the two LSPs.

Figures 6.2.4 and 6.2.5 show the two dimensional distributions of M_T^{V} as a function of R_{ISR} for the two main Standard Model backgrounds and two signal samples for events passing the preselection criteria, $N^{\mathrm{ISR}}_{b-\mathrm{jet}} = 0$ and $p^{\mathrm{CM}}_{\mathrm{ISR},T} > 50$ GeV. The final state signal events populate low values of M_T^{V} with a complementarity with high values of R_{ISR}. Vice versa for the backgrounds events, in particular for the di-boson Standard Model background which is shown in Figure 6.2.4a, simultaneous low values of M_T^{V} and R_{ISR} close to one are unlikely.

Using the two RJR observables in concert provides a increasingly powerful discrimination the smaller the absolute and relative mass splitting of the signal samples.

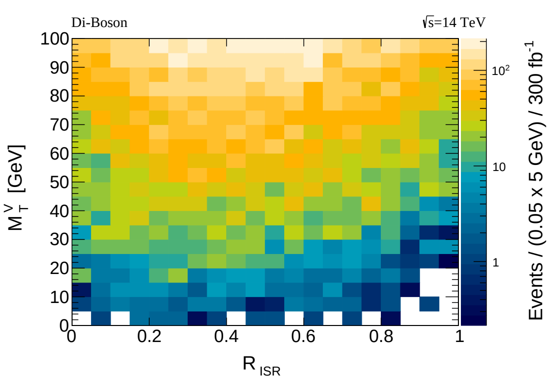

(a) The scatter plot R_{ISR} vs M_T^{V} refers to the di-boson Standard Model background.

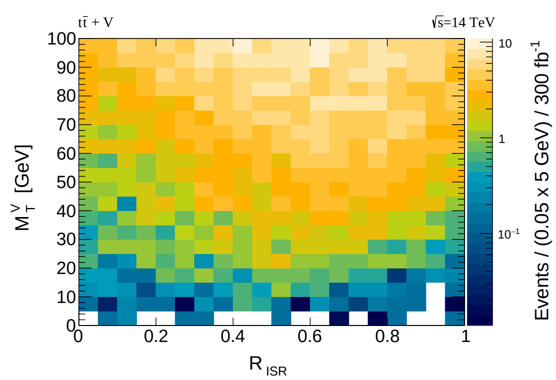

(b) The scatter plot R_{ISR} vs M_T^{V} refers to the $t\bar{t}$ plus vector boson background.

Figure 6.2.4: Distribution of the M_T^{V} as a function of R_{ISR} for the two main Standard Model backgrounds. The two-dimensional histograms show the number of events expected per bin for an integrated luminosity of 300 fb^{-1} satisfying the preselection criteria, $N^{\mathrm{ISR}}_{b-\mathrm{jet}} = 0$ and $p^{\mathrm{CM}}_{\mathrm{ISR},T} > 50$ GeV for low values of the transverse mass of the V-system: $M_T^{\mathrm{V}} < 100$ GeV.

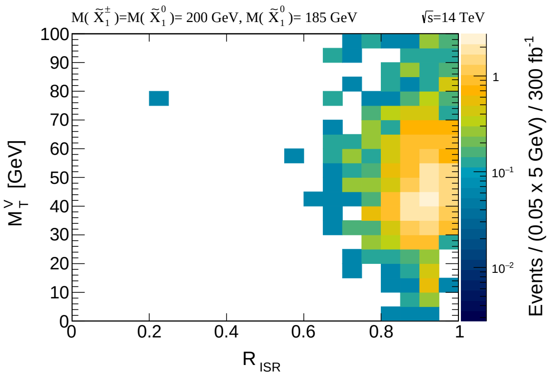

(a) The scatter plot R_{ISR} vs M_T^{V} refers to the signal sample $M_{\tilde{\chi}_1^\pm} = M_{\tilde{\chi}_2^0}$=200 GeV, $M_{\tilde{\chi}_1^0}$=185 GeV.

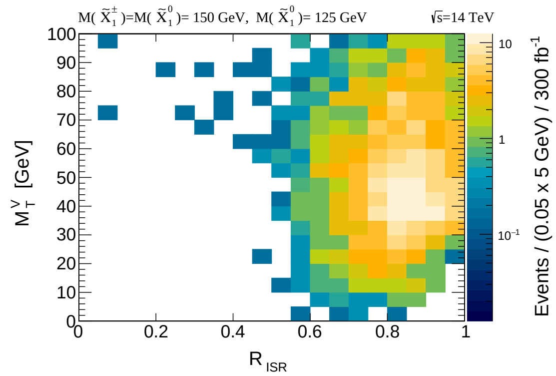

(b) The scatter plot R_{ISR} vs M_T^{V} refers to the signal sample $M_{\tilde{\chi}_1^\pm} = M_{\tilde{\chi}_2^0}$=150 GeV, $M_{\tilde{\chi}_1^0}$=125 GeV.

Figure 6.2.5: Distribution of the M_T^{V} as a function of R_{ISR} for two signal samples with $\Delta M = 15$ GeV (6.2.5a) and $\Delta M = 25$ GeV (6.2.5b). Preselection criteria, $N_{b-\text{jet}}^{\text{ISR}} = 0$, $p_{\text{ISR},T}^{\text{CM}} > 50$ GeV and $M_T^{\text{V}} < 100$ GeV are demanded.

In the low M_T^{V} regime, additional handles to decrease the SM background yields are provided by the compressed-transverse RJR angles and $M_{l^+l^-}$. Figures 6.2.6 show the two-dimensional distributions of $\Delta\phi_{\text{ISR,I}}$, $\Delta\phi_{\text{CM,I}}$ and $M_{l^+l^-}$ as a function of the ratio R_{ISR} for $M_T^{\text{V}} < 100$ GeV for the di-boson processes, the $t\bar{t}$+V backgrounds and two signal samples. For high values of R_{ISR}, signal events tend to populate higher values of the angular variable $\Delta\phi_{\text{ISR,I}}$, and values closer to zero for $\Delta\phi_{\text{CM,I}}$ than the backgrounds. The distributions of $M_{l^+l^-}$ vs R_{ISR} are shown for final states with two leptons with same flavour and opposite electric charge or sign (SFOS), while the third lepton in the V-system is identified with different flavour. The transverse mass for the two SFOS leptons provides an additional handle in order to discriminate between putative compressed sparticle signals and SM backgrounds. For the signal, as shown in Figures 6.2.6i and 6.2.6l, the transverse mass of the two leptons has a clean maximum at $\triangle M$. Figure 6.2.7 shows the one-dimensional distributions for $R_{\text{ISR}} > 0.6$.

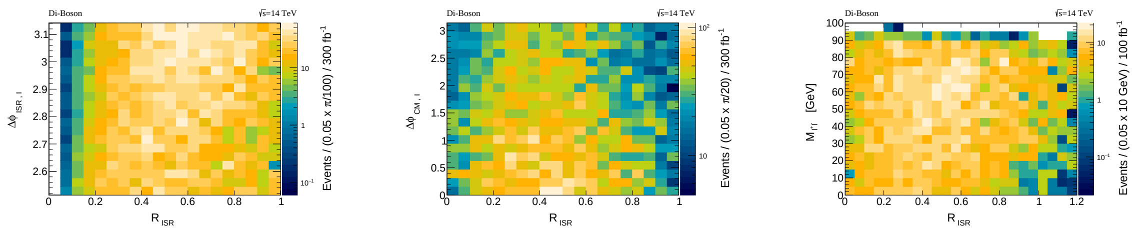

(a) R_{ISR} vs $\Delta\phi_{\text{ISR,I}}$. (b) R_{ISR} vs $\Delta\phi_{\text{CM,I}}$. (c) R_{ISR} vs $M_{l^+l^-}$ for final states with two SFOS leptons.

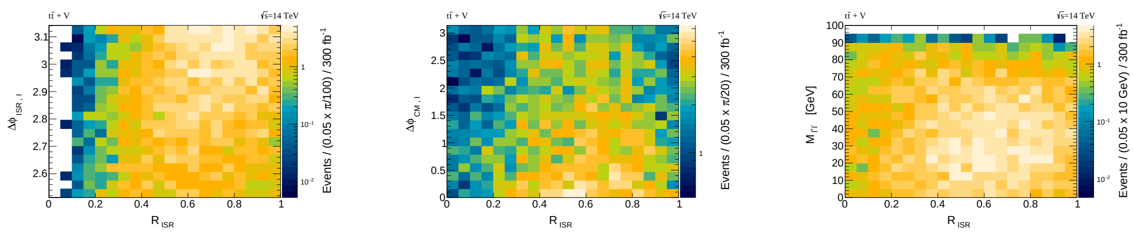

(d) R_{ISR} vs $\Delta\phi_{\text{ISR,I}}$. (e) R_{ISR} vs $\Delta\phi_{\text{CM,I}}$. (f) R_{ISR} vs $M_{l^+l^-}$ for final states with two SFOS leptons.

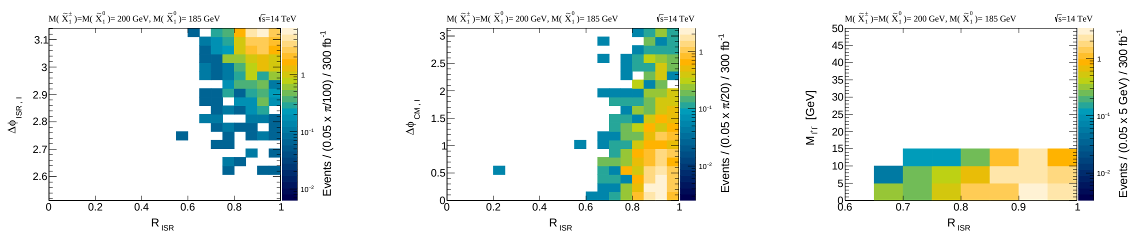

(g) R_{ISR} vs $\Delta\phi_{\text{ISR,I}}$. (h) R_{ISR} vs $\Delta\phi_{\text{CM,I}}$. (i) R_{ISR} vs $M_{l^+l^-}$ for two SFOS leptons.

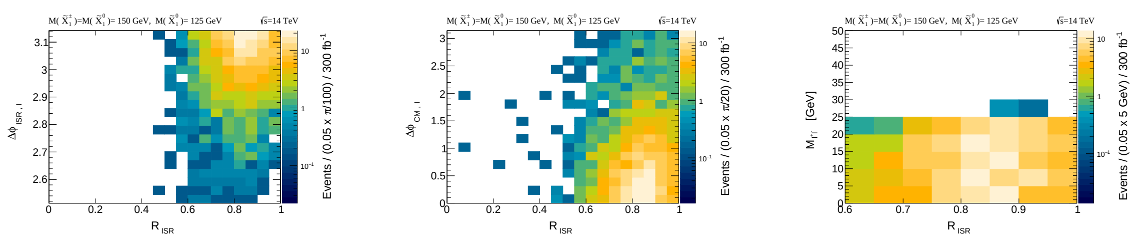

(j) R_{ISR} vs $\Delta\phi_{\text{ISR,I}}$. (k) R_{ISR} vs $\Delta\phi_{\text{CM,I}}$. (l) R_{ISR} vs $M_{l^+l^-}$ for final states with two SFOS leptons.

Figure 6.2.6: Two-dimensional distributions of $\Delta\phi_{\text{ISR,I}}$ (left), $\Delta\phi_{\text{CM,I}}$(centre) and $M_{l^+l^-}$ (right) as a function of R_{ISR} for the Standard Model di-boson background (6.2.6a - 6.2.6b - 6.2.6c), $t\bar{t}$+V background (6.2.6d - 6.2.6e - 6.2.6f), the signal sample $M_{\tilde{P}}$=200 GeV, $M_{\tilde{\chi}}$=185 GeV (6.2.6g - 6.2.6h - 6.2.6i) and the signal sample $M_{\tilde{P}}$=150 GeV, $M_{\tilde{\chi}}$=125 GeV (6.2.6j - 6.2.6k - 6.2.6l). The two-dimensional histograms show the number of events expected per bin for an integrated luminosity of 300 fb^{-1} satisfying the preselection criteria, $N_{b-\text{jet}}^{\text{ISR}} = 0$, $p_{\text{ISR},T}^{\text{CM}} > 50\,\text{GeV}$ and $M_T^{\text{V}} < 100$ GeV.

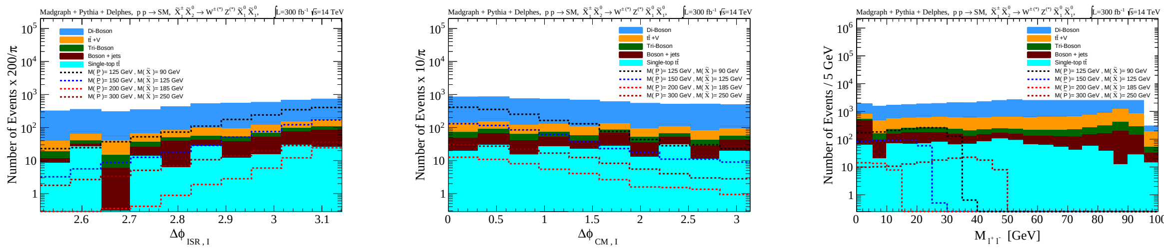

(a) (b) (c)

Figure 6.2.7: Distributions of the $\Delta\phi_{\mathrm{ISR,I}}$ (6.2.7a), $\Delta\phi_{\mathrm{CM,I}}$(6.2.7b) and $M_{l^+l^-}$ (6.2.7c) for the events satisfying the preselection criteria, $N^{\mathrm{ISR}}_{b\mathrm{-jet}} = 0$, $p^{\mathrm{CM}}_{\mathrm{ISR},T} > 50$ GeV, $M^{\mathrm{V}}_{T} < 100$ GeV and $R_{\mathrm{ISR}} > 0.6$.

6.2.3 Signal regions

Selection criteria defined with the compressed RJR observables result in signal regions used to investigate chargino-neutralino associated pair-production in final states with three leptons and missing transverse momentum. One or more additional jets are assumed to be radiated from the initial state and a minimal requirement on $p^{\mathrm{CM}}_{\mathrm{ISR},T}$ allow us to focus on the final states of interest. The strategy is based on a simple cut and count analysis with a moderate optimisation.

The signal regions target five mass splittings as shown in Table 6.2. A special treatment is assumed for R_{ISR} for the samples investigated, being the ratio related to the mass ratio $M_{\tilde{\chi}}/M_{\tilde{P}}$ rather than the absolute value of the mass splitting.

The first row refers to common *objects*-criteria and a veto is applied on the number of b-jets. Tighter criteria are used for the only large scale variables ($p^{\mathrm{CM}}_{\mathrm{ISR},T}$ and $\not{E}_T$), and $\Delta\phi_{\mathrm{CM,I}}$ whereas for larger mass differences (ΔM = 50, 75 GeV) the R_{ISR} requirement is relaxed.

The highest impact of the RJR observables is for the samples of mass difference in the range 20-40 GeV. For ΔM=15 GeV the challenge come from the inefficiency in the reconstruction of three leptons while for the highest values (ΔM = 50, 75 GeV) the ratio $M_{\tilde{\chi}}/M_{\tilde{P}}$ decreases substantially. For these scenarios the light jet multiplicity in the ISR-system is constrained to a maximum of two jets in order to restrict the

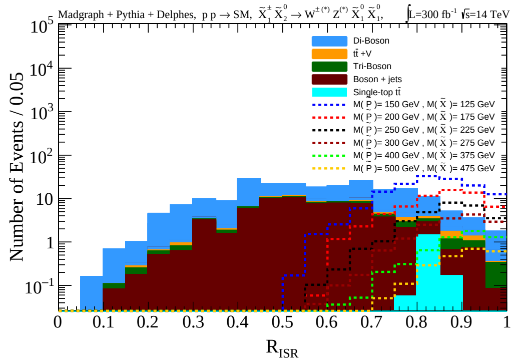

(a) The distribution of $R_{\rm ISR} = \frac{|\vec{p}^{\,\rm CM}_{\rm I,\mathit{T}} \cdot \hat{p}^{\rm CM}_{\rm ISR,\mathit{T}}|}{p^{\rm CM}_{\rm ISR,\mathit{T}}}$, for the signal and BG events passing the selection criteria in Table 6.2 column 2.

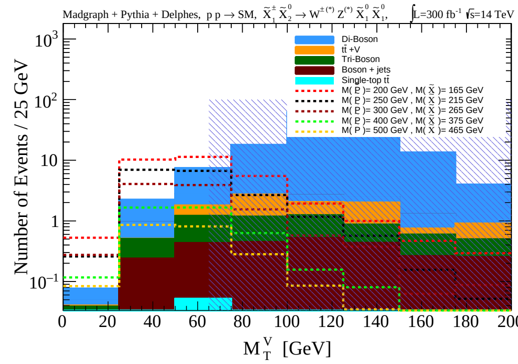

(b) The distribution of $M_T^{\rm V}$ for signal samples with $\Delta M = 35$ GeV and SM backgrounds after the application of the requirements in Tables 6.2.

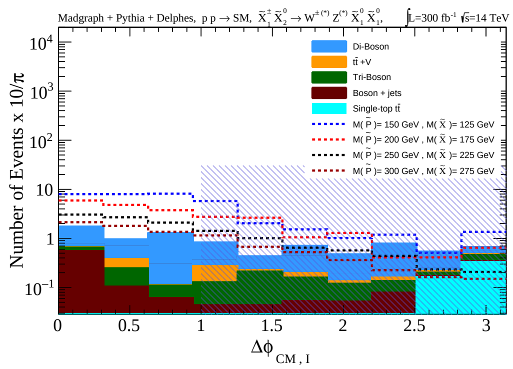

(c) The distribution of $\Delta\phi_{\rm CM,I}$ for signal samples with $\Delta M = 25$ GeV and SM backgrounds after the application of the N-1 requirements in Tables 6.2.

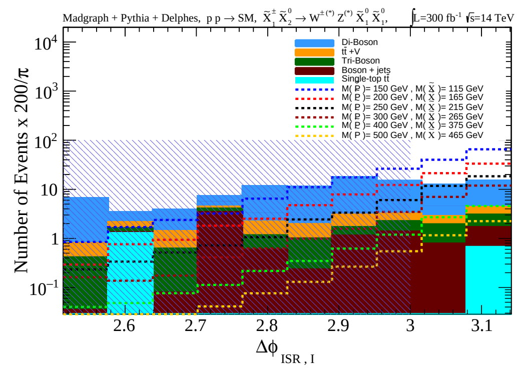

(d) The distribution of $\Delta\phi_{\rm ISR,I}$ for signal samples with $\Delta M = 35$ GeV and SM backgrounds after the application of the N-1 requirements in Table 6.2.

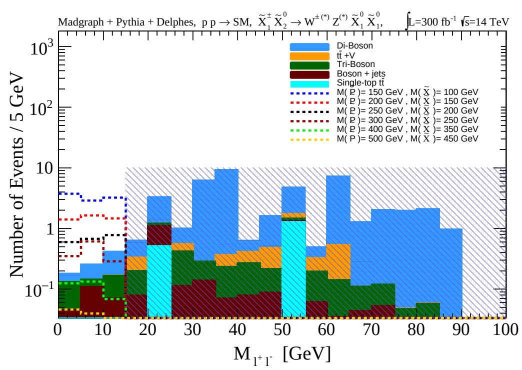

(e) The distribution of the transverse mass of the two SFOS leptons for signal samples with $\Delta M = 50$ GeV and SM backgrounds after the application of the N-1 requirements in Table 6.2 in final states with $M_T^{\rm V}$ <100 GeV and the third lepton with different flavour.

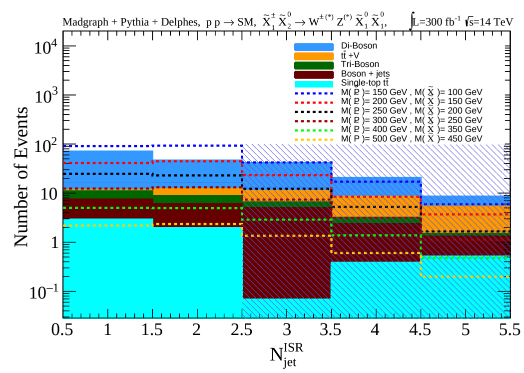

(f) The distribution of $M_T^{\rm V}$ for signal samples with $\Delta M = 50$ GeV and SM backgrounds after the application of the N-1 requirements in Table 6.2.

Figure 6.2.8: The distributions of the RJR observables sensitive to compressed scenarios for signal and Standard Model background events passing the selection criteria in one signal regions of Table 6.2. All selection criteria are applied, except the requirement on the variable that is displayed.

<table>
<tr><th></th><th colspan="5">Mass Splitting [GeV]</th></tr>
<tr><th>Variable</th><th>$\Delta M = 15$</th><th>$\Delta M = 25$</th><th>$\Delta M = 35$</th><th>$\Delta M = 50$</th><th>$\Delta M = 75$</th></tr>
<tr><td>Object multiplicity selection criteria</td><td colspan="5">3 Leptons (e and μ) with $p_T^{\rm lep} > 10$ GeV,
At least one jet, $p_T^{\rm jet} > 20$ GeV, $N_{b-\rm jet}^{\rm ISR} = 0$</td></tr>
<tr><td>$p_{{\rm ISR},T}^{\rm CM}$ ($\not{E}_T$) > [GeV]</td><td colspan="3">50</td><td>70</td><td>120</td></tr>
<tr><td>$N_{\rm jet}^{\rm ISR}$ <</td><td>3</td><td colspan="2">4</td><td colspan="2">3</td></tr>
<tr><td>$M_T^{\rm V}$ <, for 3 SFL [GeV]</td><td>40</td><td>50</td><td>65</td><td>75</td><td>90</td></tr>
<tr><td>$M_{l^+l^-}$ <, for 2 SFL [GeV] ($M_T^{\rm V} < 100$ GeV)</td><td>15</td><td>25</td><td>35</td><td>50</td><td>75</td></tr>
<tr><td>$\Delta\phi_{\rm CM,I}$ <</td><td colspan="3">1</td><td>0.7</td><td>0.5</td></tr>
<tr><td>$\Delta\phi_{\rm ISR,I}$ ></td><td colspan="5">3</td></tr>
<tr><td>$R_{\rm ISR}$ ></td><td>0.85, 0.9</td><td>0.8, 0.85
0.9</td><td>0.8, 0.85</td><td>0.7, 0.8
0.85</td><td>0.65, 0.7
0.75</td></tr>
</table>

Table 6.2: A conservatively optimised set of selection criteria for signal regions in the analysis of chargino neutralino production in final states with three leptons and missing energy.

background events.

The requirement on $M_T^{\rm V}$ is an upper bound and the maximum grows with ΔM, while $M_{l^+l^-}$ has a maximum defined exactly by the mass splitting itself. In final states with three electrons or three muons only the $M_T^{\rm V}$ requirement is applied while for events with two same flavour leptons and one different flavour lepton the selection on $M_{l^+l^-}$ is required together with $M_T^{\rm V}$ <100 GeV. An optimisation based on the distribution of $\Delta\phi_{\rm ISR,I}$ could be performed. We tune the criterion on $R_{\rm ISR}$ so that the minimal requirement increases for decreasing relative mass splittings: equivalent to increasing $M_{\tilde{P}}$ maintaining ΔM fixed or decreasing ΔM with $M_{\tilde{P}}$ fixed. The criteria assume values interspersed by 0.05, which provides a moderate optimisation.

For example, Figure 6.2.8a suggests to demand $R > 0.8$ for the signal sample with $M_{\tilde{P}} = 150$ GeV, $R > 0.85$ for $M_{\tilde{P}} = 200$ and 250 GeV and $R > 0.9$ for the remaining three samples. Other distributions for the RJR observables are shown in Figure 6.2.8 applying the N-2 criteria in Table 6.2 and a fixed requirement for $R_{\rm ISR}$.

6.2.4 Results

Selection criteria on the RJR observables are imposed for the definition of the signal regions in Table 6.2. Such signal regions are applied to calculate sensitivities for compressed spectra signal samples for a projection of 300 fb^{-1}. The topology investigated is shown in the Feynman diagram in Figure 6.1.1: the $\sqrt{s}$=14 TeV proton-proton scattering produces a chargino neutralino pair, with 125 GeV$\leq M_{\tilde{P}} \leq$ 500 GeV, in final states with three leptons and two LSPs, with mass differences in the range 15 GeV$\leq \Delta M \leq$ 75 GeV. Figures 6.2.9 shows the Z-score or Z_{Bi} calculated assuming the metric [94] and described in Section 3.5.1. A flat systematic uncertainty of 20% is assumed for the overall Standard Model background. The main contribution arises from the irreducible WZ associated production.

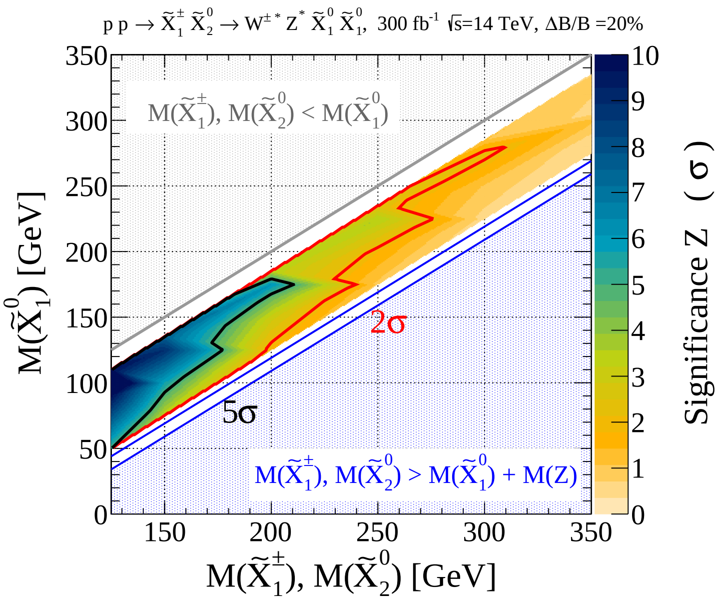

Figure 6.2.9: Projected exclusion and discovery reach for chargino-neutralino associated production in the compressed region (15 GeV $\leq \Delta M \leq$ 75 GeV) at $\sqrt{s}$ = 14 TeV for an integrated luminosity of 300 fb^{-1}.

For mass splittings in the range 20-40 GeV the RJR observables provide great potential to distinguish signal from background. The signal yields in the extreme compressed scenarios can benefit from an improvement in the efficiencies of the detector in the

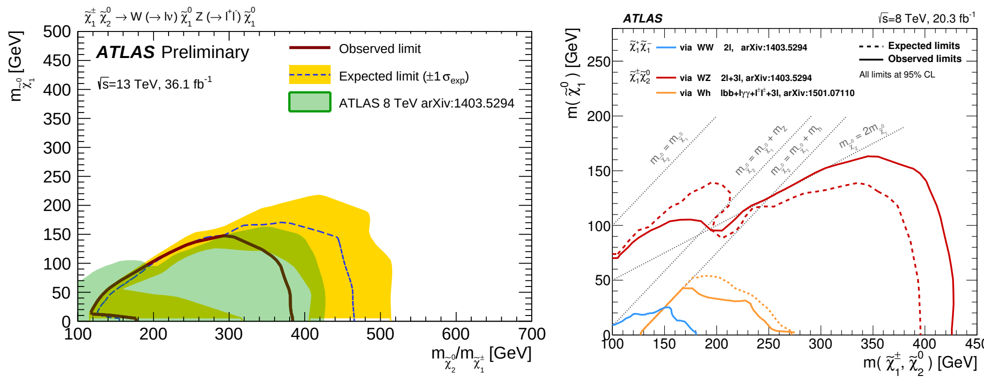

(a) (b)

Figure 6.2.10: Observed and expected exclusion contours at the 95% CL in the $M_{\tilde{\chi}_1^\pm} = M_{\tilde{\chi}_2^0}$ vs $M_{\tilde{\chi}_1^0}$ plane. Current results from the ATLAS collaboration for the search of the SUSY simplified topology $pp \to \tilde{\chi}_1^\pm \tilde{\chi}_2^0, (\tilde{\chi}_1^\pm \to W^\pm \tilde{\chi}_1^0), (\tilde{\chi}_2^0 \to Z\tilde{\chi}_1^0)$ at $\sqrt{s}$=13 TeV [133] (a). Summary plot for the topologies $pp \to \tilde{\chi}_1^\pm \tilde{\chi}_2^0, (\tilde{\chi}_1^\pm \to W^\pm \tilde{\chi}_1^0), (\tilde{\chi}_2^0 \to Z(h)\tilde{\chi}_1^0)$ and $pp \to \tilde{\chi}_1^+ \tilde{\chi}_1^- (\tilde{\chi}_1^\pm \to W^\pm \tilde{\chi}_1^0)$, at $\sqrt{s}$=8 TeV (b). Few scenarios are excluded in the compressed region.

reconstruction of low-momentum leptons, which is outside the scope of this work. On the other hand, the significances decrease for mass differences close to the W pole mass due the difficulty of discriminating background events derived from topologies with absolute and relative mass scales very close to the signal ones.

For an integrated luminosity 300 fb^{-1}, degenerate charginos and neutralinos would be discovered for masses $M_{\tilde{\chi}_1^\pm} = M_{\tilde{\chi}_2^0}$ >150 GeV for a portion of the samples investigated and excluded up to 300 GeV for the best scenarios.

The value ΔM =15 GeV must not be considered as a threshold: the minimum mass difference achievable with any technique is strongly related to the efficiencies for the detector to reconstruct low-momentum leptons. For extremely compressed scenarios, a similar analysis could be used to probe the same final states topology with only two low-momentum leptons reconstructed, although the background would differ in that case. In such analysis, one could require two same sign leptons to suppress the SM yield.

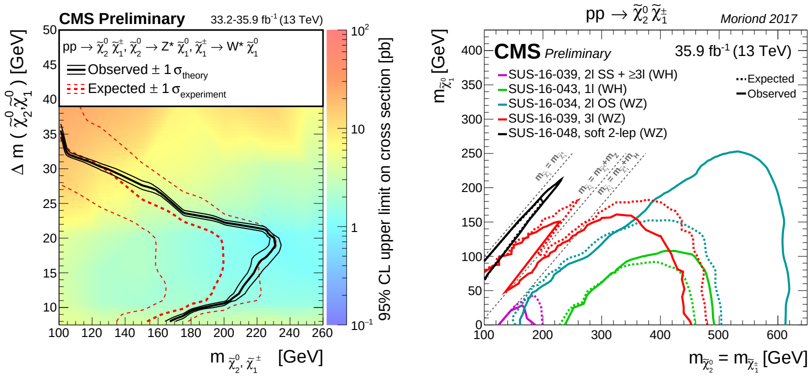

(a) (b)

Figure 6.2.11: Current results from the CMS collaboration for the search of the SUSY simplified topology $pp \to \tilde{\chi}_1^{\pm}\tilde{\chi}_2^0, (\tilde{\chi}_1^{\pm} \to W^{\pm}\tilde{\chi}_1^0), (\tilde{\chi}_2^0 \to Z\tilde{\chi}_1^0)$ in final states with two soft leptons [89] (a). The exclusion limits at the 95% CL correspond to the black lines in Figure (b). The study in this thesis should be compared with the red line.

6.3 Chargino pair-production

The signal samples are simulated proton-proton collisions at $\sqrt{s} = 14$ TeV producing a pair of charginos with opposite electric charge. The focus is on final states with two leptons as illustrated in the Feynman diagram in Figure 6.1.2. The samples are generated within the mass ranges 100 GeV $\leq M_{\tilde{\chi}_1^{\pm}} \leq$ 300 GeV, with the five mass splittings $\Delta M = M_{\tilde{P}} - M_{\tilde{\chi}} = 15$, 25, 35, 50 and 75 GeV.

In order to improve the signal-to-background discrimination we enrich the simplified version of the compressed RJR tree by specifying the substructure of the S-system. This is feasible since in the two lepton final state one has no doubt of reconstructing all the visible sparticle decay products. In any case, the useful transverse variables of the simplified tree can be computed. In the previous study, a similar approach could be used to increase the number of RJR observables and improve the performance of the method.

For the chargino pair topology, there are two options: reconstruct the whole chain or consider each chargino to decay to a visible and an invisible object. In the first case each hemisphere of the S-system would have two invisible and one visible object.

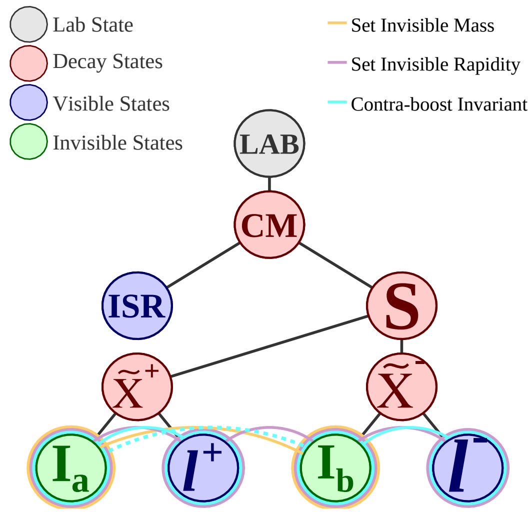

Figure 6.3.1: The RJR decay tree for the analysis of compressed chargino pair-production in events with ISR. The substructure of the SUSY system is the follow: each chargino decays in a visible (lepton) and an invisible (neutrino + neutralino) object.

There are not enough jigsaw rules in order to assign the unknown d.o.f. for the four invisible weakly interacting particles, because two leptons are the only particles reconstructed by the detector decaying from the S-system. Test masses for the invisible systems are not suitable for the three body decay kinematics. We could fake the neutrinos by assigning the same three-momenta of the correspondent leptons. In this case each W-system would be faked by a massless object with twice the lepton three-momentum. Here, we do not adopt this strategy. One of the purposes of the RJR technique is to amplify the uncorrelation, avoiding redundant information, for the basis of observables. Reconstructing the whole tree assuming *a priori* the three-momenta of the neutrinos means to redistribute, event-by-event, the same final state information between more RJR observables.

The RJR tree is shown in Figure 6.3.1. Electrons and muons are associated with the l^+ and l^- systems, depending to the electric charge, while the jets are associated with the ISR-system. The S-system frame is the approximation for the centre-of-mass of the two charginos and each one decays to a lepton and an invisible system. Each invisible system collects the neutrino-neutralino contribution of the hemisphere a and b.

In the overall centre-of-mass frame the ISR and S-system are back-to-back. The invariant mass of the invisible objects in this simple case would correspond to the invariant mass of the two leptons (see Eq. 4.2.17). The rapidity is assigned as to the chargino centre-of-mass (S-system) and the contra-boost invariant jigsaw rule repartitions the remaining two unknown degrees of freedom.

The lepton multiplicity of the final state determines the main contributions of the Standard Model processes. Roughly, the smaller the number of electrons plus muons, the larger the main contributions from the Standard Model backgrounds. The dileptonic channels of a pair of W bosons, constitute the main process resulting in a final state with two opposite sign leptons and missing transverse momentum, in the absence of hadronic jets.

Searches for chargino pair-production in a final state with two leptons are challenging for open mass spectra due to the huge W^+W^- irreducible background, while other contributions are often negligible. As amply discussed, in the compressed regime the challenge is exacerbated by the low momenta of invisible and visible objects and the subsequent kinematics. Requiring a transverse momentum for the ISR-system introduces an additional complication for the analysis in the compressed regime: other Standard Model backgrounds can contribute significantly.

6.3.1 Another look at the RJR observables

Considering the three-dimensional view of the event, and the S-system not divided into the simple V-I substructure, a basis of RJR observables can be extracted. Nevertheless, having in mind the simplified tree, where I corresponds to the sum of the two invisible systems $\mathrm{I} = \mathrm{I}_a + \mathrm{I}_b$ and V to the sum of the two lepton systems $\mathrm{V} = l^+ + l^-$, we can still define the transverse observables:

- $R_{\mathrm{ISR}} = \frac{\left|\vec{p}^{\,\mathrm{CM}}_{\mathrm{I},T} \cdot \hat{p}^{\,\mathrm{CM}}_{\mathrm{ISR},T}\right|}{p^{\mathrm{CM}}_{\mathrm{ISR},T}}$: variable sensitive to the mass ratio parent LSP.

- $p^{\mathrm{CM}}_{\mathrm{ISR},T}$: magnitude of vector-sum of the jets transverse momentum evaluated in the CM frame.

- $\Delta\phi_{\mathrm{ISR,I}}$: opening angle between the ISR-system and the I-system, evaluated in the CM frame.

The observables assume values slightly different from the case with the simplified compressed RJR tree since the old I-system is treated as a unique massless particle. Three-dimensional scale-mass variables and additional angular observables include:

- M^{V}: mass associated to the V-system (invariant mass of $l^+ + l^-$).

- $M^{\tilde{\chi}^{\pm}}$: mass associated to the chargino system.

- $\Delta\phi_{\mathrm{l}^+,\mathrm{I}}$ ($\Delta\phi_{\mathrm{l}^-,\mathrm{I}}$): polar angle between the positive (negative) charge lepton and $\vec{\not\!\!E}_T$ computed in the Lab frame.

- $\Delta\phi_{\mathrm{CM,I}}$: opening angle between the CM system and the I-system.

- $\cos\theta \equiv \hat{\beta}^{\mathrm{CM}}_{S} \cdot p^{\mathrm{S}}_{\mathrm{I},T}$: the dot product between the direction of the boost from CM to the reconstructed S frame and the transverse momentum of the I-system in the S frame.

- object multiplicities.

For the RJR tree specified in Figure 6.3.1, the contra-boost invariant rule for the two chargino S-system depends on the d.o.f. of only two visible objects: the two leptons in the final state. In such a case, not only the re-partition of the unknown d.o.f. is such that $M^{\tilde{\chi}^+} = M^{\tilde{\chi}^-}$, but in each chargino frame the three-momenta of the lepton and the invisible system are identical and correspond to half of $M^{\tilde{\chi}^{\pm}}$ in the limit of massless objects (see Eq. 4.2.37 with $N = L$). In other words, the energies of the leptons in the reconstructed chargino rest frames give no additional information.

Category	Snowmass label (sub-categories description)
Boson + jets	BJ-B-LL(Vector Boson + jets, Drell-Yan in di-lepton)
t + X	TT-TB-TJ-TTB (top pair, top pair (off shell $t^* \to Wj$), single top plus jets, top pair plus bosons + jets)
Di-boson	BB-BLL (Di-Vector + jets, off-shell Di-Vector in di-lepton +jets)
Others	BJJ-BBB-H (Vector boson fusion, tri-Vector +jets, Higgs associated +jets)

Table 6.3: Four categories summarizing all the main Standard Model backgrounds as part of the Snowmass study. The category name is indicative of the sub-processes.

The important scale observable, labelled $M^{\tilde{\chi}^{\pm}}$, will not reproduce the true chargino mass, being that the true LSP is massive and the $\mathrm{I}_{a,b}$ systems, in each hemisphere, are simplifications of the neutralino+neutrino contribution. Nevertheless, the distribution of $M^{\tilde{\chi}^{\pm}}$ is expected to be particularly useful to distinguish the signal from the SM processes in which small mass objects populate the $\tilde{\chi}^{\pm}$ system.

Since the experimental observables are a combination based on the imposition of a simplified transverse RJR tree and a more complicated tree plus additional canonical handles, several details are described for their key features and impact to reduce different SM background yields.

6.3.2 Preselection

In this section the distributions of the main RJR observables are described for the events satisfying preselection criteria. Two leptons (electrons and muons) are required in the final state with $p_T > 10$ GeV and at least one jet with $p_T > 20$ GeV is associated to the ISR-system. The requirement of jets in the final state associated with the ISR-system, in order to exploit the RJR technique in the compressed regime, inevitably increases the contribution of several Standard Model backgrounds otherwise negligible with a jet veto.

The main Standard Model backgrounds are categorised in four groups and specified in Table 6.3. The boson + jet (in blue) background is mainly $Z \to l^+l^-$+ jets. The t+X (in yellow) background is the sum of all the Standard Model contributions with at least one

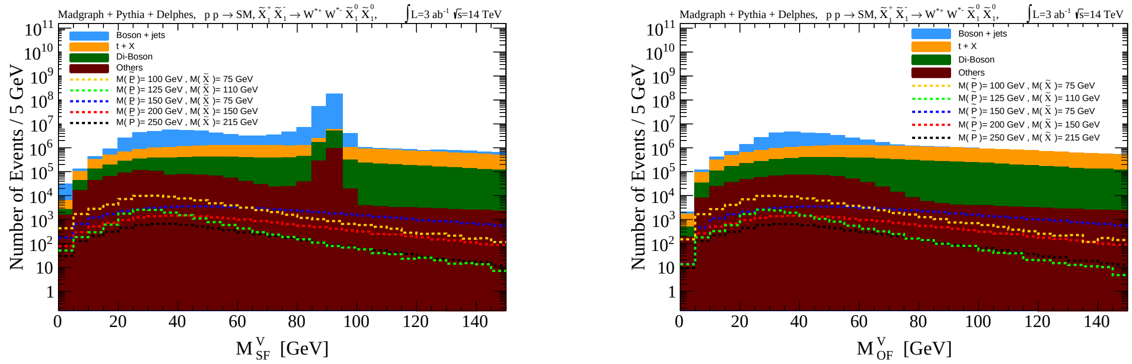

(a) (b)

Figure 6.3.2: The distributions of the invariant mass of the two leptons for same (6.3.2a) or different (6.3.2b) flavour.

top quark. The LHC can be considered a $t\bar{t}$ factory due to the production cross section and the di-leptonic channel for the two tops provides a non-negligible contribution. The green background is substantially the irreducible W^+W^- in final states with two leptons and missing transverse momentum. Finally "other" contributions, summarised in red and described in Table 6.3, are mainly di-boson fusion and $h \to W^+W^-$ or $h \to \tau^+\tau^-$processes.

Firstly, consider the invariant mass of the two leptons, corresponding to the RJR observable $M^{\mathrm{V}}$for the final state topology investigated. Figure 6.3.2 shows the distribution of the invariant mass of the two leptons for same and different flavour assuming a minimal value for the missing transverse momentum $\not{E}_T > 20$ GeV. A feature which is worth to notice is the peak around 90 GeV for same flavour leptons in the M^{V} distribution, due to the Standard Model backgrounds Z + jets (in blue), moderately for the WZ (in green) and di-boson fusion and tri-boson (in red). Requiring a different flavour for the two leptons cuts all the backgrounds with a contribution $Z \to l^+l^-$, but reduces the statistics by half. Stringent criteria on $\not{E}_T$ and $p^{\mathrm{CM}}_{\mathrm{ISR},T}$ are efficient only for the single Z background. In the compressed regime the final state events for all the signal distributions tend to populate low values of M^{V} and a requirement $M^{\mathrm{V}} < 70$, or more stringent, will be used in the signal regions. Here, in order to have a better understanding of the distributions of the RJR observables, final states with two same flavour leptons with an invariant mass in the Z window are excluded: $M^{\mathrm{V}}_{SF} < 70$ GeV or $M^{\mathrm{V}}_{SF} > 110$ GeV.

Notice the additional peak for low values of M^{V}, mainly due to the $Z+$ jets and di-boson fusion contributions resulting in a comparable number of events for the cases with two leptons with same or different flavour. The main processes to contribute are $Z \to \tau^+\tau^- \to l^+l^-\nu\nu\nu\nu$, and moderately Dell-Yan processes with missing transverse momentum $(Z^*(\gamma^*) \to \tau^+\tau^-)$ or the single W boson via the leptonic channel with an additional lepton faked by a jet or a photon. For the di-leptonic decay of the Z boson via taus the value of M^{V} is clearly expected to be smaller than the Z mass, challenging the analysis for the compressed scenarios of chargino pair-production.

Herein, the preselection criteria are the following: two leptons, at least one jet, and a minimal $\not{E}_T > 50$ GeV are required. In addition, for final states with two same flavour leptons, $M^{\mathrm{V}}_{SF}< 70$ GeV or $M^{\mathrm{V}}_{SF} > 110$ GeV is imposed.

The RJR observables are shown in Figures 6.3.3 and 6.3.4 for the events passing the preselection criteria.

For the signal sample with ΔM =15 GeV (green dashed curve) the number of events passing the preselection criteria is small, considering the production cross section, when compared to the other samples. Similarly to the previous study this is a consequence of the conservative minimal value chosen for the transverse momenta of electrons and muons (10 GeV). The number of events passing the criteria decrease significantly when the mass splitting approaches this regime because the kinematics is such that one of the two leptons likely has a transverse momentum smaller than 10 GeV and so is not considered as a reconstructed object by the detector.

Figure 6.3.3a shows the distribution of R_{ISR}. The observable provides a good signal-to-background discrimination, but additional selection criteria are necessary. The R_{ISR} distributions have the shapes expected. The signal distributions scale with the ratio of the LSP mass to the parent sparticle mass. The observable is expected to be peaked

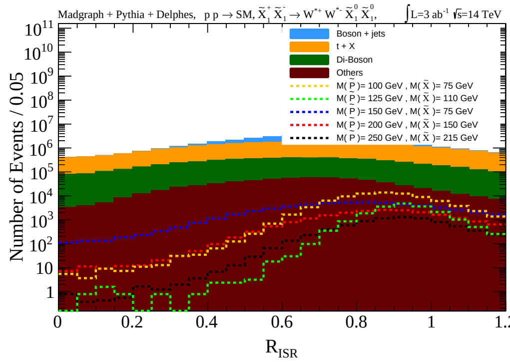

(a) Distribution of $R_{\mathrm{ISR}} = \frac{\left|\vec{p}^{\,\mathrm{CM}}_{\mathrm{I},T} \cdot \hat{p}^{\mathrm{CM}}_{\mathrm{ISR},T}\right|}{p^{\mathrm{CM}}_{\mathrm{ISR},T}}$: variable sensitive to the mass ratio LSP to parent sparticle.

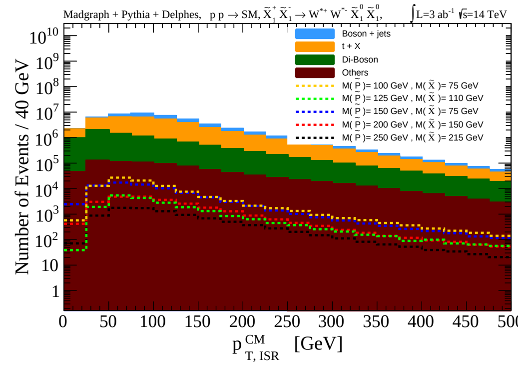

(b) Distribution of $p^{\mathrm{CM}}_{\mathrm{ISR},T}$: magnitude of the jets vector-sum transverse momentum of ISR-system evaluated in the CM frame.

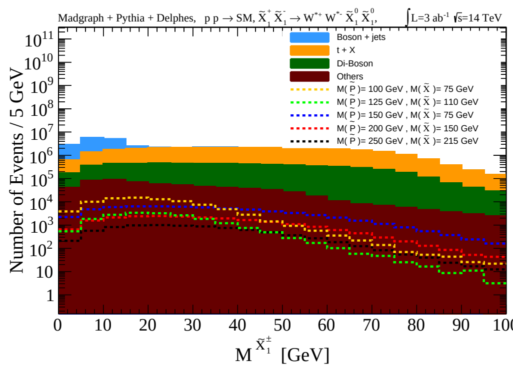

(c) Distribution of $M^{\tilde{\chi}^{\pm}}$: the mass associated with the chargino system.

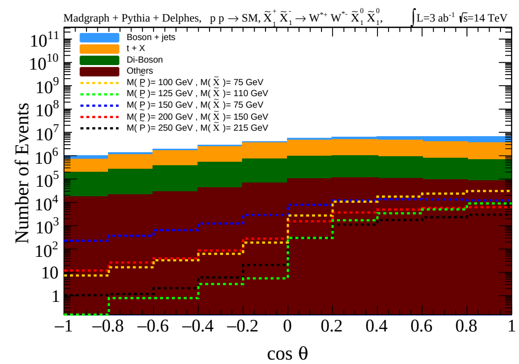

(d) Distribution of $\cos\theta = \hat{\beta}^{\mathrm{CM}}_{S} \cdot p^{\mathrm{S}}_{\mathrm{I},T}$.

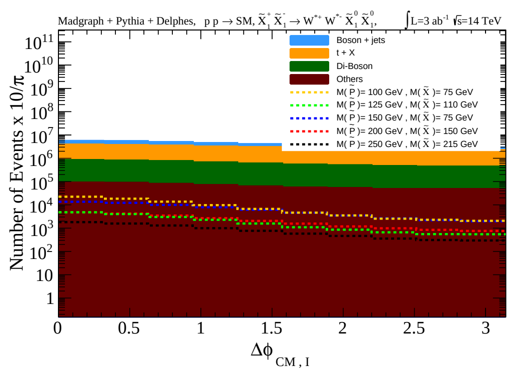

(e) Distribution of $\Delta\phi_{\mathrm{CM,I}}$: opening angle between the CM system and the I-system.

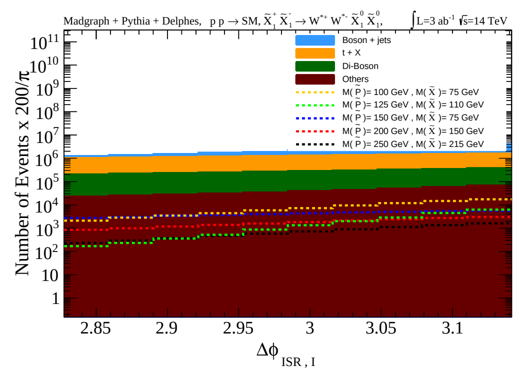

(f) Distribution of $\Delta\phi_{\mathrm{ISR,I}}$: opening angle between the ISR-system and the I-system, evaluated in the CM frame.

Figure 6.3.3: Distributions of the RJR observables sensitive to compressed scenarios for events that have satisfied the preselection criteria. Standard Model backgrounds are stacked together, while the overlaid dashed curves refer to five signal samples as in Figure 6.1.2. All the contributions are scaled with an integrated luminosity of 3 ab^{-1} at 14 TeV.

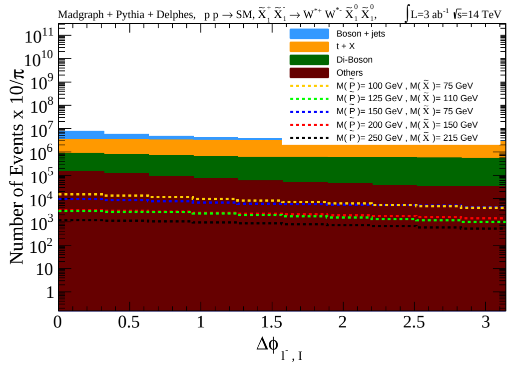

(a) Distribution of $\Delta\phi_{l^-,I}$: angle between the negative charge lepton and $\vec{\not{E}}_T$ in the *Lab* frame.

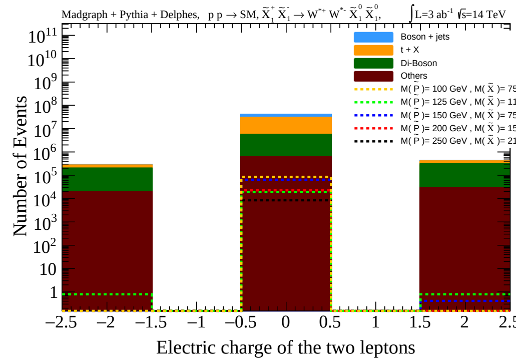

(b) Sum of the electric charge of the two leptons.

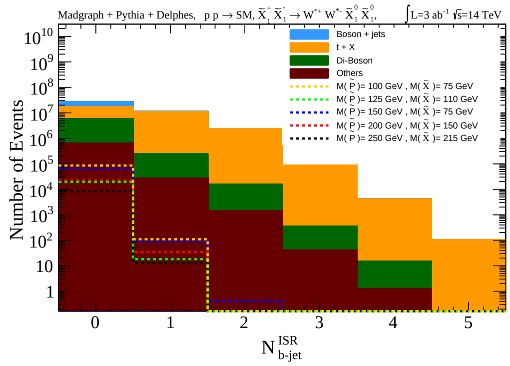

(c) Distribution of N^{ISR}_{b-jet}: number of b-jet in the final state.

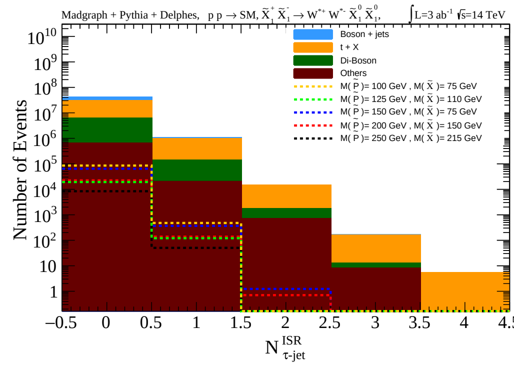

(d) Distribution of $N^{\mathrm{ISR}}_{\tau-jet}$: number of τ-jet in the final state.

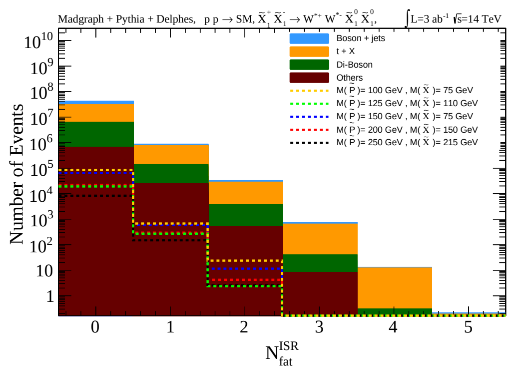

(e) Distribution of N^{ISR}_{fat}: number of fat-jet in the final state ($M(jet) > 60$ GeV).

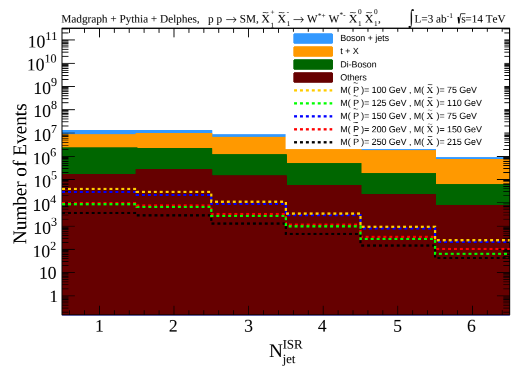

(f) Distribution of N^{ISR}_{jet}: number of light jet in the final state.

Figure 6.3.4: Distributions of the jet multiplicities and additional RJR observables for events that have satisfied the preselection criteria. Standard Model backgrounds are stacked together, while the overlaid dashed curves refer to four signal samples as in Figure 6.1.2. All the contributions are scaled with an integrated luminosity of 3 ab^{-1} at 14 TeV.

for values greater than $M_{\tilde{\chi}}/M_{\tilde{P}}$ due to the additional contribution to $\not{E}_T$ due to the two or more neutrino momenta. The ratio assumes values greater than one when some objects are forced into the V-system. The assignment of the different objects in the compressed tree is performed with no ambiguity: it is unnecessary to focus on the high ISR regime in order to have a good resolution for the ratio.

Notably the resolution is not only accurate but also moderately dependent to the absolute value of the mass difference as can be seen comparing the distributions of the two samples with same mass ratio $M_{\tilde{\chi}}/M_{\tilde{P}}$. The dashed red and yellow lines peak to the same maximum, while the widths are moderately dependent on ΔM because only two, among the six or more supersymmetric decay products, are visible. For this reason values of R_{ISR} larger than one are not considered in this study.

Figure 6.3.3b shows the distribution of $p^{\mathrm{CM}}_{\mathrm{ISR},T}$. The hard scales for the signal and background samples are similar and the variable has no impact. A minimal requirement on $p^{\mathrm{CM}}_{\mathrm{ISR},T}$ is essential to exploit the RJR technique with multi-lepton final states.

Figure 6.3.3c shows the distribution for the mass associated to the chargino system. This scale observable is extremely useful to discriminate the signal respect the single boson plus jets background.

Figures 6.3.3d, 6.3.3e and 6.3.3f refer to the distributions of $\cos\theta \equiv \hat{\beta}^{\mathrm{CM}}_{S} \cdot p^{\mathrm{S}}_{\mathrm{I},T}$, the opening angles between the CM system and the invisible system and between the ISR-system and the invisible system respectively.

Figure 6.3.4 shows the distributions for the b-jet, τ-jet, fat-jet and light jet multiplicities. A veto is applied to all the jets tagged as different with respect the light ones. The Standard Model backgrounds are expected to have an higher light jet multiplicity due to non-ISR jets: in particular restrictive criteria will be applied in order to suppress the $t\bar{t}$ Standard Model background. As can be seen from Figure 6.3.4b, requiring opposite charge leptons we can get rid of a class of events attributable to SM background, in particular processes with a high lepton multiplicity, but only two same-sign leptons reconstructed by the detector.

6.3.3 Reducing the boson plus jets and $t\bar{t}$ Standard Model backgrounds

Several Standard Model contributions challenge the feasibility to probe compressed chargino-LSP spectra at the LHC. In this section the focus is on the boson plus jets and the Standard Model processes involving at least one top quark. These backgrounds are reducible in an analysis dedicated to open mass spectra vetoing jets in the final state and requiring a large value for the missing transverse momentum.

From now on, we consider events with only opposite charge leptons and a veto is applied for all final states with jets tagged as b, τ and fat: $N^{\mathrm{ISR}}_{b-\mathrm{jet}} = 0$, $N^{\mathrm{ISR}}_{\tau-\mathrm{jet}} = 0$ and $N^{\mathrm{ISR}}_{\mathrm{fat}} = 0$. For all the chargino masses, and until $\Delta M = 75$ GeV, signal events tend to populate low values for the invariant mass of the two leptons so the criterion $M^{\mathrm{V}} < 70$ GeV is considered. This requirement excludes a large portion of the Standard Model final state events, in particular $t\bar{t}$ and multi-bosons processes, independently from the flavour of the two leptons reconstructed.

Nevertheless, numerous Standard Model processes result in a low value of M^{V}, in particular the boson plus jets contribution. The focus is on the process $Z \to \tau^+\tau^- \to l^+l^-\nu\nu\nu\nu$ plus jets. For such events the role of the chargino system in Figure 6.3.1 is assumed by the leptonically decaying tau, while the I systems reconstruct the information of the two neutrinos in each hemisphere. For these background events $M^{\tilde{\chi}^\pm}$ is a reconstruction for the mass of the lepton and two neutrinos resulting from the τ.

The first three plots in Figure 6.3.5 show the two-dimensional distributions between $M^{\tilde{\chi}^\pm}$and the ratio R_{ISR} for the boson plus jets backgrounds and two signal samples with same ratio $M_{\tilde{\chi}}/M_{\tilde{P}}$, but different values for ΔM and for the hard scale. The larger the parent sparticle mass, the larger the separation between the signal-like events with respect the events resulting from a single vector boson. Figure 6.3.5d shows the distribution of $M^{\tilde{\chi}^\pm}$ for the five signal samples and for the on-shell and off-shell boson plus jets backgrounds.

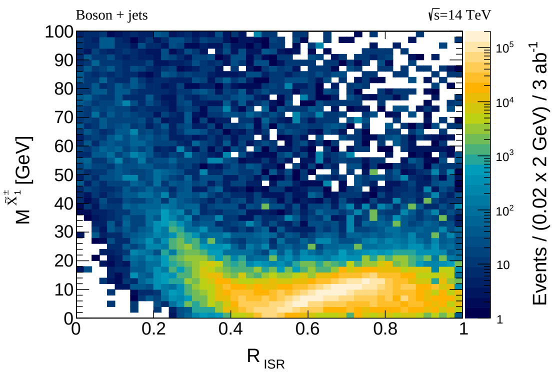

(a) The scatter plot: R_{ISR} vs $M^{\tilde{\chi}^{\pm}}$ for Boson + jets backgrounds.

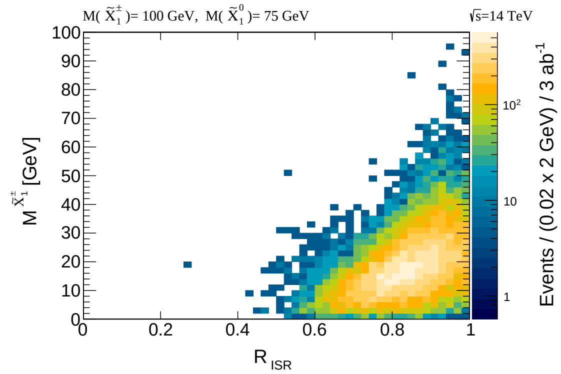

(b) The scatter plot: R_{ISR} vs $M^{\tilde{\chi}^{\pm}}$ for the signal sample $M_{\tilde{\chi}_1^{\pm}}$=100 GeV and $M_{\tilde{\chi}_1^{0}}$=75 GeV.

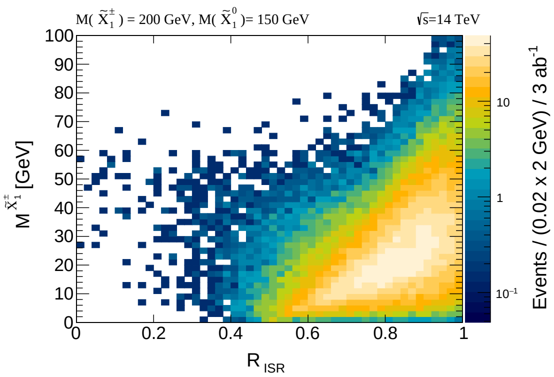

(c) The scatter plot: R_{ISR} vs $M^{\tilde{\chi}^{\pm}}$ for the signal sample $M_{\tilde{\chi}_1^{\pm}}$=200 GeV and $M_{\tilde{\chi}_1^{0}}$=150 GeV.

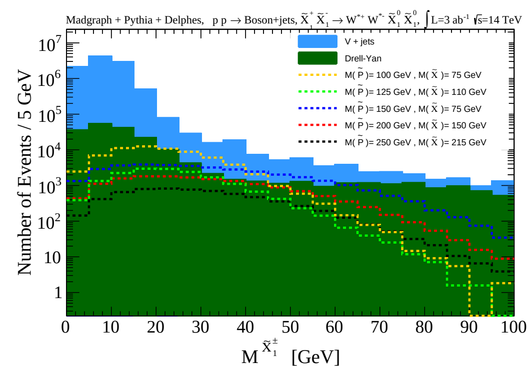

(d) The distribution of $M^{\tilde{\chi}^{\pm}}$: the scale observable associated with the chargino system.

Figure 6.3.5: Two-dimensional distribution of $M^{\tilde{\chi}^{\pm}}$ as a function of R_{ISR} for the Standard Model di-boson background and the signal samples $M_{\tilde{\chi}_1^{\pm}}$=100, 200 GeV and $M_{\tilde{\chi}_1^{0}}$=75, 150 GeV. Figure 6.3.5d shows the distribution of $M^{\tilde{\chi}^{\pm}}$ for the boson plus jets background and five signal samples. The histograms show the number of events expected per bin for an integrated luminosity of 3 ab^{-1} satisfying the preselection criteria and the additional requirements $N^{\mathrm{ISR}}_{b-\mathrm{jet}} = 0$, $N^{\mathrm{ISR}}_{\tau-\mathrm{jet}} = 0$, $N^{\mathrm{ISR}}_{\mathrm{fat}} = 0$ and $M^{V} < 70$ GeV.

We impose $M^{\tilde{\chi}^{\pm}} > 24$ GeV in order to suppress the V+jets background.

With this requirement the SM background is dominated by $t+X$ processes as described in Table 6.3. The main subprocess contributions involve a pair of (on-shell or off-shell) top quarks in the di-leptonic channels. Figure 6.3.6 shows the distribution of the light jet multiplicity as a function of the ratio.

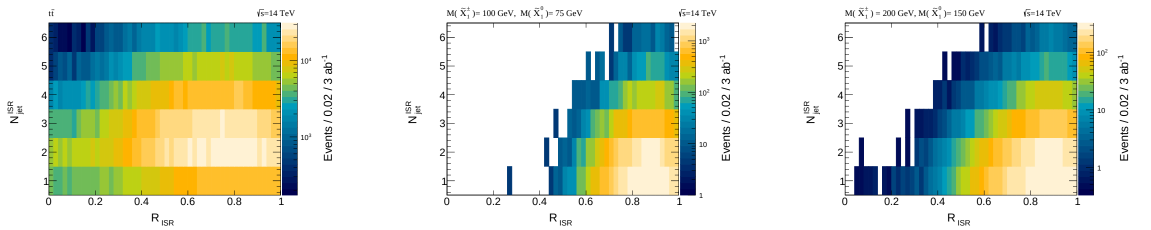

(a) The scatter plot: R_{ISR} vs $N_{\text{jet}}^{\text{ISR}}$ for the $\bar{t}t$ background.

(b) The scatter plot: R_{ISR} vs $N_{\text{jet}}^{\text{ISR}}$ or the signal sample $M_{\tilde{\chi}_1^\pm}$=100 GeV and $M_{\tilde{\chi}_1^0}$=75 GeV.

(c) The scatter plot: R_{ISR} vs $N_{\text{jet}}^{\text{ISR}}$ for the signal sample $M_{\tilde{\chi}_1^\pm}$=200 GeV and $M_{\tilde{\chi}_1^0}$=150 GeV.

Figure 6.3.6: Two-dimensional distributions of $N_{\text{jet}}^{\text{ISR}}$ as a function of R_{ISR} for the Standard Model $\bar{t}t$ background and the signal samples $M_{\tilde{\chi}_1^\pm}$=100, 200 GeV and $M_{\tilde{\chi}_1^0}$=75, 150 GeV. Preselection criteria, $N_{b-\text{jet}}^{\text{ISR}} = 0$, $N_{\tau-\text{jet}}^{\text{ISR}} = 0$, $N_{\text{fat}}^{\text{ISR}} = 0$, $M^V < 70$ GeV and $M^{\tilde{\chi}^\pm} >$ 24 GeV are required.

In order to attenuate the $t\bar{t}$ contribution only one jet in the final state is required. At this stage, the veracity of the statement of the LHC as a top pair factory can be appreciated. Despite the $N_{\text{jet}}^{\text{ISR}} = 1$ requirement, and vetoing on jets coming from the fragmentation of bottoms, the $t\bar{t}$ backgrounds is still not suppressed sufficiently. If the requirement $N_{\text{fat}}^{\text{ISR}} = 0$ moderates the contribution with the two jets flying in the same direction, one of the two jets could be outside the geometrical acceptance or too soft to be reconstructed. Also if these events are relatively rare, their contribution is not negligible due to the cross section $\sigma_{t\bar{t}} \sim\mathcal{O}(10^3 \text{ pb})$ of LHC14.

Figures 6.3.7a and 6.3.7b show the two-dimensional distributions of the opening angle between the positive electric charge lepton and the missing transverse momentum as a function of the ratio for the $t\bar{t}$ processes and the signal sample $M_{\tilde{\chi}_1^\pm}$=200 GeV and $M_{\tilde{\chi}_1^0}$=150 GeV. Figures 6.3.7c and 6.3.7d show the distribution of $\Delta\phi_{\text{l+},\text{I}}$ and $\Delta\phi_{\text{l−},\text{I}}$ respectively, for the signal samples and the t + X backgrounds. The subprocesses involving at least one top quark, categorised in TB, TT, Tj, TTB in the Snowmass study, are stacked together as shown in the legend. The events from top pair contributions (TB and TT) tend to populate value close to π, while signal-like events populate low values.

Figures 6.3.7e and 6.3.7f show the two-dimensional distribution $\Delta\phi_{\mathrm{l}^+,\mathrm{I}}$ vs $\Delta\phi_{\mathrm{l}^-,\mathrm{I}}$ for the $t\bar{t}$ background and the signal sample $M_{\tilde{\chi}_1^\pm}$=200 GeV and $M_{\tilde{\chi}_1^0}$=150 GeV, with the selection criteria described and requiring $R_{\mathrm{ISR}} > 0.6$. The requirements select background events with kinematics similar to the signal events: in particular a simultaneous large value of $\Delta\phi_{\mathrm{l}^\pm,\mathrm{I}}$ for both the leptons is disfavoured. A similar two-dimensional distribution as in Figure 6.3.7f is provided by all the signal samples.

In order to suppress the $t + X$ SM processes we demand a unique light jet associated to the ISR-system and $\Delta\phi_{\mathrm{l}^+,\mathrm{I}} + \Delta\phi_{\mathrm{l}^-,\mathrm{I}} < 2$. This is a two-dimensional requirement and must be explained. Events passing the selection criteria applied, likely contain two top quarks produced with low transverse momenta resulting in a final state with two reconstructed leptons and one jet not properly tagged. In the transverse plane, one of the two leptons is expected to fly close to the reconstructed jet (associated to the ISR-system), while the other is expected to be closer to the invisible system. As a consequence the sum $\Delta\phi_{\mathrm{l}^+,\mathrm{I}} + \Delta\phi_{\mathrm{l}^-,\mathrm{I}}$ is expected to be large, while for the signal events is expected to be limited.

In the low-ISR regime, the two low-momentum leptons do not necessarily fly in the direction of the invisible system, and a portion of the signal events are excluded by the criterion $\Delta\phi_{\mathrm{l}^+,\mathrm{I}} + \Delta\phi_{\mathrm{l}^-,\mathrm{I}} < 2$. Nevertheless, this requirement reduces the $t\bar{t}$ backgrounds by two orders of magnitude. More stringent criteria on $p^{\mathrm{CM}}_{\mathrm{ISR},T}$, the ratio, $\Delta\phi_{\mathrm{ISR,I}}$ or $\cos\theta$ select signal events with still lower values of $\Delta\phi_{\mathrm{l}^+,\mathrm{I}} + \Delta\phi_{\mathrm{l}^-,\mathrm{I}}$.

6.3.4 The irreducible W^+W^- background

In the last section a strategy based on a few RJR observables has been used to reduce the boson plus jets and $t\bar{t}$ Standard Model backgrounds. Applying these selection criteria, the dominant Standard Model process is the irreducible di-boson background: W^+W^-.

The goal is to distinguish between signal and background events with similar kinematics,

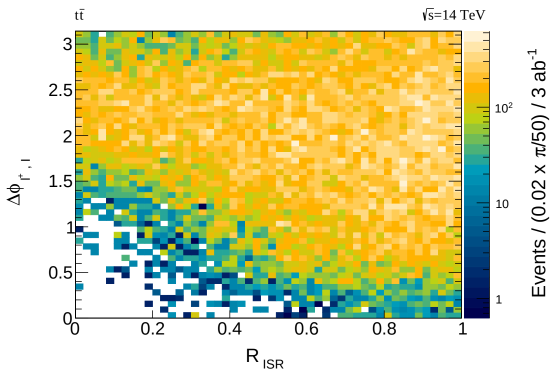

(a) The two-dimensional distribution of $\Delta\phi_{\mathrm{l}+,\mathrm{I}}$ as a function of R_{ISR} for the $t\bar{t}$ background.

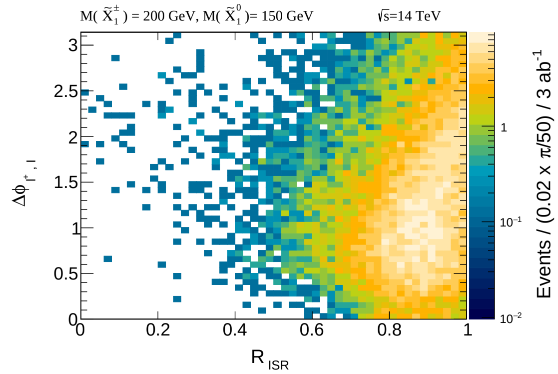

(b) The two-dimensional distribution of $\Delta\phi_{\mathrm{l}+,\mathrm{I}}$ as a function of R_{ISR} for the signal sample $M_{\tilde{\chi}_1^\pm}= 200$ GeV and $M_{\tilde{\chi}_1^0}= 150$ GeV.

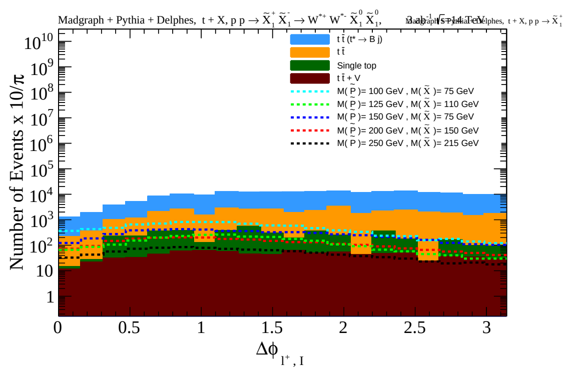

(c) The distribution of $\Delta\phi_{\mathrm{l}+,\mathrm{I}}$. The Standard Model t + X backgrounds are stacked together, while the overlaid dashed curves refer to five signal samples.

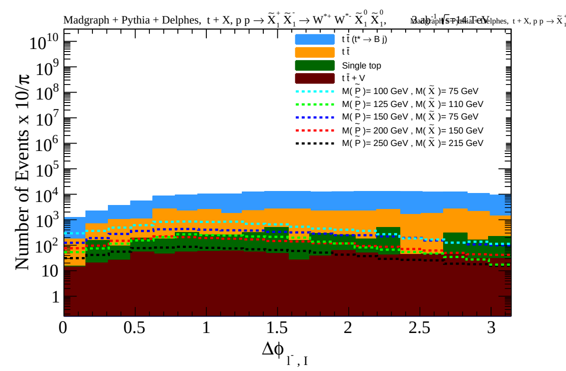

(d) The distribution of $\Delta\phi_{\mathrm{l}-,\mathrm{I}}$. The Standard Model t + X backgrounds are stacked together, while the overlaid dashed curves refer to five signal samples.

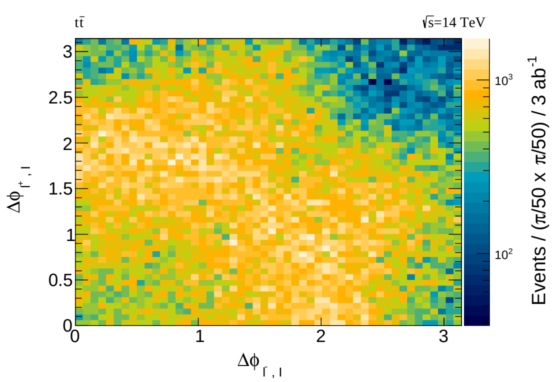

(e) The scatter plot $\Delta\phi_{\mathrm{l}+,\mathrm{I}}$ vs $\Delta\phi_{\mathrm{l}-,\mathrm{I}}$ for the $t\bar{t}$ background. The additional criterion $R_{\mathrm{ISR}} > 0.6$ is required.

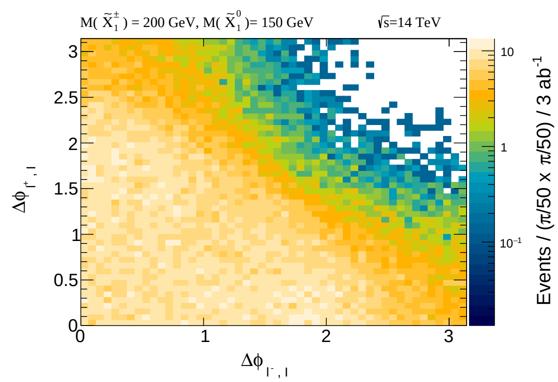

(f) The scatter plot $\Delta\phi_{\mathrm{l}+,\mathrm{I}}$ vs $\Delta\phi_{\mathrm{l}-,\mathrm{I}}$ for the signal sample $M_{\tilde{\chi}_1^\pm}= 200$ GeV and $M_{\tilde{\chi}_1^0}= 150$ GeV. The additional criterion $R_{\mathrm{ISR}} > 0.6$ is required.

Figure 6.3.7: One and two-dimensional distributions of the opening angle between the lepton and the I-system for events passing preselection criteria and the additional requirements $N^{\mathrm{ISR}}_{b-\mathrm{jet}} = 0$, $N^{\mathrm{ISR}}_{\tau-\mathrm{jet}} = 0$, $N^{\mathrm{ISR}}_{\mathrm{fat}} = 0$, $M^V < 70$ GeV, $M^{\tilde{\chi}^\pm} > 24$ GeV and $N^{\mathrm{ISR}}_{\mathrm{jet}} = 1$ All the contributions are scaled with an integrated luminosity of 3 ab^{-1} at $\sqrt{s}$ =14 TeV.

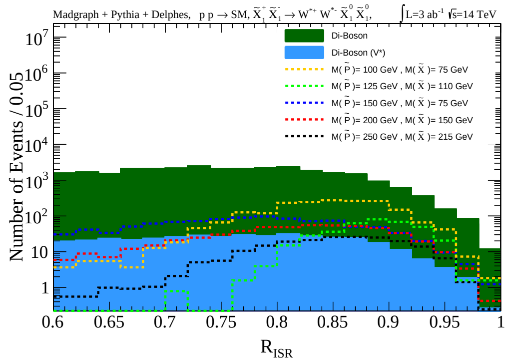

(a) The distribution of $R_{\text{ISR}} = \frac{\left|\vec{p}^{\,\text{CM}}_{\text{I},T}\cdot\hat{p}^{\,\text{CM}}_{\text{ISR},T}\right|}{p^{\text{CM}}_{\text{ISR},T}}$

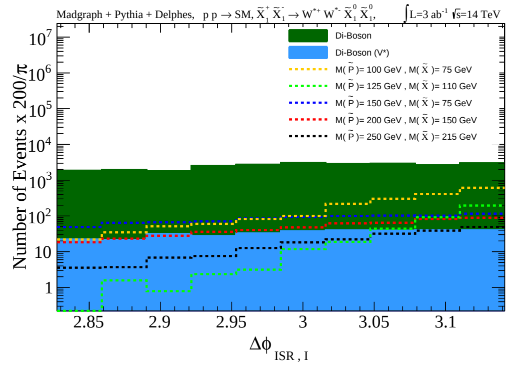

(b) The distribution of $\Delta\phi_{\text{ISR,I}}$.

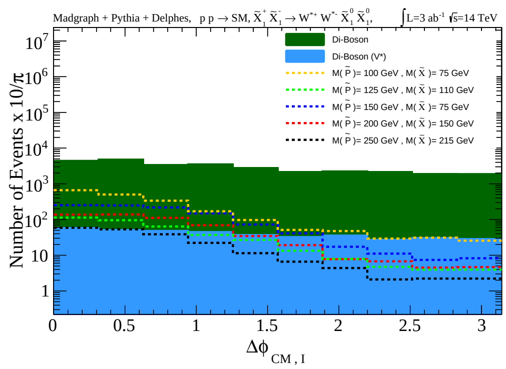

(c) The distribution of $\Delta\phi_{\text{CM,I}}$.

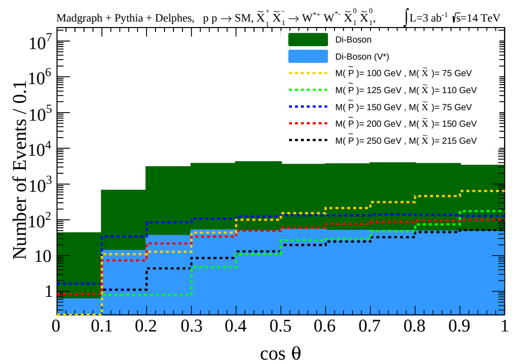

(d) The distribution of $\cos\theta_{\text{V,I}}$.

Figure 6.3.8: Distributions of RJR observables for signal samples and di-boson Standard Model background, for events passing preselection criteria and the additional requirements $N^{\text{ISR}}_{b-\text{jet}} = 0$, $N^{\text{ISR}}_{\tau-\text{jet}} = 0$, $N^{\text{ISR}}_{\text{fat}} = 0$, $M^{\text{V}} < 70$ GeV, $M^{\tilde{\chi}^{\pm}} > 24$ GeV, $N^{\text{ISR}}_{\text{jet}} = 1$, $R_{\text{ISR}} > 0.6$ and $\Delta\phi_{\text{l+},\text{I}} + \Delta\phi_{\text{l}-,\text{I}} < 2$. All the contributions are scaled with an integrated luminosity of 3 ab^{-1} at 14 TeV.

in particular when selection criteria close to the final configuration are applied. The only difference is as follows: mainly, the I-system $(I_a + I_b)$ for the W^+W^- background is constituted by two neutrinos, while for the signal-events by four weakly interacting particles. Figure 6.3.8 shows the RJR observables sensitive to separate events resulting from compressed charginos samples with respect to W^+W^-sample. The ratio R_{ISR} is once again the variable with greater impact for the signal-background distinction and selection criteria can be tuned depending on the ratio $M_{\tilde{\chi}}/M_{\tilde{P}}$. Figure 6.3.8b shows the distribution of $\Delta\phi_{\text{ISR,I}}$. Signal events tend to have values closer to π, the smaller the mass difference $\Delta M = M_{\tilde{P}} - M_{\tilde{\chi}}$. Figure 6.3.8c shows the distribution of the angle between the CM and I-system. Signal events tend to zero almost independently of ΔM or $M_{\tilde{\chi}}/M_{\tilde{P}}$. Finally, the distribution of $\cos\theta \equiv \hat{\beta}_S^{\rm CM} \cdot p_{{\rm I},T}^{\rm S}$ is shown in Figure 6.3.8d.

For nearly degenerate parent-child superparticles, the direction of the LSP is roughly the same as that of the parent sparticle as seen in Section 4.6.2. For the signal, the sum of the transverse momenta of the two charginos is the transverse momentum of the S-system, while the main contribution to the direction of the transverse momentum of the I-system is given by the two LSPs: each neutrino has an angular separation with respect to the associated LSP direction, but the sum of the two contributions is expected to be zero on average. In the transverse plane the resulting direction of the V-system is expected to be very close to the I-system resulting from four particles. For the background instead the angular separation of each neutrino with respect to the original W direction is distributed much more democratically. The resulting I direction can differ considerably from the S direction of the two Ws, providing in such a case a larger separation from the V-system in the transverse plane. The same behaviour must occur in three dimensions.

The observable $\cos\theta$ is expected to be sensitive to the angular separation between the V=$l^+ + l^-$ and the I=$I_a + I_b$ system and the imposition of $p_{{\rm I},z}^{\rm S} = 0$ tends to subtract the rapidity contribution of the invisible system. Hence the observable, also partially correlated to $\Delta\phi_{\rm ISR,I}$, is expected to provide additional information. Figures 6.3.9 and 6.3.10 show all the two-dimensional distributions of these four experimental observables for the di-boson background and two signal samples.

6.3.5 Signal regions

Selection criteria defined with the compressed RJR observables result in signal regions used to investigate chargino pair-production in final states with two leptons and missing transverse momentum. Table 6.4 presents the signal regions. The trend is similar to the previous analysis and once again the requirements for the observable $R_{\rm ISR}$ are tuned

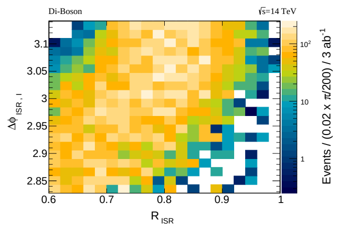

(a) $R_{\rm ISR}$ vs $\Delta\phi_{\rm ISR,I}$ for the di-boson background.

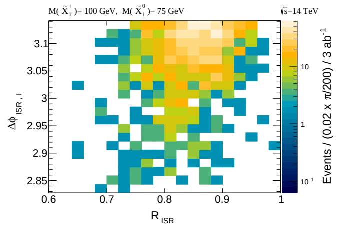

(b) $R_{\rm ISR}$ vs $\Delta\phi_{\rm ISR,I}$ for the signal sample $M_{\tilde{\chi}_1^\pm}$=100 GeV and $M_{\tilde{\chi}_1^0}$=75 GeV.

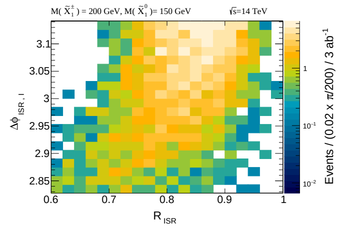

(c) $R_{\rm ISR}$ vs $\Delta\phi_{\rm ISR,I}$ for the signal sample $M_{\tilde{\chi}_1^\pm}$=200 GeV and $M_{\tilde{\chi}_1^0}$=150 GeV.

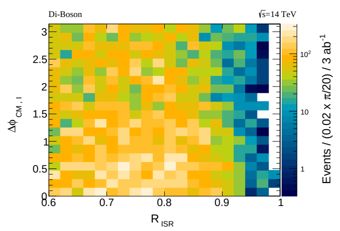

(d) $R_{\rm ISR}$ vs $\Delta\phi_{\rm CM,I}$ for the di-boson background.

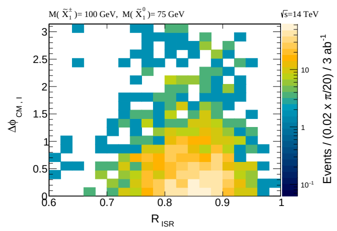

(e) $R_{\rm ISR}$ vs $\Delta\phi_{\rm CM,I}$ for the signal sample $M_{\tilde{\chi}_1^\pm}$=100 GeV and $M_{\tilde{\chi}_1^0}$=75 GeV.

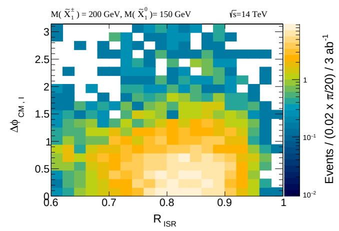

(f) $R_{\rm ISR}$ vs $\Delta\phi_{\rm CM,I}$ for the signal sample $M_{\tilde{\chi}_1^\pm}$=200 GeV and $M_{\tilde{\chi}_1^0}$=150 GeV.

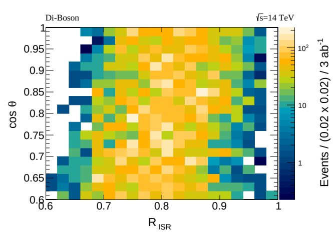

(g) $R_{\rm ISR}$ vs $\cos\theta$ for the di-boson background.

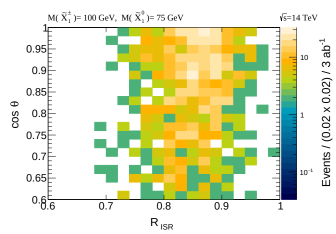

(h) $R_{\rm ISR}$ vs $\cos\theta$ for the signal sample $M_{\tilde{\chi}_1^\pm}$=100 GeV and $M_{\tilde{\chi}_1^0}$=75 GeV.

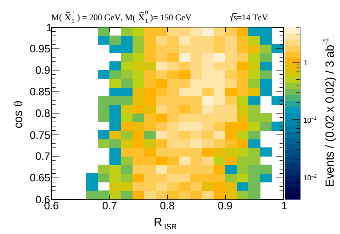

(i) $R_{\rm ISR}$ vs $\cos\theta$ for the signal sample $M_{\tilde{\chi}_1^\pm}$=200 GeV and $M_{\tilde{\chi}_1^0}$=150 GeV.

Figure 6.3.9: The two-dimensional distributions of the RJR observables for the Standard Model di-boson background and the signal samples $M_{\tilde{\chi}_1^\pm}$=100, 200 GeV and $M_{\tilde{\chi}_1^0}$=75, 150 GeV. We require preselection criteria, $N^{\rm ISR}_{b-\rm jet}=0$, $N^{\rm ISR}_{\tau-\rm jet}=0$, $N^{\rm ISR}_{\rm fat}=0$, $M^V<70$ GeV, $M^{\tilde{\chi}^\pm}>24$ GeV, $N^{\rm ISR}_{\rm jet}=1$, $R_{\rm ISR}>0.6$ and $\Delta\phi_{\rm l^+,I}+\Delta\phi_{\rm l^-,I}<2$.

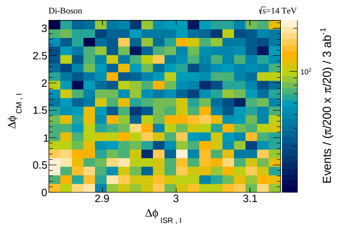

(a) $\Delta\phi_{\mathrm{ISR,I}}$ vs $\Delta\phi_{\mathrm{CM,I}}$ for the di-boson background.

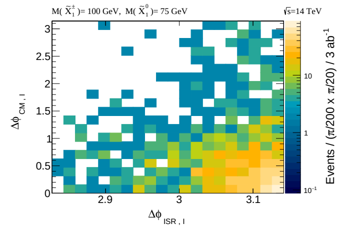

(b) $\Delta\phi_{\mathrm{ISR,I}}$ vs $\Delta\phi_{\mathrm{CM,I}}$ for the signal sample $M_{\tilde{\chi}_1^\pm}$=100 GeV and $M_{\tilde{\chi}_1^0}$=75 GeV.

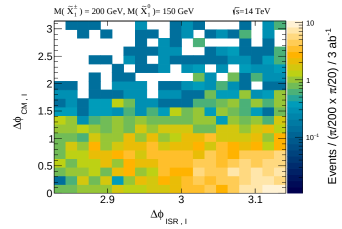

(c) $\Delta\phi_{\mathrm{ISR,I}}$ vs $\Delta\phi_{\mathrm{CM,I}}$ for the signal sample $M_{\tilde{\chi}_1^\pm}$=200 GeV and $M_{\tilde{\chi}_1^0}$=150 GeV.

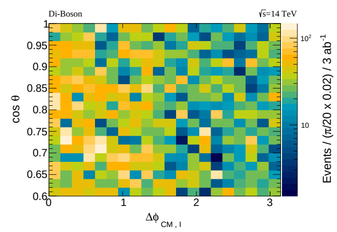

(d) $\Delta\phi_{\mathrm{CM,I}}$ vs $\cos\theta$ for the di-boson background.

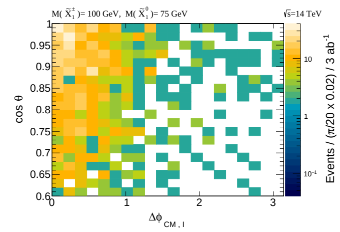

(e) $\Delta\phi_{\mathrm{CM,I}}$ vs $\cos\theta$ for the signal sample $M_{\tilde{\chi}_1^\pm}$=100 GeV and $M_{\tilde{\chi}_1^0}$=75 GeV.

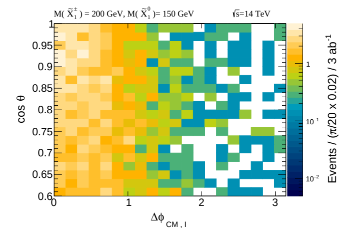

(f) $\Delta\phi_{\mathrm{CM,I}}$ vs $\cos\theta$ for the signal sample $M_{\tilde{\chi}_1^\pm}$=200 GeV and $M_{\tilde{\chi}_1^0}$=150 GeV.

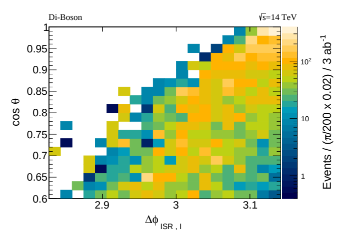

(g) $\Delta\phi_{\mathrm{ISR,I}}$ vs $\cos\theta$ for the di-boson background.

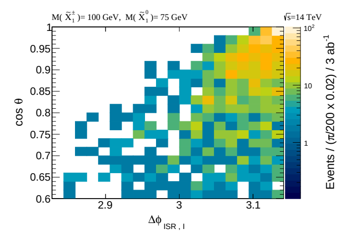

(h) $\Delta\phi_{\mathrm{ISR,I}}$ vs $\cos\theta$ for the signal sample $M_{\tilde{\chi}_1^\pm}$=100 GeV and $M_{\tilde{\chi}_1^0}$=75 GeV.

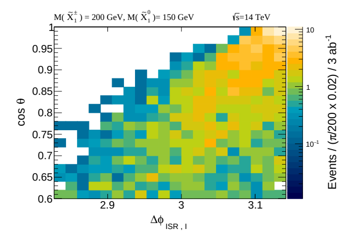

(i) $\Delta\phi_{\mathrm{ISR,I}}$ vs $\cos\theta$ for the signal sample $M_{\tilde{\chi}_1^\pm}$=200 GeV and $M_{\tilde{\chi}_1^0}$=150 GeV.

Figure 6.3.10: The two-dimensional distributions of the RJR observables for the Standard Model di-boson background and the signal samples $M_{\tilde{\chi}_1^\pm}$=100, 200 GeV and $M_{\tilde{\chi}_1^0}$=75, 150 GeV. We demand preselection criteria, $N^{\mathrm{ISR}}_{b-\mathrm{jet}} = 0$, $N^{\mathrm{ISR}}_{\tau-\mathrm{jet}} = 0$, $N^{\mathrm{ISR}}_{\mathrm{fat}} = 0$, $M^V < 70$ GeV, $M^{\tilde{\chi}^\pm} > 24$ GeV, $N^{\mathrm{ISR}}_{\mathrm{jet}} = 1$, $R_{\mathrm{ISR}} > 0.6$ and $\Delta\phi_{\mathrm{l+,I}} + \Delta\phi_{\mathrm{l-,I}} < 2$.

	Mass Splitting [GeV]				
Variable	$\Delta M = 15$	$\Delta M = 25$	$\Delta M = 35$	$\Delta M = 50$	$\Delta M = 75$
Object multiplicity selection criteria	2 OS Leptons (e and μ) with $p_T^{\text{lep}} > 10$ GeV, $N_{\text{jet}}^{\text{ISR}} = 1$, $N_{b-\text{jet}}^{\text{ISR}} = 0$, $N_{\tau-\text{jet}}^{\text{ISR}} = 0$ and $N_{\text{fat}}^{\text{ISR}} = 0$				
$p_{\text{ISR},T}^{\text{CM}}$ ($\not{E}_T$)> [GeV]	50				
$M^{\text{V}} <$ [GeV]	50			60	70
$\Delta\phi_{\text{l}+,\text{I}} + \Delta\phi_{\text{l}-,\text{I}} <$	2				
$M^{\tilde{\chi}_1^{\pm}} >$ [GeV]	24				
$\Delta\phi_{\text{CM,I}} <$	0.5	0.5	0.45		
$\Delta\phi_{\text{ISR,I}} >$	3.12	3.10	3.06	3.05	3.04
$\cos\theta >$	0.9	0.85	0.8	0.75	0.7
$R_{\text{ISR}} >$	$0.85,\ 0.9$	$0.85,\ 0.9$	$0.8,\ 0.85$ 0.9	$0.8,\ 0.85$	$0.75,\ 0.8$ 0.85

Table 6.4: Selection criteria for signal regions in the analysis of chargino pair-production in final states with two leptons and missing transverse momentum.

depending on the mass ratio. These criteria are more stringent than the chargino-neutralino associated study due to the larger multiplicity of weakly interacting particles in the final state.

Figure 6.3.11 shows the distributions of two RJR observables for SM background and signal sample events passing the selection criteria in Table 6.4 with a fixed value of R_{ISR}. Figure 6.3.12 shows the distributions of R_{ISR} and $M^{\tilde{\chi}^{\pm}}$ for the signal region selection criteria. For the lowest mass splitting the requirement $R_{\text{ISR}} > 0.85$ is applied only for the sample $M_{\tilde{\chi}_1^{\pm}} = 100$ GeV, while for $\Delta M = 25$ GeV we demand this criterion for three samples ($M_{\tilde{\chi}_1^{\pm}} \leq 150$ GeV).

6.3.6 Results

The signal regions expressed by the selection criteria of the RJR observables defined in Table 6.4 are applied to calculate projected sensitivities for compressed spectra signal samples. Figure 6.3.13 shows the value of Z_{Bi} described in Section 3.5.1 at $\sqrt{s}$=14 TeV for an integrated luminosity of 3000 fb^{-1}. We consider a systematic uncertainty

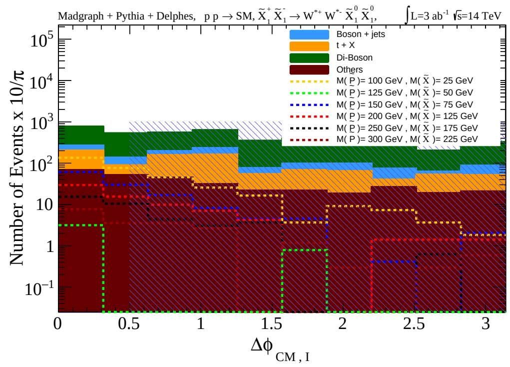

(a) Distribution of $\Delta\phi_{\mathrm{CM,I}}$. Selection criteria as in column 5 with $R_{\mathrm{ISR}} > 0.75$ are imposed.

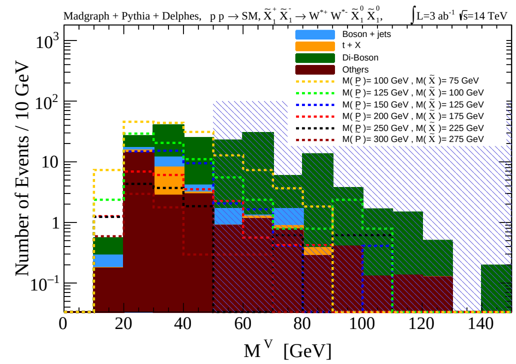

(b) Distribution of the M^{V}. Selection criteria as in column 2 with $R_{\mathrm{ISR}} > 0.85$ are required.

Figure 6.3.11: Distributions of the RJR observables for signal and background events passing N-2 selection criteria in table 6.4 and a requirement for R_{ISR}.

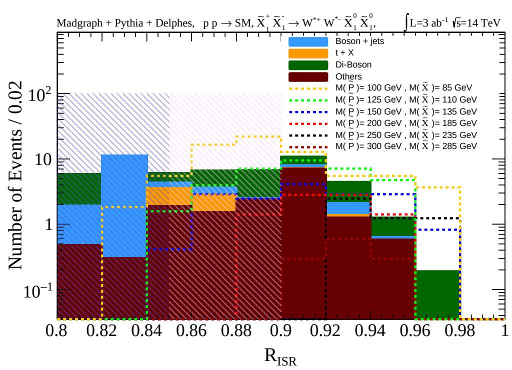

(a)

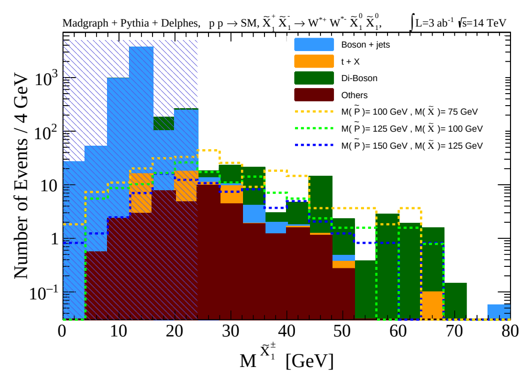

(b)

Figure 6.3.12: The distributions of R_{ISR} for the signal and BG events passing the N-1 selection criteria in Table 6.4 column 1 (6.3.12a) and of $M^{\tilde{\chi}^{\pm}}$imposing the requirements in column 2 with $R_{\mathrm{ISR}} > 0.85$ (6.3.12b).

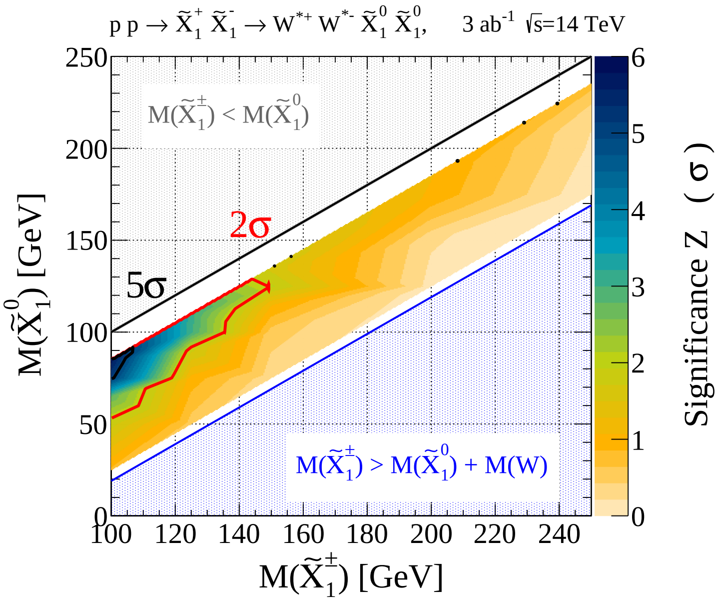

Figure 6.3.13: Projected exclusion and discovery reach for chargino pair-production in the compressed regions: 15 GeV $\leq \Delta M \leq$ 75 GeV at $\sqrt{s}$ = 14 TeV for an integrated luminosity of 3000 fb^{-1}.

of 20% for the overall Standard Model background: a compromise between a large data sample projection (10 times the integrated luminosity of the associated chargino-neutralino production analysis) and stringent selection criteria assumed to suppress the background yields.

With enough data collection limits for the compressed chargino pair-production topology at LHC14 can be set. Leveraging the RJR technique one can exclude masses up to $\sim$ 150 GeV at the 95% CL in the best scenarios.

6.4 Summary

We have introduced an original approach to searches for compressed electroweakinos based on the imposition of the decay trees as in Figures 4.6.1 and 6.3.1 for the interpretation of reconstructed events, using the Recursive Jigsaw Reconstruction technique.

Putative wino-like chargino neutralinos could be discovered at LHC14 with masses

$M_{\tilde{\chi}_1^\pm} = M_{\tilde{\chi}_2^0}$>150 GeV for a large portion of the samples investigated (15 GeV$\lesssim \Delta M \lesssim$ 50 GeV) assuming an integrated luminosity of 300 fb^{-1} and leveraging only *transverse* observables. The RJR technique is sensitive to the extremely challenging chargino pair topology scenarios in the compressed regime. A strategy based on several experimental observables has been used to reduce the W^+W^- and the other main background yields due to the necessity of requiring jets in the final state to be associated to the ISR-system. A potential 95% confidence level exclusion limit can be obtained for an assumed data set of 3 ab^{-1} and assuming a 20% of systematic uncertainty for sample spectra with $\Delta M \lesssim 50$ GeV.

For both the topologies, the signal yields in the extreme compressed scenarios can benefit from an improvement in the efficiencies of the detector in the reconstruction of low transverse momentum leptons (< 10 GeV). On the other hand, for large mass splittings ($\Delta M \gtrsim M_Z$) the bulk analysis should be preferred to a compressed investigation, while for intermediate scenarios 60 GeV $\lesssim \Delta M \lesssim M_Z$ one can exploit the complementarity of observables based on a reconstruction of the event with or without the ISR-system.

The method is expected to have still more impact in the cases of final state topologies with larger lepton multiplicity: pair-production of charginos and/or neutralinos with slepton mediated decays. The RJR technique can be extended to these studies and to the pair-production of heavy neutralinos in final states with four leptons exploiting the simplified tree in Figure 4.6.1, with a simple modification in the assignment of the objects in the case of sleptons of the third generation.

The results from the simplified models investigated in this work can be partially reinterpreted assuming different compositions for the electroweakinos. The method can be applied for Higgsino-dominated charginos and neutralinos, with the last one decaying via an off-shell Standard Model Higgs, requiring two b-jets and one lepton in the V-system. For chargino pair-production with a mixed Higgsino-wino nature, one can reweight the signal yields with the appropriate cross sections; typically the contributions from off-shell charged Higgs or other sparticles can be neglected since $M_S, M_{H^\pm} \gg M_W$

in most SUSY models.

Chapter 7

Study of gluino mediated sbottom pair-production in final states with four b-jets and missing transverse momentum

7.1 Preamble

Although some of the SUSY regions probed in this study have been excluded by the recent limits obtained by the ATLAS and CMS collaborations, the results can be extended considering a larger integrated luminosity, comparable to the LHC data-sample collected with Run 2. Furthermore, evidence and exclusion reaches demonstrated in this study can be re-interpreted considering proper branching fractions (or re-weighting $\sigma \times BR$ in Eq. 3.1.3) for the simplified topology. More generally, the results and strategy developed in this chapter for a challenging final state topology, reaches of kinematic and combinatoric ambiguities, can be translated to probe a wide variety of final state phenomenologies, typical of models based on a $\mathbb{Z}_2$ symmetry. In particular, the sensitivity of the RJR observables demonstrated in this study can be exploited for the discovery prospects of many SUSY open mass spectra cascades.

7.2 Introduction

Pair-production of gluinos and squarks by either quark-gluon or gluon-gluon fusion are considered the dominant production modes in practically all supersymmetric scenarios. How a SUSY signal may be evidenced at one of the LHC discovery experiments greatly depends on the mass spectrum and the branching fractions of the produced superparticles.

Section 2.3 describes how the mass eigenstates $\tilde{q}_1$ and $\tilde{q}_2$ of squarks are a mixture of the gauge eigenstates $\tilde{q}_L$ and $\tilde{q}_R$. This mixing effect is proportional to the Yukawa couplings, hence to the masses of the SM fermion partners and definitively larger for the third generation. Natural models suggest limited masses for the sparticles with the largest coupling to the Higgs. In particular the mass eigenstates of the superpartners of the top and bottom quark must be not too far above the electroweak scale and the gluino, involved in the second loop corrections, is expected to be not too much heavier in order to prevent an unnatural fine tuning for the Higgs mass. Most natural SUSY scenarios provide relatively light stops and sbottoms with respect to all other squarks considering the renormalisation group equations.

Searching for evidence of the $\tilde{t}_1$ and $\tilde{b}_1$, either produced directly or from the decay of gluinos, is therefore highly topical. Since the direct pair-production cross sections of the stop and sbottom are in general smaller than that of gluino pair-production, searches for third generation squarks produced via gluino decay present an attractive avenue to probe SUSY. The additional objects afforded by the richer final states can be used to reduce several pernicious SM backgrounds.

In this work new observables are introduced for the study of the gluino mediated light sbottom ($\tilde{b}_1$) pair-production in final states with four $b-$jets and missing transverse

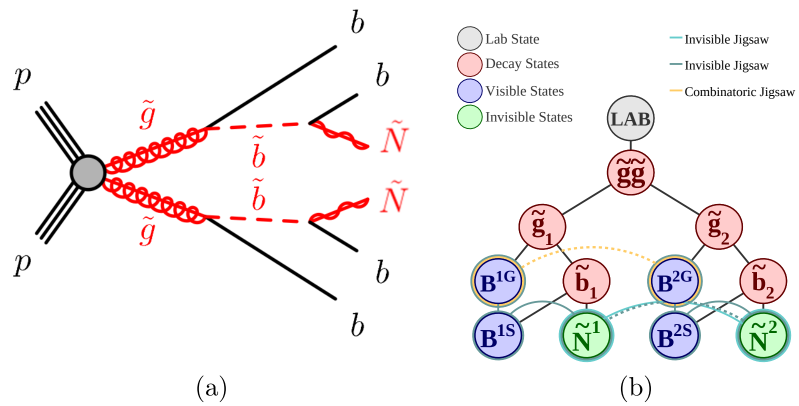

Figure 7.2.1: Feynman diagram for gluino pair-production and its decay chain ($pp \to \tilde{g}\tilde{g}$, $\tilde{g} \to \tilde{b}b$, $\tilde{b} \to b\tilde{N}$) (7.2.1a). The corresponding RJR tree (7.2.1b). The two decay hemispheres are separated using the labels "1" and "2". Visible decay objects are drawn in blue circles: "B" denotes a b-jet and "G" or "S" the superparticle mother. Invisible LSPs are drawn in green circles while intermediate states are drawn in red circles.

momentum. The gluino is a Majorana fermion and can decay with equal probability to a particle or an antiparticle, but just through an on-shell or off-shell squark. In this study we do not specify the electric charge and we refer to the light mass eigenstate of the sbottom as $\tilde{b}$ and to the LSP as $\tilde{N}$. If a two body decay $\tilde{g} \to q\tilde{q}$ is open it will dominate because of the QCD strength of the coupling. In the simplified model studied in this work the $\tilde{b}$ is the lightest squark and all the other squarks are heavier than the gluino so we can assume $BR\left(\tilde{g} \to b\tilde{b}\right) = 100\%$ until the bound $m_{\tilde{g}} > m_b + m_{\tilde{b}}$ is passed. Each sbottom is assumed to decay exclusively to the LSP via $\tilde{b} \to b\tilde{N}$.

The Feynman diagram is shown in Figure 7.2.1a and the final state topology can be investigated imposing the same decay tree introduced in Section 4.4.1. In Figure 7.2.1b the RJR tree is illustrated naming the four bottoms as B^{1G}, B^{1S}, B^{2G} and B^{2S}, where 1 and 2 once again denote the hemisphere and the labels G and S are a reminder for the gluino or sbottom "mother" superparticle. The WIMP and combinatoric jigsaw rules for the assignment of the four identical visible objects in the final state are described in Section 4.5.2. Other possible strategies and results are shown in the next sections.

$M_{\tilde{g}}$	$M_{\tilde{b}}$	$M_{\tilde{N}}$	$\Delta M_{\tilde{g}\tilde{b}} = M_{\tilde{g}} - M_{\tilde{b}}$	$\Delta M_{\tilde{b}\tilde{N}} = M_{\tilde{b}} - M_{\tilde{N}}$
1500 GeV	600 GeV	100 GeV	900 GeV	500 GeV
1500 GeV	800 GeV	100 GeV	700 GeV	700 GeV
1500 GeV	1000 GeV	100 GeV	500 GeV	900 GeV
1500 GeV	1400 GeV	100 GeV	100 GeV	1300 GeV
1500 GeV	510 GeV	500 GeV	990 GeV	10 GeV
1500 GeV	600 GeV	500 GeV	900 GeV	100 GeV
1500 GeV	800 GeV	500 GeV	700 GeV	300 GeV
1500 GeV	1000 GeV	500 GeV	500 GeV	500 GeV
1500 GeV	1200 GeV	500 GeV	300 GeV	700 GeV
1500 GeV	1400 GeV	500 GeV	100 GeV	900 GeV
1700 GeV	1400 GeV	100 GeV	300 GeV	1300 GeV
1700 GeV	1400 GeV	500 GeV	300 GeV	900 GeV
2000 GeV	1400 GeV	100 GeV	600 GeV	1300 GeV
2000 GeV	1400 GeV	500 GeV	600 GeV	900 GeV
2000 GeV	1900 GeV	500 GeV	100 GeV	1400 GeV

Table 7.1: Superparticle masses and mass splittings.

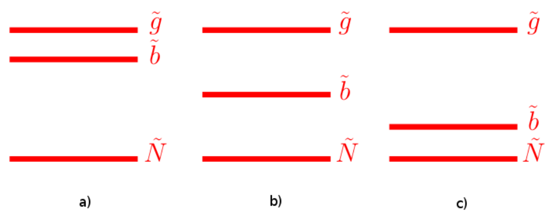

Figure 7.3.1: Three qualitative sample mass spectra showing the superparticles we are interested in: a) $\Delta M_{\tilde{g}\tilde{b}} < \Delta M_{\tilde{b}\tilde{N}}$, b) $\Delta M_{\tilde{g}\tilde{b}} \simeq \Delta M_{\tilde{b}\tilde{N}}$ and c) $\Delta M_{\tilde{g}\tilde{b}} > \Delta M_{\tilde{b}\tilde{N}}$.

7.3 Preselection and RJR observables

The main SM processes expected to contribute to the background, as described in Chapter 3, are compared with the SUSY signal scenarios shown in Tab. 7.1. We demand the preselection criteria described in Table 7.2.

The jets are ordered based on their transverse momentum ($jet1$ is the leading jet in p_T, and so on). The $b-$tagging requirement is not extended to four jets, hence the full acceptance for the hadronic calorimeter ($|\eta| < 5$) is considered.

These selection criteria are minimal and no selection is applied for the missing transverse

Variable	Requirement
N_{jet}	≥ 4, with $\|\eta\| < 5$
p_T^{jet}	$p_T^{jet1} > 120$ GeV, $p_T^{jet2} > 100$ GeV, $p_T^{jet3} > 60$ GeV ($p_T^{jet4} > 20$ GeV)
$N_{b-\text{jet}}$	≥ 3
N_{lep}	Lepton veto ($N_e = 0$ and $N_\mu = 0$)

Table 7.2: Preselection criteria.

momentum. The selection criteria on the transverse momentum of the jets are not stringent and the one on the third jet is the most efficient to reduce the main Standard Model backgrounds ($t\bar{t}$ plus bosons and $t\bar{t}$).

Imposing the RJR tree in Figure 7.2.1b, the same basis of experimental observables illustrated in Section 4.4.4 are obtained, here rewritten with the proper superparticle labels:

- $M_{\tilde{g}\tilde{g}}$ is a variable sensitive to the invariant mass of the two hemispheres, hence to the overall mass scale.
- $\cos\theta_{\tilde{g}g}$ is the cosine of half of the angle between the two gluinos.
- $\triangle\varphi_{\tilde{g}_1\tilde{g}_1}$ is the azimuthal angle between the decay planes of $\tilde{g}_1$and $\tilde{g}_2$.
- $\cos\theta_{\tilde{g}_1}$ ($\cos\theta_{\tilde{g}_2}$) is the cosine of the gluino decay angle: half of the angle between the b-jet produced by the gluino and sbottom in the hemisphere 1(2).
- $\cos\theta_{\tilde{b}_1}$ ($\cos\theta_{\tilde{b}_2}$) is the cosine of the sbottom decay angle: half of the angle between the b-jet produced by the sbottom and the neutralino in the hemisphere 1 (2).
- $\triangle\varphi_{\tilde{g}_1\tilde{b}_1}(\triangle\varphi_{\tilde{g}_2\tilde{b}_2})$ is the azimuthal angle between the first and second decay planes in the hemisphere 1(2): the first plane is described by the b-jet from gluino and sbottom $\widehat{B^G - \tilde{b}}$ the second by the b-jet from sbottom and neutralino $\widehat{B^S - \tilde{N}}$.
- B_0^{1G}, B_0^{2G}, B_0^{1S} and B_0^{2S} are the energies of the b-jets in the gluino and sbottom approximated rest frames.

These last scale variables, have a monochromatic value in the hypothesis of perfect reconstruction of the rest frames and perfect assignment of the objects in the right position. Their distributions are expected to give information to the mass of the sbottom (see Figure 7.3.1) in the hypothesis of unambiguous assignment.

7.4 Combinatoric jigsaw rule

7.4.1 Additional motivations

In this work we refer to hemisphere 1 as the one with the highest transverse momentum b-jet. This results in a moderate asymmetry for the RJR observables. Event-by-event, twelve possible combinations result for the assignment of each b-jet to the corresponding b-quark as seen in Section 4.5.2.

Experimentally, we cannot know a priori which b-jet is the result of the fragmentation of the bottom produced by the first or second gluino or by the first or second scalar bottom. A hypothetical knowledge of the original b electric charges cannot completely solve this ambiguity because of the Majorana fermion nature of the gluino. For example, knowing with full efficiency the electric charge of all the four b-jets would reduce the ambiguity for the separation of the two hemispheres to two possible choices, because each hemisphere must contain a bottom and an antibottom.

Considering the four leading jets (b-jets) in p_T, the minimum between the three possible invariant mass combinations of b-jet pairs, as seen in Eq. 4.5.2, remains the only plausible way to separate the two hemispheres. The efficiency for the correct separation is related to several factors like the jet multiplicity or H_T. For example, it improves with increasing missing transverse momentum or if the two gluinos recoil against ISR in cases where the ISR jets satisfy $p_T < p_T^{jet4}$, while it is practically 1/3 for gluinos produced near the threshold or for low values of p_T^{CM}. Applying the preselection criteria it is in the range $\sim 40\% - 50\%$ for the samples investigated.

For the assignment of the first and second b-jet in each hemisphere we use the second minimisation as in Eq. 4.5.3. As emphasised in Section 4.5.2, it corresponds to a minimisation of $M_{\tilde{b}}$ in the two hemispheres and it is feasible because the estimation of the neutralino four-momenta depends of the overall visible hemisphere 1 and 2 and hence, it has a dependence only on the first combinatoric minimisation.

Consider another possible approach based on the energy hierarchy (or the transverse momentum hierarchy) between the first and second b-jet in each hemisphere. For example, we could choose $E_{1G}^{Lab} > E_{1B}^{Lab}$ and $E_{2G}^{Lab} > E_{2B}^{Lab}$ or $E_{1G}^{Lab} < E_{1B}^{Lab}$ and $E_{2G}^{Lab} < E_{2B}^{Lab}$, while an opposite hierarchy for the two hemispheres has no deep meaning. In these two cases the assignment can be made at the beginning, namely in the Lab frame before the WIMP jigsaw rules. These possibilities are motivated by the ratio R in the limit of massless jets

$$R = \frac{B_0^{\text{true}\,\tilde{g}_1}}{B_0^{\text{true}\,\tilde{b}_1}} = \frac{B_0^{\text{true}\,\tilde{g}_2}}{B_0^{\text{true}\,\tilde{b}_2}} = \frac{M_{\tilde{b}}(M_{\tilde{g}}^2 - M_{\tilde{b}}^2)}{M_{\tilde{g}}(M_{\tilde{b}}^2 - M_{\tilde{N}}^2)} \tag{7.4.1}$$

which is valid if we could exactly estimate the superparticles rest frames and assign the objects with no ambiguity. A complete analysis has been made choosing $E_{1(2)G}^{Lab} < E_{1(2)B}^{Lab}$ for mass spectra like a) and b) in Figure 7.3.1 and $E_{1(2)G}^{Lab} > E_{1(2)B}^{Lab}$ for the mass spectrum like c). Those choices were motivated by the assumption that Eq. 7.4.1 tends to favour the denominator for mass spectra of type b) ($R < 1$) and the same behaviour is expected in the Lab frame. The results of this analysis are not described in this thesis, but the final significance can reproduce, in the best scenarios, the same results obtained with the double minimisation procedure, when more signal regions based on different selection criteria are defined to target the specific samples.

Assuming the four leading jets in the final state are the visible decay products, the efficiency for the right assignment is most of all due to the first combinatoric minimisation. The observables have different dependences from the specific combinatoric jigsaw rule. For example, $\cos\theta_{\tilde{g}\tilde{g}}$ depends only on the first minimisation, B_0^{1G} on the first and the second minimisation relative to only the first hemisphere, while $\triangle\varphi_{\tilde{g}_1\tilde{g}_1}$ depends on the entire assignment of the four objects. Hence a choice based on a priori assumption of the mass spectrum that does not improve significantly the efficiency and reduces the final sensitivity, or requires numerous optimised signal regions, must be disfavoured with respect to a more robust and scenario-independent approach.

Each time we want to distinguish between two experimental identical objects in a node along the chain a combinatoric mass minimisation is applied.

7.4.2 Knowing the assignment

What if there exists a method to solve the combinatoric challenge without ambiguity? From our simulation, we know the four-momentum of each parton. Even if a perfect parton-jet equivalence does not exist, we can associate each of four (b)-jets from the Delphes final state response to the best matching the b-particle kinematic from Pythia comparing ΔR and the two energies. This gives a sort of best detector scenario output.

The distributions for the RJR variables are presented in Figures 7.4.1-7.4.2c. The distributions for the scale observables relative to the signal samples are overlapped with the overall SM backgrounds obtained with the double minimisation procedure. All the background distributions are scaled for an integrated luminosity of 10 fb^{-1} using the procedure outlined in [75] applying the input cross sections and k-factors provided therein as described in Chapter 3. The signal distributions are scaled with the same procedure applying a k-factor=1 and the cross sections for simplified topologies are $\sigma = 0.0219$, 0.00757 and 0.00170 pb for $M_{\tilde{g}}$ =1.5, 1.7 and 2 TeV respectively [121].

In Figure 7.4.1 supersymmetric signal samples with fixed $M_{\tilde{g}}$ =1.5 TeV span values for $\Delta M_{\tilde{g}\tilde{b}}$ and $\Delta M_{\tilde{b}\tilde{N}}$ of 900, 700, 500 and 300 GeV. The dominant background to contribute to the phase space arises from $t\bar{t}$ and $t\bar{t} + V$.

In this study all the scale variables are extremely useful in order to increase the signal-to-background ratio, because signal-like events populate higher values than background-like events. We expect high energy b-jets in the reconstructed decay frames for the signal distributions, while for the background, their energies are expected to be lower

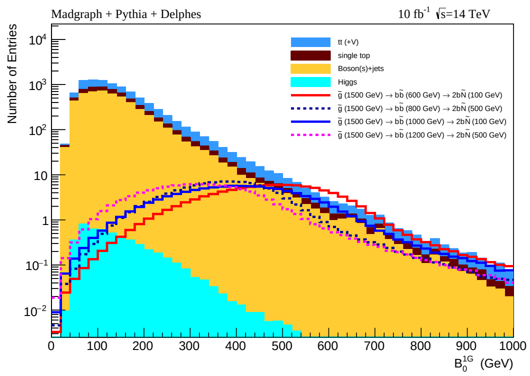

(a)

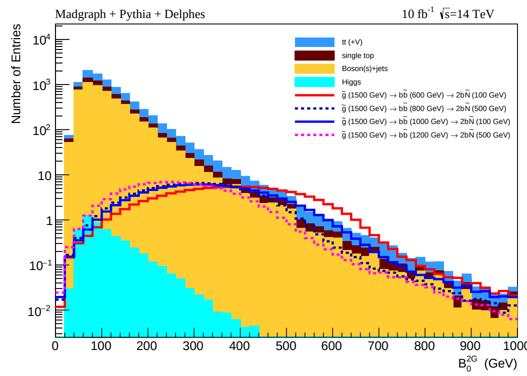

(b)

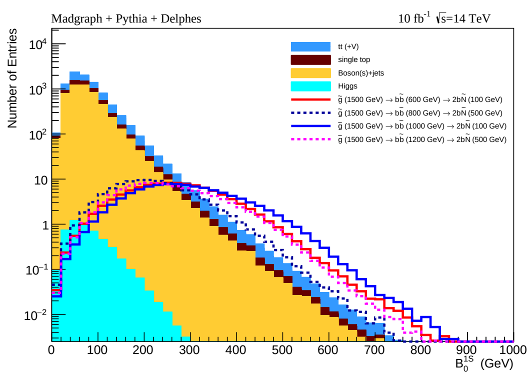

(c)

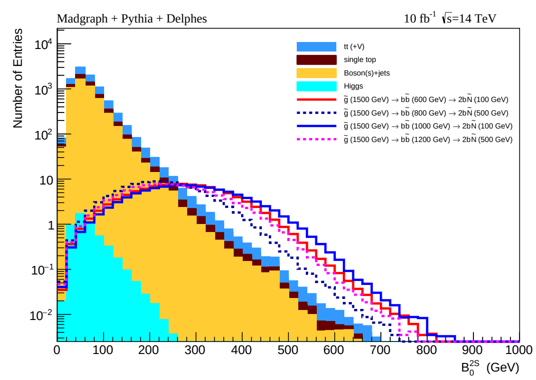

(d)

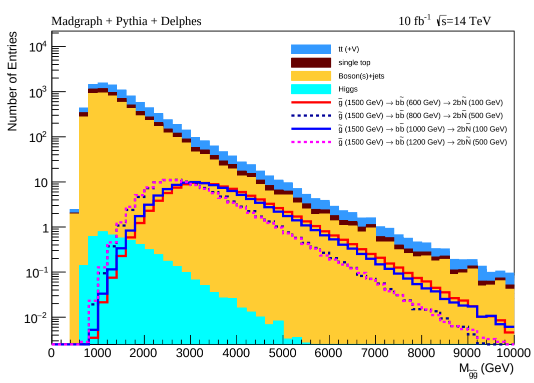

(e)

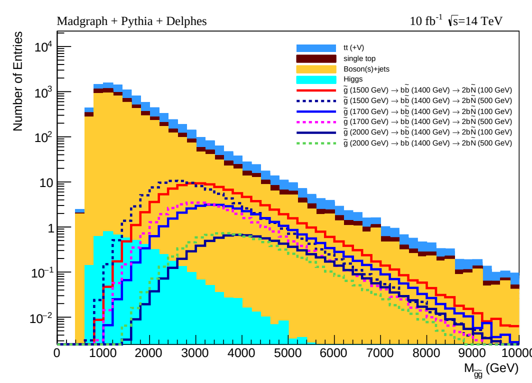

(f)

Figure 7.4.1: Distributions of the scale observables for the events satisfying the preselection criteria. Contributions of all SM backgrounds and the overlaid signal curves are scaled to a luminosity of 10 fb^{-1} at 14 TeV. For the signal samples, the assignment is resolved matching the four jets in the final state with the parton-level. Figures 7.4.1a and 7.4.1b show the distributions for the variables sensitive to the size of the first mass splitting plotted for each of the two hemispheres, Figures 7.4.1c and 7.4.1d for the second mass splitting and Figure 7.4.1e for the overall mass scale. The SUSY scenarios refer to fixed $M_{\tilde{g}} = 1.5$ TeV, $M_{\tilde{N}}$=100 GeV (solid lines) and $M_{\tilde{N}}$=500 GeV (dashed lines) while in Figure 7.4.1f are presented SUSY samples with fixed $M_{\tilde{b}} = 1.4$ TeV.

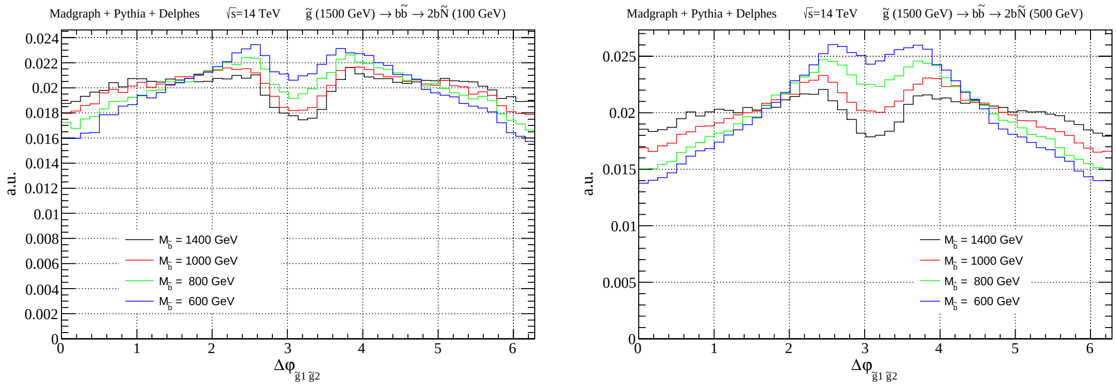

(a) Azimuthal angle between the first decay planes of the two hemispheres.

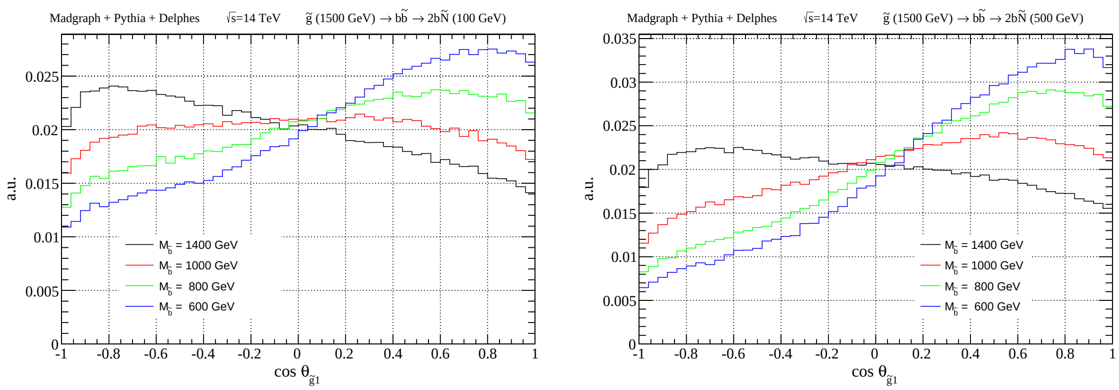

(b) Angular distribution of the decay angle from the first mass splitting for the first hemisphere.

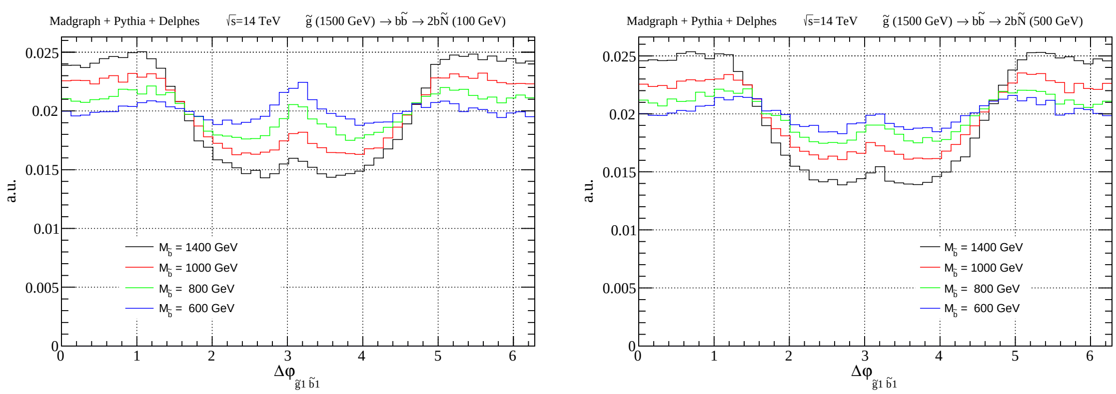

(c) Azimuthal angle between the gluino and sbottom decay planes in the hemisphere 1.

Figure 7.4.2: Normalised angular distributions for SUSY samples with $M_{\tilde{g}} = 1.5$ TeV and $M_{\tilde{N}} = 100$ GeV (left), $M_{\tilde{N}} = 500$ GeV (right).

because the SM spectrum is below the SUSY spectra investigated.

There is not a perfect symmetry between the two hemispheres due to the choice of the first hemisphere being the one with the highest momentum b-jet. This asymmetry can be noticed both for the signal and for the backgrounds and with an overall shift to higher values for the scale variables.

The *scale* variables scale with the mass splittings: with the neutralino mass fixed, we can appreciate in Figures 7.4.1a and 7.4.1b how the distributions of B_0^{iG}, where $i = 1$ or 2, are sensitive to the first mass splitting and in Figures 7.4.1c and 7.4.1d how B_0^{iS} give information for the second mass spitting. We have demonstrated that the mass for the invisible system is a Lorentz invariant greater than or equal to the true value based on the asymptotic requirement of massless invisible objects (see Eq. 4.4.3); hence the distributions for the scale observables have an overall shift to lower values compared to the monochromatic one due to a massive LSP. In other words, the smaller the phase space, the less accurate the reconstruction of the rest frames: the shift increases going from $M_{\tilde{N}}$ =100 GeV (solid lines) to $M_{\tilde{N}}$ =500 GeV (dashed lines).

Figure 7.4.1e shows the distribution of $M_{\tilde{g}\tilde{g}}$ for the SM backgrounds and the same SUSY samples mass spectra of the other scale variables, while Figure 7.4.1f shows scenarios with $M_{\tilde{b}}$= 1.4 TeV. In the absence of strange correlations or dependences from the selection criteria, the observable should peak at twice the mass of the gluino for a massless LSP. The peak is shifted to lower values of a quantity roughly equal to the neutralino mass hence this variable is, in such a way, sensitive to the overall mass scale.

Figures 7.4.2a-7.4.2c show the normalised distributions for some of the angular observables for the SUSY samples with different values of $M_{\tilde{b}}$ maintaining fixed $M_{\tilde{g}}$ and $M_{\tilde{N}}$ = 100 GeV (left) and $M_{\tilde{N}}$ = 500 GeV (right). They provide moderate additional sensitivity to the mass splittings and hence to the sbottom mass. Figures 7.4.3a and 7.4.3b show the evolutions of a two-dimensional distribution for different mass splittings with $M_{\tilde{N}}$ fixed to 100 and 500 GeV respectively. We see how the shapes are quite similar and particularly sensitive to the first mass splitting.

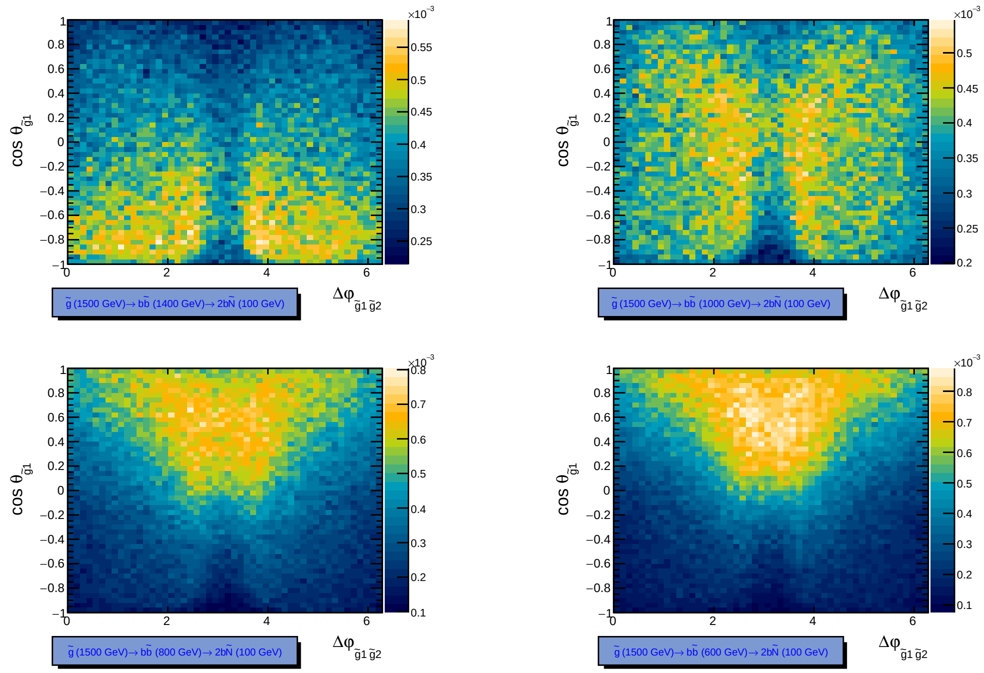

(a) $\cos\theta_{\tilde{g}_1}$ vs $\triangle\varphi_{\tilde{g}_1\tilde{g}_1}$ with $M_{\tilde{g}} = 1.5$ TeV and $M_{\tilde{N}} = 100$ GeV.

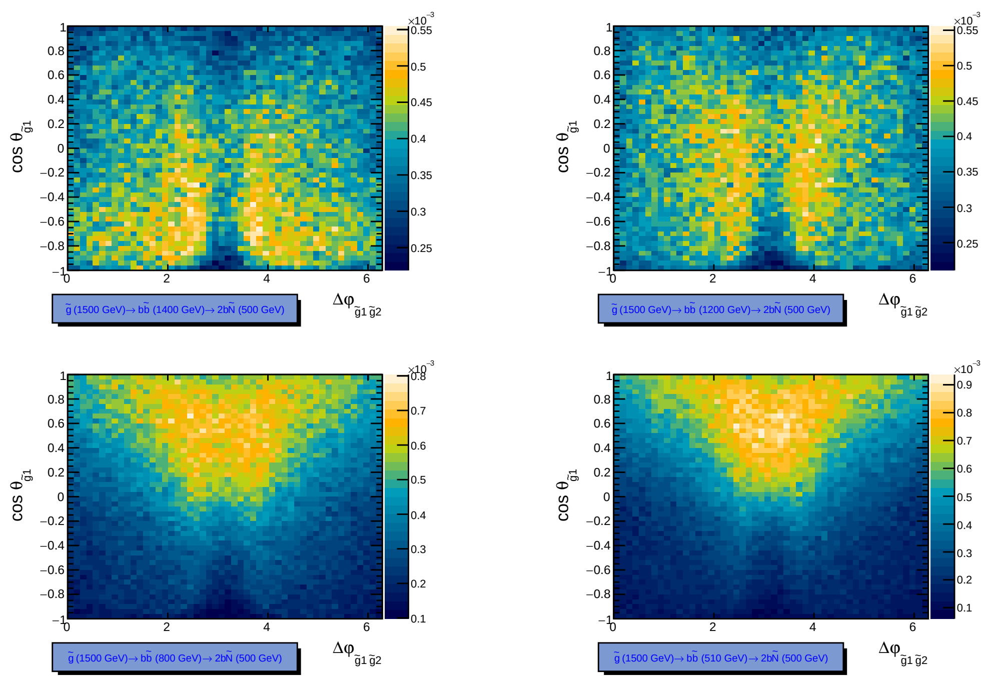

(b) $\cos\theta_{\tilde{g}_1}$ vs $\triangle\varphi_{\tilde{g}_1\tilde{g}_1}$ with $M_{\tilde{g}} = 1.5$ TeV and $M_{\tilde{N}} = 500$ GeV.

Figure 7.4.3: Scatter plot of the decay angle from the first mass splitting for the first hemisphere and the azimuthal angle between the decay planes of the first and second mass splittings for the two hemispheres.

7.5 The analysis

7.5.1 Signal and background RJR variable distributions

The four leading jets in p_T, three of them identified as resulting from the hadronisation of a bottom quark, are assigned to one of the positions in the RJR tree in Figure 7.2.1b. The procedure for the assignment of identical objects into the RJR tree is the combinatoric jigsaw rule based on the minimisation of the masses. Figures 7.5.1 and 7.5.2 show the distributions for the scale and angular RJR observables for signal and background events satisfying the preselection criteria.

The distribution of $M_{\tilde{g}\tilde{g}}$ remains substantially unchanged comparing the signal distributions with the case where the assignment was reconstructed using the simulation information. The minimum invariant mass between the pairs of visible objects provides an observable sensitive to the overall mass scale also in the hypothesis of wrong assignment. This is because the evaluation of the neutralino four-momenta (Eq. 4.2.4) moderately depends on the choice for the masses. Moreover, an incorrect assignment is likely in the cases of similar values for the mass pairs: large angular separations between the directions of the four objects.

The other scale and angular variables lose sensitivity to the mass splittings. With a fixed overall mass scale, the dashed and solid lines are overlapped for the scale variables while the angular variables provide similar distributions independently from the mass spectrum. Figure 7.5.3 shows the comparison for the normalised distributions of B_0^{1G} knowing the correct assignment as described in Section 7.4.2 (left) or using the combinatoric jigsaw rule (right).

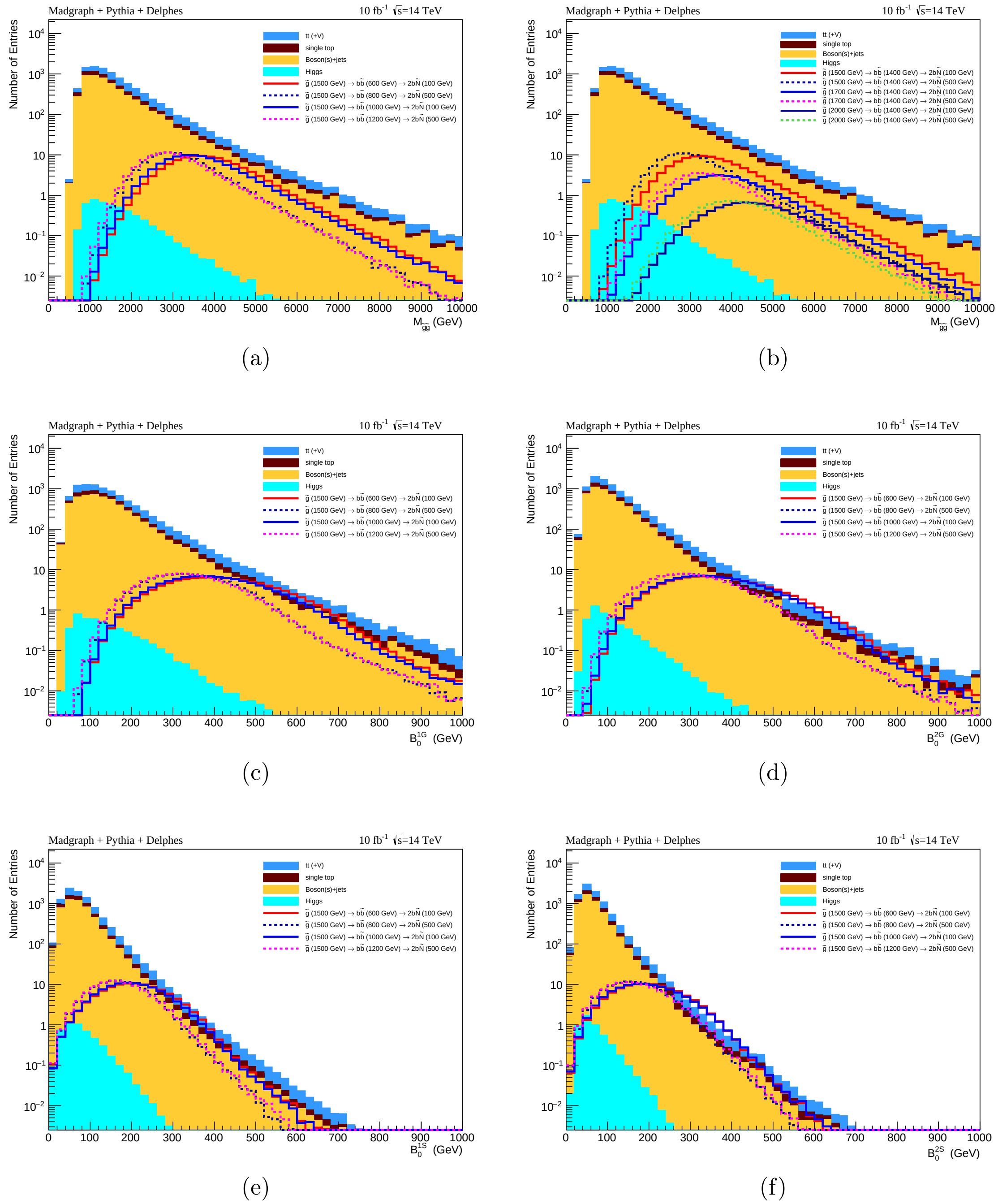

Figure 7.5.1: **The RJR scale observables.** Distributions of the scale observables for the events satisfying the preselection criteria. Contributions of all SM backgrounds and the overlaid signal curves are scaled to a luminosity of 10 fb^{-1} at 14 TeV. SUSY scenarios with fixed $M_{\tilde{g}} = 1.5$ TeV, $M_{\tilde{N}}$=100 GeV (solid lines) and $M_{\tilde{N}}$=500 GeV (dashed lines).

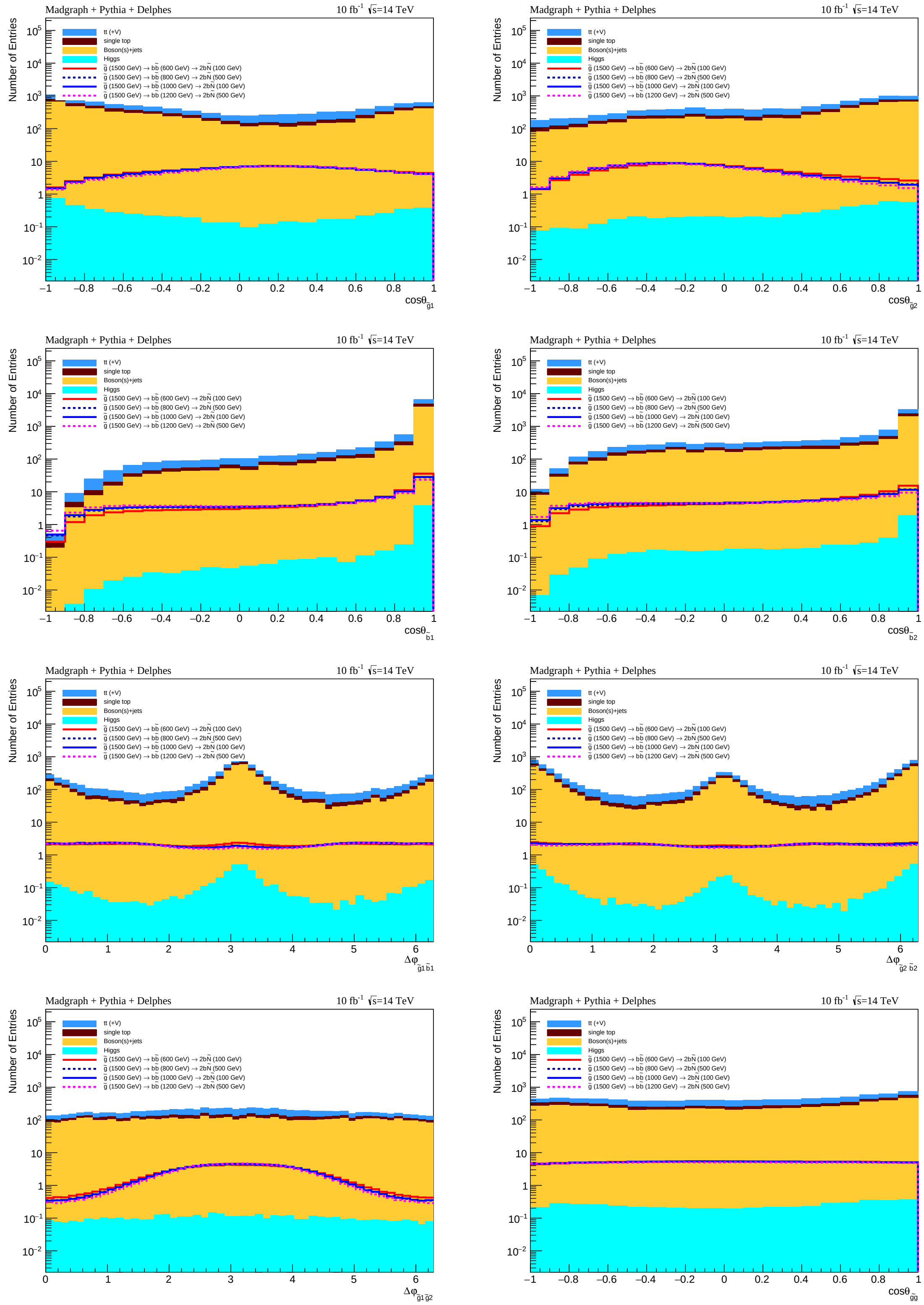

Figure 7.5.2: **The RJR angular observables.** Distributions of the scaleless variables for the events satisfying the preselection criteria. Contributions of all SM backgrounds and the overlaid signal curves are scaled to a luminosity of 10 fb^{-1} at 14 TeV. SUSY scenarios with fixed $M_{\tilde{g}}$ = 1.5 TeV, $M_{\tilde{N}}$=100 GeV (solid lines) and $M_{\tilde{N}}$=500 GeV (dashed lines).

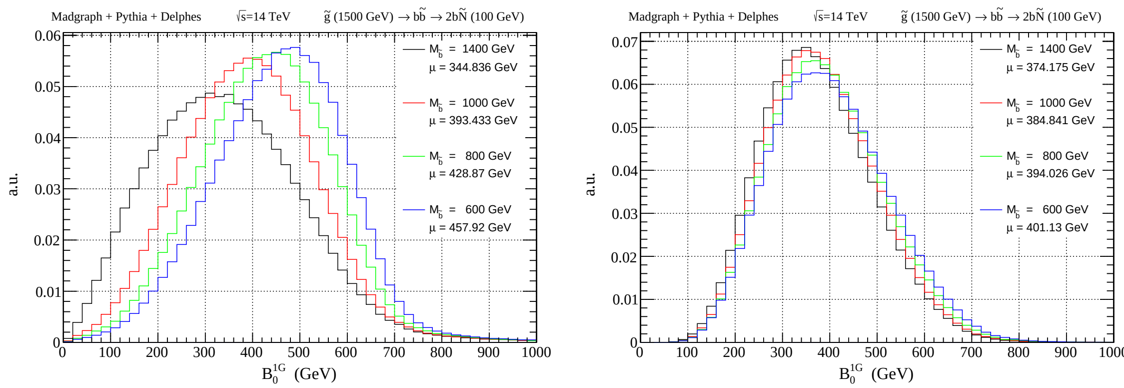

Figure 7.5.3: Normalised distributions of B_0^{1G} for the truth-level matching case (left) and the RJR combinatoric jigsaw assignment (right). Supersymmetric scenarios with $M_{\tilde{g}} = 1.5$ TeV $M_{\tilde{N}}$ =100 GeV and different values of $M_{\tilde{b}}$ are compared.

7.5.2 Angular and scale signal regions

A determined effort to correctly assign the four identical objects in the final state in order to gain sensitivity to intermediate mass splittings is not necessarily worthwhile. The combinatoric jigsaw rules based on the minimisation of the masses provide RJR scale and angular variables with great impact in the discrimination of the signal with respect to the SM background processes.

Signal-like events tend to populate higher values than background-like events for the scale variables as evident from Figure 7.5.1. Furthermore, signal-like events tend to have different features than background-like events for the decay angle distributions. The backgrounds differ significantly from the signal distributions around ± 1 for $\cos\theta_{\tilde{g}_1}$ and $\cos\theta_{\tilde{g}_2}$ and for $\cos\theta_{\tilde{g}\tilde{g}}$, while the difference becomes pronounced around one for $\cos\theta_{\tilde{b}_1}$ and $\cos\theta_{\tilde{b}_2}$. The distributions of the SM background for the azimuthal angle between the two decay planes in each hemisphere are somewhat peaked around 0, π and 2π. To conclude, consider closely the signal distribution of $\triangle\varphi_{\tilde{g}_1\tilde{g}_2}$, the azimuthal angle between the decay planes of the two gluinos picked around π. In principle, the combinatoric jigsaw based on the double minimisation is sensitive to the property that the two gluinos are back-to-back in the gluino CM frame and the sbottom and the beauty quark are

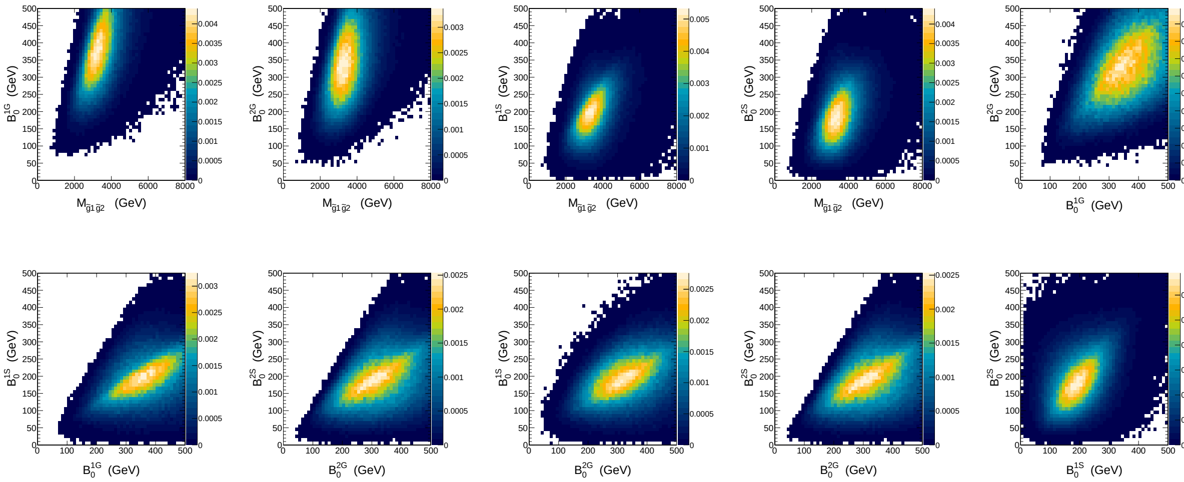

Figure 7.5.4: Two-dimensional distributions between the scale jigsaw variables applied in the analysis. A sample with $M_{\tilde{g}} = 1.5$ TeV, $M_{\tilde{b}} = 1$ TeV and $M_{\tilde{N}} = 100$ GeV is used.

back-to-back in each gluino decay frame. In the CM frame, $\triangle\varphi_{\tilde{g}_1\tilde{g}_2}$ is computed as the difference between the unit vectors of $\vec{B}^G \wedge (\vec{B}^S + \vec{N})$ in each hemisphere. The second minimisation tends to associate to the LSP the b-jet closer in direction, so the reconstructed $\tilde{b}$ direction is close to this b-jet. In this way, the minimisation of the two hemispheres, computed only with the visible objects, is substantially maintained and the two gluinos are reconstructed mostly back-to-back. For a simpler one-step decay topology, with the superparticle produced by the proton scattering decaying directly to the LSP and a visible particle of the SM, $\triangle\varphi_{\tilde{g}_1\tilde{g}_2} = \pi$.

In order to use our variables to increase the signal-to-background ratio we wish to study their correlations. Figures 7.5.4-7.5.6 display the two-dimensional distributions between the RJR variables applied in the ensuing analysis for the signal sample with $M_{\tilde{g}} = 1.5$ TeV, $M_{\tilde{b}} = 1$ TeV and $M_{\tilde{N}} = 100$ GeV.

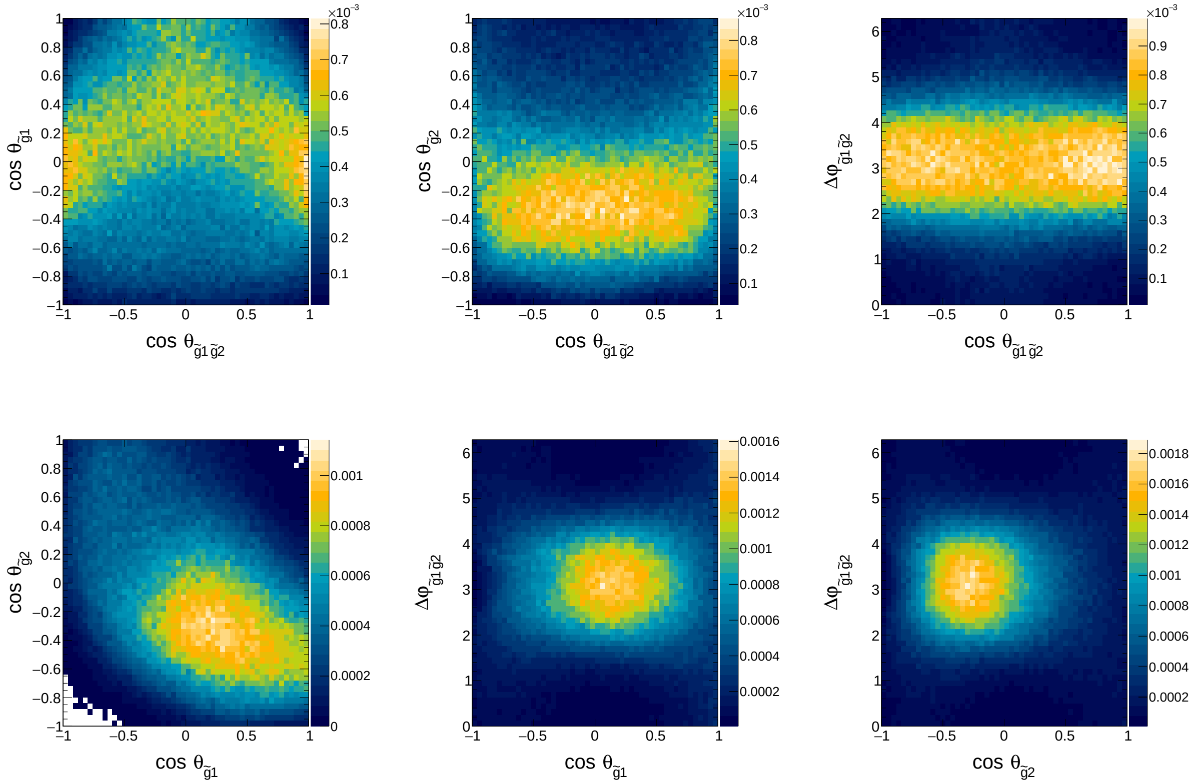

Figure 7.5.5: Two-dimensional distributions between the main angular jigsaw variables applied in the analysis. A sample with $M_{\tilde{g}} = 1.5$ TeV, $M_{\tilde{b}} = 1$ TeV and $M_{\tilde{N}} = 100$ GeV is used.

Signal scale RJR variables are slightly correlated (Figure 7.5.4) while angular variables are mostly uncorrelated with their own and with the scale observables (Figures 7.5.5 and 7.5.6). The jigsaw observables are largely uncorrelated for all the signal scenarios investigated in this work.

The double minimisation procedure used to solve the assignment issue provides us with a powerful method to increase the signal-to-background ratio. Angular Jigsaw distributions are similar for all the SUSY mass spectra investigated in this work and the kinematic distributions depend mostly on $M_{\tilde{g}}$ and $M_{\tilde{N}}$. We exploit this characteristic by defining a simple strategy with a single signal region based on angular variables only. These angular selection criteria are complemented by selections imposed on scale sensitive variables.

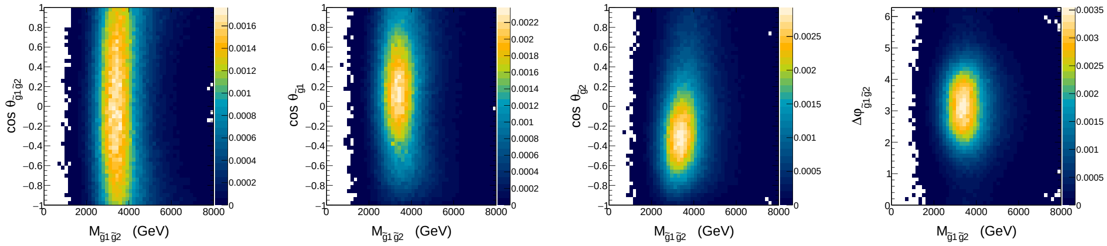

(a) Scatter plots between $M_{\tilde{g}_1\tilde{g}_2}$ and the angular jigsaw variables.

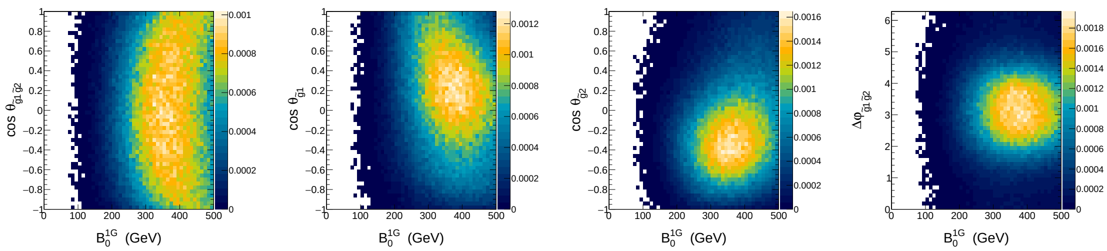

(b) Scatter plots between B_0^{1G} and the angular jigsaw variables.

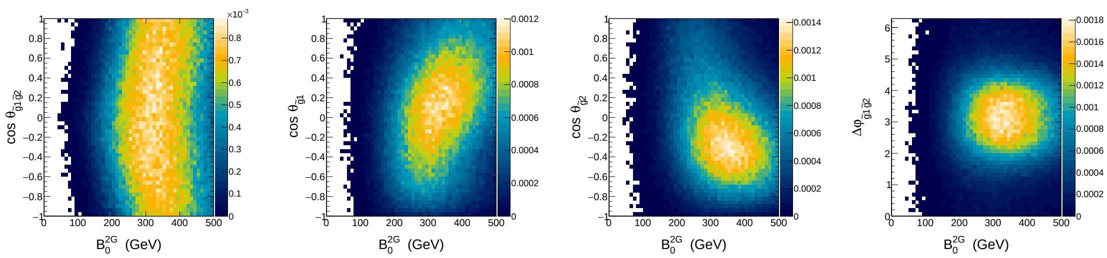

(c) Scatter plots between B_0^{2G} and the angular jigsaw variables.

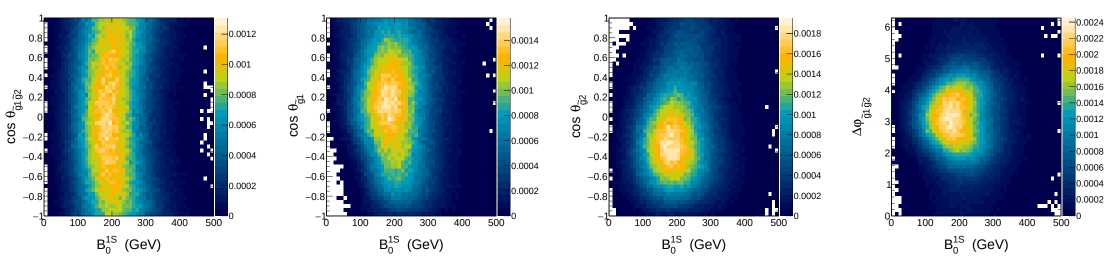

(d) Scatter plots between B_0^{1S} and the angular jigsaw variables.

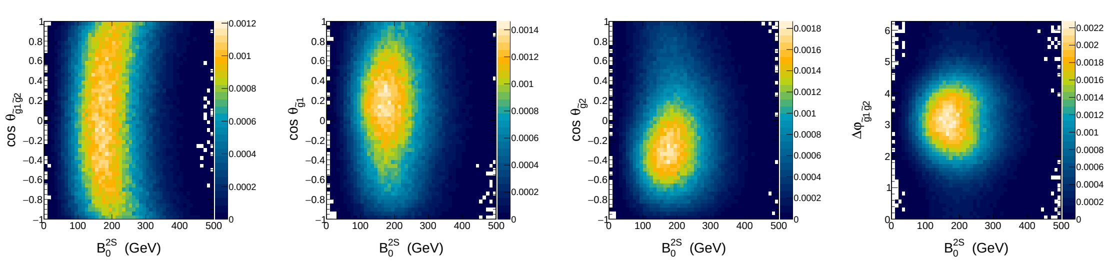

(e) Scatter plots between B_0^{2S} and the angular jigsaw variables.

Figure 7.5.6: Two-dimensional distributions between the scale and angular RJR variables applied in the analysis. A sample with $M_{\tilde{g}} = 1.5$ TeV, $M_{\tilde{b}} = 1$ TeV and $M_{\tilde{N}} = 100$ GeV is used.

Angular jigsaw selection criteria

- $-0.9 < \cos\theta_{\tilde{g}_1} < 0.8$
- $-0.9 < \cos\theta_{\tilde{g}_2} < 0.6$
- $\cos\theta_{\tilde{b}_1} < 0.8$
- $\cos\theta_{\tilde{b}_2} < 0.8$
- $\triangle\varphi_{\tilde{g}_1\tilde{b}_1} < \frac{5}{6}\pi$ and $\triangle\varphi_{\tilde{g}_1\tilde{b}_1} > \frac{7}{6}\pi$
- $\triangle\varphi_{\tilde{g}_2\tilde{b}_2} < \frac{5}{6}\pi$ and $\triangle\varphi_{\tilde{g}_2\tilde{b}_2} > \frac{7}{6}\pi$
- $\frac{\pi}{4} < \triangle\varphi_{\tilde{g}_1\tilde{g}_1} < \frac{7}{4}\pi$
- $-0.9 < \cos\theta_{\tilde{g}\tilde{g}} < 0.9$

Figures (7.5.7 - 7.5.8) show some of the RJR variable distributions after the angular only selection criteria.[1] The comparison of Figures 7.5.1 with 7.5.7 demonstrates the efficiency of the angular selection criteria to increase the signal-to-background ratio for the scale distributions. Signal and background distributions maintain their own shapes and their different features before and after the angular selection criteria. The backgrounds differ significantly from the signal distributions around ± 1 for $\cos\theta_{\tilde{g}_1}$ and $\cos\theta_{\tilde{g}_2}$ while $\triangle\varphi_{\tilde{g}_1\tilde{g}_2}$ is peaked around π. Now we complement the angular selection criteria by selections on scale variables.

Scale jigsaw selection criteria

- $B_0^{1G} > 240$ GeV
- $B_0^{2G} > 220$ GeV

[1] The figures in 7.5.8 show the $N-1$ selection criteria: the requirement of the displayed angular variable is under the shaded region.

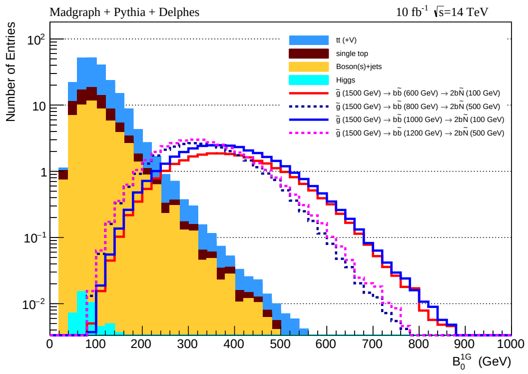

(a)

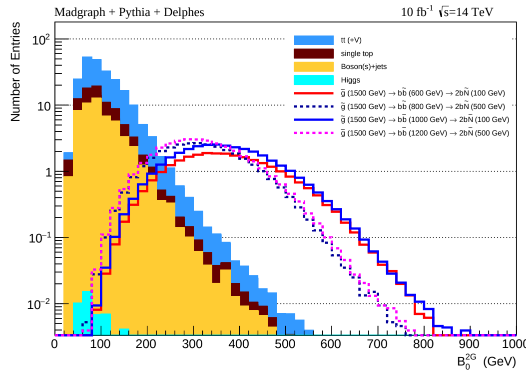

(b)

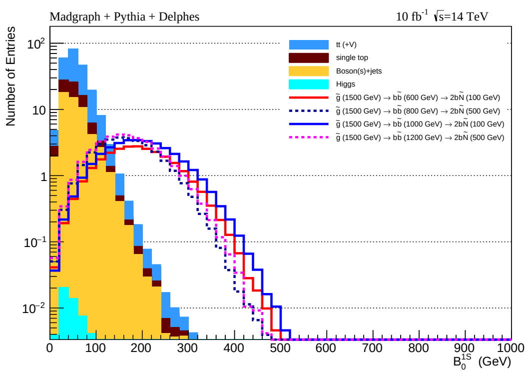

(c)

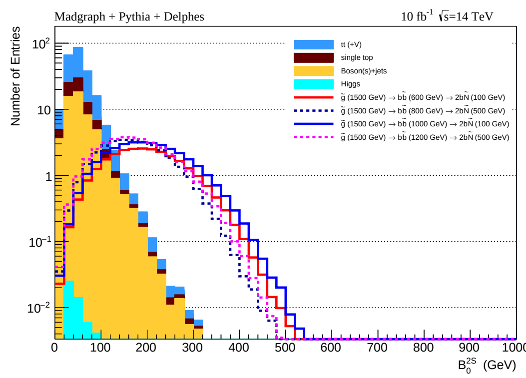

(d)

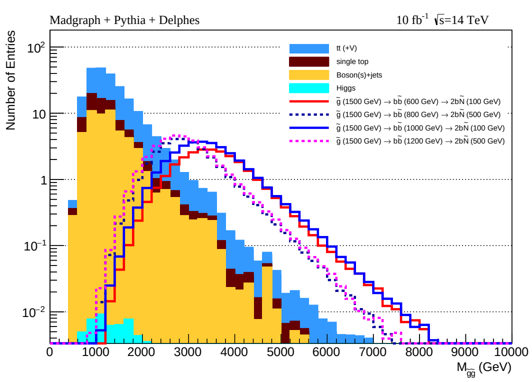

(e)

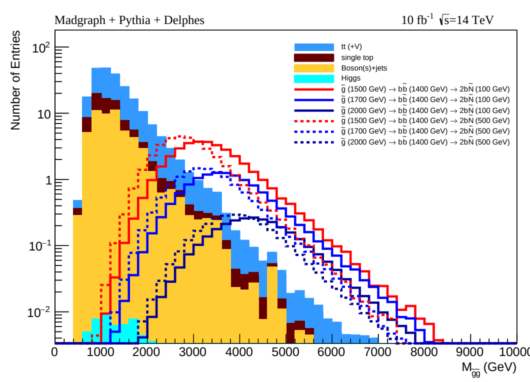

(f)

Figure 7.5.7: Distributions of the scale observables for the events satisfying the angular selection criteria. Contributions of all SM backgrounds and the overlaid signal curves are scaled to an integrated luminosity of 10 fb^{-1} at $\sqrt{s} = 14$ TeV. SUSY scenarios with $M_{\tilde{N}}$=100 GeV (solid lines) and $M_{\tilde{N}}$=500 GeV (dashed lines).

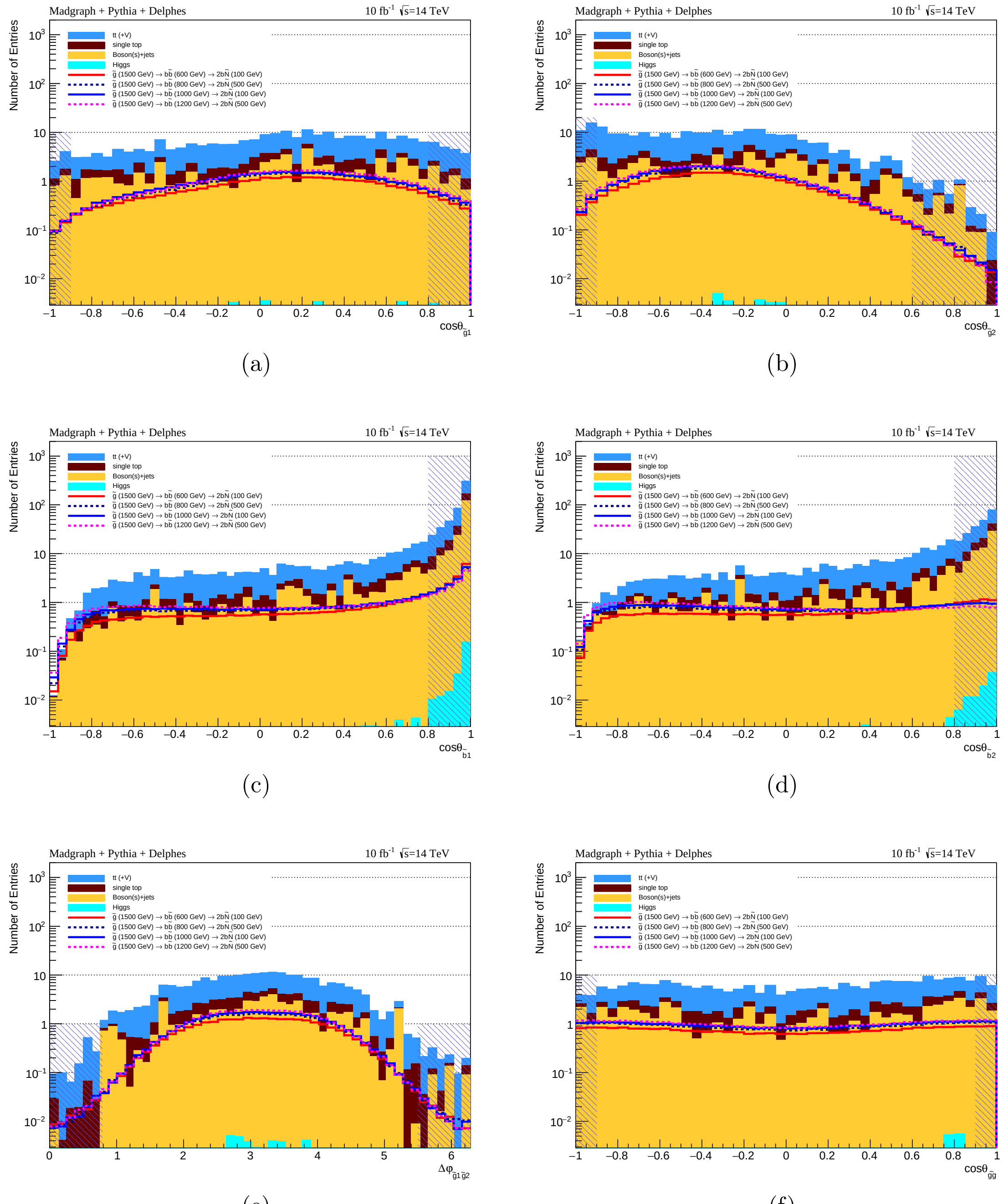

Figure 7.5.8: Distributions of the scaleless observables for the events satisfying the N-1 angular selection criteria. Contributions of all SM backgrounds and the overlaid signal curves are scaled to an integrated luminosity of 10 fb^{-1} at $\sqrt{s} = 14$ TeV. SUSY scenarios with fixed $M_{\tilde{g}} = 1.5$ TeV, $M_{\tilde{N}}$=100 GeV (solid lines) and $M_{\tilde{N}}$=500 GeV (dashed lines).

- $B_0^{1S} > 80$ GeV
- $M_{\tilde{g}\tilde{g}} > 2.4$ TeV

Figures 7.5.9 and 7.5.10 show the distributions of the RJR observables after the angular and scale selection criteria. Notice that a requirement on B_0^{2S} seems not to be necessary. One could have chosen to randomise the two hemispheres instead of defining the first one, the one with the leading p_T jet. One can demonstrate how the distributions for the RJR observables and the following selection criteria would be symmetric in such a case.

The RJR selection criteria for the signal region are applied primarily to angular variables and increase the sensitivity to distinguish between signal or background-like events. The variable sensitive to the overall mass scale maintains its shape after the RJR selection criteria for the signal distributions. There is a negligible overall shift to higher values because of the selection criteria on the other scale variables.

7.6 Conclusions

7.6.1 Results

This signal region can be used to obtain the discovery prospects of gluino mediated pair-production of sbottoms (Figure 7.2.1). Figure 7.6.1 shows the significance as function of $M_{\tilde{b}}$ for all the scenarios studied with $M_{\tilde{g}}$=1.5 TeV for a 30% total uncertainty of the Standard Model background using this single signal region.

Figure 7.6.1 displays significances roughly constant for fixed $M_{\tilde{N}}$ and $M_{\tilde{g}}$ while varying $M_{\tilde{b}}$. The small reduction of the Z-score, described in Section 3.5.1, for a small value of $M_{\tilde{b}}$ is due to the selection criteria applied on $\cos\theta_{\tilde{b}_1}$ and $\cos\theta_{\tilde{b}_2}$, while the gap between $M_{\tilde{N}} = 100$ GeV and $M_{\tilde{N}} = 500$ GeV increases with more stringent scale selection criteria. For an integrated luminosity of 2 fb^{-1} and 30% background uncertainty, 3 σ

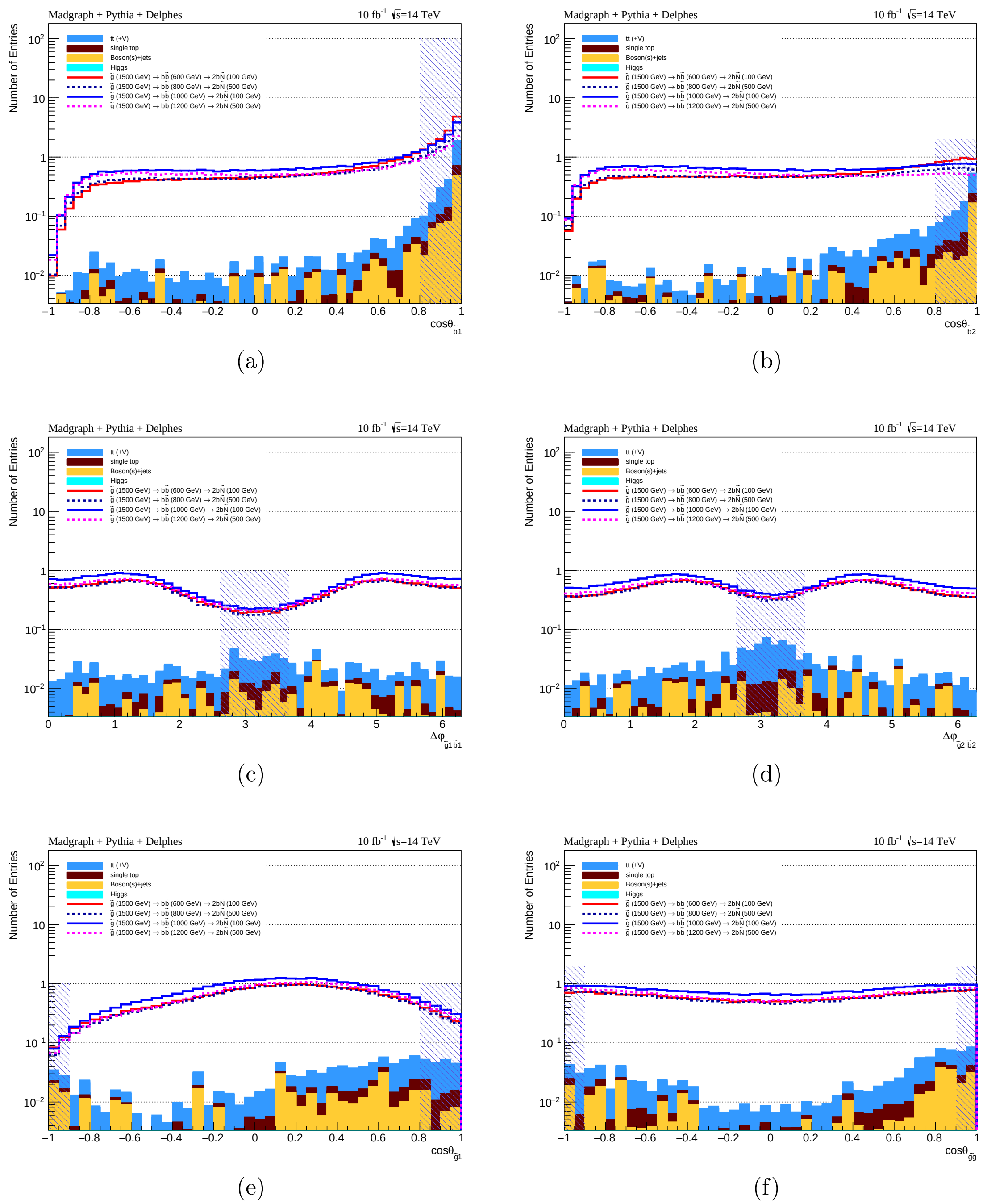

(a) (b)

(c) (d)

(e) (f)

Figure 7.5.9: Distributions for the angular observables for the events satisfying the RJR selection criteria. Contributions of all SM backgrounds and the overlaid signal curves are scaled to a luminosity of 10 fb^{-1} at 14 TeV. SUSY scenarios with fixed $M_{\tilde{g}} = 1.5$ TeV, $M_{\tilde{N}}$=100 GeV (solid lines) and $M_{\tilde{N}}$=500 GeV (dashed lines).

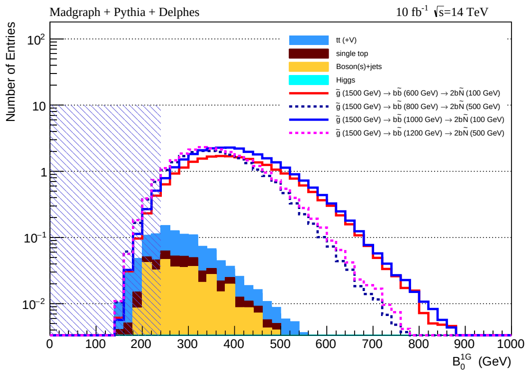

(a)

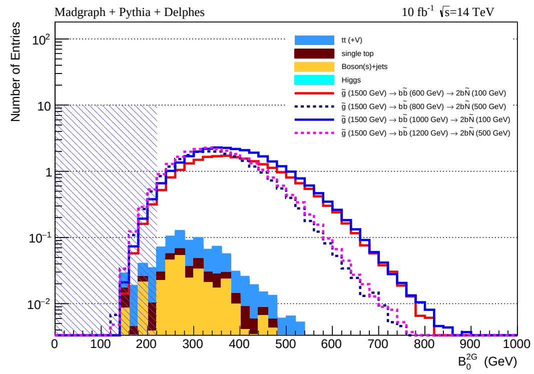

(b)

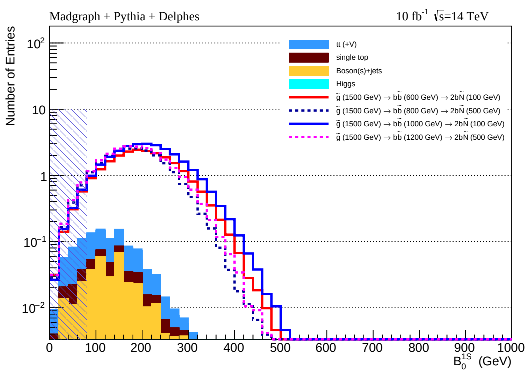

(c)

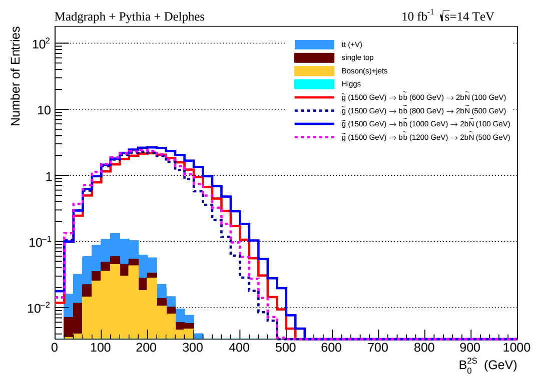

(d)

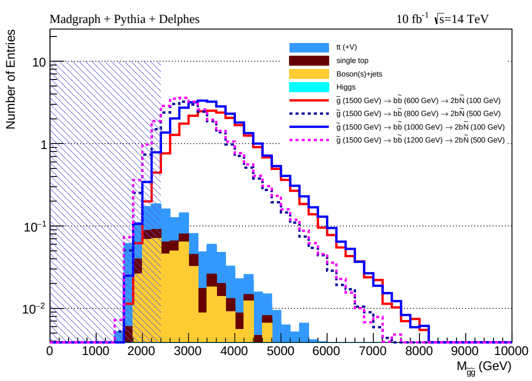

(e)

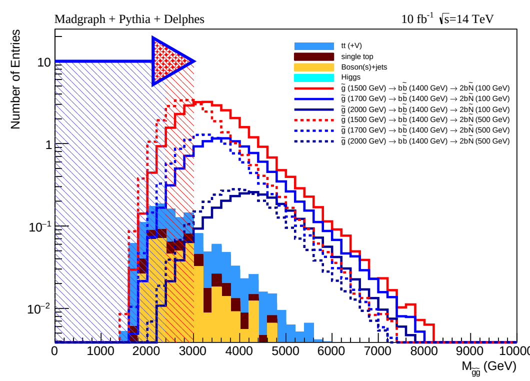

(f)

Figure 7.5.10: Distributions for the scale observables for the events passing the RJR selection criteria. Contributions of all SM backgrounds and the overlaid signal curves are scaled to a luminosity of 10 fb^{-1} at 14 TeV. SUSY scenarios with $M_{\tilde{N}}$=100 GeV (solid lines) and $M_{\tilde{N}}$=500 GeV (dashed lines).

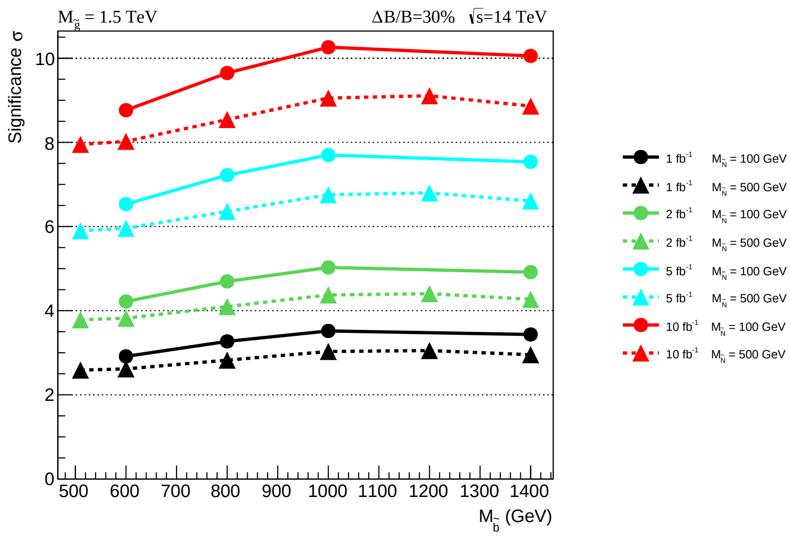

Figure 7.6.1: Significance as a function of the sbottom mass for the total integrated luminosity for the jigsaw signal region. The uncertainty on the total SM background is fixed to 30%. SUSY scenarios have fixed $M_{\tilde{g}} = 1.5$ TeV, $M_{\tilde{N}}$=100 GeV and 600 GeV $\leq M_{\tilde{b}} \leq 1.4$ TeV (solid lines) and $M_{\tilde{N}}$=500 GeV and 510 GeV $\leq M_{\tilde{b}} \leq 1.4$ TeV (dashed lines).

evidence can be obtained for $M_{\tilde{g}} = 1500$ GeV, all the sbottom masses investigated in this work and $M_{\tilde{N}}$ above 500 GeV.

The sensitivity achieved, mostly independent of the sbottom mass, can be extended from $M_{\tilde{N}} + m_b < M_{\tilde{b}} < M_{\tilde{g}} - m_b$ to $M_{\tilde{b}} > M_{\tilde{g}}$. For the topology studied, the double minimisation procedure provides angular jigsaw distributions with a similar shape and a small dependence on the mass spectrum. In order to investigate higher values for $M_{\tilde{g}}$ and $M_{\tilde{b}}$ it is sufficient to use more stringent scale selection criteria. Figure 7.5.10f anticipates what happens when we increase the selection criterion for the overall mass scale: we gain sensitivity for higher values of the gluino mass with a negligible loss for the yields resulting from lower mass spectra. This feature is common for all of the scale variables and the loss in sensitivity is higher for higher values of the LSP mass because of the more compressed mass spectra. For example, if we maintain the same angular selection criteria yet tighten the scale variables such that:

- $B_0^{1G} > 300$ GeV,

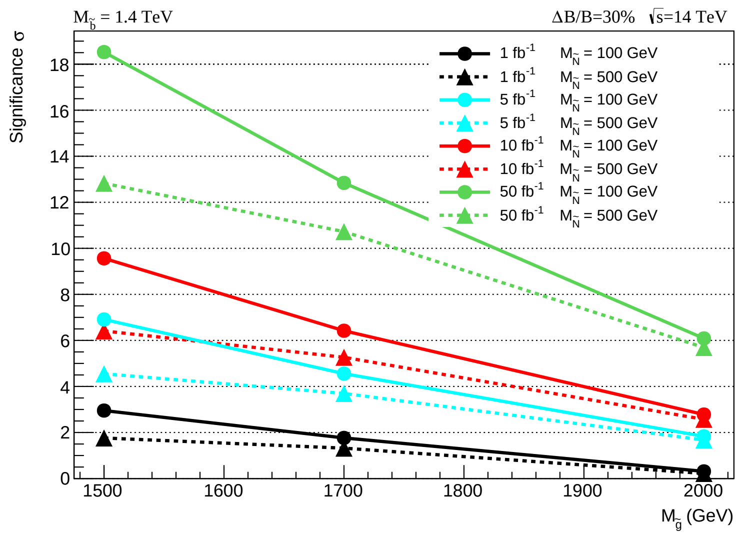

Figure 7.6.2: Significance as a function of the gluino mass for the total integrated luminosity for the jigsaw signal region. The uncertainty on the total SM background is fixed to 30%. SUSY scenarios have fixed $M_{\tilde{b}} = 1.4$ TeV, $M_{\tilde{N}}$=100 GeV (solid lines) and $M_{\tilde{N}}$=500 GeV (dashed lines).

- $B_0^{2G} > 300$ GeV,
- $B_0^{1S} > 120$ GeV,
- $M_{\tilde{g}\tilde{g}} > 3$ TeV,

the discovery reach ($Z_{\text{Bi}} > 5\sigma$) is achieved for $M_{\tilde{g}}$ until 2 TeV and beyond for $\int L = 50$ fb^{-1}, as displayed in Figure 7.6.2.

Figure 7.6.2 shows how with the signal region defined with the fixed angular selection criteria and more stringent scale criteria and with the 30% background uncertainty, 4σ evidence can be obtained for $M_{\tilde{g}}$ ∼1900 GeV, $M_{\tilde{b}}$= 1400 GeV, $M_{\tilde{N}}$= 100 GeV with an integrated luminosity of 10 fb^{-1}, while 2σ exclusion limit for $M_{\tilde{g}}$ ∼2 TeV, $M_{\tilde{b}}$= 1400 GeV, $M_{\tilde{N}}$= 500 GeV with an integrated luminosity of 5 fb^{-1}. These results are mostly insensitive to the intermediate $M_{\tilde{b}}$.

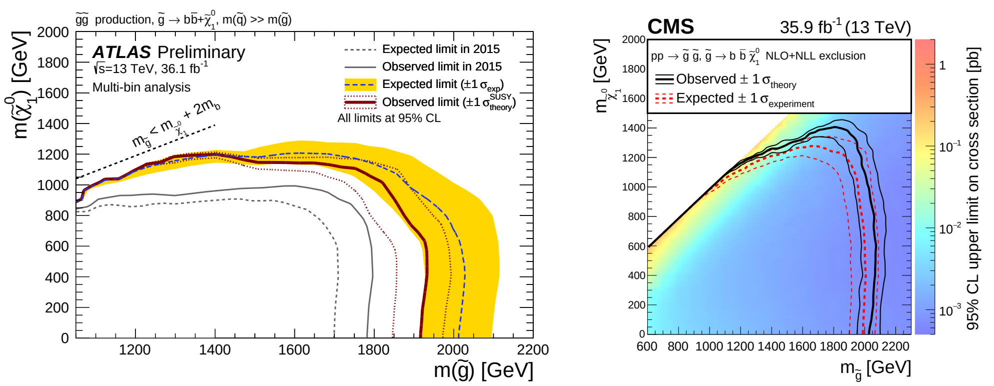

(a) (b)

Figure 7.6.3: Current results from ATLAS and CMS collaborations for the search of the SUSY simplified topology $pp \to \tilde{g}\tilde{g}(\tilde{g} \to b\bar{b}\tilde{\chi}_1^0)$. Figures from [134] (a) and [123] (b).

7.6.2 Summary

We have applied the Recursive Jigsaw Reconstruction technique to study a final state with gluino mediated third generation particles with on-shell bottom squarks decaying to a b-jet and the LSP. This analysis neglects final states with top quarks and their SUSY partners. Such topologies will be studied in a future work as outline in the Chapter 9, leveraging hadronic top decays and boosted object reconstruction methods.

A selection applied primarily to scaleless variables can reduce the SM background to a level where discovery of certain scenarios can be made with the data collected so far from the LHC experiments. Gluinos with mass above 2 TeV would be discovered with an integrated luminosity of 50 fb^{-1} for all the scalar bottom and LSP masses investigated. With this approach we demonstrate useful features that may be exploited, not only in measuring a signal for this channel, but in using the various scale sensitive variables to extract the properties of the particle spectrum once discovery is made.

The sensitivity to the gluino mass remains constant as a function of the bottom squark mass as shown in Figure 7.6.1. This feature suggests that it is useful to investigate the corresponding three body decay simplified SUSY topology ($\tilde{g} \to b\bar{b}\tilde{\chi}_1^0$) with the RJR technique and estimate reach/exclusion limits in the $M_{\tilde{g}}$ vs $M_{\tilde{\chi}_1^0}$ plane. Such a study should probe larger masses for the LSP, including the analyses of the compressed phenomenology for small mass splittings (see Figure 4.6.2), by imposing an ISR branch in the RJR tree for final states with $N_{\text{jet}} > 4$.

Chapter 8

Sbottom pair-production in final states with two b-jets and missing transverse momentum

8.1 Introduction

Among the SUSY sought-after experimental outcomes, the observation of signatures due to the sbottom pair-production is topical since relatively light scalar partners of the beauty quark are motivated by natural models as described in Section 2.3.6. This study [116] focuses on the simplified topology represented by the Feynman diagram in Figure 8.1.1. A pair of light sbottoms are assumed to be produced at the LHC each decaying to a b-quark and a neutralino LSP: $pp \to \tilde{b}_1\bar{\tilde{b}}_1$, ($\tilde{b}_1 \to b\tilde{\chi}_1^0$, $\bar{\tilde{b}}_1 \to \bar{b}\tilde{\chi}_1^0$).[1]

Armed with the strategies and results obtained with the RJR technique in the previous proposed analyses concerning fully hadronic final states and compressed studies; open, intermediate and compressed scenarios are probed in this chapter. In Chapter 7 we use the canonical strategy for open mass spectra based on the assumption that the leading

[1]From now on, we refer to the light sbottom simply as $\tilde{b}$ with no distinction for the antiparticle.

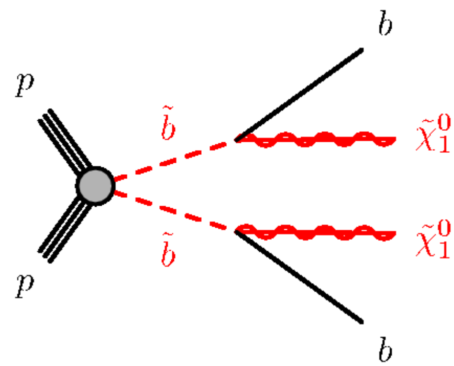

Figure 8.1.1: Feynman diagram for the scalar bottom pair-production in final states with two b-jets and missing transverse momentum.

jets in p_T are the result of the hadronisations produced by the quark decay products. On the other hand, in Chapter 5 the minimisation of the ISR vs SUSY masses is implemented for the assignment of the light jets in the compressed regime, while in Chapter 6 electrons and muons are assumed to be decay products of the S-system.

In this study, we elaborate a sort of combination of these strategies together with the b-tagging information, with the purpose to reconstruct not just the centre-of-mass of the two sbottoms or S-system, but to have additional handles useful for compressed or intermediate mass spectra. For this reason, QCD radiation from initial and final states hadronising into isolated jets provide information that is useful to maintain in order to probe the SUSY scale more accurately, constructing additional RJR observables to distinguish possible signals of new physics from SM-like events.

8.2 RJR tree motivation

Signal samples are pp collision at $\sqrt{s} = 14$ TeV producing a pair of light sbottoms with masses in the range 600 GeV$\leq M_{\tilde{b}} \leq 1.5$ TeV, while the mass splittings span from full open ($M_{\tilde{\chi}_1^0} = 0$ GeV), to extremely compressed ($\Delta M = M_{\tilde{b}} - M_{\tilde{\chi}_1^0} = 25$ GeV), scenarios.

Since a large mass of the sbottom, the scattering partons carry a large fraction of the proton momenta. Initial state QCD radiation can result in high energy jets in the signal

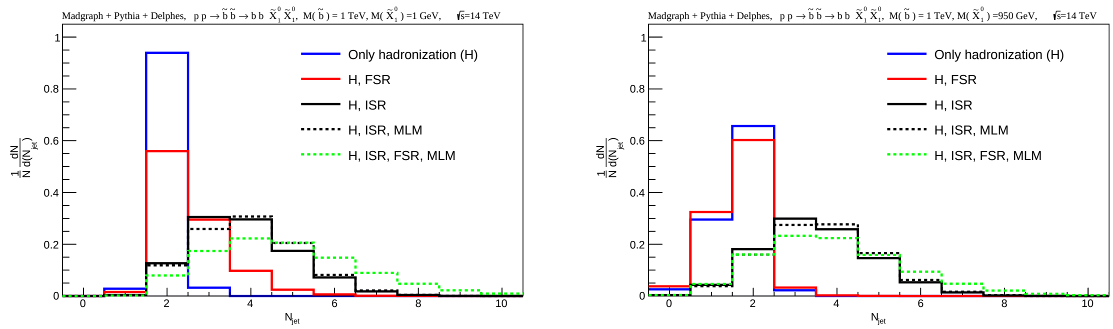

(a) (b)

Figure 8.2.1: Final state jet multiplicity for open (a) and compressed (b) SUSY samples with the activation of different effects in the Madgraph + Pythia + Delphes simulation.

events. Figure 8.2.1 shows the jet multiplicity of two signal samples in the Madgraph + Pythia + Delphes framework turning on different effects described in Section 3.2.2.[2]

We notice how the dominant impact in increasing the jet multiplicity from the value two is due to ISR more than FSR. For example, the black and red continuous lines in Figure 8.2.1a with means respectively ~ 2.6 and ~ 3.8 can be compared. The dashed lines refer to the distribution of the jet multiplicity for events resulting from the MLM-matching in the Madgraph + Pythia context. The mean value of the black dashed curve is slightly larger than the corresponding solid one due to the veto effect resulting in non-matched events when two jets fly in the same direction as described in Section 3.4.1. The final effect in the jet multiplicity due to FSR can be seen comparing the two dashed lines.[3]

Furthermore, we demonstrate that QCD radiation in the initial state results in jets generally with higher transverse momentum than FSR, with increasing separation reducing the mass difference between the superparticles. This effect can be inferred from Figure

[2]The samples used in this study and in any other proposed analyses are the equivalent of the dashed green lines plus the multiple interaction (MPI) effect. For signal samples, the contribution from MPI can be neglected and it is not reported separately in the figure.

[3]This final FSR effect corresponds to the Pythia parton shower contribution from sbottoms, b-quarks and additional partons in the matrix elements hadronising in isolated jets. Hence, strictly speaking, it contains QCD radiation from ISR.

8.2.1b showing the same distributions for $\Delta M = 50$ GeV. Compressed spectra result in an overall lower jet multiplicity due to the possibility of no reconstruct low-momentum b-quarks as jets, as can be seen by comparing to the corresponding distributions of Figure 8.2.1a. Moreover, final states with only one jet are favoured when the FSR effect is activated with respect to the distribution referred to as the "only hadronisation" case (red vs blue curve). Imagine an event with two b-quarks with transverse momenta close to the lower bound defined by the anti-k_T algorithm ($p_T = 20$ GeV). When one of the two partons radiates a consistent fraction of its energy outside the jet cone likely neither the bottom-quark initiated jet, nor the FSR-jet are reconstructed.

We then must decide which jets should be assigned to the b-systems, assumed to be the decay products of the sbottoms. The choice of the two leading jets in p_T is not the optimal one, in particular for compressed mass spectra. Assuming a minimum of two jets in the final state and minimising the masses for the distinction of an ISR vs SUSY system tends to assign QCD ISR in the wrong system resulting in a biased reconstruction for the S-system and relative observables. The choice of the two leading b-jets in p_T is much better, but we want to take care of the information due to perturbative effects in the event.

We define two orthogonal regions depending on the jet multiplicity and applies two corresponding RJR trees as shown in Figure 8.2.2. When in the final state there are only two b-jets, we use the tree in Figure 8.2.2a. For a higher multiplicity the two leading b-jets are assigned to the S-system while the other jets to the ISR-system as in Figure 8.2.2b. In both cases the S-system is divided into two hemispheres (1 and 2) and each branch is a $\tilde{b}_{1(2)}$-system decaying to a visible $b_{1(2)}$ and to an invisible $\mathrm{I}_{1(2)}$ object which corresponds to the contribution of $\tilde{\chi}_1^0$.

The RJR tree in Figure 8.2.2b is the same to the tree employed for the compressed study of chargino pair-production in final states with two leptons and additional jets assigned to the ISR-system with the only difference being the number of weakly interacting particles that the $\mathrm{I}_{1(2)}$ system should represent. Similar observables can be defined

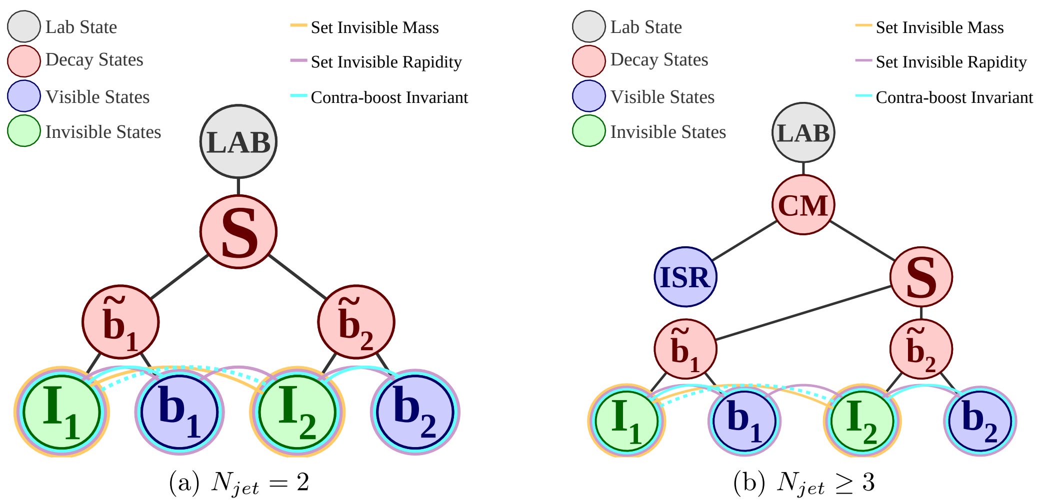

Figure 8.2.2: RJR trees for the sbottom pair-production in final states with two b-jets and missing transverse momentum. The two trees correspond to the two orthogonal regions with $N_{\text{jet}} = 2$ and $N_{\text{jet}} \geq 3$.

considering the S-system as divided into a V-system ($b_1 + b_2$) and I-system (I_1+I_2) as for the compressed simplified RJR tree in Figure 4.6.1. As described in Chapter 3, the two b-jets are required to have $|\eta| < 2.5$, while for light jets $|\eta| < 5$ is assumed.

We could use a different strategy based on the minimisation of the masses in order to assign the N-2 jets in the final state not associated with the b-systems. For example, we can impose a first combinatoric jigsaw rule, requiring at least one jet in the ISR system which is equivalent to defining an additional orthogonal region. In other words, for the case ($N_{\text{jet}} > 3$), N-2 jets would be assigned to ISR or identified as FSR for the $\tilde{b}_1$ or $\tilde{b}_2$ system using two combinatoric minimisation of masses jigsaw rules, requiring inclusively at least one jet in the ISR-system. This decay tree is shown in Figure 8.2.3, where the J_1-system expresses explicitly the fact that at least one jet is associated to ISR and FSR_1 and FSR_2 are potential QCD radiations associated to the sbottoms or to the b-quarks.

This strategy for $N_{\text{jet}} > 3$ is not used for two reasons. From the two expected jets, additional hadronic activity in the final state is likely ISR as shown in Figure 8.2.1 with generally non preferential direction. The bias due to the wrong assignment of QCD

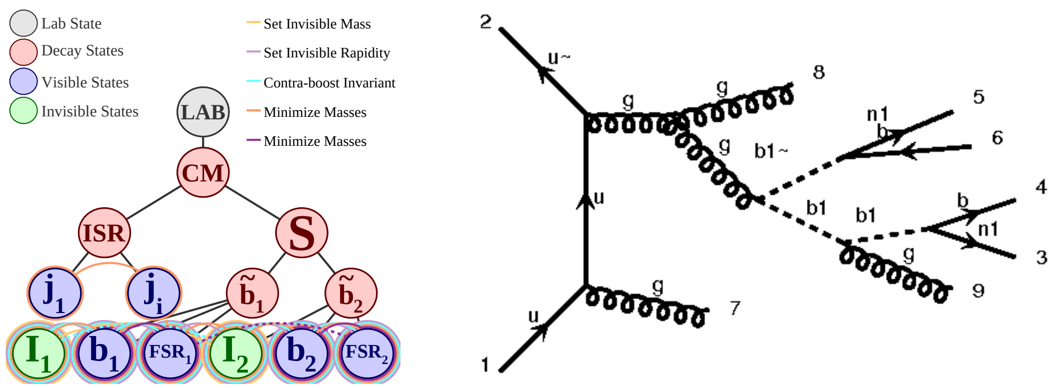

(a) (b)

Figure 8.2.3: Potential RJR tree for $N_{\text{jet}} \geq 4$ not used in this study (a). Feynman diagram for the $u\bar{u}$ fusion in two sbottoms (with $\tilde{b} \to b\tilde{\chi}_1^0$) and QCD radiation expected to result in three additional reconstructed jets (b).

ISR in a FSR-system, and hence in the S-system, would be worse than the converse. In other words, FSR-jets are expected to be low, both in number and in p_T, and their incorrect assignment has a negligible effect. Nevertheless, an analysis with three trees for three regions ($N_{\text{jet}} = 2$, $N_{\text{jet}} = 3$ and $N_{\text{jet}} > 3$) produces results very close to those presented in this chapter.

Herein we refer to the mass of a system as M^{sys} to avoid ambiguity. For example, M^{S} is the equivalent of M_{PP} of Section 4.4.4 and corresponds to the centre-of-mass energy of the two sbottoms in their CM frame. Its value is considered an estimate for the collision energy of the two partons, $\sqrt{\hat{s}}$, in the absence of other effects (see Section 4.4.4). In principle, one could define ISR as all the radiation not associated with the two sbottoms or the two b-quarks in the final state and the question if this perturbative effect should be considered or not in the estimate of $\sqrt{\hat{s}}$ is more an interpretation due to the vision of the mind than a rigorous definition. Consider for example the three gluons (7, 8 and 9) in Figure 8.2.3b. The RJR tree in Figure 8.2.3 is based on the expectation to associate the gluon number 7 to ISR and the gluon number 9 to FSR. Nevertheless, the incorrect assignment of an ISR-jet to the S-system results in an overestimation for M^{S}, and for all the other scale observables inheriting the wrong information. In the presence of perturbative effects, we consider M^{CM} the estimate for $\sqrt{\hat{s}}$.

In the extreme compressed regime, another possibility consists in taking a transverse view of the events and in assigning the jets between the ISR and S-system minimising M^{S} and M^{ISR}. Then one can apply selection criteria on the number of b-jets in the two systems. At this point, requiring for example $N^{\mathrm{ISR}}_{b-\mathrm{jet}} = 0$ and $N^{\mathrm{S}}_{b-\mathrm{jet}} \geq 1$ is not optimal, while much better are the criteria $N^{\mathrm{S}}_{b-\mathrm{jet}} = 2$ or $N^{\mathrm{S}}_{b-\mathrm{jet}} \geq 2$. In such a case, the number of signal events would be less than the number obtained by assigning the two low-momentum b-jets to the S-system from the beginning because a fraction of the events would be vetoed when reconstructed in the ISR-system. Furthermore, real ISR could populate the S-system compromising for example the reconstruction of M^V, as will be clear in the following.

The ATLAS and CMS detectors provide remarkable efficiencies for the identification of, and hence distinction between, different objects in the final state (leptons vs jets or b-jets vs light jets). Neglecting the contribution of QCD radiation in the initial state due to b-quarks, light jets can be assigned with no ambiguity to the ISR-system when no expected from the SUSY chains as in the case of the electroweakinos study in fully leptonic decay products. The combinatoric jigsaw rule for the distinction between ISR and S system are leveraged for the assignment of identical objects (light jets vs light jets or photons vs photons) or can be used when the identification efficiencies are too low (or inefficiencies for the mis-tagging too high) as can be the case of c-jets vs light jets (or vs b-jets) at the current time [135, 136].

With the choice used in this work all the RJR observables reconstructed in the S-system are identical applying the tree in Figure 8.2.2a or the tree in Figure 8.2.2b for $N_{\mathrm{jet}} \geq 2$. The jigsaw rules (Set Invisible Rapidity, Set Invisible Mass and Contra-Boost Invariant) defined by the d.o.f. of the only two leading b-jets in p_T and $\vec{\not{E}}_T$ reconstruct the same approximation for the S-system and recursively for the two $\tilde{b}$-systems independently of the ISR-system. In other words, the two trees in Figure 8.2.2 can be summarised by the tree in Figure 8.2.2b where the ISR-system can be populated from a number of jets

Category	Snowmass label (sub-categories description)
Boson + jets	BJ-BJJ (Vector boson + jets, vector boson fusion)
$t\bar{t}$ (+V)	TT, TTB (Top pair +jets, top pair plus bosons: $t\bar{t}$+Z, $t\bar{t}$+W and $t\bar{t}$+h + jets)
single top	TJ-TB (Single top + jets, top pair (off shell $t^* \to Wj$) + jets)
Di-/Tri-Boson	BBB-BB-BLL-B-LL (tri-Vector + jets, Di-Vector + jets, Drell-Yan in leptons)
Higgs	H (Gluon fusion + jets)

Table 8.1: Five categories summarizing all the main Standard Model backgrounds as part of the Snowmass study. The category name is indicative of the dominant sub-category backgrounds.

greater than or equal to zero.

8.3 Preselection

Zero leptons (electrons and muons), two jets tagged as originating from the fragmentation of bottom quarks and the minimal value of the missing transverse momentum $\not{E}_T > 50$ GeV are the preselection criteria for this proposed analysis. The SM backgrounds are summarised in Table 8.1 characterised by the Snowmass labels described in Section 3.5.1.

From Figure 8.2.1 we see how the case with exactly two jets in the final state corresponds to ∼10-15% of the signal events and this proportion is maintained requiring two b-jets. The orthogonal region $N_{\text{jet}} = 2$ could be used to increase the signal yields by applying more stringent selection criteria on the observables related to the S-system, neglecting additional handles defined with the ISR-system. To avoid ambiguity, the same requirements will be employed for the two cases. Herein, we show the distributions for the case $N_{\text{jet}} \geq 3$.

Figures 8.3.1, 8.3.2 and 8.3.3 show the distributions of the main scale, angular and other scaleless RJR observables used in this study for the signal and background events satisfying preselection criteria assuming an integrated luminosity of 50 fb^{-1}. These variables correspond to the basis associated with the RJR tree in Figure 8.2.2b and other observables associated to the simplified version of the tree S→VI. The six SUSY signals are scenarios with two values for the masses of the sbottom $M_{\tilde{b}} = 1$ TeV (solid lines) and $M_{\tilde{b}} = 1.3$ TeV (dashed lines) and with three values for the mass splitting or types of compression: open with $\Delta M \sim 1$ TeV (blue), intermediate with $\Delta M = 200$ GeV (pink) and compressed with $\Delta M = 50$ GeV (black).

The main SM background arises from vector boson + jets, with two processes dominating. The dominant background arises from the Z-boson decaying invisibly ($Z \to \nu\nu$) plus additional jets and b-jets, due for example to QCD radiation such as $g \to b\bar{b}$ or mis-tagged jets. Secondly, the W + jets contribution where neutrinos and unreconstructed leptons ($W \to l\nu$) or mis-reconstructed jets provide a source of missing transverse momentum. The minimal requirement on the missing transverse momentum together with the lepton veto in the preselection, reduces the $t\bar{t}$ background, involving semi-leptonic decay with unreconstructed leptons and processes with additional vector bosons or ISR, as sub-dominant contributions. Processes involving single-top, multi-boson and Higgs boson contributions are sub-dominant or negligible.

The scale variable with the most impact for the discrimination of open signal samples w.r.t. background processes is the mass of the sbottom systems $M^{\tilde{b}}$, followed by the missing transverse momentum reconstructed in the CM frame $p_{\mathrm{T,I}}^{\mathrm{CM}}$ as shown in Figures 8.3.1a and 8.3.1b. For open mass spectra a large proportion of signal events populates the tail of the BG distribution for the the reconstruction of $M^{\tilde{b}_1} = M^{\tilde{b}_2} \equiv M^{\tilde{b}}$.

Other scale observables, such $M^{\mathrm{CM}} = E_{\mathrm{S}}^{\mathrm{CM}} + E_{\mathrm{ISR}}^{\mathrm{CM}}$ or M^{S}, have less sensitivity, with the distribution for the latter shown in Figure 8.3.1c. The distribution for the inverse of the contra-boost Lorentz factor, γ_c^{-1}, is shown in Figure 8.3.1d. It is the scaleless variable introduced in Section 4.4.4 and its importance to reduce the SM background process yields will be clear when other selection criteria are imposed.

Figures 8.3.1e and 8.3.1f show histograms for the number of jets in the ISR-system tagged as τ and b respectively. A veto can be applied for these two categories with the

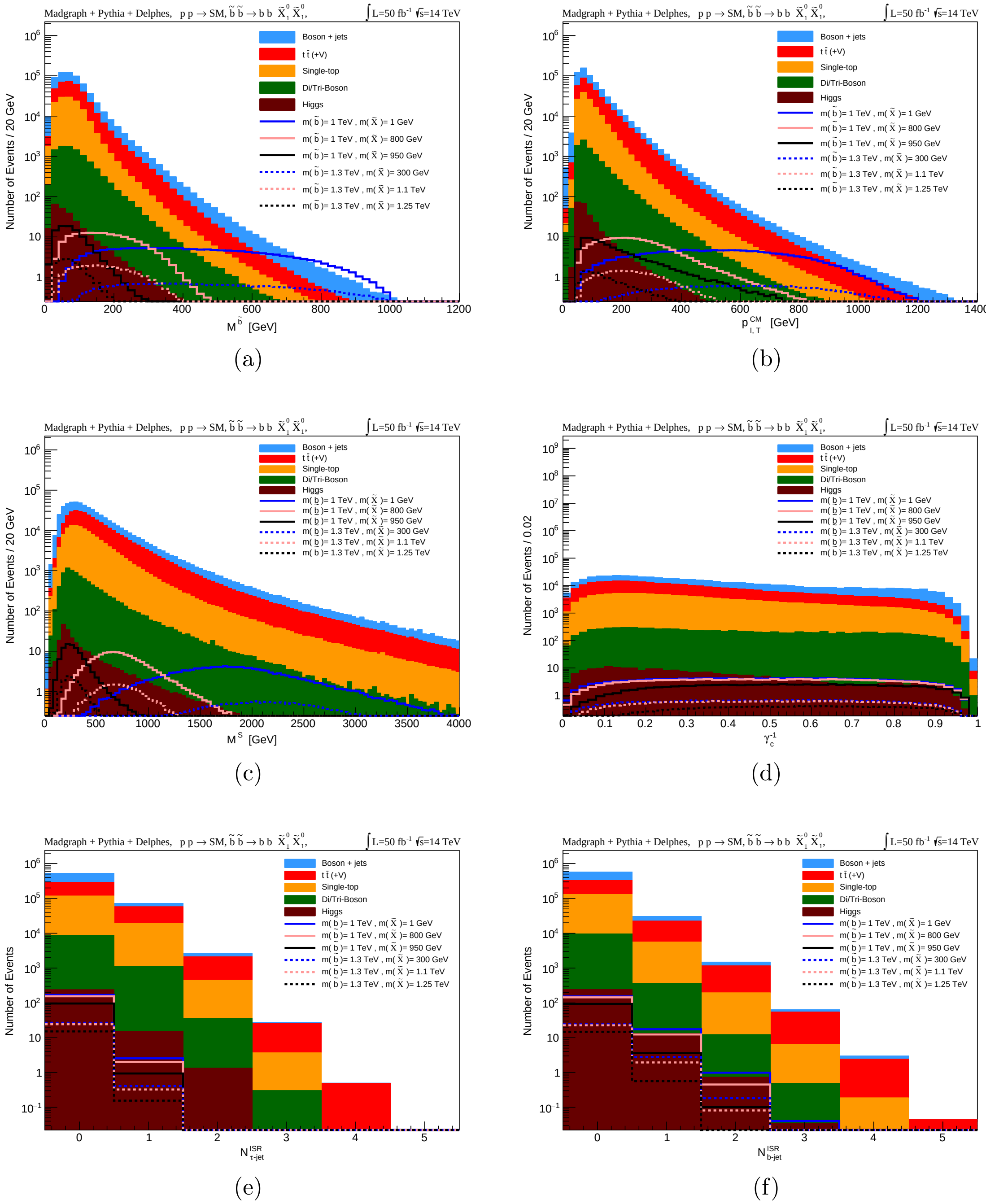

Figure 8.3.1: Distributions of RJR observables for events satisfying the preselection criteria. Contributions of all SM backgrounds and the overlaid signal curves are scaled to an integrated luminosity of 50 fb^{-1} at 14 TeV. Solid lines refer to signal samples with $M_{\tilde{b}} = 1$ TeV, while dashed lines to $M_{\tilde{b}} = 1.3$ TeV.

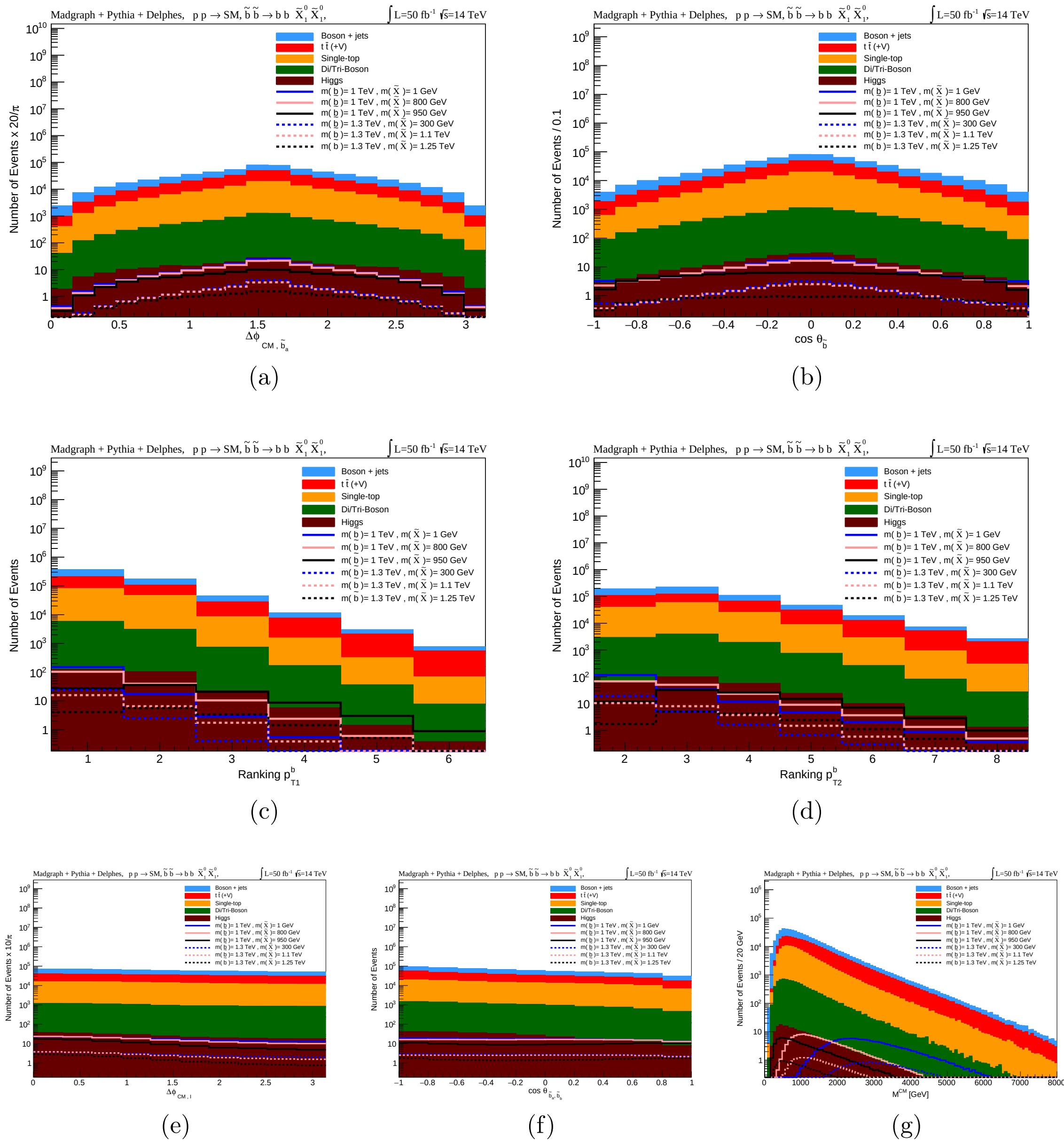

Figure 8.3.2: Distributions of RJR observables for events satisfying the preselection criteria. Contributions of all SM backgrounds and the overlaid signal curves are scaled to an integrated luminosity of 50 fb^{-1} at 14 TeV. Solid lines refer to signal samples with $M_{\tilde{b}} = 1$ TeV, while dashed lines to $M_{\tilde{b}} = 1.3$ TeV.

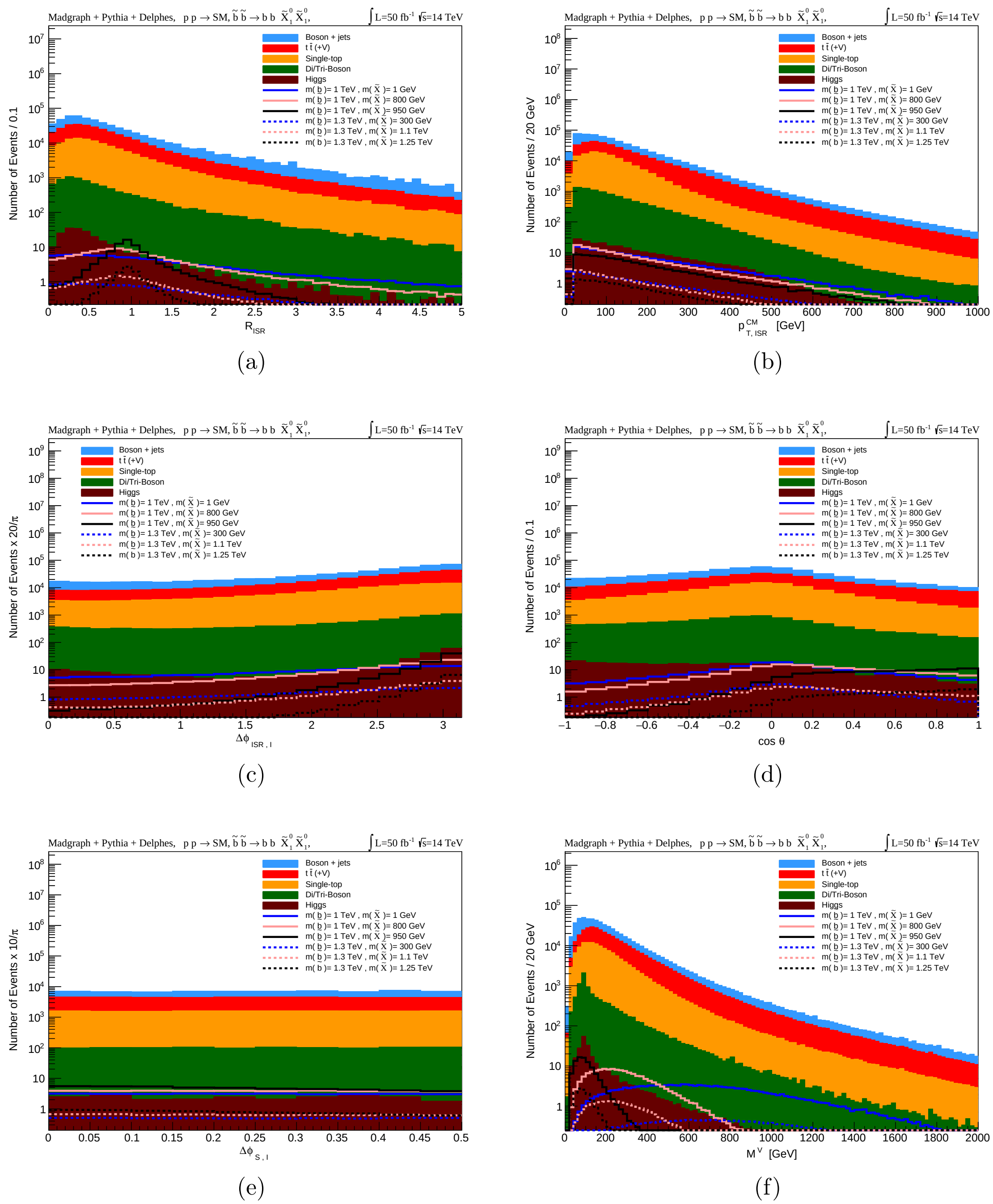

Figure 8.3.3: Distributions of RJR observables for events satisfying the preselection criteria. Contributions of all SM backgrounds and the overlaid signal curves are scaled to an integrated luminosity of 50 fb^{-1} at 14 TeV. Solid lines refer to signal samples with $M_{\tilde{b}} = 1$ TeV, while dashed lines to $M_{\tilde{b}} = 1.3$ TeV.

main impact given from the requirement $N^{\mathrm{ISR}}_{\tau-\mathrm{jet}} = 0$.

Figure 8.3.2a shows the distribution of $\Delta\phi_{\mathrm{CM},\tilde{\mathrm{b}}}$, the azimuthal angle between the plane formed by the ISR and S systems and the decay plane of one of the sbottom system ($\Delta\phi_{\mathrm{CM},\tilde{\mathrm{b}}_1} = \Delta\phi\left(\bar{\mathrm{ISR}}^{\mathrm{Lab}} \times \bar{S}^{\mathrm{Lab}}, \bar{b}^{\mathrm{S}}_1 \times \bar{I}^{\mathrm{S}}_1\right)$).

Figure 8.3.2b shows the distribution of $\cos\theta_{\tilde{b}}$ with $\theta_{\tilde{b}}$ the decay angle of the sbottom, Figure 8.3.2f shows the distribution of $\cos\theta_{\tilde{b}_1\tilde{b}_2}$ where $\theta_{\tilde{b}_1\tilde{b}_2}$ is half of the opening angle between the two $\tilde{b}$-systems and the opening angle between the momenta of the CM-system and the I-system evaluated in the Lab frame $\Delta\phi_{\mathrm{CM,I}} = \Delta\phi\left(\hat{p}_{\mathrm{CM}}, \hat{p}_{\mathrm{I}}\right)$ is shown in Figure 8.3.2e.

Figures 8.3.2c and 8.3.2d show two non RJR observables: the ranking of the leading and sub-leading b-jets in p_T with respect to the other jets in the final state. For example, "Ranking $p^b_{\mathrm{T}1}$ ", is 1 when a b-jet is the leading jet in p_T, 2 if it is the second and so on. Of course "Ranking $p^b_{\mathrm{T}2}$ " starts from two. Notice the opposite trend for the signal distributions for open and compressed mass spectra.

Other RJR observables with low impact in the discrimination of SUSY-like events w.r.t. SM-like events are not discussed. Remember how for the one step decay topology in the SUSY-system, other observables are dependent with respect to the ones presented here; for example: $E^{\tilde{b}_1}_{b_1} = E^{\tilde{b}_2}_{b_2} \simeq {}^1\!/_2 M^{\tilde{b}}$, except for nonphysical and negligible deviations related to the mass of the jets, $\cos\theta_{\tilde{b}_1} = -\cos\theta_{\tilde{b}_2}$, $\Delta\phi_{\mathrm{CM},\tilde{\mathrm{b}}_1} = \pi - \Delta\phi_{\mathrm{CM},\tilde{\mathrm{b}}_2}$ and $\Delta\phi_{\tilde{\mathrm{b}}_1,\tilde{\mathrm{b}}_2} = \pi$. Those observables provide additional information in the case of longer chains as described in the analysis of Chapter 7 with the gluino taking the place of the sbottom.

Figure 8.3.3 shows the distributions of the RJR observables useful for probing compressed scenarios. Notably, $R_{\mathrm{ISR}} = \left|\vec{p}^{\,\mathrm{CM}}_{\mathrm{I},T} \cdot \hat{p}^{\mathrm{CM}}_{\mathrm{ISR},T}\right| \left(p^{\mathrm{CM}}_{\mathrm{ISR},T}\right)^{-1}$ assumes the characteristic shape with a peak on the SUSY mass ratio ${}^{M_{\tilde{\chi}^0_1}}\!/_{M_{\tilde{b}}}$, with finer resolution moving from open to intermediate and compressed mass splittings. The modulus of the transverse momentum of the ISR-system evaluated in the CM frame $p^{\mathrm{CM}}_{\mathrm{ISR},T}$ is shown in Figure 5.2.2b. Differently from the other scale observables, the signal slopes are mostly independent of the mass splittings.

Figure 8.3.2g shows the distribution of $\Delta\phi_{\mathrm{ISR,I}}$: the opening angle between the ISR-system and the I=I_1+I_2 system in the transverse plane. Figures 8.3.3d and 8.3.3e show the distribution of the two observables $\cos\theta \equiv \hat{\beta}_S^{\mathrm{CM}} \cdot \hat{p}_{\mathrm{I},T}^{\mathrm{S}}$ and $\Delta\phi_{\mathrm{S,I}} = \Delta\phi\left(\hat{\beta}_S^{\mathrm{CM}}, \hat{\mathrm{I}}^{\mathrm{S}}\right)$. Although these observables are partially correlated to $\Delta\phi_{\mathrm{ISR,I}}$, they provide additional information because they are defined with one or two three-dimensional unitary vectors. Finally, M^{V}, shown in Figure 8.3.3f, is a scale variable that can be used both for open and compressed mass spectra requiring a lower or an upper limit respectively. The rules applied for the separation of the ISR vs SUSY objects result in a precise estimate of this observable related to the mass difference. For compressed scenarios a peak resolves below the hard scale associated with a top pair, the single top and below the Z and Higgs masses associated to the SM contributions $Z \to b\bar{b}$ and $h \to b\bar{b}$ respectively in green and red, while SM processes involving $g \to b\bar{b}$ present no resonance bumps.

8.4 RJR complementarity

In this study we define seven signal regions: SRO1, SRO2, SRI1, SRI2, SRI3, SRC1 and SRC2, depending on the mass splitting. They can be summarised in three types: *compressed* 25 GeV$\leq \Delta M <$ 100 GeV where the observables constructed with the ISR-system are the most useful, *open* $\Delta M \geq$ 500 GeV when the variables related to the SUSY system have more impact and *intermediate* 100 GeV$\leq \Delta M <$ 500 when both the observable categories are necessary to improve the signal to background ratio. For intermediate scenarios the typical background hard scale, identifiable with the sum of the masses of SM particles produced in the pp collision event, is comparable with ΔM.

Generally, the RJR observables are largely orthogonal between them with a moderate correlation between scale vs scale variables and some angular vs angular compressed variables. Some of the most interesting features are presented in Figures 8.4.1-8.4.3.

Figure 8.4.1 shows two-dimensional distributions of the RJR observables particularly useful in the open regime. Figure 8.4.1a shows that BG events can populate low values of $p_{\mathrm{I},T}^{\mathrm{CM}}$ for large values of $M^{\tilde{b}}$ while for open mass spectra a partial correlation between the two observables as expected is shown in Figure 8.4.1b.

Figure 8.4.1d shows the two-dimensional distribution of $M^{\tilde{b}}$ as a function of $\cos\theta_{\tilde{b}}$ for the signal sample $M_{\tilde{b}} = 1$ TeV, $M_{\tilde{\chi}_1^0} = 1$ GeV. For signal events, the distribution of the decay angle of the sbottom is mostly independent of the reconstructed mass, while for large value of $M^{\tilde{b}}$, BG events can populate values close to ± 1 due to cases where the missing transverse momentum is close in direction to one of the two b-jets ($\cos\theta_{\tilde{b}_1} = -\cos\theta_{\tilde{b}_2}$) as notable from Figure 8.4.1c.

Figures 8.4.1e and 8.4.1g show the two-dimensional distributions of the scaleless observable $\gamma_c^{-1} = 2M^{\tilde{b}}/M^{\mathrm{S}}$ as a function of $\cos\theta_{\tilde{b}}$ for the overall BG and the open signal sample demanding $M^{\tilde{b}} > 400$ GeV. Different SM processes with different kinematic provide peculiar behaviours for this distribution as shown in Figure 8.4.1f where we demand $p_{\mathrm{I},T}^{\mathrm{CM}} > 450$ GeV.

For $t\bar{t}$ background the two b-jets are likely associated to the S-system, but the two top quarks are mostly back to back in the Laboratory frame and hence, the two b-jets tend to fly apart with large angular separation in the reconstructed CM frame of reference. The value of M^{S} for such background events tends to be large compared to $M^{\tilde{b}}$ resulting in a low value for γ_c^{-1}. For vector boson plus jets processes, such as $Z \to \nu\nu$ or $W \to l\nu$ with unreconstructed lepton plus $g \to b\bar{b}$, the reconstructed mass of the S-system arising from the d.o.f. of the two jets and $\vec{E}\!\!\!/_T$ can be low relatively to $M^{\tilde{b}}$ when the vector boson and gluon fly in a similar direction. For the signal, the distribution of γ_c^{-1} exhibits no visible dependence on the mass splitting and ultimately on the true LSP and sbottom masses. The shape of the distribution is common for all the SUSY scenarios with the number of events decreasing with the production cross section.

For intermediate mass spectra we must relax selection criteria on scale sensitive observables such as M^{S} and $M^{\tilde{b}}$, the smaller ΔM. Figure 8.4.2 shows two-dimensional distributions for some RJR observables for the overall SM background in the first column,

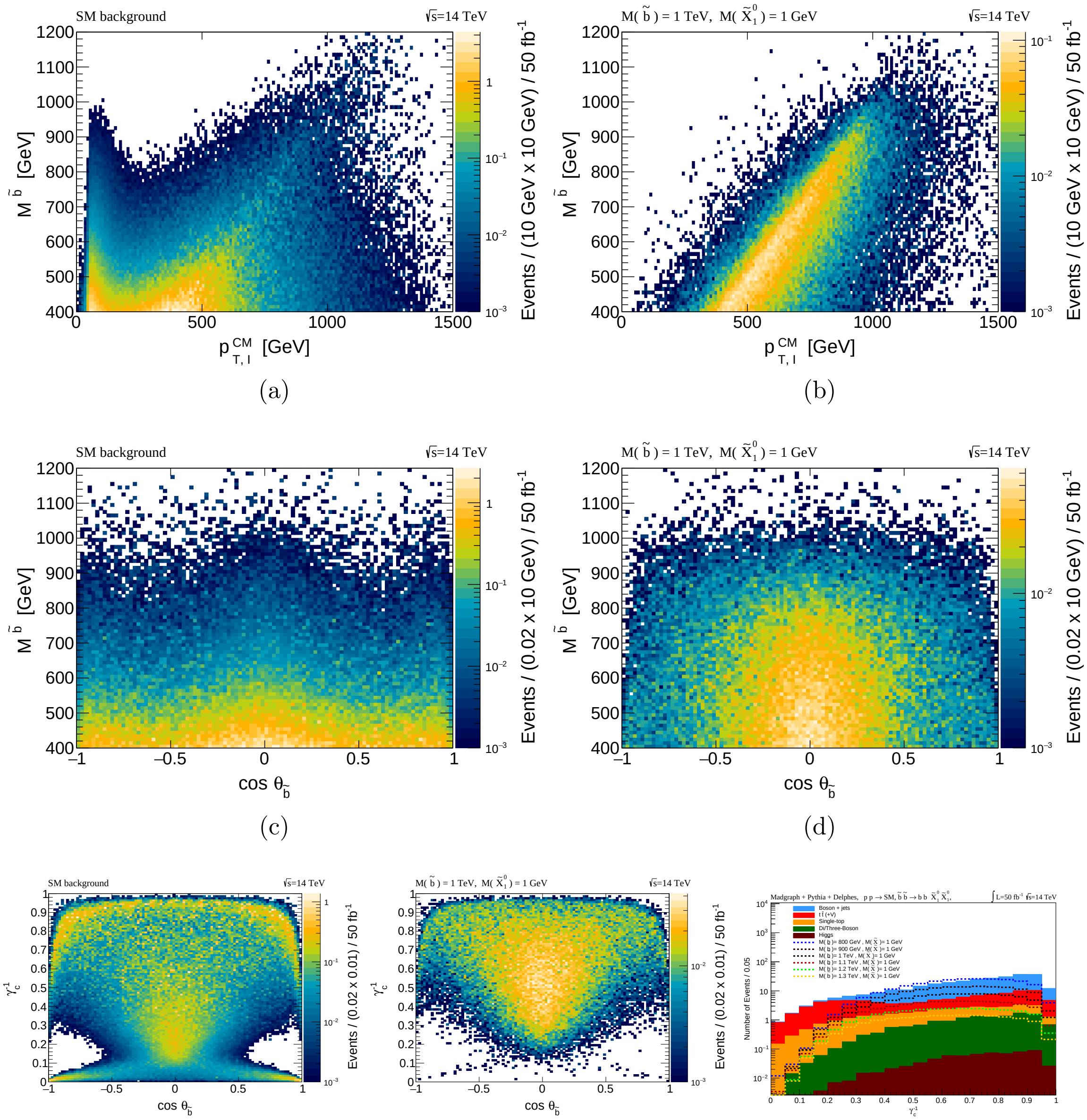

(a) (b)

(c) (d)

(e) $M^{\tilde{b}} > 400$ GeV (f) $M^{\tilde{b}} > 400$ GeV (g) $p_{\mathrm{I},T}^{\mathrm{CM}} > 450$ GeV

Figure 8.4.1: Two-dimensional distributions of RJR observables for the SM background (a, c, e) and the signal sample $M_{\tilde{b}} = 1$ TeV, $M_{\tilde{\chi}_1^0} = 1$ GeV (b, d, f) showing the number of events expected per bin for an integrated luminosity of 50 fb^{-1} satisfying preselection criteria and $M^{\tilde{b}} > 400\,$GeV. Distribution of γ_c^{-1} for SM background and six open SUSY scenarios with $M_{\tilde{\chi}_1^0} = 1$ GeV (g) demanding $M^{\tilde{b}} > 400\,$GeV and $p_{\mathrm{I},T}^{\mathrm{CM}} > 450$ GeV.

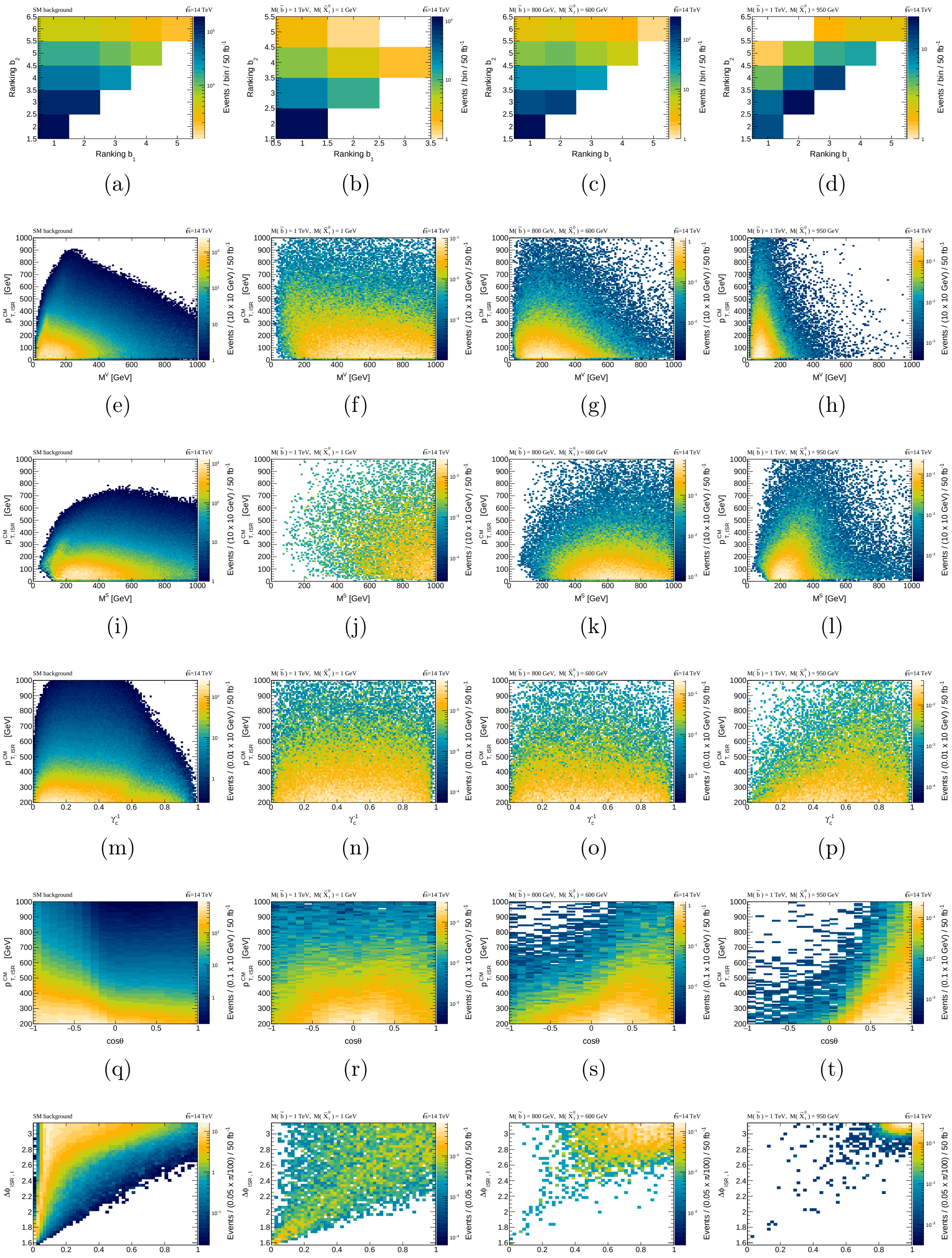

(a) (b) (c) (d)

(e) (f) (g) (h)

(i) (j) (k) (l)

(m) (n) (o) (p)

(q) (r) (s) (t)

(u) $p_{\mathrm{ISR},T}^{\mathrm{CM}} > 600$ GeV (v) $p_{\mathrm{ISR},T}^{\mathrm{CM}} > 600$ GeV (w) $p_{\mathrm{ISR},T}^{\mathrm{CM}} > 600$ GeV (x) $p_{\mathrm{ISR},T}^{\mathrm{CM}} > 600$ GeV

Figure 8.4.2: Two-dimensional distributions of RJR observables for the overall SM background (first column) and three SUSY scenarios: open with $M_{\tilde{b}} = 1$ TeV, $M_{\tilde{\chi}_1^0} = 1$ GeV (second column), intermediate with $M_{\tilde{b}} = 800$ GeV, $M_{\tilde{\chi}_1^0} = 600$ GeV (third column) and compressed with $M_{\tilde{b}} = 1$ TeV, $M_{\tilde{\chi}_1^0} = 950$ GeV (fourth column).

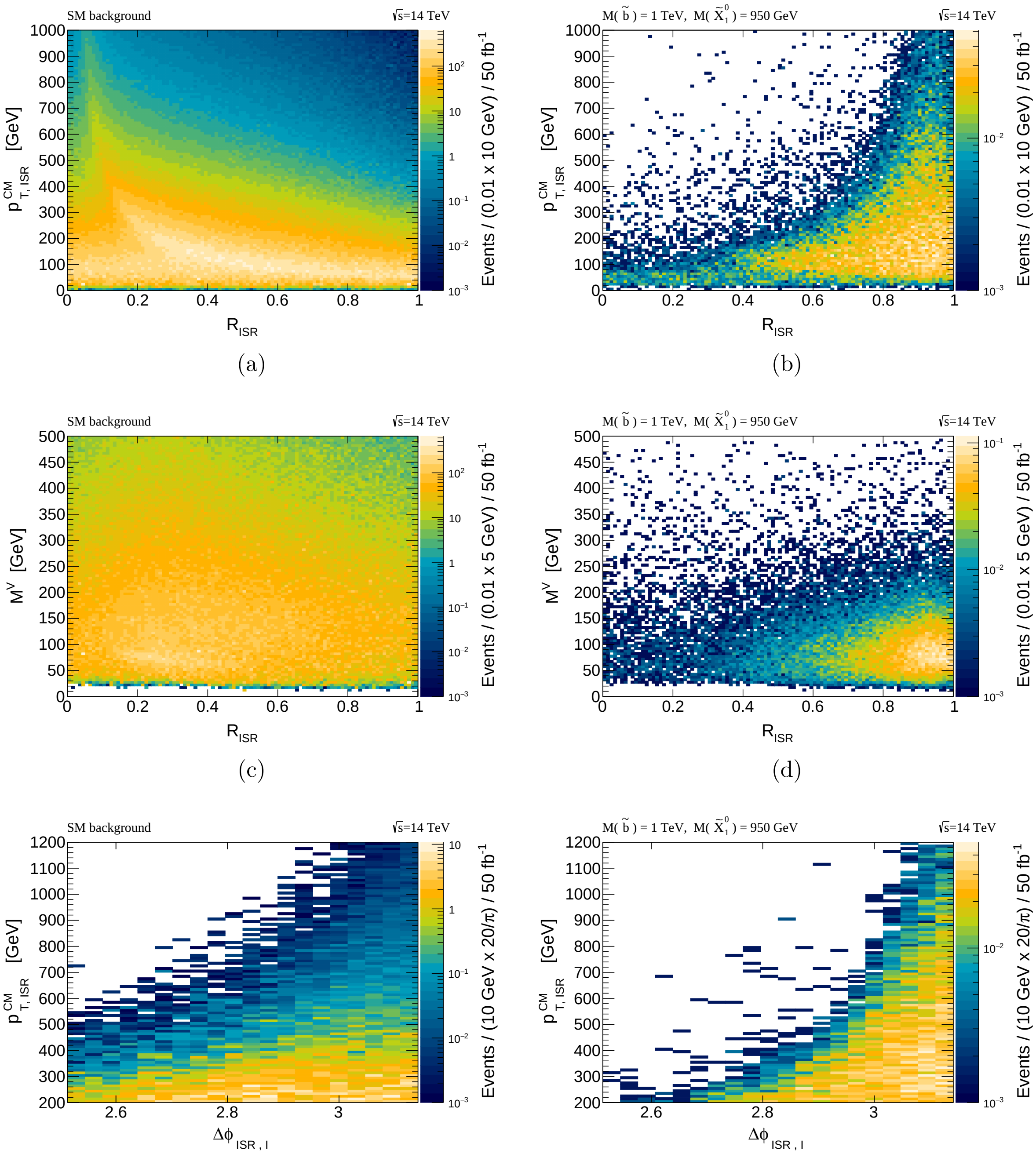

(a) (b)

(c) (d)

(e) $R_{\mathrm{ISR}} > 0.8$, $M^{\mathrm{V}} < 100$ GeV (f) $R_{\mathrm{ISR}} > 0.8$, $M^{\mathrm{V}} < 100$ GeV

Figure 8.4.3: Two-dimensional distributions of RJR observables for the overall SM background (left) and the signal sample $M_{\tilde{b}} = 1$ TeV, $M_{\tilde{\chi}_1^0} = 950$ GeV (right). The figures show the number of events expected per bin for an integrated luminosity of 50 fb^{-1} at $\sqrt{s} = 14$ TeV satisfying the preselection criteria. We demand $R_{\mathrm{ISR}} > 0.8$, $M^{\mathrm{V}} < 100$ and $p^{\mathrm{CM}}_{\mathrm{ISR},T} > 200$ GeV in Figures (e) and (f).

the open signal sample $M_{\tilde{b}} = 1$ TeV, $M_{\tilde{\chi}_1^0} = 1$ GeV in the second column, the intermediate sample $M_{\tilde{b}} = 800$ GeV, $M_{\tilde{\chi}_1^0} = 600$ GeV in the third column and the compressed sample $M_{\tilde{b}} = 1$ TeV, $M_{\tilde{\chi}_1^0} = 950$ GeV in the fourth one.

The scatter plot of Ranking $p^b_{\mathrm{T}1}$ vs Ranking $p^b_{\mathrm{T}2}$ is shown for the overall SM BG process in Figure 8.4.2a and open, intermediate and compressed SUSY scenarios in Figures 8.4.2b, 8.4.2c and 8.4.2d respectively. Compressed SUSY sample events tend to have low-momenutum b-jets and likely large value of the rankings, while the distribution for the intermediate scenario is much similar to the BG one. The observables are particularly useful in the open regime: requiring the two b-jets being the leading and sub-leading jets in p_T can reduce the V + jets yield.

Figures 8.4.2e-8.4.2h show the two-dimensional distributions of $p^{\mathrm{CM}}_{\mathrm{ISR},T}$ as a function of M^{V} for the SM backgrounds and same signal samples. We require a lower bound for M^{V} for open and intermediate scenarios and an upper bound in the compressed regime. The M^{V} sensitivity for intermediate mass splittings is moderate and we use more stringent criteria on $p^{\mathrm{CM}}_{\mathrm{ISR},T}$ since it is independent from the S-system observables. The distribution of $p^{\mathrm{CM}}_{\mathrm{ISR},T}$ can provide additional information in order to distinguish the SUSY hard scale from the background one: QCD radiation from partons with a large fraction of the proton momentum can result in high-energy jets.

Figures 8.4.2i-8.4.2t show two-dimensional distributions of $p^{\mathrm{CM}}_{\mathrm{ISR},T}$ as a function of the scale observable M^{S}, useful for open and intermediate scenarios, the scaleless variable γ_c^{-1}, used independently of ΔM, and the angular observable $\cos\theta$, useful in the compressed regime. We exploit the complementarity of $p^{\mathrm{CM}}_{\mathrm{ISR},T}$ with other observables related to the S-system.

Requiring large values of the transverse momentum of the ISR-system promotes compressed observables in the intermediate regime. An example is given by the two-dimensional distributions of $\Delta\phi_{\mathrm{ISR,I}}$ as a function of R_{ISR} shown in Figures 8.4.2u-8.4.2x demanding $p^{\mathrm{CM}}_{\mathrm{ISR},T} > 600$ GeV. Differently from background and open distributions, intermediate and compressed signal events tend to populate values close to π for $\Delta\phi_{\mathrm{ISR,I}}$

and values close to one for R_{ISR} with increasing tendency reducing the mass difference.

Figure 8.4.3 shows two-dimensional distributions of compressed RJR observables for the overall SM background and the signal sample $M_{\tilde{b}} = 1$ TeV, $M_{\tilde{\chi}_1^0} = 950$ GeV. The similarities to the figures referring to analogous observables in the previous compressed studies is quite remarkable.

For background events it is increasingly hard to have large values of R_{ISR} for higher values of $p_{\mathrm{ISR},T}^{\mathrm{CM}}$ as shown in Figure 8.4.3a, while for the SUSY compressed scenarios R_{ISR} is a proxy for ${}^{M_{\tilde{\chi}_1^0}}/{}_{M_{\tilde{b}}}$ with increasingly fine resolution for larger values of $p_{\mathrm{ISR},T}^{\mathrm{CM}}$ as shown in Figure 8.4.3b.

Figures 8.4.3c and 8.4.3d show the two-dimensional distributions of M^{V} as a function of R_{ISR}. The lack of correlation between the two observables provides us with the possibility to impose an upper bound on the mass of the $\mathrm{V} = b_1 + b_2$ system in order to suppress the background yield. This kinematic feature, used in the electroweakino study for leptonic decay products, would be biased employing a different jigsaw rule based on the minimisation of the masses resulting in an overestimate of M^{V} in the case of wrong assignment of ISR-jets in one of the b-systems and hence in the V-system.

Requiring values for R_{ISR} close to one, and small values for M^{V}, other angular RJR observables can be used as shown in Figure 8.4.3e and 8.4.3f for the distribution of $p_{\mathrm{ISR},T}^{\mathrm{CM}}$ as a function of the opening transverse angle between the ISR and I systems. Compressed SUSY-like events populate values closer to π than SM-like events with an increasing tendency for larger values of $p_{\mathrm{ISR},T}^{\mathrm{CM}}$.

8.5 Signal regions

Selection criteria applied on RJR observables define seven signal regions targeting different mass splitting intervals. Two open signal regions, SRO1 and SRO2, are applied for scenarios with $\Delta M \geq 1$ TeV and 500 GeV$\leq \Delta M < 1$ TeV respectively and are the results of selection criteria mainly on observables related to the SUSY branches of the tree. Only open signal regions use final states with exactly two b-jets and the corresponding RJR tree in Figure 8.2.2a.

Three intermediate signal regions, SRI1, SRI2 and SRI3, are constructed with requirements on observables related to the S-ISR ensemble and are applied for probing samples with 350 GeV$\leq \Delta M < 500$ GeV, 200 GeV$\leq \Delta M < 350$ GeV and 100 GeV$\leq \Delta M < 200$ GeV respectively. The requirements on SRI1 are more focused on open SUSY observables while SRI3 on compressed observables.

The signal regions SRC1 and SRC2 target extremely compressed mass spectra: 100 GeV$\leq \Delta M < 50$ GeV and 50 GeV$\leq \Delta M < 25$ GeV. In the compressed and partially in the intermediate regime, except for the object requirements in the final state, we define selection criteria resembling those used in the previous studies in Chapters 5 and 6.

The categorisation of signal regions by mass splitting intervals is driven by the expectation to have common features for most of the RJR signal distributions, independently of the selection applied: similar shapes scaled by different cross sections. For the distribution of $R_{\rm ISR}$ the idea is to encode an average behaviour.

The signal regions are described in Table 8.2, where selection criteria on observables typical of the open regime are written in blue, while compressed RJR requirements appear in red. The scaleless observable γ_c^{-1} is used in all the signal regions, while a lower or upper bound is imposed on $M^{\rm V}$ depending on the scenario investigated. For intermediate SUSY scenarios all the selection criteria on scale observables are lower limits, tight for SRI1, while a stringent requirement on $p^{\rm CM}_{{\rm ISR},T}$ is defined in SRI2 and SRI3 in order to exploit the other compressed handles. In the same regime, we impose an upper limit on $R_{\rm ISR}$ of greater than one, in order to improve the signal yields, due to the lower resolution of the signal distributions w.r.t. the extremely compressed scenarios. For final states with exactly two jets, the same criteria of higher multiplicity are applied in SRO1 and SRO2 except for a moderate requirement on $\Delta\phi_{{\rm CM},\tilde{\rm b}}$ and $\Delta\phi_{\rm ISR,I}$.[4] For intermediate and compressed mass spectra only final states with $N_{\rm jet} \geq 3$

[4] The variables need an ISR-system to be computed and the asterisks remind the impossibility to

	Signal Region						
Variable	SRO1	SRO2	SRI1	SRI2	SRI3	SRC1	SRC2
Preselection criteria	Lepton veto (no isolated electrons and muons) At least two b-jets, $p_T^{\mathrm{jet}} > 20$ GeV, $\not{E}_T > 50$ GeV						
$N^{\mathrm{ISR}}_{\tau-\mathrm{jet}}$	$= 0$						
$N^{\mathrm{ISR}}_{b-\mathrm{jet}}$	$= 0$			≥ 0		$= 0$	
$N^{\mathrm{ISR}}_{\mathrm{jet}}$	≥ 0		≥ 1				
$M^{\tilde{b}} >$ [GeV]	650	500	420	200	140	–	–
$p^{\mathrm{CM}}_{\mathrm{I},T} >$ [GeV]	650	550	450	–	–	–	–
$M^{\mathrm{S}} >$ [GeV]	1700	1200	1050	650	–	–	–
$\lvert\cos\theta_{\tilde{b}}\rvert <$	0.8	0.75	0.75	0.8	0.9	–	–
$< \Delta\phi_{\mathrm{CM},\tilde{\mathrm{b}}} <$	$\frac{\pi}{3} - \frac{2\pi}{3}$ *	$\frac{\pi}{3} - \frac{2\pi}{3}$ *	$0.5 - 2.2$	$0.5 - 2.8$	–	–	–
ranking $p_T(b_1)$	$(= 1)$	$(= 1)$	–	–	–	–	–
ranking $p_T(b_2)$	$= 2$	$= 2$	–	–	–	–	–
$\Delta\phi_{\mathrm{CM,I}} <$			$\frac{3}{4}\pi$				
M^{V} [GeV]	>400	>400	>300	>200	–	<100	<80
$p^{\mathrm{CM}}_{\mathrm{ISR},T} >$ [GeV]	–	–	–	530	580	600	600
$< R_{\mathrm{ISR}} <$	–	–	–	$0.7 - 1.3$	$0.8 - 1.1$	$0.9 - 1$	$0.9 - 1$
$\Delta\phi_{\mathrm{ISR,I}} >$	–	0.4*	2.0	2.6	2.9	3.05	3.07
$\Delta\phi_{\mathrm{S,I}} <$	–	–	–	–	–	$\frac{4\pi}{25}$	$\frac{3\pi}{25}$
$\cos\theta >$	–	–	0.1	0.2	0.45	0.7	0.8
$< \gamma_c^{-1} <$	$0.4 - 0.85$	$0.4 - 0.85$	$0.55 - 0.85$	$0.5 - 0.9$	$0.5 - 0.9$	$0.5 - 0.9$	$0.35 - 0.9$

Table 8.2: A set of selection criteria for signal regions in the analysis of sbottom pair production in final states with two b-jets and missing transverse momentum.

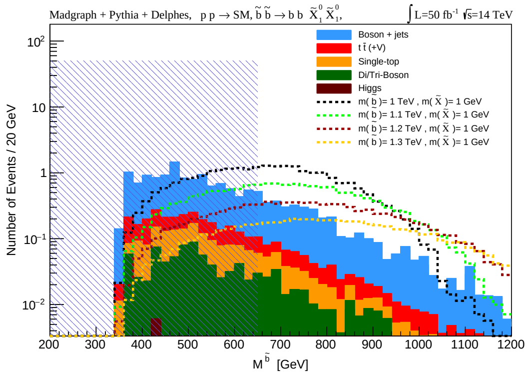

(a) SRO1: SUSY samples with $M_{\tilde{\chi}_1^0} = 1$ GeV.

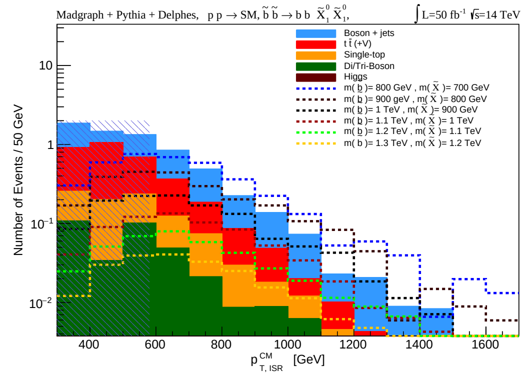

(b) SRI3: SUSY samples with $\Delta M = 100$ GeV.

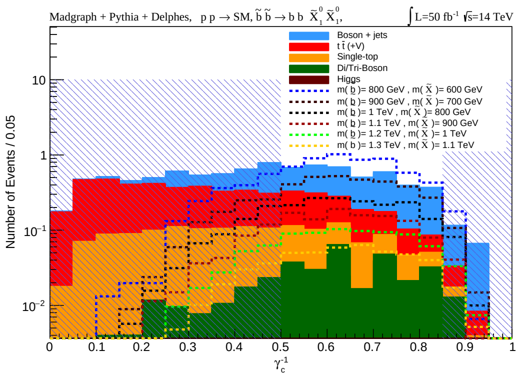

(c) SRI2: SUSY samples with $\Delta M = 200$ GeV.

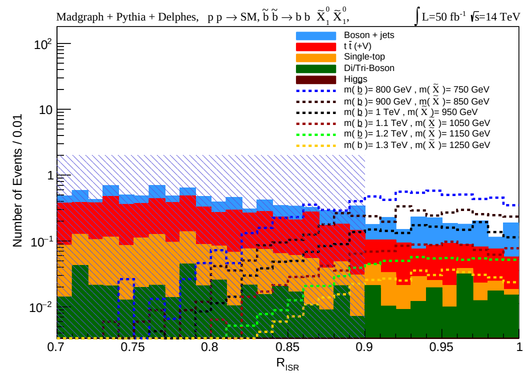

(d) SRC1: SUSY samples with $\Delta M = 50$ GeV.

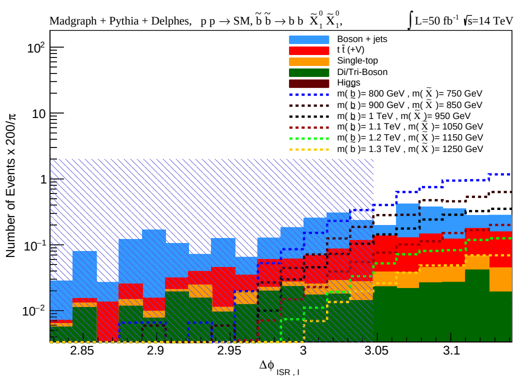

(e) SRC1: SUSY samples with $\Delta M = 50$ GeV.

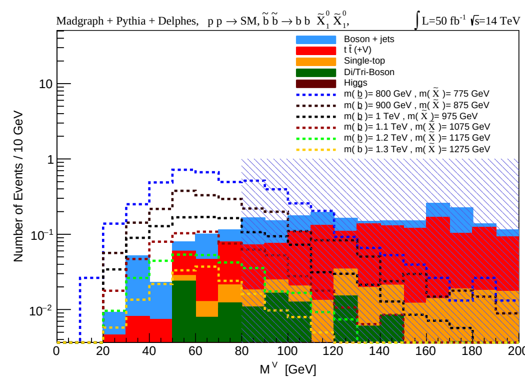

(f) SRC2: SUSY samples with $\Delta M = 25$ GeV.

Figure 8.5.1: Distributions of the RJR observables for events passing the selection criteria defined in the corresponding SR column in Table 8.2. Contributions of all SM backgrounds and overlaid signal curves are scaled to an integrated luminosity of 50 fb^{-1} at $\sqrt{s}$ =14 TeV.

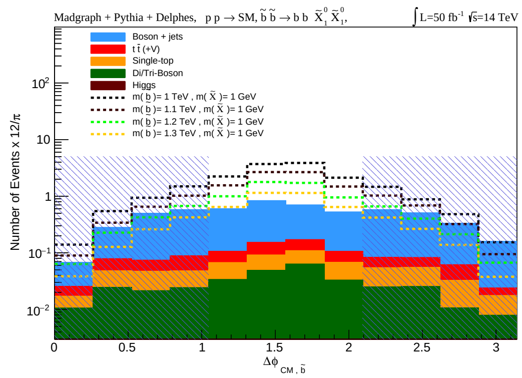

(a) SRO1: SUSY samples with $M_{\tilde{\chi}_1^0} = 1$ GeV.

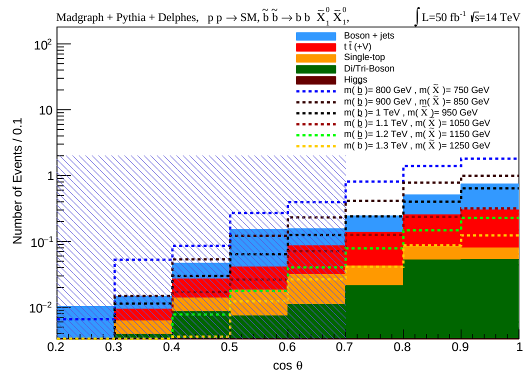

(b) SRC1: SUSY samples with $\Delta M = 50$ GeV.

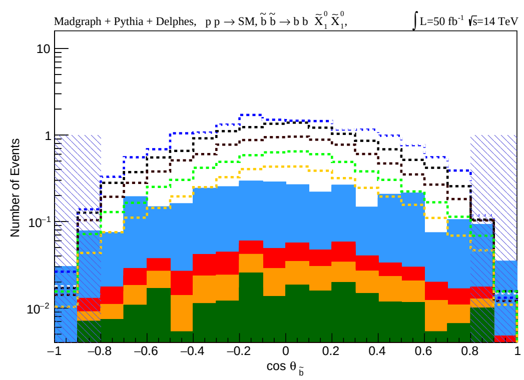

(c) SRO1: SUSY samples with $M_{\tilde{\chi}_1^0} = 1$ GeV.

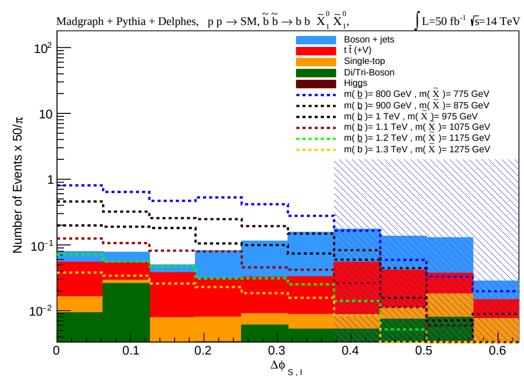

(d) SRC2: SUSY samples with $\Delta M = 25$ GeV.

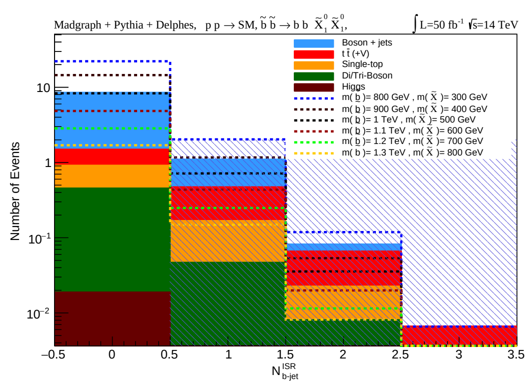

(e) SRO2: SUSY samples with $\Delta M = 500$ GeV.

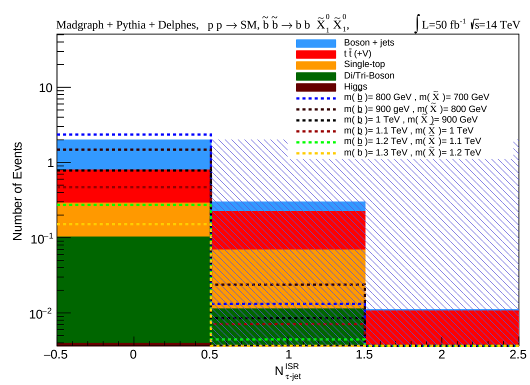

(f) SRI3: SUSY samples with $\Delta M = 100$ GeV.

Figure 8.5.2: Distributions of the RJR observables for the events passing the selection criteria defined in Table 8.2. Contributions of all SM backgrounds and overlaid signal curves are scaled to an integrated luminosity of 50 fb^{-1} at $\sqrt{s}$ =14 TeV.

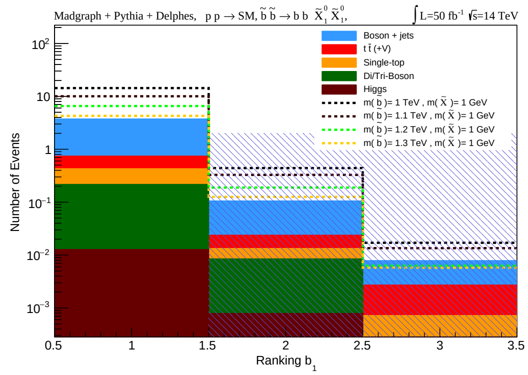

(a) SRO1, no selection on Ranking b_2.

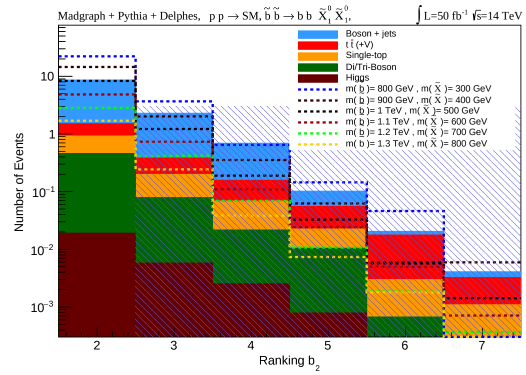

(b) SRO2: SUSY samples with $\Delta M = 500$ GeV.

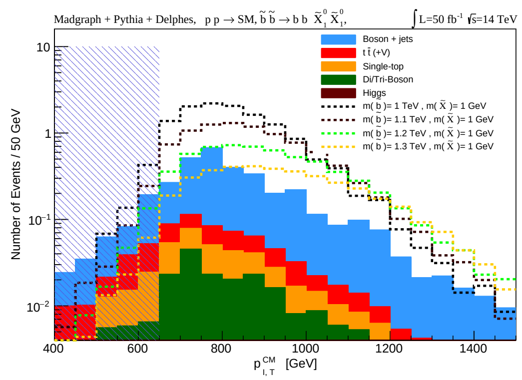

(c) SRO1: SUSY samples with $M_{\tilde{\chi}_1^0} = 1$ GeV.

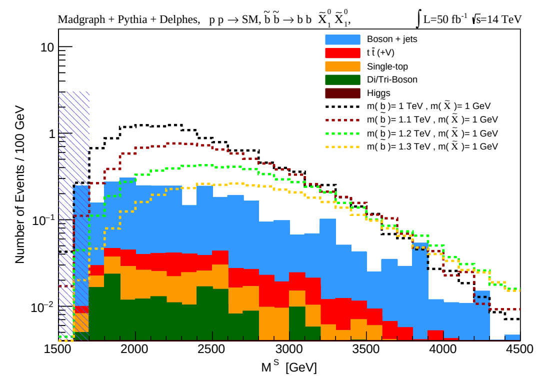

(d) SRO1: SUSY samples with $M_{\tilde{\chi}_1^0} = 1$ GeV.

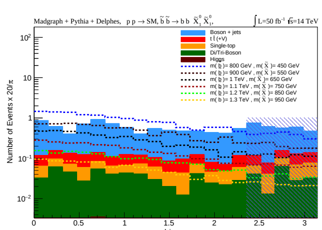

(e) SRI1: SUSY samples with $\Delta M = 350$ GeV.

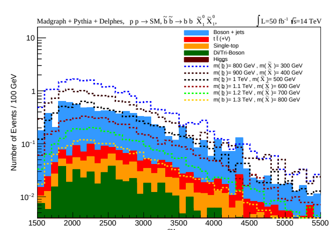

(f) SRO2: No selection on this observable.

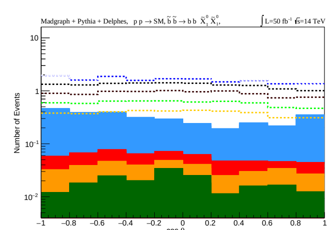

(g) SRO2: No selection on this observable.

Figure 8.5.3: Distributions of the RJR observables for the events passing the selection criteria defined in Table 8.2. Contributions of all SM backgrounds and overlaid signal curves are scaled to an integrated luminosity of 50 fb^{-1} at $\sqrt{s}$ =14 TeV.

are taken into account: at least one jet is assigned to the ISR-system. The scaleless observable $\Delta\phi_{\mathrm{CM,I}}$ has limited sensitivity in the open and compressed regimes and is employed for intermediate scenarios only, where selection criteria on dedicated handles are relaxed.

Figures 8.5.1, 8.5.2 and 8.5.3 show distributions of the RJR observables used for probing open, intermediate and compressed sbottom scenarios for events that have satisfied all the relative selection criteria in Table 8.2 except for the requirement on the variable that is displayed. The impact of the selection criterion on the displayed variable can be observed in the shaded region. The histograms show the distribution for the overall SM background with the five categories described in Table 8.1 in different colours stacked together and for SUSY samples belonging to a common SR. The overlaid dashed lines are signal distributions for a fixed value of the LSP mass ($M_{\tilde{\chi}_1^0} = 1$ GeV) for SRO1 and for fixed mass splittings for the other signal regions corresponding to the minimum value of ΔM in the SR interval (SRC2 with $\Delta M = 25$ GeV, SRC1 with $\Delta M = 50$ GeV, SRI3 with $\Delta M = 100$ GeV, SRI2 with $\Delta M = 200$ GeV, SRI1 with $\Delta M = 350$ GeV and SRO2 with $\Delta M = 500$ GeV).

The distributions of the RJR observables shown in Figure 8.5.1 are the most useful in discriminating signal to background events in one or more regimes. Lower limits on the scale observable $M^{\tilde{b}}$ are required in the open and intermediate signal regions and its distribution is shown in Figure 8.5.1a. For intermediate and compressed scenarios stringent criteria are imposed on $p^{\mathrm{CM}}_{\mathrm{ISR},T}$, shown in Figure 8.5.1b for SRI2. Figure 8.5.1c shows the inverse of contra-boost factor γ_c^{-1} useful in any regime. The ratio R_{ISR} and $\Delta\phi_{\mathrm{ISR,I}}$, provide progressively improving discrimination between signal and background events reducing the mass splitting investigated. Their distributions are shown in Figures 8.5.1d and 8.5.1e for SRC1. An upper limit is imposed on the only scale observable M^{V} in the compressed regime whose distribution is shown in Figure 8.5.1f for SRC2.

Background yields can be decreased imposing selection criteria on the other RJR vari-

---

apply the selection criterion for the case of exactly two jets in the final state.

ables as shown for the distributions in Figures 8.5.2 and 8.5.3. The scale observables $p_{\mathrm{T,I}}^{\mathrm{CM}}$ and M^{S} have limited impact when other requirements are applied and the corresponding selection criteria in Table 8.2 are specified for completeness. The distribution of M^{S} can provide information for the mass spectrum in case of SUSY discovery maintaining for example a maximum around twice the sbottom mass in the limit of massless LSP.

8.6 Results and summary

The imposition of the RJR trees and rules shown in Figure 8.2.2 result in a basis of variables proposed for analysing the simplified topology corresponding to the Feynman diagram in Figure 8.1.1. Seven signal regions described in Table 8.2 are defined by selection criteria on these RJR observables and are used to compute discovery-exclusion prospects of sbottom pair-production in final states with two b-jets and missing transverse momentum at the LHC experiments.

Figure 8.6.1 shows the value of Z_{Bi}, defined by Eq. 3.5.5 and 3.5.8, describing the significance for the expected SUSY final state events in the SM background hypothesis for pp collisions with a centre-of mass energy of 14 TeV and for an integrated luminosity of 50 fb^{-1}.

A common value of 20% is assumed for the SM systematic uncertainty (ΔB/B) in the $M_{\tilde{b}}$ vs $M_{\tilde{\chi}_1^0}$ plane, where explicitly 2σ and 4σ continuous contour lines are drawn in black and red respectively. Assuming the same selection criteria as in Table 8.2, other projections are drawn. The 2σ (red) and 4σ (black) dashed contour lines are computed assuming ΔB/B = 30%, while the continuous gray line refers to the 95% CL exclusion limit assuming ΔB/B = 20% and $BR^2(\tilde{b} \to b\tilde{\chi}_1^0) = 50\%$. This can be interpreted as the 2σ contour obtained from any product $\sigma_{\mathrm{LHC14}}(pp \to \tilde{b}\tilde{b}) \times BR$ resulting in half of the signal final state events (see Eq. 3.1.3). Assuming ΔB/B = 20%, the 2σ exclusion lines are computed for an integrated luminosity of 30 fb^{-1} and 200 fb^{-1}. The latter reach can be simply extended requiring more stringent selection criteria.

Selection criteria on RJR observables related mainly to the S-system provide excellent results for open mass spectra and good reach in SRI1. The complementarity of R_{ISR}, $p^{\mathrm{CM}}_{\mathrm{ISR},T}$, M^{V} and the other angular observables, such as $\Delta\phi_{\mathrm{ISR,I}}$, provide sensitivity for probing compressed scenarios, while requiring a stringent criterion on the scale observable $p^{\mathrm{CM}}_{\mathrm{ISR},T}$ we exploit its orthogonality with the other open RJR variables and R_{ISR} increasing the sensitivity in the intermediate regions SRI2 and SRI3.

Although a correct estimate and understanding of the systematic uncertainty based on SM candles and control regions remains an experimental prerogative, in the compressed regime the results appear quite robust or almost independent of ΔB/B due to the suppression of the SM background yield, as can be noticed in the corresponding figures in the previous section. For intermediate, and partially for open mass spectra, the assumption of larger systematic uncertainties can result in a larger separation between the contour lines. This is the case for low masses of the sbottom ($\lesssim$ 600 GeV) due to a stringent requirement on R_{ISR} in the intermediate regime or on the scale observables in SRO2 and SRI1. An improvement requires more signal regions for the corresponding ΔM or $M_{\tilde{b}}$, or a relaxation of such requirements to the detriment of the results obtained for larger sbottom masses. Overall, in this phenomenological study as in the previous one, the parametrisation for the b-tagging efficiency [70] is very conservative with respect to the recent improvements in the ATLAS [137] and CMS [135] performances.

For an integrated luminosity of 50 fb^{-1}, the RJR technique provides sensitivity to compressed sbottom-neutralino scenarios at LHC14 excluding spectra with $M_{\tilde{b}}$ above 800 GeV assuming ΔB/B = 20%, well beyond the current experimental limits [123,138, 139] shown in Figure 8.6.2.

For scenarios with $m_{\mathrm{bottom}} < \Delta m < m_W$, the assumption $BR(\tilde{b} \to b\tilde{\chi}^0_1) = 100\%$ is well motivated, since the multi-body decay modes via top and stop such as $\tilde{b} \to t^*(W^*b)\tilde{\chi}^\pm_i(W^*\tilde{\chi}^0_1)$ and $\tilde{b} \to W^*\tilde{t}(b\tilde{\chi}^\pm_i(W^*\tilde{\chi}^0_1))$ are expected to be suppressed.

Compressed results are paradoxically better than some intermediate outcomes (100

GeV$\lesssim \Delta M \lesssim$300 GeV) where the efficacy of both open and compressed observables is limited: regions where the mass splitting ΔM approaches the value corresponding to the dominant SM processes hard scale.

While for compressed and intermediate scenarios the observable R_{ISR} is a proxy for the LSP-to-sbottom mass ratio, with increasing resolution for smaller ΔM and larger $p^{\mathrm{CM}}_{\mathrm{ISR},T}$, for open scenarios the scale observable $M^{\tilde{b}}$ maintains substantially the end-point and tail shape dependency on ΔM after the imposition of other selection criteria. This is due to the orthogonality between the RJR observables, which provides the possibility to extract additional information on the mass spectrum from the distribution of M^{S} in the hypothesis of discovery. The bottom squark would be excluded with masses above 1.2 TeV and LSP with masses up to 400 GeV assuming $\Delta\mathrm{B}/\mathrm{B} = 20\%$ for an integrated luminosity of 50 fb^{-1} at $\sqrt{s} = 14$ TeV.

In the compressed regime, the same RJR tree and strategy can be applied for probing the production of a pair of scalar tops decaying to charm quarks and LSPs ($\tilde{t} \to c\tilde{\chi}^0_1$) with the differences arising from the charm tagging [136] and SM processes to contribute. In such a case a jigsaw rule based on the minimisation of the masses in order to separate the ISR and S systems as adopted in [111] is expected to be favoured considering the current experimental efficiency in the c-tagging.

Comparing Figure 8.6.1 with the expected curves from ATLAS and CMS in Figure 8.6.2 we see dramatic improvements are possible in the compressed regions, while there are still improvements in open cases. Coupled with developments in heavy flavour jet identification demonstrated by the experiments [135,137], compared to the conservative approach taken herein, we could envisage further improvements.

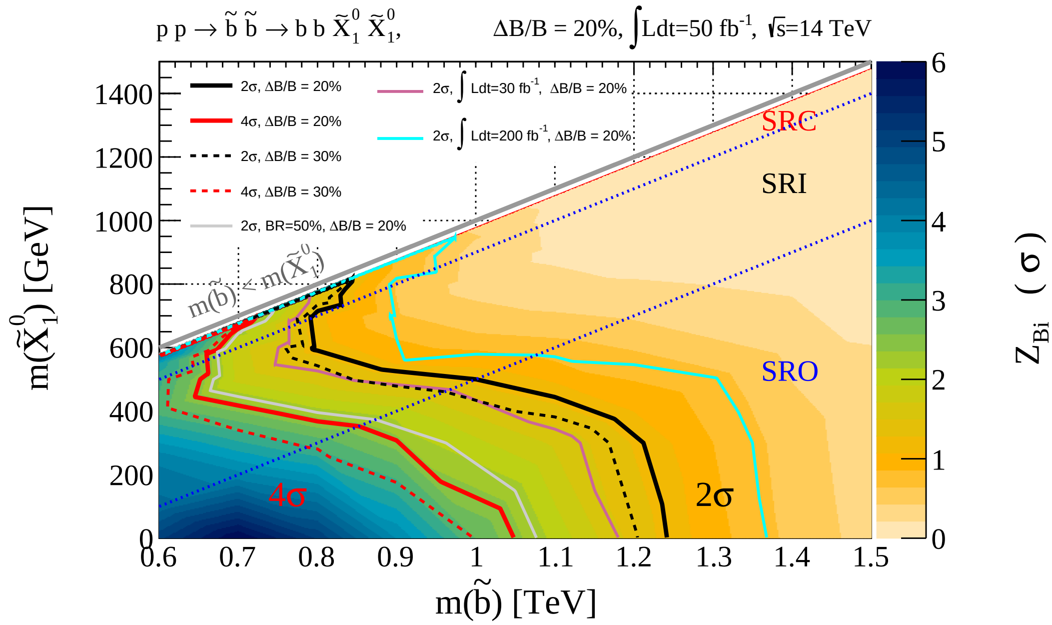

Figure 8.6.1: $Z_{\rm Bi}$-value in the $m_{\tilde{\chi}_1^0}$ vs $m_{\tilde{b}}$ plane for an integrated luminosity of 50 fb^{-1} at $\sqrt{s}$ = 14 TeV computed imposing the signal regions in Table 8.2 and assuming a systematic uncertainty (ΔB/B) of 20% for the SM background. Continuous black and red contour lines show explicitly the 95% CL exclusion limit and the 4σ evidence. Same selection criteria are applied to compute the 2σ contour lines for a projection of $\int L\text{dt} = 50$ fb^{-1} (purple line) and $\int L\text{dt} = 200$ fb^{-1} (cyan line) or assuming half of the branching fraction for the simplified topology ($BR^2(\tilde{b} \to b\tilde{\chi}_1^0) = 50\%$ gray line), while the dashed curves refer to ΔB/B = 30%.

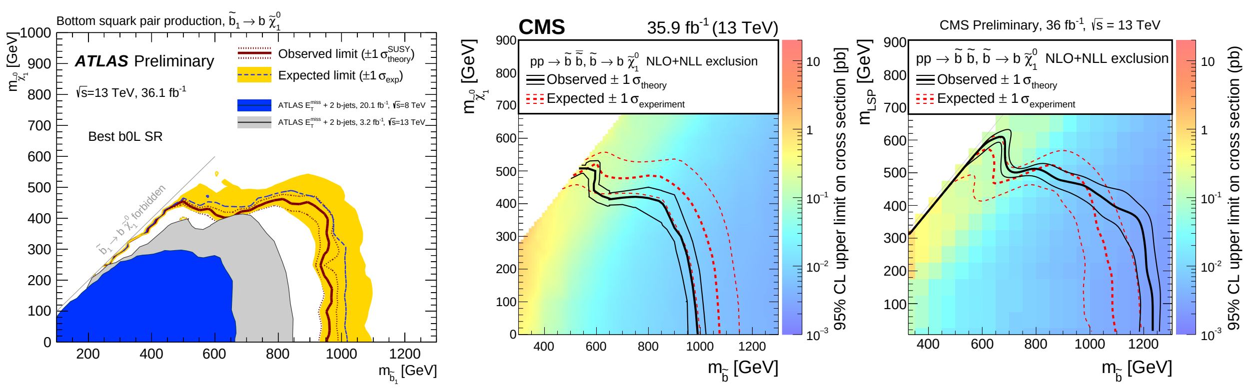

(a) (b) (c)

Figure 8.6.2: Recent observed and expected exclusion contours at the 95% CL from ATLAS and CMS collaborations for the search of the SUSY simplified topology $pp \to \tilde{b}\tilde{b}(\tilde{b} \to b\tilde{\chi}_1^0)$. Figures from [138] (a), [139] (b) and [123] (c).

Chapter 9

Outlook

9.1 Higgs plus $t\bar{t}$ in the di-leptonic channel

9.1.1 Preamble

On 2012, both the CMS and ATLAS experiments announced the discovery of a particle, with a significance exceeding 5σ, compatible with the SM Higgs combining the observations for the processes $h \to \gamma\gamma$ and $h \to ZZ^* \to 4l$. Precision measurements from the LHC Run 2 point still more strongly towards the boson $J^{\mathrm{PC}} = 0^{++}$ with mass ~ 125 GeV introduced by Higgs which completes the missing peace of the SM. The golden channel to study the CP-nature of this scalar is the final state with four leptons (electrons plus muons) via an on-shell and an off-shell Z-boson. In this brief section we present some features for the associated production of a boson with a top-antitop using the RJR strategy.

9.1.2 Introduction

We apply the RJR technique as example for the study the CP-nature of the Higgs boson in a complex final state. The samples are three MadGraph + Pythia + Delphes simulations of proton-proton collision at $\sqrt{s}$=13 TeV of the associated production of a pair of tops in the di-leptonic channel and a boson decaying to a pair of b-jets. Hence, the final state investigated has two leptons (electrons or muons), four b-jets and missing transverse momentum following the process cascade $pp \to t\bar{t} + X$ with $t \to bW^+(l^+v)$, $\bar{t} \to \bar{b}W^-(l^-\bar{v})$ and $X \to b\bar{b}$.

Figure 9.1.1 shows the process and resulting RJR tree with the positively charged lepton associated with the hemisphere 1 in the $t\bar{t}$ system by convention. For this tree the five jigsaw rules are the same described in Section 4.5.3 and correspond to two combinatoric minimisations of the masses for the assignment of four identical b-jets and three WIMP jigsaw rules (the Set Invisible Rapidity, Mass and Contra-Boost jigsaw rules). The RJR tree shows two systems: an H-system and a $t\bar{t}$-system, the latter divided in two identical hemispheres.

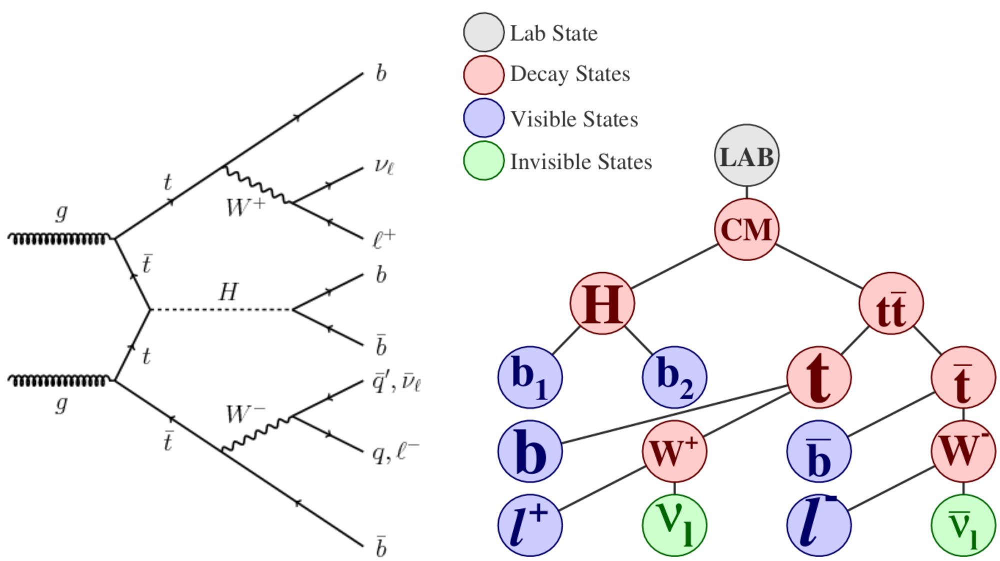

(a) (b)

Figure 9.1.1: Feynman diagram (a) and corresponding RJR decay tree (b) for the process $pp \to H + t\bar{t}$ in the di-leptonic channel.

This study focuses on the nature of the Higgs boson and three different samples are considered depending on the boson decaying in a pair of bottom quarks $X \to b\bar{b}$: a

CP-even or SM-like Higgs boson and a CP-odd Higgs boson with masses 125 GeV, and what is assumed to constitute the main irreducible background $Z \to b\bar{b}$.

9.1.3 CP-sensitive observables

We require final states with two opposite sign leptons ($l = e$ or μ) and four jets among which at least one is reconstructed as b-jet in each system $N^{\mathrm{H}}_{b-\mathrm{jet}} \geq 1$ and $N^{\mathrm{t\bar{t}}}_{b-\mathrm{jet}} \geq 1$. The normalised distributions of the main experimental observables sensitive to the CP-nature of the Higgs boson are shown in Figure 9.1.2.

Figure 9.1.2a shows a good resolution for the reconstruction of the mass for the H-system. Considering the complexity of the final state topology and the uncertainty related to the physics of the jets for the reconstruction of an invariant mass, the result is a remarkable separation between the Higgs and Z-boson mass peaks.

Figure 9.1.2b shows the distribution of p_h^{CM}: the three-momentum of the H-system (or $t\bar{t}$-system) estimated in the centre-of-mass frame. The CP-odd Higgs events tend to populate larger values.

The remaining figures show the distributions of the main angular observables sensitive to the nature of the boson produced in association with a pair of top-quarks decaying leptonically. For such variables, the distributions corresponding to the CP-odd Higgs boson sample are similar to the spin 1 gauge boson ones, while the distributions for the CP-even scalar tend to have a different behaviour. Figure 9.1.2c shows the distribution of $\cos\theta_{\mathrm{H,t\bar{t}}}$, namely the cosine of half of the angle between the two systems (H and $t\bar{t}$) computed in the CM frame, while Figure 9.1.2d shows the distribution of $\cos\theta_{\mathrm{t\bar{t}}}$ sensitive to the angular separation of the two tops evaluated in the $t\bar{t}$-system. Figure 9.1.2e is the distribution of $\cos\theta(l^t, l^{\bar{t}})$ where θ is the angular separation between the direction of the positively charged lepton evaluated in the top rest-frame and the direction of the negative charged lepton evaluated in the anti-top rest frame: $\hat{p}^t(l^+) \cdot \hat{p}^{\bar{t}}(l^-)$. Finally, Figure 9.1.2f shows the distribution of $\Delta\phi_{\mathrm{CM},t\bar{t}}$: the azimuthal angle between the decay plane spanned by the H-system and the $t\bar{t}$-system and the decay plane formed by the two tops: $(\triangle\varphi\left[\bar{H}^{\,\mathrm{Lab}}\times(t\bar{t})^{\,\mathrm{Lab}}, t^{\,\mathrm{CM}}\times\bar{t}^{\,\mathrm{CM}}\right])$.

Figure 9.1.3 shows two-dimensional distributions of scale and angular observables for the CP-even Higgs sample. The first three distributions show the correlation between scale variables.

Figure 9.1.3a shows the reconstruction for the masses of the two W systems. The reconstructions are close to the true values and a large uncorrelation between the two hemispheres is shown. This feature is common among the other samples sign that the combinatoric and WIMP jigsaw rules are such that the W^+ and W^- systems and hence, the top and antitop systems, and the overall $t\bar{t}$-system are reconstructed with remarkable precision for this complex final state topology involving massless weakly interacting particles. This behaviour is mostly independent of the jet multiplicity of the final state suggesting that the correct b-jet is associated to the corresponding lepton in the tree. Figure 9.1.3b shows the two-dimensional distribution between the two scale variables sensitive to the X nature, while Figure 9.1.3c shows the histogram between the mass of the H-system and $M_{t\bar{t}}$: the mass of the $t\bar{t}$-system. The scale variables present an overall low correlation between them and the same is observed for the other samples.

Figures 9.1.3d, 9.1.3e and 9.1.3f show the two-dimensional distributions between the mass of the H-system and $\Delta\phi_{\mathrm{CM},t\bar{t}}$, $\cos\theta(l^t, l^{\bar{t}})$ and $\cos\theta_{\mathrm{H,t\bar{t}}}$ respectively. These figures manifest the uncorrelated nature between scale and angular variables and similar features appear for the other two samples with a concentration of the events around the Z-pole for the gauge boson sample.

Finally, Figures 9.1.3g, 9.1.3h and 9.1.3i show orthogonality between angular vs angular RJR observables. Furthermore, SM-like Higgs events tend to populate higher values for $\cos\theta(l^t, l^{\bar{t}})$ independently of the other observables.

A detailed analysis requires the generation of all the main possible backgrounds including $t\bar{t}$ in the di-leptonic channel + ISR, with focus on the radiation $g\to b\bar{b}$ and any other

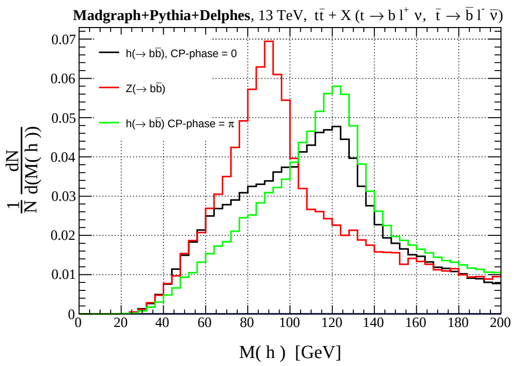

(a)

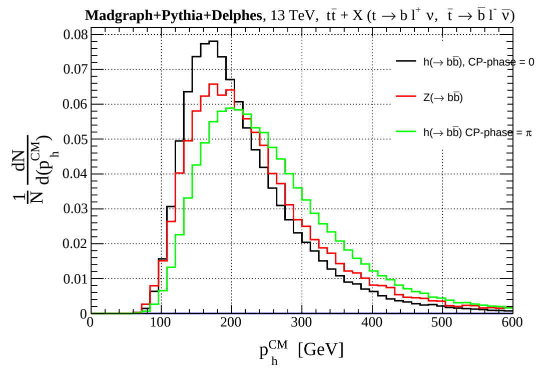

(b)

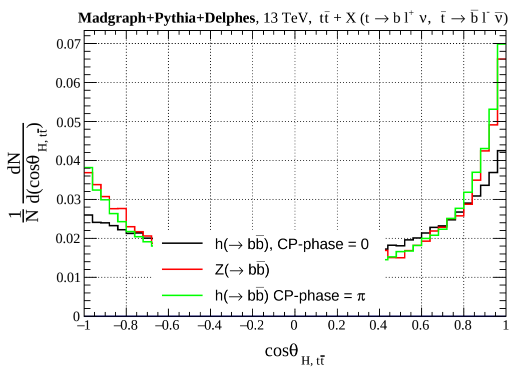

(c)

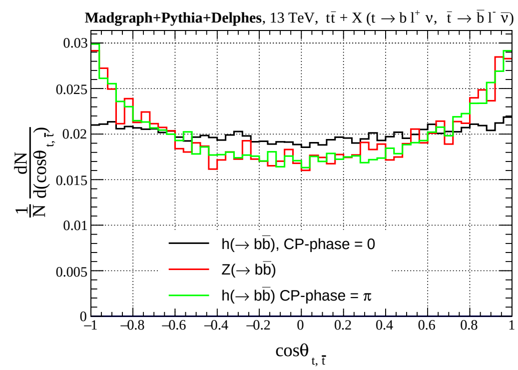

(d)

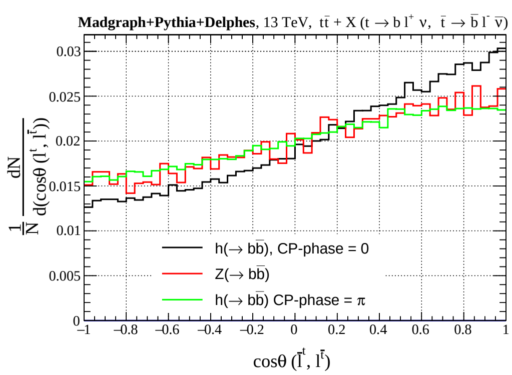

(e)

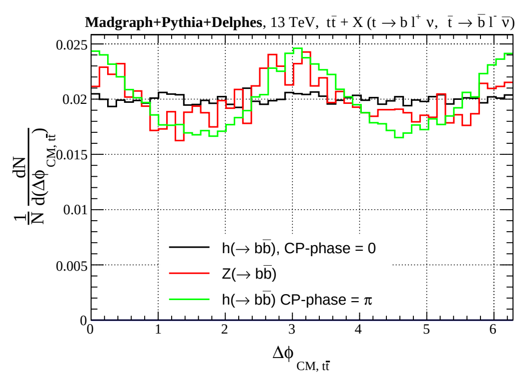

(f)

Figure 9.1.2: Distributions for the main scale and angular RJR observables sensitive to the nature of the Higgs boson for the process $pp \to t\bar{t}+h$, $\left(t \to b\nu l^{+},\ \bar{t} \to \bar{b}\bar{\nu}l^{-},\ h \to b\bar{b}\right)$. The black line corresponds to a SM-like Higgs boson, the green line to a CP-odd Higgs boson and the red line to a Z boson.

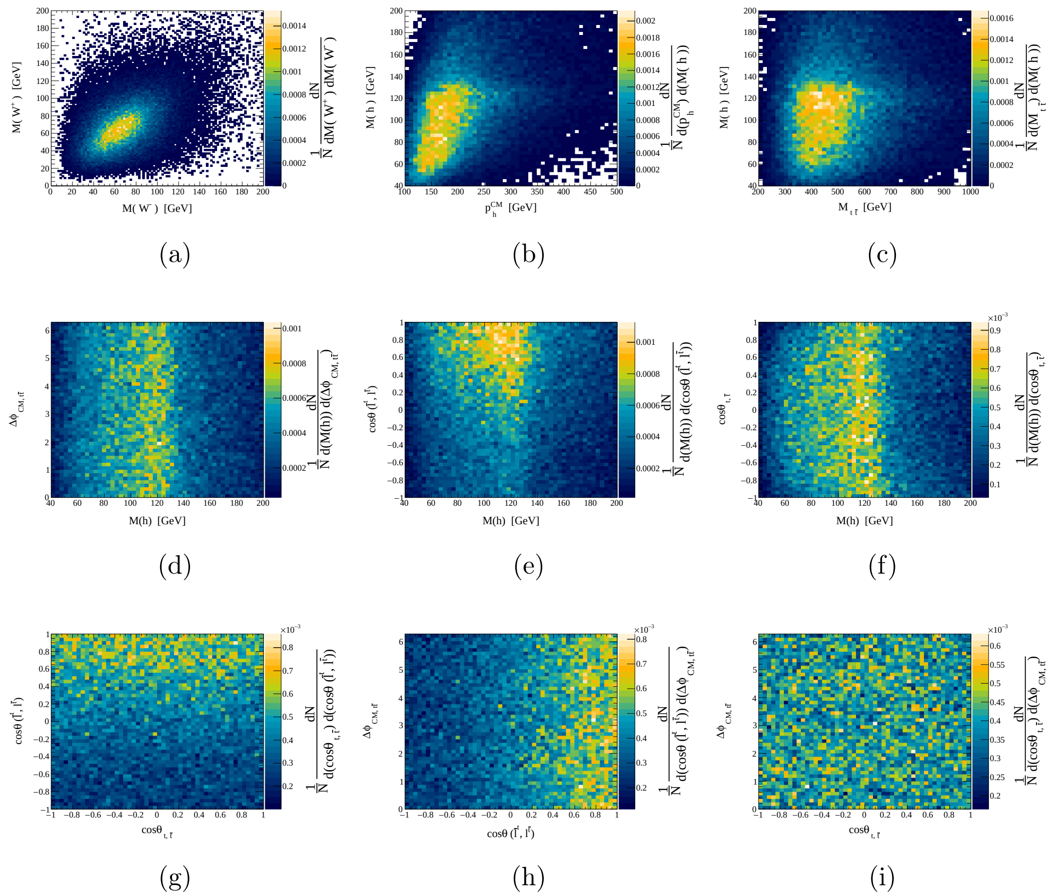

Figure 9.1.3: Two-dimensional distributions between scale and angular RJR observables for the events of the process: CP-even Higgs boson produced in association with a pair of tops decaying in the di-leptonic channel.

possible process involving two opposite-sign leptons, high jet multiplicity and missing transverse momentum such as $t\bar{t} + W(\rightarrow \text{had})$ with mis-tagged jets. This analysis is supposed to investigate the feasibility of the process $t\bar{t} + h$ in the di-leptonic channel at LHC as well as study the CP-nature of the Higgs boson. Selection criteria applied to scale observables such as the mass of the H-system, $M_{t\bar{t}}$ and the missing transverse momentum could be used to suppress possible background processes together with appropriate $b-$tagging requirements, while one can leverage the distribution of p_h^{CM} and in particular on the other angular observables described in this section, in order to both increase the significance for the signal-to-background ratio and extract additional information regarding the nature of the Higgs.

9.2 Other potential future works

The RJR technique has been used for probing open mass spectra, investigating two hemisphere topology examples, and for compressed mass spectra leveraging on an ISR-system. In Chapter 8 we fuse the two strategies in order to probe the entire supersymmetric phase-space.

The SUSY phenomenology allows a multitude of possible investigations. Furthermore, the re-interpretation of the results using different branching fractions for different modes allow the opportunity to study a vast variety of final state topologies assuming the same, or similar, superparticle pair-production. A typical example consists in assuming a 50% branching ratio for each of the two modes $\tilde{q} \rightarrow \tilde{\chi}_1^0 q$ and $\tilde{q} \rightarrow \tilde{\chi}_1^{\pm} q$, which is equivalent to employ the simplified topology assumption $(BR = 1)$ for each gauge eigenstates $\tilde{q}_R \rightarrow \tilde{\chi}_1^0 q$ and $\tilde{q}_L \rightarrow \tilde{\chi}_1^{\pm} q$. Another possibility consists in combining results obtained analysing a specific final state produced from similar topologies with similar kinematics. The unambiguous way to present a re-interpretation of an analysis result consists in the assumption of a branching fraction for the specific process, which is equivalent to scale the quantity $\sigma \times BR$, and hence the number of expected signal events, independently of the other decay modes.

The jigsaw rules described in this thesis can be customised and applied to study any supersymmetric final state topology. Some additional examples considering the only third generation of squarks include:[1]

- Stop pair-production: $pp \to \tilde{t}\tilde{t}(\tilde{t} \to X\tilde{\chi}_1^0)$. In such a case X summarises different potential decay products depending on the mass splitting. In particular the different modes described in Eq. 2.3.30 should be investigated.

- Gluino mediated stop production. For example, the process $pp \to \tilde{g}\tilde{g}(\tilde{g} \to \tilde{t}(t\tilde{\chi}_1^0)t)$ can produce a final state reach of extra b-jets and one can leverage the large cross-section for the gluino pair-production.

- Sbottoms mediated stop production: $pp \to \tilde{b}\tilde{b}(\tilde{b} \to \tilde{t}(X\tilde{\chi}_1^0)b)$. Except for $\tilde{b} \to b\tilde{\chi}_1^0$, this is the favourite mode for the sbottom and when the stop-sbottom mass splitting is reasonably small, similar cross section respect the direct stop production can be exploited together with the two potential additional b-jets reconstructed by the detector.

- Di-gluino production $pp \to \tilde{g}\tilde{g}(\tilde{g} \to bb\tilde{\chi}_1^0)$. In Chapter 7 we have shown how applying RJR to the two step decays study provides results mostly independent of the mass of the sbottom. One can extend the investigation to the three body decay using a similar strategy as adopted in Chapter 8 employing an ISR-system for large jet multiplicity ($N_{\text{jet}} > 4$).

- Other possible topologies including intermediate electroweakinos can be investigated either for the direct production of sbottoms or mediated by the gluino pair.

For on-shell tops, and in particular for scenarios with large mass splittings, boosted

[1] The labels for the anti-particles and light eigenstates of mass are erased.

tops technique should be employed. While disfavoured, RJR can be applied to mixed gluino two/three body decays as described in Ref. [112] ($\tilde{g} \to b\tilde{b}$ and $\tilde{g} \to bb\tilde{\chi}_1^0$).

More generally, RJR can be used for probing any final state with weakly interacting particles. For example, two classes of theoretical frameworks called Little Higgs Models [140–143] and theories of extra dimensions [144–147] are alternative approaches to SUSY for the solution of the hierarchy problem. Some of the possible interactions of the Little Higgs models are constrained by experimental measurements and can be removed imposing the conservation of a $\mathbb{Z}_2$ symmetry, referred to as T-parity. Theories of extra dimensions assume the strong and electroweak forces are confined in the four-dimensional space, while gravity can propagate to additional dimensions, including models of compact extra dimensions and warped geometries a la Randal-Sundrum. For example, with one compact extra dimension new fields are odd under a discrete symmetry called KK-parity.

In both cases the conservation of such discrete symmetries provide a lightest stable weakly interacting particle KK- or T-odd which would be consistent with a candidate for dark matter. At the LHC, a pair of odd particles under KK or T-parity could be produced providing cascades resembling those one of the SUSY phenomenology. Final state topologies would involve SM particles plus a pair of DM candidates and the RJR technique could be applied imposing trees and rules as described in this thesis.

Chapter 10

Summary

Recursive Jigsaw Reconstruction (RJR) introduced in Chapter 4 is a proposed high energy physics technique dedicated to the study of final state topologies containing ambiguities due to unknown kinematic degrees of freedom when particles not interacting with the detector are present and/or combinatoric challenges due to the presence of indistinguishable visible particles. The problem is factorised by the imposition of jigsaw rules moving recursively through the decay tree to reconstruct the event approximating the relevant frames of reference.

The result is a complete basis of kinematic observables sensitive to the masses and decay angles of the resonances appearing in the tree which can be used to distinguish signatures of new physics from the SM background. In this thesis, RJR is applied to analyses in the context of the supersymmetric theoretical framework. Selection criteria applied on RJR variables are imposed for the definition of signal regions targeting the final state topologies investigated.

Gluino and squark compressed scenarios in fully hadronic final states ($\tilde{g} \rightarrow qq\tilde{\chi}_1^0$ and $\tilde{q} \rightarrow q\tilde{\chi}_1^0$) are studied in Chapter 5. Results are presented in Figures 5.5.1 and 5.5.2 for an integrated luminosity of 100 fb^{-1} and for a centre-of-mass collision energy of 14 TeV, assuming a systematic uncertainty of 15% for the SM background.

In Chapter 6 RJR is used to investigate the SUSY electroweak sector. Associated neutralino-chargino production in final states with three leptons ($\tilde{\chi}_2^0 \to Z^*(l^+l^-)\tilde{\chi}_1^0$, $\tilde{\chi}_1^\pm \to W^{*\pm}(l^\pm\nu)\tilde{\chi}_1^0$) are probed leveraging on only compressed transverse observables. Discovery reach and exclusion limits are shown in Figure 6.2.9 for an integrated luminosity of 300 fb^{-1} at $\sqrt{s} = 14$ TeV assuming a 20% systematic uncertainty constant in the SUSY phase space. A more sophisticated investigation is dedicated to the scenarios involving compressed charginos in final states with two opposite charge leptons and missing transverse momentum ($\tilde{\chi}_1^+ \to W^{*+}(l^+\nu)\tilde{\chi}_1^0$, $\tilde{\chi}_1^- \to W^{*-}(l^-\bar{\nu})\tilde{\chi}_1^0$). A large data sample of 3 ab^{-1} is necessary to put the first exclusion limits in the $M_{\tilde{\chi}_1^0}$ vs $M_{\tilde{\chi}_1^\pm}$ plane assuming a flat 20% systematic uncertainty for the SM background processes at LHC14 as shown in Figure 6.3.13.

Gluino mediated sbottom production in final state with four b-jets and missing transverse momentum ($\tilde{g} \to b\tilde{b}_1(b\tilde{\chi}_1^0)$) are investigated in Chapter 7 for several scenarios spanning on the gluino, sbottom and LSP masses. Two signal regions are defined for the discovery prospects of such scenarios and the significances are presented in Figure 7.6.1 and Figure 7.6.2 for different projections of the integrated luminosity assuming a 30% systematic uncertainty for the SM background at $\sqrt{s} = 14$ TeV.

Scenarios involving the direct production of light sbottoms in final states with two b-jets and missing transverse momentum ($\tilde{b}_1 \to b\tilde{\chi}_1^0$) are studied in Chapter 8 with results presented in the $M_{\tilde{b}_1}$ vs $M_{\tilde{\chi}_1^0}$ plane in Figure 8.6.1 assuming a data sample of 50 fb^{-1} of LHC14 and systematic uncertainties of 20% and 30% for the SM background.

Using the data collected during 2015 and 2016 of Run 2 of LHC13, no significant deviations from the SM expectation arise from the myriad searches for BSM physics performed by the experiments. A large proportion of the SUSY phase space has been excluded assuming the hypothesis of simplified models or in the context of MSSM and beyond. The difficulty arising for probing regions of the SUSY phase space particularly challenging, such as the case of compressed scenarios, or due to combinatoric and kinematic ambiguities in the final state can be attenuated by employing RJR. Novel searches by the ATLAS collaboration leverage RJR for probing light squarks and gluinos in final states with jets and missing transverse momentum [122]. Analyses in the SUSY electroweak sector and concerning squarks of the third generation are highly topical and it has been demonstrated in this thesis how significant improvements can be made in performing these searches.

Bibliography

[1] S. Weinberg, *A Model of Leptons*, *Phys. Rev. Lett.* **19** (1967) 1264–1266. 2.1.1

[2] F. Halzen and A. D. Martin, *QUARKS AND LEPTONS: AN INTRODUCTORY COURSE IN MODERN PARTICLE PHYSICS*. 1984. 2.1.1

[3] M. E. Peskin and D. V. Schroeder, *An introduction to quantum field theory*. Advanced book program. Westview Press Reading (Mass.), Boulder (Colo.), 1995. 2.1.1, 3.4

[4] I. J. R. Aitchison and A. J. G. Hey, *Gauge theories in particle physics: A practical introduction. Vol. 1: From relativistic quantum mechanics to QED*. 2003. 2.1.1

[5] A. Shomer, *A Pedagogical explanation for the non-renormalizability of gravity*, `0709.3555`. 1

[6] C.-N. Yang and R. L. Mills, *Conservation of Isotopic Spin and Isotopic Gauge Invariance*, *Phys. Rev.* **96** (1954) 191–195. 2.1.4

[7] H. D. Politzer, *Reliable Perturbative Results for Strong Interactions?*, *Phys. Rev. Lett.* **30** (1973) 1346–1349. 2.1.4

[8] D. J. Gross and F. Wilczek, *Ultraviolet Behavior of Nonabelian Gauge Theories*, *Phys. Rev. Lett.* **30** (1973) 1343–1346. 2.1.4

[9] S. L. Glashow, *Partial Symmetries of Weak Interactions*, *Nucl. Phys.* **22** (1961) 579–588. 2.1.5

[10] P. W. Anderson, *Plasmons, Gauge Invariance, and Mass*, *Phys. Rev.* **130** (1963) 439–442. 2.1.6

[11] G. S. Guralnik, C. R. Hagen and T. W. B. Kibble, *Global Conservation Laws and Massless Particles*, *Phys. Rev. Lett.* **13** (1964) 585–587. 2.1.6

[12] T. W. B. Kibble, *Symmetry breaking in nonAbelian gauge theories*, *Phys. Rev.* **155** (1967) 1554–1561. 2.1.6

[13] P. W. Higgs, *Broken Symmetries and the Masses of Gauge Bosons*, *Phys. Rev. Lett.* **13** (1964) 508–509. 2.1.6

[14] F. Englert and R. Brout, *Broken Symmetry and the Mass of Gauge Vector Mesons*, *Phys. Rev. Lett.* **13** (1964) 321–323. 2.1.6

[15] P. W. Higgs, *Spontaneous Symmetry Breakdown without Massless Bosons*, *Phys. Rev.* **145** (1966) 1156–1163. 2.1.6

[16] H. K. Dreiner, H. E. Haber and S. P. Martin, *Two-component spinor techniques and Feynman rules for quantum field theory and supersymmetry*, *Phys. Rept.* **494** (2010) 1–196, [0812.1594]. 2.1.8

[17] S. Dodelson, *Modern Cosmology*. Academic Press, Amsterdam, 2003. 2.2.1.1

[18] E. W. Kolb and M. S. Turner, *The Early Universe*, *Front. Phys.* **69** (1990) 1–547. 2.2.1.1

[19] K. Garrett and G. Duda, *Dark Matter: A Primer*, *Adv. Astron.* **2011** (2011) 968283, [1006.2483]. 8

[20] L. Bergstrom and A. Goobar, *Cosmology and particle astrophysics*. 1999. 8

[21] LUX collaboration, D. S. Akerib et al., *Improved WIMP scattering limits from the LUX experiment*, `1512.03506`. 2.2.1.1

[22] Planck collaboration, R. Adam et al., *Planck 2015 results. I. Overview of products and scientific results*, `1502.01582`. 2.2.1.1

[23] S. P. Martin, *A Supersymmetry primer*, *Adv.Ser.Direct.High Energy Phys.* **21** (2010) 1–153, [`hep-ph/9709356`]. 2.2.8, 10, 2.3.2

[24] J. Wess and B. Zumino, *A lagrangian model invariant under supergauge transformations*, *Physics Letters B* **49** (1974) 52 – 54. 2.3

[25] H. Miyazawa, *Baryon Number Changing Currents*, *Prog.Theor.Phys.* **36** (1966) 1266–1276. 2.3

[26] P. Ramond, *Dual Theory for Free Fermions*, *Phys.Rev.* **D3** (1971) 2415–2418. 2.3

[27] Y. Golfand and E. Likhtman, *Extension of the Algebra of Poincare Group Generators and Violation of p Invariance*, *JETP Lett.* **13** (1971) 323–326. 2.3

[28] A. Neveu and J. Schwarz, *Factorizable dual model of pions*, *Nucl.Phys.* **B31** (1971) 86–112. 2.3

[29] A. Neveu and J. Schwarz, *Quark Model of Dual Pions*, *Phys.Rev.* **D4** (1971) 1109–1111. 2.3

[30] D. Volkov and V. Akulov, *Is the Neutrino a Goldstone Particle?*, *Phys.Lett.* **B46** (1973) 109–110. 2.3

[31] J. Wess and B. Zumino, *Supergauge Transformations in Four-Dimensions*, *Nucl.Phys.* **B70** (1974) 39–50. 2.3

[32] P. Binetruy, *Supersymmetry: Theory, experiment and cosmology*, . 2.3

[33] M. Drees, R. Godbole and P. Roy, *Theory and phenomenology of sparticles: An account of four-dimensional N=1 supersymmetry in high energy physics*. 2004. 2.3

[34] J. D. Lykken, *Introduction to supersymmetry*, in *Fields, strings and duality. Proceedings, Summer School, Theoretical Advanced Study Institute in Elementary Particle Physics, TASI'96, Boulder, USA, June 2-28, 1996*, pp. 85–153, 1996, hep-th/9612114, http://lss.fnal.gov/cgi-bin/find$_{p}aper.pl?pub-96-445-T$. 10

[35] S. R. Coleman and J. Mandula, *All Possible Symmetries of the S Matrix*, *Phys. Rev.* **159** (1967) 1251–1256. 2.3.1

[36] R. Haag, J. T. Lopuszanski and M. Sohnius, *All Possible Generators of Supersymmetries of the s Matrix*, *Nucl. Phys.* **B88** (1975) 257. 2.3.1

[37] Super-Kamiokande collaboration, K. Kobayashi et al., *Search for nucleon decay via modes favored by supersymmetric grand unification models in Super-Kamiokande-I*, *Phys. Rev.* **D72** (2005) 052007, [hep-ex/0502026]. 12

[38] P. Fayet and J. Iliopoulos, *Spontaneously Broken Supergauge Symmetries and Goldstone Spinors*, *Phys. Lett.* **B51** (1974) 461–464. 2.3.3

[39] L. O'Raifeartaigh, *Spontaneous Symmetry Breaking for Chiral Scalar Superfields*, *Nucl. Phys.* **B96** (1975) 331–352. 2.3.3

[40] R. Barbieri, L. J. Hall and A. Strumia, *Violations of lepton flavor and CP in supersymmetric unified theories*, *Nucl. Phys.* **B445** (1995) 219–251, [hep-ph/9501334]. 2.3.4.1

[41] Particle Data Group collaboration, C. Patrignani et al., *Review of Particle Physics*, *Chin. Phys.* **C40** (2016) 100001. 2.3.4.1, 6.1.2.2

[42] Z. King and A. J. Schwartz, *Recent results from the Belle experiment*, *J. Phys. Conf. Ser.* **770** (2016) 012015, [1612.03493]. 2.3.4.1

[43] BaBar collaboration, J. P. Lees et al., *Exclusive Measurements of $b \to s\gamma$ Transition Rate and Photon Energy Spectrum*, *Phys. Rev.* **D86** (2012) 052012, [1207.2520]. 2.3.4.1

[44] J. R. Ellis, S. Ferrara and D. V. Nanopoulos, *CP Violation and Supersymmetry*, *Phys. Lett.* **B114** (1982) 231–234. 2.3.4.1

[45] LHCb Collaboration collaboration, R. Aaij, B. Adeva and M. a. Adinolfi, *Measurement of the $B_s^0 \to \mu^+\mu^-$ branching fraction and effective lifetime and search for $B^0 \to \mu^+\mu^-$ decays*, *Phys. Rev. Lett.* **118** (Mar, 2017) 191801. 19 p. 2.3.4.4

[46] Muon g-2 collaboration, G. W. Bennett et al., *Final Report of the Muon E821 Anomalous Magnetic Moment Measurement at BNL*, *Phys. Rev.* **D73** (2006) 072003, [hep-ex/0602035]. 2.3.4.4

[47] X. Prudent et al., *Constrained Supersymmetry after two years of LHC data: a global view with Fittino*, *PoS* **ICHEP2012** (2013) 116, [1301.3633]. 2.3.4.4

[48] GAMBIT collaboration, P. Athron et al., *Global fits of GUT-scale SUSY models with GAMBIT*, 1705.07935. 2.3.3

[49] CMS collaboration, V. Khachatryan et al., *Search for dark matter, extra dimensions, and unparticles in monojet events in proton–proton collisions at $\sqrt{s} = 8$ TeV*, *Eur. Phys. J.* **C75** (2015) 235, [1408.3583]. 2.3.5

[50] J. Barnard, B. Farmer, T. Gherghetta and M. White, *Natural gauge mediation with a bino NLSP at the LHC*, *Phys. Rev. Lett.* **109** (2012) 241801, [1208.6062]. 2.3.5

[51] A. Strumia, *The Fine-tuning price of the early LHC*, *JHEP* **04** (2011) 073, [1101.2195]. 2.3.4

[52] R. Barbieri and G. F. Giudice, *Upper Bounds on Supersymmetric Particle Masses*, *Nucl. Phys.* **B306** (1988) 63–76. 2.3.6, 6.1

[53] H. Baer, V. Barger, P. Huang, A. Mustafayev and X. Tata, *Radiative natural SUSY with a 125 GeV Higgs boson*, *Phys. Rev. Lett.* **109** (2012) 161802, [1207.3343]. 2.3.6

[54] K. Agashe and R. Contino, *The Minimal composite Higgs model and electroweak precision tests*, *Nucl. Phys.* **B742** (2006) 59–85, [hep-ph/0510164]. 2.3.6

[55] A. M. Galper et al., *The PAMELA experiment: a decade of Cosmic Ray Physics in space*, *J. Phys. Conf. Ser.* **798** (2017) 012033. 3.1

[56] AMS 02 collaboration, F. Barao, *AMS: Alpha Magnetic Spectrometer on the International Space Station*, *Nucl. Instrum. Meth.* **A535** (2004) 134–138. 3.1

[57] Fermi-LAT collaboration, M. Ackermann et al., *The Fermi Large Area Telescope On Orbit: Event Classification, Instrument Response Functions, and Calibration*, *Astrophys. J. Suppl.* **203** (2012) 4, [1206.1896]. 3.1

[58] LUX collaboration, P. Beltrame, *Dark Matter Searches with the LUX Experiment*, in *Proceedings, 11th Patras Workshop on Axions, WIMPs and WISPs (Axion-WIMP 2015): Zaragoza, Spain, June 22-26, 2015*, pp. 11–15, 2015, DOI. 3.1

[59] XENON collaboration, E. Aprile et al., *First Dark Matter Search Results from the XENON1T Experiment*, 1705.06655. 3.1

[60] R. Feynman, *Photon-Hadron Interactions*. Advanced Book Program Series. Avalon Publishing, 1998. 3.1

[61] K. Jakobs, *Physics at the LHC – From Standard Model measurements to Searches for New Physics*, in *Proceedings, 2011 European School of High-Energy Physics (ESHEP 2011): Cheile Gradistei, Romania, September 7-20, 2011*, pp. 309–358, 2014, 1206.7024, DOI. 3.1.2, 3.1.3

[62] L. Evans and P. Bryant, *LHC Machine*, *JINST* **3** (2008) S08001. 3.2, 3.2.1

[63] C. Lefèvre, "The CERN accelerator complex. Complexe des accélérateurs du CERN." Dec, 2008. 3.2.1

[64] T. Gleisberg, S. Höche, F. Krauss, M. Schönherr, S. Schumann, F. Siegert et al., *Event generation with sherpa 1.1*, *Journal of High Energy Physics* **2009** (2009) 007. 3.2.2

[65] C. W. Fabjan and F. Gianotti, *Calorimetry for particle physics*, *Rev. Mod. Phys.* **75** (2003) 1243–1286. 3.3.1

[66] C. Kourkoumelis and S. Vourakis, *Hypatia—an online tool for atlas event visualization*, *Physics Education* **49** (2014) 21. 3.3.1

[67] ATLAS collaboration, G. Aad et al., *The ATLAS Experiment at the CERN Large Hadron Collider*, *JINST* **3** (2008) S08003. 3.3.2, 3.3.2

[68] CMS collaboration, S. Chatrchyan et al., *The CMS experiment at the CERN LHC*, *JINST* **3** (2008) S08004. 3.3.2, 3.3.3

[69] T. A. collaboration, *Search for the direct pair production of top squarks decaying to a b quark, a tau lepton, and weakly interacting particles, in $\sqrt{s} = 8TeV$ pp collisions using* $20\ fb^{-1}$ *of ATLAS data*, . 3.3.2

[70] J. Anderson, A. Avetisyan, R. Brock, S. Chekanov, T. Cohen et al., *Snowmass Energy Frontier Simulations*, 1309.1057. 3.4, 8.6

[71] J. Alwall, M. Herquet, F. Maltoni, O. Mattelaer and T. Stelzer, *MadGraph 5 : Going Beyond*, *JHEP* **1106** (2011) 128, [1106.0522]. 3.4, 3.4.1

[72] J. Pumplin, D. R. Stump, J. Huston, H. L. Lai, P. M. Nadolsky and W. K. Tung, *New generation of parton distributions with uncertainties from global QCD analysis*, *JHEP* **07** (2002) 012, [hep-ph/0201195]. 3.4

[73] T. Sjostrand, S. Mrenna and P. Z. Skands, *PYTHIA 6.4 Physics and Manual*, *JHEP* **05** (2006) 026, [hep-ph/0603175]. 3.4, 3.4.1

[74] M. Selvaggi, *DELPHES 3: A modular framework for fast-simulation of generic collider experiments*, *J.Phys.Conf.Ser.* **523** (2014) 012033. 3.4, 3.4.2

[75] A. Avetisyan, J. M. Campbell, T. Cohen, N. Dhingra, J. Hirschauer et al., *Methods and Results for Standard Model Event Generation at $\sqrt{s}$ = 14 TeV, 33 TeV and 100 TeV Proton Colliders (A Snowmass Whitepaper)*, 1308.1636. 3.4, 3.5.1, 7.4.2

[76] T. Sjostrand, S. Mrenna and P. Z. Skands, *A Brief Introduction to PYTHIA 8.1*, *Comput.Phys.Commun.* **178** (2008) 852–867, [0710.3820]. 3.4.1

[77] S. Catani, F. Krauss, R. Kuhn and B. R. Webber, *QCD matrix elements + parton showers*, *JHEP* **11** (2001) 063, [hep-ph/0109231]. 3.4.1

[78] N. Lavesson and L. Lonnblad, *W+jets matrix elements and the dipole cascade*, *JHEP* **07** (2005) 054, [hep-ph/0503293]. 3.4.1

[79] L. Lonnblad, *Correcting the color dipole cascade model with fixed order matrix elements*, *JHEP* **05** (2002) 046, [hep-ph/0112284]. 3.4.1

[80] S. Mrenna and P. Richardson, *Matching matrix elements and parton showers with HERWIG and PYTHIA*, *JHEP* **05** (2004) 040, [hep-ph/0312274]. 3.4.1

[81] M. L. Mangano, M. Moretti, F. Piccinini and M. Treccani, *Matching matrix elements and shower evolution for top-quark production in hadronic collisions*, *JHEP* **01** (2007) 013, [hep-ph/0611129]. 3.4.1

[82] "Jets at cms and the determination of their energy scale." http://cms.web.cern.ch/news/jets-cms-and-determination-their-energy-scale. 3.4.3

[83] H.-n. Li, *Quantum Chromodynamics (CERN-2014-001)*, in *Proceedings, 1st Asia-Europe-Pacific School of High-Energy Physics (AEPSHEP): Fukuoka, Japan, October 14-27, 2012*, pp. 95–135, 2014, 1406.7689, DOI. 3.4.2.4

[84] M. Cacciari, G. P. Salam and G. Soyez, *The Anti-k(t) jet clustering algorithm*, *JHEP* **0804** (2008) 063, [0802.1189]. 3.4.2.4

[85] M. Cacciari, G. P. Salam and G. Soyez, *Fastjet user manual*, *The European Physical Journal C* **72** (2012) 1896. 3.4.2.4

[86] J. M. Butterworth, A. R. Davison, M. Rubin and G. P. Salam, *Jet substructure as a new Higgs search channel at the LHC*, *Phys. Rev. Lett.* **100** (2008) 242001, [0802.2470]. 3.4.2.4

[87] D. Krohn, J. Thaler and L.-T. Wang, *Jet Trimming*, *JHEP* **02** (2010) 084, [0912.1342]. 3.4.2.4

[88] S. D. Ellis, C. K. Vermilion and J. R. Walsh, *Techniques for improved heavy particle searches with jet substructure*, *Phys. Rev.* **D80** (2009) 051501, [0903.5081]. 3.4.2.4

[89] CMS collaboration, *Search for new physics in the compressed mass spectra scenario using events with two soft opposite-sign leptons and missing momentum energy at 13 TeV*, . 3.4.2.6, 1, 6.2.1, 6.2.11

[90] ATLAS collaboration, C. Gemme, *Latest ATLAS results from Run 2*, in *Proceedings, 9th International Workshop on Top Quark Physics (TOP 2016): Olomouc, Czech Republic, September 19-23, 2016*, 2016, 1612.01987, https://inspirehep.net/record/1501935/files/arXiv:1612.01987.pdf. 3.5.1

[91] J. Alwall, P. Schuster and N. Toro, *Simplified Models for a First Characterization of New Physics at the LHC*, *Phys. Rev.* **D79** (2009) 075020, [0810.3921]. 3.5.1

[92] LHC New Physics Working Group collaboration, D. Alves, *Simplified Models for LHC New Physics Searches*, *J. Phys.* **G39** (2012) 105005, [1105.2838]. 3.5.1

[93] T. S. Virdee, *Beyond the standard model of particle physics*, *Phil. Trans. Roy. Soc. Lond.* **374** (2016) 20150259. 3.5.2

[94] R. D. Cousins, J. T. Linnemann and J. Tucker, *Evaluation of three methods for calculating statistical significance when incorporating a systematic uncertainty into a test of the background-only hypothesis for a Poisson process*, *Nucl. Instrum. Meth.* **A595** (2008) 480–501. 3.5.1, 5.5, 6.2.4

[95] R. Brun and F. Rademakers, *ROOT: An object oriented data analysis framework*, *Nucl. Instrum. Meth.* **A389** (1997) 81–86. 6

[96] I. Hinchliffe, F. E. Paige, M. D. Shapiro, J. Soderqvist and W. Yao, *Precision SUSY measurements at CERN LHC*, *Phys. Rev.* **D55** (1997) 5520–5540, [hep-ph/9610544]. 3.5.2

[97] C. Lester and D. Summers, *Measuring masses of semiinvisibly decaying particles pair produced at hadron colliders*, *Phys.Lett.* **B463** (1999) 99–103, [hep-ph/9906349]. 3.5.2

[98] A. Barr, C. Lester and P. Stephens, *m(T2): The Truth behind the glamour*, *J.Phys.* **G29** (2003) 2343–2363, [hep-ph/0304226]. 3.5.2

[99] W. S. Cho, K. Choi, Y. G. Kim and C. B. Park, *Measuring superparticle masses at hadron collider using the transverse mass kink*, *JHEP* **0802** (2008) 035, [0711.4526]. 3.5.2

[100] M. Burns, K. Kong, K. T. Matchev and M. Park, *Using Subsystem MT2 for Complete Mass Determinations in Decay Chains with Missing Energy at Hadron Colliders*, *JHEP* **0903** (2009) 143, [0810.5576]. 3.5.2

[101] G. Polesello and D. R. Tovey, *Supersymmetric particle mass measurement with the boost-corrected contransverse mass*, *JHEP* **1003** (2010) 030, [0910.0174]. 3.5.2, 3.5.2

[102] K. T. Matchev and M. Park, *A General method for determining the masses of semi-invisibly decaying particles at hadron colliders*, *Phys. Rev. Lett.* **107** (2011) 061801, [0910.1584]. 3.5.2, 3.5.2

[103] CMS collaboration, V. Khachatryan et al., *Search for Supersymmetry in pp Collisions at 7 TeV in Events with Jets and Missing Transverse Energy*, *Phys. Lett.* **B698** (2011) 196–218, [1101.1628]. 3.5.2

[104] M. R. Buckley, J. D. Lykken, C. Rogan and M. Spiropulu, *Super-Razor and Searches for Sleptons and Charginos at the LHC*, *Phys. Rev.* **D89** (2014) 055020, [1310.4827]. 3.5.2, 3.5.2

[105] W. S. Cho, J. S. Gainer, D. Kim, K. T. Matchev, F. Moortgat, L. Pape et al., *On-shell constrained M_2 variables with applications to mass measurements and topology disambiguation*, *JHEP* **08** (2014) 070, [1401.1449]. 3.5.2

[106] CMS collaboration, S. Chatrchyan et al., *Search for supersymmetry with razor variables in pp collisions at $\sqrt{s}$=7 TeV*, 1405.3961. 3.5.2

[107] P. Konar and A. K. Swain, *Reconstructing semi-invisible events in resonant tau pair production from higgs*, *Physics Letters B* **757** (2016) 211 – 215. 3.5.2

[108] C. Rogan, *Kinematical variables towards new dynamics at the LHC*, 1006.2727. 3.5.2

[109] I.-W. Kim, *Algebraic Singularity Method for Mass Measurement with Missing Energy*, Phys. Rev. Lett. **104** (2010) 081601, [0910.1149]. 3.5.2

[110] A. J. Barr, T. J. Khoo, P. Konar, K. Kong, C. G. Lester, K. T. Matchev et al., *Guide to transverse projections and mass-constraining variables*, Phys. Rev. **D84** (2011) 095031, [1105.2977]. 3.5.2

[111] P. Jackson, C. Rogan and M. Santoni, *Sparticles in motion: Analyzing compressed susy scenarios with a new method of event reconstruction*, Phys. Rev. D **95** (Feb, 2017) 035031, [1607.08307]. 4.1, 4.6.1, 4.6.2, 5.1, 8.6

[112] P. Jackson and C. Rogan, *Recursive Jigsaw Reconstruction: HEP event analysis in the presence of kinematic and combinatoric ambiguities*, 1705.10733. 4.1, 4.2.2, 4.2.4, 9.2

[113] P. Jackson, *The Recursive Jigsaw Reconstruction Technique*, *PoS* **ICHEP2016, 1219** (2017) . 4.1

[114] P. Jackson, *Compressed SUSY searches with Recursive Jigsaw Reconstruction*, *PoS* **EPS-HEP2017, 292** (2017) . 4.1

[115] M. Santoni, *Probing compressed mass spectra in electroweak supersymmetry with Recursive Jigsaw Reconstruction*, *In preparation* (2017) . 4.1, 6.1

[116] M. Santoni, *Probing open and compressed supersymmetric mass spectra using a new method of reconstruction of the events*, *In preparation* (2017) . 4.1, 8.1

[117] C. Rogan, *RestFrames*, *http://RestFrames.com* . 4.1.1, 4.6.2

[118] H. An and L.-T. Wang, *Opening up the compressed region of top squark searches at 13 TeV LHC*, Phys. Rev. Lett. **115** (2015) 181602, [1506.00653]. 4.6.1.2

[119] S. Macaluso, M. Park, D. Shih and B. Tweedie, *Revealing Compressed Stops Using High-Momentum Recoils*, JHEP **03** (2016) 151, [1506.07885]. 4.6.1.2

[120] A. Delgado, A. Martin and N. Raj, *Extending the Reach of Compressed Gluinos at the LHC*, *Phys. Rev.* **D94** (2016) 115010, [1605.06479]. 4.6.1.2

[121] C. Borschensky, M. Krämer, A. Kulesza, M. Mangano, S. Padhi, T. Plehn et al., *Squark and gluino production cross sections in pp collisions at $\sqrt{s}$ = 13, 14, 33 and 100 TeV*, *Eur. Phys. J.* **C74** (2014) 3174, [1407.5066]. 5.1, 7.4.2

[122] ATLAS collaboration, *Search for squarks and gluinos in final states with jets and missing transverse momentum using 36 1/fb of $\sqrt{s} = 13$ TeV pp collision data with the ATLAS detector*, Tech. Rep. ATLAS-CONF-2017-022, CERN, Geneva, Apr, 2017. 5.4, 5.5, 5.5.3, 10

[123] CMS collaboration, A. M. Sirunyan et al., *Search for new phenomena with the MT2 variable in the all-hadronic final state produced in proton-proton collisions at sqrt(s) = 13 TeV*, 1705.04650. 5.5.4, 7.6.3, 8.6, 8.6.2

[124] M. Lisanti and N. Weiner, *Electroweakinos Hiding in Higgs Searches*, *Phys. Rev.* **D85** (2012) 115005, [1112.4834]. 6.1

[125] T. Han, S. Padhi and S. Su, *Electroweakinos in the Light of the Higgs Boson*, *Phys. Rev.* **D88** (2013) 115010, [1309.5966]. 6.1

[126] P. Schwaller and J. Zurita, *Compressed electroweakino spectra at the LHC*, *JHEP* **03** (2014) 060, [1312.7350]. 6.1

[127] J. Bramante, P. J. Fox, A. Martin, B. Ostdiek, T. Plehn, T. Schell et al., *Relic Neutralino Surface at a 100 TeV Collider*, *Phys. Rev.* **D91** (2015) 054015, [1412.4789]. 6.1

[128] J. Bramante, N. Desai, P. Fox, A. Martin, B. Ostdiek and T. Plehn, *Towards the Final Word on Neutralino Dark Matter*, *Phys. Rev.* **D93** (2016) 063525, [1510.03460]. 6.1

[129] ATLAS collaboration, M. Aaboud et al., *Dark matter interpretations of ATLAS searches for the electroweak production of supersymmetric particles in $\sqrt{s} = 8$ TeV proton-proton collisions*, *JHEP* **09** (2016) 175, [1608.00872]. 6.1

[130] G. H. Duan, K.-i. Hikasa, L. Wu, J. M. Yang and M. Zhang, *Leptonic mono-top from single stop production at the LHC*, *JHEP* **03** (2017) 091, [1611.05211]. 6.1

[131] B. Fuks, M. Klasen, D. R. Lamprea and M. Rothering, *Gaugino production in proton-proton collisions at a center-of-mass energy of 8 TeV*, *JHEP* **10** (2012) 081, [1207.2159]. 6.1.2.1, 6.1.2.1

[132] B. Fuks, M. Klasen, D. R. Lamprea and M. Rothering, *Precision predictions for electroweak superpartner production at hadron colliders with* RESUMMINO, *Eur. Phys. J. C* **73** (2013) 2480, [1304.0790]. 6.1.2.1, 6.1.2.1

[133] ATLAS collaboration, *Search for electroweak production of supersymmetric particles in the two and three lepton final state at $\sqrt{s} = 13$ TeV with the ATLAS detector*, Tech. Rep. ATLAS-CONF-2017-039, CERN, Geneva, Jun, 2017. 6.2.10

[134] ATLAS collaboration, *Search for production of supersymmetric particles in final states with missing transverse momentum and multiple b-jets at $\sqrt{s} = 13$ TeV proton-proton collisions with the ATLAS detector*, Tech. Rep. ATLAS-CONF-2017-021, CERN, Geneva, Apr, 2017. 7.6.3

[135] CMS collaboration, *CMS Phase 1 heavy flavour identification performance and developments*, . 8.2, 8.6

[136] *Performance and Calibration of the JetFitterCharm Algorithm for c-Jet Identification*, Tech. Rep. ATL-PHYS-PUB-2015-001, CERN, Geneva, Jan, 2015. 8.2, 8.6

[137] A. Collaboration, *Performance of b-jet identification in the atlas experiment*, *Journal of Instrumentation* **11** (2016) P04008. 8.6

[138] ATLAS collaboration, *Search for Supersymmetry in events with b-tagged jets and missing transverse energy in pp collisions at $\sqrt{s} = 13$ TeV with the ATLAS detector*, Tech. Rep. ATLAS-CONF-2017-038, CERN, Geneva, May, 2017. 8.6, 8.6.2

[139] CMS collaboration, A. M. Sirunyan et al., *Search for supersymmetry in multijet events with missing transverse momentum in proton-proton collisions at 13 TeV*, 1704.07781. 8.6, 8.6.2

[140] N. Arkani-Hamed, A. G. Cohen, E. Katz and A. E. Nelson, *The Littlest Higgs*, *JHEP* **07** (2002) 034, [hep-ph/0206021]. 9.2

[141] M. Schmaltz and D. Tucker-Smith, *Little Higgs review*, *Ann. Rev. Nucl. Part. Sci.* **55** (2005) 229–270, [hep-ph/0502182]. 9.2

[142] J. Hubisz, S. J. Lee and G. Paz, *The Flavor of a little Higgs with T-parity*, *JHEP* **06** (2006) 041, [hep-ph/0512169]. 9.2

[143] M. Asano, S. Matsumoto, N. Okada and Y. Okada, *Cosmic positron signature from dark matter in the littlest Higgs model with T-parity*, *Phys. Rev.* **D75** (2007) 063506, [hep-ph/0602157]. 9.2

[144] T. Appelquist, H.-C. Cheng and B. A. Dobrescu, *Bounds on universal extra dimensions*, *Phys. Rev. D* **64** (Jun, 2001) 035002. 9.2

[145] H.-C. Cheng, K. T. Matchev and M. Schmaltz, *Radiative corrections to kaluza-klein masses*, *Phys. Rev. D* **66** (Aug, 2002) 036005. 9.2

[146] A. Datta, K. Kong and K. T. Matchev, *Discrimination of supersymmetry and universal extra dimensions at hadron colliders*, *Phys. Rev. D* **72** (Nov, 2005) 096006. 9.2

[147] L. Randall and R. Sundrum, *An alternative to compactification*, *Phys. Rev. Lett.* **83** (Dec, 1999) 4690–4693. 9.2